

Utah State University

DigitalCommons@USU

All Graduate Theses and Dissertations, Spring
1920 to Summer 2023

Graduate Studies

8-2012

The Chemical Evolution of Oceanic and Continental Lithosphere: Case Studies in the US Cordillera

Marlon Mauricio Jean
Utah State University

Follow this and additional works at: <https://digitalcommons.usu.edu/etd>



Part of the [Geology Commons](#)

Recommended Citation

Jean, Marlon Mauricio, "The Chemical Evolution of Oceanic and Continental Lithosphere: Case Studies in the US Cordillera" (2012). *All Graduate Theses and Dissertations, Spring 1920 to Summer 2023*. 1281.
<https://digitalcommons.usu.edu/etd/1281>

This Dissertation is brought to you for free and open access by the Graduate Studies at DigitalCommons@USU. It has been accepted for inclusion in All Graduate Theses and Dissertations, Spring 1920 to Summer 2023 by an authorized administrator of DigitalCommons@USU. For more information, please contact digitalcommons@usu.edu.



THE CHEMICAL EVOLUTION OF OCEANIC AND CONTINENTAL
LITHOSPHERE: CASE STUDIES IN THE US CORDILLERA

by

Marlon Mauricio Jean

A dissertation submitted in partial fulfillment
of the requirements for the degree

of

DOCTOR OF PHILOSOPHY

in

Geology

Approved:

John W. Shervais
Major Professor

Barry B. Hanan
Committee Member

Carol M. Dehler
Committee Member

Anthony R. Lowry
Committee Member

James P. Evans
Committee Member

Keith D. Putirka
Committee Member

Mark R. McLellan
Vice President for Research and
Dean of the School of Graduate Studies

UTAH STATE UNIVERSITY
Logan, Utah

2012

ABSTRACT

The Chemical Evolution of Oceanic and Continental Lithosphere:

Case Studies in the US Cordillera

by

Marlon M. Jean, Doctor of Philosophy

Utah State University, 2012

Major Professor: Dr. John W. Shervais
Department: Geology

Investigations into ophiolite from California demonstrated that these ultramafic rocks formed within the mantle wedge of a subduction zone. Fore-arc locales are dominated by highly refractory peridotite, formed by hydrous-fractional partial melting that began in the garnet stability field and ended in the spinel stability field. These ophiolites also displayed enriched fluid-mobile element concentrations. Based on melt models, these elements should have extremely low concentrations, yet all pyroxenes display enriched compositions. A new algorithm was derived to model this fluid enrichment process, which represents the total addition of material to the mantle wedge source region and can be applied to any refractory mantle peridotite that has been modified by melt extraction and/or metasomatism. Investigations into the interaction of a mantle plume with continental lithosphere demonstrated that Yellowstone-Snake River Plain olivine tholeiites are compatible with genesis from a deep-seated mantle plume and were modeled via mixing of three components. The variable age, thickness, and composition of North American lithosphere guide this process. Drill core near Twin Falls, ID was examined to assess (1) the chemical evolution of olivine tholeiite, (2) how basalt evolves in continental settings, and (3) the dominant fractionation process, e.g., fractional crystallization, Raleigh fractional crystallization, or assimilation fractional crystallization.

(216 pages)

PUBLIC ABSTRACT

The Chemical Evolution of Oceanic and Continental Lithosphere:

Case Studies in the US Cordillera

by

Marlon M. Jean, Doctor of Philosophy

Utah State University, 2012

Major Professor: Dr. John W. Shervais
Department: Geology

Among the terrestrial planets, only Earth has volcanism and plutonism that is related to plate tectonics. At the bottom of the oceans, mid-ocean ridges form where tectonic plates drift apart. More visible, and explosively dangerous, is volcanism related to the subduction of oceanic plates back into the Earth's mantle. Less clear is the origin of the third major type of volcanism, the so-called intra-plate volcanism, which is thought to represent thermally driven upwellings from the lower mantle. This dissertation investigates two of these unique volcano-tectonic settings which occur in the western United States.

Subduction zones are regions of intense earthquake activity and explosive volcanism. The sinking of oceanic lithosphere in subduction zones provides most of the force needed to drive the plates and cause mid-ocean ridges to spread, with the result that plate tectonics and subduction zones are both surficial and interior expressions of Earth's dominant tectonic mode. Subduction zones deliver raw materials to the "subduction factory," where oceanic lithosphere, sediments, and seawater re-equilibrate with the mantle, triggering melting and incidentally creating continental crust. What is not recycled in the upper few hundred kilometers of a subduction zone sinks to the core-mantle boundary, where this residue may be reheated for a billion years or so until it is resurrected as a mantle plume.

Mantle plumes or “hotspots” are thought to play a crucial role in the Earth’s thermal and tectonic evolution and are one of the major processes affecting the interior of the Earth. They have long been implicated in the rifting and breakup of continents, and plume-derived melts play a significant role in the creation and modification of sub-continental mantle lithosphere. Hot spots are zones of anomalous volcanism that cannot be directly associated with plate tectonic processes. They are typically thought to be supported by columnar upwellings of hot material or “plumes,” that arise from the deep mantle and punch through the mobile, convecting, shallow mantle to reach the surface. The term ‘hotspot’ is often applied to any long-lived volcanic center that is not part of the global network of mid-ocean ridges and island arcs. This concept of stationary heat sources in the mantle was first introduced in the 1960’s, with more evidence gathered thereafter. Although direct evidence for the existence of mantle plumes is sparse, their occurrence is consistent with our present understanding of mantle dynamics.

This dissertation investigates the Coast Range Ophiolite, California and the Snake River Plain, Idaho, which represent two distinct provinces within the North American Cordillera and ultimately concluded that the Coast Range Ophiolite and the Snake River Plain formed in response to a subduction zone and hotspot setting, respectively. The objectives of this research were to integrate the chemical and physical structure of these provinces, combine mantle geochemistry with geophysics, and trace each province back to their respective mantle provenance. The methods used to attain these objectives include major and trace element chemistry, which represents first-order data needed to understand fractional crystallization, magma recharge and mixing, assimilation of lower crust and/or pre-existing mafic intrusions, melting in the upper mantle at different depths, and variations in the composition of the mantle source region. Isotope data were also required to sort out the processes responsible for the major and trace element chemistry of eruptive products, distinguish the magma source components, and to constrain the time periods and dynamics of magmatic processes.

ACKNOWLEDGMENTS

As the saying goes, “it takes a village...” I’ve realized that as I have advanced through my academic career, many people in my “geo-village” have stepped up and guided me when times were good and especially when times were tough. I would like to acknowledge these mentors here because they helped me to become a better geologist, passed on skills and life lessons that I will never lose, and never lost faith in my abilities as a researcher. To Sam Mukasa and Steve Kesler (University of Michigan): you two first realized the potential in me that at the time I could never dream the heights I would one day reach, never let my spirits get too low even when rejection letters were flying in, nurtured my curiosity, and allowed me to follow my instincts. To Keith Putirka and John Wakabayashi (Fresno State): you challenged me to become a better and more thorough researcher, helped to improve my writing, and treated me more as a colleague and peer, rather than just another student. Lastly to John Shervais (Utah State University): no words can express my gratitude for taking me on as one of your last students and showing me how to balance research, writing, and teaching. You opened up my world-view by allowing me to explore new areas of the US and of the globe, in addition to meeting new friends whom I would never have met otherwise. Lastly, I appreciate deeply the friendship we have constructed and grown through the years. I would also like to acknowledge the hundreds of other faculty members, undergraduate students, and graduate students whom I’ve taught, interacted with, and worked with while at Michigan, Fresno State, and Utah State; your assistance, insight, and friendship have helped me immensely through the years.

Marlon M. Jean

CONTENTS

vi

	Page
ABSTRACT.....	ii
PUBLIC ABSTRACT.....	iii
ACKNOWLEDGMENTS.....	iv
LIST OF TABLES.....	viii
LIST OF FIGURES.....	ix
LIST OF SYMBOLS, NOTATION, DEFINITIONS.....	xi
CHAPTER	
1. INTRODUCTION.....	1
2. MELT EXTRACTION AND MELT REFERTILIZATION IN MANTLE PERIDOTITE OF THE COAST RANGE OPHIOLITE: AN LA-ICP-MS STUDY	
Abstract.....	10
Introduction.....	11
Geologic Setting.....	13
Previous Work.....	14
Analytical Methods.....	15
Results.....	17
Discussion.....	23
Conclusions.....	34
References.....	36
3. MULTI-COMPONENT MIXING FOR YELLOWSTONE-SNAKE RIVER PLAIN BASALTS: IMPLICATIONS FOR SUB-CONTINENTAL LITHOSPHERIC SOURCES AND THEIR INTERACTION WITH THE YELLOWSTONE HOTSPOT	
Abstract.....	60
Introduction.....	61
Geologic Setting.....	63
Methods.....	65
Results.....	66
Discussion.....	68
Summary.....	78
References.....	80

4.	LATE PLIOCENE TO QUATERNARY BASALTS FROM THE WENDELL RASA TEST WELL: ASSIMILATION- FRACTIONATION-RECHARGE PROCESSES OF THE CENTRAL SNAKE RIVER PLAIN, IDAHO	
	Abstract	99
	Introduction.....	100
	Regional Setting.....	102
	Core Observations.....	103
	Analytical Methods.....	108
	Geochemical Results.....	109
	Discussion.....	110
	Crustal and Mantle Processes of the central YSRP.....	120
	Conclusions.....	121
	References.....	122
5.	SUMMARY AND CONCLUSIONS.....	144
APPENDICIES		
A.	INSIDE THE SUBDUCTION FACTORY: FLUID MOBILE TRACE ELEMENTS IN THE MANTLE WEDGE ABOVE A SUBDUCTION ZONE	
	Abstract	151
	Introduction.....	152
	Regional Setting.....	154
	Analytical Methods.....	156
	Results.....	157
	Discussion.....	158
	Modeling Fluid Mobile Elements in Arc Volcanics.....	164
	Conclusions.....	165
	References.....	170
B.	WENDELL RASA GEOCHEMICAL-DEPTH STATISTICAL ANALYSIS.....	190
C.	CO-AUTHOR AND JOURNAL REPRINT RELEASE LETTERS	
	Sung-Hi Choi release letter.....	196
	Samuel Mukasa release letter.....	197
	Duane Champion release letter.....	198
	Contributions to Mineralogy and Petrology copyright release.....	199
	CURRICULUM VITAE.....	202

LIST OF TABLES

Table		Page
2-1	Average major element (wt%) and trace element (ppm) compositions of CRO clinopyroxene.....	45
2-2	Average major element (wt%) and trace element (ppm) compositions of CRO orthopyroxene.....	46
2-3	Input parameters for melting models.....	47
2-4	Melt refertilization model.....	48
3-1	Sr-Nd-Pb-Hf isotopic values for eastern, central, and western SRP, and Owyhee Plateau basalts.....	90
3-2	End-member isotope ratios and elemental abundances	91
3-3	Three component mixing model results.....	92
4-1	ICP-MS precision; comparison of USGS standard W-2.....	131
4-2	Snake River Group bulk-rock elemental analyses. Major oxides in wt%; trace elements and REE in ppm.....	132
4-3	Idaho Group bulk-rock elemental analyses. Major oxides in wt%; trace elements and REE in ppm.....	133
4-4	Input parameters for Snake River Plain batch melt models.....	134
A-1	Mean Error and Detection Limits of NIST 612 Glass Standard.....	181
A-2	Mean trace element compositions, 1σ error, detection limits, and ranges for Coast Range Ophiolite clinopyroxene.....	182
A-3	Results from fluid addition calculation at 0.5% melt increment of RAM source.....	183
A-4	Fluid-mobile element composition of fluid added to the mantle wedge.....	184

LIST OF FIGURES

Figure	Page
2-1 CRO Location map.....	49
2-2 Pyroxene quadrilateral plot.....	50
2-3 Photomicrographs of CRO peridotites.....	51
2-4 Minor and trace element variations in pyroxene as a function of Cr# in pyroxene.....	52
2-5 Chondrite-normalized REE concentrations for clinopyroxene in Group A Lherzolites and Group B Harzburgites.....	53
2-6 Multi-element variation diagrams.....	54
2-7 Correlation between Dy and Yb in CRO pyroxene.....	55
2-8 Melting models for clinopyroxene.....	56
2-9 Melting models for orthopyroxene.....	57
2-10 Extent of melting calculated from Cr# in spinel.....	58
2-11 Effects of melt refertilization.....	59
3-1 Digital elevation map of the Snake River Plain.....	93
3-2 Isotopic compositions for analyzed basalts.....	94
3-3 Compositions of SRP basalts vs. radial distance from Yellowstone.....	95
3-4 Mass fraction of SCLM-1 and SCLM-2 versus Sublithosphere mass fraction.....	96
3-5 Old and Young components vs. radial distance from Yellowstone.....	97
3-6 Schematic West-East cross sections of the SRP.....	98
4-1 Snake River Plain location map.....	135
4-2 Lithologic log and Paleomagnetic inclination results of Wendell RASA test hole 7S-15E-12CBA1	136
4-3 Classification of Wendell RASA lavas based on Total Alkalis (Na ₂ O + K ₂ O) vs. SiO ₂	137
4-4 Major and trace element compositions of Wendell RASA basalts.....	138
4-5 Primitive Mantle-normalized multi-element spider diagrams	139

		x
4-6	Comparison between a generalized stratigraphic column, paleomagnetic inclination data, and the chemical composition of Wendell RASA basalts, as a function of depth below surface (in meters).....	140
4-7	Crystallization and assimilation models for Wendell RASA basalts.....	141
4-8	Partial melting models for different mantle sources.....	142
4-9	Trace element co-variation diagrams.....	143
A-1	Geologic sketch map of California showing the location of Coast Range ophiolite localities.....	185
A-2	Trace element concentrations in clinopyroxene.....	186
A-3	Melt models of a DMM-source.....	187
A-4	DMM-normalized compositions of the fluid-added to the clinopyroxene.....	188
A-5	Comparison to arc melt compositions.....	189
B-1	Regression analysis of Snake River Group basalts.....	193
B-2	Regression analysis of Idaho Group basalts.....	194

LIST OF SYMBOLS, NOTATION, DEFINITIONS

Coast Range Ophiolite

$C_{\text{cpx,model}}$ = concentration of element i in clinopyroxene after partial melting

$C_{0,\text{wr}}$ = initial whole rock concentration of element i

D_{cpx} = partition coefficient of element i in clinopyroxene

D_{bulk} = bulk partition coefficient of element i

P = proportion of mineral phase entering liquid

F = fraction of partial melting

$C_{\text{cpx,obs}}$ = measured ppm concentration of element i via LA-ICP-MS

$C_{\text{cpx,added}}$ = added ppm value of element i to clinopyroxene

$C_{\text{wr,add}}$ = added ppm value of element i to whole rock

Snake River Plain

$Z_{\text{SCLM-1}}$ = mass fraction of old/depleted component

$Z_{\text{SCLM-2}}$ = mass fraction of young/enriched component

$Z_{\text{Sublithosphere}}$ = mass fraction of plume component

x_i/y_i = isotope ratio of end-member component 1, 2, or 3

x/y = measured isotope values from sample

n_1 = SCLM-1:Sublithosphere trace element ratio

n_2 = SCLM-2:Sublithosphere trace element ratio

CHAPTER 1

INTRODUCTION

The mantle is Earth's largest chemical reservoir (~ 68% by mass); therefore understanding the mantle is essential for interpreting Earth's long-term geochemical evolution. The ultramafic and mafic rocks manufactured above subduction zones and mantle plumes offer the best opportunity to study and model mantle processes. The extraction of magmas from the mantle is therefore a fundamental process towards understanding the construction of oceanic and continental crust. The North American Cordillera offers two classic settings where the melt extraction process and resulting volcanism are studied: the Coast Range Ophiolite, California and the Snake River Plain, Idaho.

This dissertation studies several aspects of the formation of Earth's oceanic and continental crust, using a variety of geologic techniques, principally major and trace elements, and radiogenic isotopes. This dissertation offers three first-authored manuscripts, with another co-authored manuscript provided in appendix A. Chapter 2 (published in *Contributions to Mineralogy and Petrology*) and appendix A (submitted to *Geochimica et Cosmochimica Acta*; in revision) focus on research into the Coast Range Ophiolite, while Chapters 3 (submitted to *Earth Planetary Science Letters*), 4 (submitted to *Bulletin of Volcanology*; in revision), and appendix B focus on research into the Snake River Plain. To address their respective genesis, analyses of major and trace elements, and radiogenic isotopes were used to trace each province back to their respective mantle origins. Furthermore, both standard and newly developed algorithms were used to model geochemical variations of ultra-mafic and mafic rocks. The goals of these studies were to: (1) apply new petrologic techniques to gain a better understanding of mantle processes, (2) gain further insight into how oceanic and continental lithosphere are constructed, (3) to relate the compositions of mafic and ultramafic rocks to their tectonic context, and (4) to integrate mantle composition with mantle dynamics.

The Coast Range Ophiolite (CRO) of California forms a discontinuous belt of ultramafic, mafic, and minor felsic igneous rocks approximately 700 km–long, and extends from the southern edge of the Klamath Mountains, Oregon, to the northern edge of Transverse Ranges, California (Shervais and Kimbrough, 1985; Hopson et al., 2008). The CRO represents an important tectonic element in understanding not only California geology, but also the formation of ophiolite sequences worldwide (Moores, 1982; Moores et al., 2000; Shervais, 2001; Metcalf and Shervais, 2008). Over the last four decades, three models have been debated extensively concerning the origin and evolution of this ophiolite complex: analogous to debates about the origin of ophiolites in general. The first model proposes formation and drift of a middle–Jurassic equatorial mid–oceanic ridge and collision with the Cordilleran margin (e.g., Hopson et al., 1981, 2008). This model is based on the stratigraphy and structure of ophiolite remnants, with emphasis on their overlying sedimentary sections (e.g., Hopson et al., 1981, 1996, 2008). The second model proposes formation in a back–arc basin, behind a middle–Jurassic island arc that was sutured to the Cordilleran margin during the late–Jurassic Nevadan orogeny (Schweickert et al., 1984; Godfrey and Klemperer, 1998). This model stresses regional tectonic relationships with primitive arc volcanism of the Sierra foothills (e.g., Godfrey and Dilek, 2000; Ingersoll, 2000). The third model proposes a supra–subduction zone (SSZ) setting above an east–dipping, proto–Franciscan subduction zone. This model focuses on the geochemistry of volcanic successions that form the upper crust of the ophiolite complex (e.g., Shervais and Kimbrough, 1985; Shervais, 1990, 2001, 2008; Stern and Bloomer, 1992; Giaramita et al., 1998; Evarts et al., 1999; Shervais et al., 2004, 2005a, 2005b).

Research into the Coast Range Ophiolite shows that this ophiolite was manufactured in a subduction setting (see Chapter 2 and Appendix A). Results show that both MOR– and SSZ–type peridotite are found within the CRO. Fore–arc locales are dominated by (or consist of) highly refractory peridotite formed by polybaric, hydrous–fractional partial melting that began in the garnet stability field and ended in the spinel stability field. Fluid mobile element (e.g., B, Ba, Li, Pb) enrichment was also documented in CRO peridotites. Melting models, based on rare–earth

and high field strength elements, show that fluid–mobile elements should have extremely low concentrations, however, all pyroxenes displayed enrichments relative to depleted MORB–mantle (DMM), e.g., B \sim 20–80x DMM and Pb \sim 4–20x DMM. A newly derived algorithm models the total addition of material to the mantle wedge source region and can be applied to any refractory mantle peridotite that has been modified by melt extraction and/or metasomatism.

The Snake River Plain (SRP) has been recognized for more than a century as a distinctive physiographic feature of the US Cordillera. It extends approximately 700 km, from the Yellowstone Plateau in northwest Wyoming, through southern Idaho, and into southeastern Oregon. This province links the voluminous basaltic outpourings from the Columbia River flood basalt province in the west to the rhyolitic volcanism from the Yellowstone Plateau in the east. It is one of several late Tertiary magmatic terranes, which also includes the Cascades magmatic arc, the Columbia River basalt, and the Oregon Plateau basalt: all of which are adjacent to the Basin and Range Province extensional system (Hughes and McCurry, 2002).

A deep–seated mantle plume, as first posited by Morgan (1972a), is one proposed model that accounts for this volcanism (Shervais and Hanan, 2008). Support for the plume model comes from recent studies of tectonic uplift along the plume track (Anders and Sleep, 1992; Smith and Braile, 1994; Pierce et al., 2002), seismic tomography of the underlying mantle (Yuan and Dueker, 2005; Waite et al., 2006; Obrebski et al., 2010), major– and trace–element chemistry of SRP lavas (Leeman, 1982a,b; Kuntz et al., 1992; Vetter and Shervais, 1992; Shervais et al., 2006), radiogenic isotopes (Reid and Leeman, 1993; Hanan and Schilling, 1997; Hanan et al., 2008), helium isotopes (Craig, 1993; Graham et al., 2009), and the 1000 km–wide geoid anomaly centered under Yellowstone (Smith and Braile, 1994). Non–plume centered models have also been proposed. Evidence cited in favor of a non–plume origin include the structure of the sub–continental lithosphere beneath the eastern SRP trend (Saltzer and Humphreys, 1997; Schutt et al., 1998; Christiansen et al., 2002), the large component of lithospheric melt inferred from some isotopic studies of SRP basalt (Leeman and Vitaliano, 1976; Hart, 1985; Reid, 1995; Leeman et al., 2009), the occurrence of other east–northeast–trending lava fields in the southern Great Basin

and Colorado Plateau (e.g., St. George volcanic trend and Jemez volcanic trend; Humphreys and Dueker, 1994; Humphreys et al., 2001), and the west–northwest anti–trend of the Oregon High Plains lavas (Jordan et al., 2004). However, many of these above observations are consistent with both models, and thus cannot be used to distinguish between the competing hypotheses.

Petrologic and geochemical investigations into the SRP detail (1) the observed geospatial and temporal isotopic trends from surface flows (see Chapter 3) and (2) the evolution of continental basalt systems through melting, assimilation, storage, and homogenization (or MASH) processes via a study of the Wendell RASA drill core (see Chapter 4 and Appendix B). These studies were designed to assess the origin of basaltic magmas in the SRP and their evolution through time. The isotope study shows that SRP olivine tholeiites can be modeled with a > 96% plume component, with varying amounts of depleted and enriched sub–continental lithospheric mantle (SCLM), consistent with previous models (e.g., Hanan et al., 2008). This process is guided by the age, thickness, and more importantly the composition of the SCLM; which includes the Grouse Creek block (> 2.5 Ga), the Farmington Zone (< 2.5 Ga), the Selway terrane (2.4 – 1.6 Ga), and the Wyoming Craton (> 2.5 Ga). Geochemical analyses on drill core samples from the central province of the SRP (1) establishes the nature and extent of chemical changes though time at a single location, where the physical, chemical, and isotopic characteristics of crust and mantle lithosphere are relatively fixed; (2) expands our knowledge of the crystal fractionation and magma recharge history of central SRP basalts; and (3) addresses how these changes relate to current models of basaltic volcanism in the SRP (e.g., Geist et al., 2002, Shervais et al., 2006).

References

- Anders MH, Sleep NH (1992) Magmatism and extension: the thermal and mechanical effects of the Yellowstone plume. *J Geophys Res* 97:15379–15393
- Christiansen RL, Foulger GR, Evans JR (2002) Upper–mantle origin of the Yellowstone hotspot. *Geol Soc Am Bull* 114:1245–1256

- Craig H (1993) Yellowstone hotspot: a continental mantle plume. *EOS* 74(43):602
- Evarts RC, Coleman RG, Schiffman P (1999) The Del Puerto ophiolite: Petrology and tectonic setting, in Wagner, D.L., and Graham, S.A., (eds.), *Geologic Field Trips in Northern California*. California Division of Mines and Geology Special Publication 119:136–149
- Geist D, Sims E, Hughes S (2002) Open–system evolution of a single cycle of Snake River Plain magmatism. *Geol Soc Am Special Paper* 353:193–204
- Giaramita MI, MacPherson GJ, Phipps SP (1998) Petrologically diverse basalt from a fossil oceanic forearc in California: The Llanada and Black Mountain remnants of the Coast Range ophiolite. *Geol Soc Am Bull* 110:553–571
- Godfrey NJ, Dilek Y (2000) Mesozoic assimilation of oceanic crust and island arc into the North American continental margin in California and Nevada: Insights from geophysical data, in Dilek, Y., Moores Eldridge, M., Elthon, D., and Nicolas, A., (eds.), *Ophiolites and oceanic crust: new insights from field studies and the Ocean Drilling Program*. *Geol Soc Am Special Paper* 349:365–382
- Godfrey NJ, Klemperer SL (1998) Ophiolite basement to a forearc basin and implications for continental growth: The Coast Range/Great Valley Ophiolite, California. *Tectonics* 17:558–570.
- Graham DW, Reid MR, Jordan BT, Grunder AL, Leeman WP, Lupton JE (2009) Mantle source provinces beneath the Northwestern USA delimited by helium isotopes in young basalts, (eds.), Morgan, Lisa A., Cathey, Hennrietta E., and Pierce, Kenneth L., *The Track of the Yellowstone Hot Spot: Multi–disciplinary Perspectives on the Origin of the Yellowstone–Snake River Plain Volcanic Province*. *J Volcanol Geotherm Res* 188(1–3):128–140
- Hanan BB, Schilling JG (1997) The Dynamic Evolution of the Iceland Mantle Plume: The Pb Isotope Perspective. *EPSL* 151(1–2):43–60
- Hanan BB, Shervais JW, Vetter SK (2008) Yellowstone plume–continental lithosphere interaction beneath the Snake River Plain. *Geology* 36(1):51–54
- Hart WK (1985) Chemical and isotopic evidence for mixing between depleted and enriched mantle, northwestern U.S.A. *Geochim Cosmochim Acta* 49(1):131–144

- Hart WK, Carlson RW (1987) Tectonic controls on magma genesis and evolution in the northwestern United States. *J Volcanol Geotherm Res* 32:119–135
- Hopson CA, Mattinson JM, Pessagno EA (1981) Coast Range Ophiolite, western California, in Ernst, W.G., (eds.), *The Geotectonic Development of California: Rubey*, v. 1, p. 418–510
- Hopson CA, Mattinson JM, Pessagno EA, Luyendyk BP (2008) California Coast Range ophiolite: Composite Middle and Late Jurassic oceanic lithosphere, in James E. Wright and John W. Shervais, (eds), *Ophiolites, Arcs, and Batholiths*, *Geol Soc Am Special Paper* 438
- Hopson CA, Pessagno EA, Mattinson JM, Luyendyk BP, Beebe W, Hull D, Munoz E, Blome C (1996) Coast Range ophiolite as paleoequatorial mid-ocean lithosphere, in Dickinson, W.R., Hopson, C.A., and Saleeby, J.B., (eds.), *Alternate origins of the Coast Range ophiolite (California): Introduction and implications*. *GSA Today* 6:1–10
- Hughes SS, McCurry M (2002) Bulk major and trace element evidence for a timespace evolution of Snake River Plain rhyolites, Idaho. *Idaho Geological Survey Bulletin* 30:161–176
- Humphreys ED, Dueker KG (1994) Physical state of the western U.S. upper mantle. *J Geophys Res* 99:9625–9650
- Humphreys ED, Dueker KG, Schutt DL, Smith RB (2001) Beneath Yellowstone; evaluating plume and non plume models using teleseismic images of the upper mantle. *GSA Today* 10:1–7
- Ingersoll RA (2000) Models for origin and emplacement of Jurassic ophiolites of northern California, in Dilek, Y., Moores, E., Elthon, D., and Nicolas, A., (eds.), *Ophiolites and Oceanic Crust*. *Geol Soc Am Special Publication* 349:395–402
- Jordan BT, Grunder AL, Duncan RA, Deino AL (2004) Geochronology of age-progressive volcanism of the Oregon High Lava Plains: Implications for the plume interpretation of Yellowstone. *J Geophys Res* 109:B10202
- Kuntz MA, Covington HR, Schorr LJ (1992) An overview of basaltic volcanism of the eastern Snake River Plain, Idaho, in P.K. Link, M.A. Kuntz, and L.B. Platt (eds.), *Regional Geology of Eastern Idaho and Western Wyoming*. *Geol Soc Am Memoir* 179:227–267

- Leeman WP (1982a) Olivine tholeiitic basalts of the Snake River Plain, Idaho, in Bonnicksen, B., and Breckenridge, R. M. (eds.), *Cenozoic geology of Idaho*. Idaho Bureau of Mines and Geology Bulletin 26:181–191
- Leeman WP (1982b) Development of the Snake River Plain–Yellowstone Plateau Province, Idaho and Wyoming: An overview and petrologic model, in Bonnicksen, B., and Breckenridge, R.M. (eds.), *Cenozoic geology of Idaho*. Idaho Bureau of Mines and Geology Bulletin 26:155–177
- Leeman WP, Schutt DL, Hughes SS (2009) Thermal structure beneath the Snake River Plain: Implications for the Yellowstone hotspot. *J Volcanol Geotherm Res* 188:57–67
- Leeman WP, Vitaliano CJ (1976) Petrology of McKinney Basalt, Snake River Plain, Idaho. *Geol Soc Am Bull* 87:1777–1792
- Metcalf RV, Shervais JW (2008) Supra–Subduction Zone (SSZ) Ophiolites: Is There Really An “Ophiolite Conundrum”? in James E. Wright and John W. Shervais (eds.), *Ophiolites, Arcs, and Batholiths: A Tribute to Cliff Hopson*. *Geol Soc Am Special Paper* 438:191–222
- Moores EM (1982) Origin and emplacement of ophiolites. *Reviews of Geophysics and Space Physics* 20:735–760
- Moores E, Kellogg LH, Dilek Y (2000) Tethyan ophiolites, mantle convection, and tectonic “historical contingency”: a resolution of the “ophiolite conundrum”, in Dilek, Y., Moores, E., Elthon, D., and Nicolas, A., (eds.), *Ophiolites and Oceanic Crust*. *Geol Soc Am Special Publication* 349:3–12
- Morgan WJ (1972a) Convection plumes and plate motions. *AAPG Bulletin* 56:203–213
- Obrebski M, Allen RM, Xue M, Hung S–H (2010) Slab–plume interaction beneath the Pacific Northwest. *Geophys Res Lett* 37:L14305
- Pierce KL, Morgan LA, Saltus RW (2002) Yellowstone Plume Head: Postulated Tectonic Relations to the Vancouver Slab, Continental Boundaries, and Climate. *Idaho Geological Survey Bulletin* 30:5–33
- Reid MR, Leeman WP (1993) Enriched mantle source of Snake River plain basalts: plume or lithosphere? *EOS* 74(43):602

- Saleeby JB (1982) Polygenetic ophiolite belt of the California Sierra Nevada: geochronological and tectonostratigraphic development. *J Geophys Res* B87:1803–1824
- Saltzer RL, Humphreys ED (1997) Upper mantle P wave velocity structure of the eastern Snake River Plain and its relationship to geodynamic models of the region. *J Geophys Res* 102 (B6):11,829–11,841
- Schweickert RA, Bogen NL, Girty GH, Hanson RE, Merguerian C (1984) Timing and structural expression of the Nevadan Orogeny, Sierra Nevada, California. *Geol Soc Am Bull* 95:967–979
- Schutt D, Humphreys ED, Dueker K (1998) Anisotropy of the Yellowstone Hot Spot Wake, Eastern Snake River Plain, Idaho. *Pure appl Geophys* 151:443–462
- Shervais JW (1990) Island arc and ocean crust ophiolites: contrasts in the petrology, geochemistry, and tectonic style of ophiolite assemblages in the California Coast Ranges. In: Malpas J, Moores EM, Panayiotou A, Xenophontos C (eds.), *Ophiolites: oceanic crustal analogues: proceedings of the symposium Troodos 1987*. Geological Survey Department, Nicosia, Cyprus, 507–520
- Shervais JW (2001) Birth, death, and resurrection: the life cycle of suprasubduction zone ophiolites. *Geochemistry Geophysics Geosystems* 2 (Paper number 2000GC000080)
- Shervais JW (2008) Tonalites, trondhjemites, and diorites of the Elder Creek ophiolite, California: low-pressure slab melting and reaction with the mantle wedge. In: Wright JE, Shervais JW (eds.), *Ophiolites, arcs, and batholiths: a tribute to Cliff Hopson*. *Geol Soc Am Special Paper* 438:113–132
- Shervais JW, Hanan BB (2008) Lithospheric topography, tilted plumes, and the track of the Snake River–Yellowstone hot spot. *Tectonics* 27 (TC5004)
- Shervais JW, Kimbrough DL (1985) Geochemical evidence for the tectonic setting of the Coast Range ophiolite; a composite island arc–oceanic crust terrane in western California. *Geology (Boulder)* 13:35–38

- Shervais JW, Kimbrough DL, Renne P, Murchey B, Hanan BB (2004) Multistage origin of the Coast Range Ophiolite, California and Oregon: implications for the life cycle of suprasubduction zone ophiolites. *Int Geol Rev* 46:289–315
- Shervais JW, Kolesar P, Andreasen K (2005b) Field and chemical study of serpentinitization—Stonyford, California: chemical fluxes and mass balance. *Int Geol Rev* 47:1–23
- Shervais JW, Murchey B, Kimbrough DL, Renne P, Hanan BB (2005a) Radioisotopic and biostratigraphic age relations in the Coast Range ophiolite, Northern California: implications for the tectonic evolution of the western Cordillera. *Geol Soc Am Bull* 117(5–6):633–653
- Shervais JW, Vetter SK, Hanan BB (2006) A Layered Mafic Sill Complex beneath the Eastern Snake River Plain: Evidence from Cyclic Geochemical Variations in Basalt. *Geology* 34:365–368
- Smith RB, Braile LW (1994) The Yellowstone hotspot. *J Volcanol Geotherm Res* 61:121–187
- Stern RJ, Bloomer SH (1992) Subduction zone infancy: examples from the Eocene Izu–Bonin–Mariana and Jurassic California. *Geol Soc Am Bull* 104:1621–1636
- Vetter, SK, Shervais, JW (1992) Continental basalts of the Boise River Group near Smith Prairie, Idaho. *J Geophys Res, B, Solid Earth and Planets* 97(6):9043–9061
- Waite GP, Smith RB, Allen, RM (2006) VP and VS structure of the Yellowstone hot spot from teleseismic tomography: Evidence for an upper mantle plume. *J Geophys Res, B, Solid Earth and Planets* 111:B04303
- Yuan H, Dueker K (2005) Telesismic P–wave tomogram of the Yellowstone plume. *Geophys Res Lett* 32:L07304

CHAPTER 2

MELT EXTRACTION AND MELT REFERTILIZATION IN MANTLE PERIDOTITE
OF THE COAST RANGE OPHIOLITE: AN LA-ICP-MS STUDY¹**Abstract**

The middle Jurassic Coast Range Ophiolite (CRO) is one of the most important tectonic elements in western California, cropping out as tectonically dismembered elements that extend 700 km from south to north. The volcanic and plutonic sections are commonly interpreted to represent a supra-subduction zone (SSZ) ophiolite, but models specifying a mid-ocean ridge origin have also been proposed. These contrasting interpretations have distinctly different implications for the tectonic evolution of the western Cordillera in the Jurassic. If an SSZ origin is confirmed, we can use the underlying mantle peridotites to elucidate melt processes in the mantle wedge above the subduction zone. This study uses laser ablation-inductively coupled plasma-mass spectrometry (LA-ICP-MS) to study pyroxenes in peridotites from four mantle sections in the CRO. Trace element signatures of these pyroxenes record magmatic processes characteristic of both mid ocean ridge and supra-subduction zone settings. Group A clinopyroxene display enriched REE concentrations [e.g., Gd (0.938–1.663 ppm), Dy (1.79–3.24 ppm), Yb (1.216–2.047 ppm), and Lu (0.168–0.290 ppm)], compared to Group B and C clinopyroxenes [e.g., Gd (0.048–0.055 ppm), Dy (0.114–0.225 ppm), Yb (0.128–0.340 ppm), and Lu (0.022–0.05 ppm)]. These patterns are also evident in orthopyroxene. The differences between these geochemical signatures could be a result of a heterogeneous upper mantle or different degrees of partial melting of the upper mantle. It will be shown that CRO peridotites were generated through fractional melting. The shapes of REE patterns are consistent with variable degrees of melting initiated within the garnet stability field. Models call for 3% dry partial melting of MORB-source asthenosphere in the garnet lherzolite field for abyssal peridotites and

¹Published manuscript: Jean MM, Shervais JW, Choi SH, Mukasa SB (2010) Melt Extraction and Melt Refertilization in Mantle Peridotite of the Coast Range Ophiolite: An LA-ICP-MS Study. *Contributions to Mineralogy and Petrology* 159:113–136

15–20% further partial melting in the spinel lherzolite field, possibly by hydrous melting for SSZ peridotites. These geochemical variations and occurrence of both styles of melting regimes within close spatial and temporal association suggest that certain segments of the CRO may represent oceanic lithosphere, attached to a large–offset transform fault and that east–dipping, proto–Franciscan subduction may have been initiated along this transform.

Introduction

Abyssal peridotites associated with oceanic crust provide important information on the process of mid–ocean ridge melt generation and subsequent mantle–melt interactions (e.g., Dick and Bullen 1984; Dick and Fisher 1984; Dick 1989; Johnson et al. 1990; Elthon 1992; Johnson and Dick, 1992; Seyler et al. 2003, 2004; Hellebrand et al. 2002). These studies have shown that abyssal peridotites represent the residues of near fractional melt extraction, with little or no retained melt porosity (“critical melting”). This process results in pyroxenes with strongly depleted light rare earth elements (LREE) relative to what would be expected from batch melting, and essentially flat MREE–HREE (e.g., Johnson et al. 1990; Hellebrand et al. 2002). Niu (1997) confirmed the melt–residue relationship between MORB and abyssal peridotite, but also revealed hidden complexities (Elthon 1992; Niu and Hekinian 1997; Niu et al., 1997).

Abyssal peridotites are dominantly spinel lherzolites formed by melting under dry conditions, from which relatively small melt fractions (~5–15%) have been extracted. In contrast, peridotites from the mantle wedge above subduction zones are typically spinel harzburgites or dunites, formed by the extraction of relatively large melt fractions (>20%) under hydrous melting conditions (e.g., Parkinson et al. 1992; Ishii et al. 1992; Arai 1994; Parkinson and Pearce 1998; Pearce et al. 2000; Widom et al. 2003). High fractions of partial melting are confirmed by high Cr/Al ratios in spinel and by whole rock incompatible trace element concentrations, which are strongly depleted when compared to abyssal peridotites (Parkinson et al. 1992; Parkinson and Pearce 1998; Pearce et al. 2000).

Detailed studies of fore–arc peridotites have been hampered by the difficulty in obtaining samples from active subduction settings. An alternative approach is to examine outcrops of ophiolite mantle that underlie crust known to have formed by supra–subduction zone (SSZ) magmatism. This mantle represents in part, the source from which the overlying crust was extracted. Moreover, its mineralogy and composition reflect the processes that have affected it through time, including melt extraction, fluid phase enrichment, and subsequent interactions with melts derived from deeper in the mantle tectosphere. These processes have been frozen in place by cooling and emplacement of the mantle lithosphere and its overlying crust. Large tracts of supra–subduction mantle are typically exposed at the base of such ophiolites, allowing us to examine their petrology and geochemistry on length scales that are larger than is currently possible in any active system (e.g., Bizimis et al. 2000; Choi et al. 2008a, b). The Coast Range ophiolite is an archetypical example of these types of ophiolites.

This study is the first to report on REE, high–field strength element (HFSE), and transition element (Sc, V) concentrations from in situ analysis of pyroxenes from the CRO peridotite section, collected by laser ablation–inductively coupled plasma–mass spectrometry (LA–ICP–MS). We use trace element systematics to constrain melting processes and melt enrichments in the mantle wedge above the Cordilleran subduction zone. A subsequent article will examine the fluid mobile elements and attempt to calculate water/rock ratios from olivine oxygen isotope compositions to calculate the total flux (melt + fluid) for the Cordilleran mantle wedge.

The data presented here show that the sub–arc mantle of the CRO is dominated by highly refractory harzburgites and dunites, which have suffered >20% melt extraction over a range of pressures, beginning in the garnet facies and ending in the spinel facies. These refractory lithologies have been re–fertilized in part, by the percolation of depleted melts derived from deeper in the mantle wedge. One locale is characterized by spinel lherzolites that are similar in composition to abyssal peridotites; these have been interpreted to represent a trapped remnant of older oceanic crust formed in a transform setting.

Geologic setting

The CRO is an assemblage of ultramafic, mafic, and minor felsic igneous rocks that crop out discontinuously from the southern edge of the Klamath Mountains in the north to the Transverse Ranges in the south (Hopson et al. 1981, 2008; Shervais and Kimbrough 1985). The crustal section of this ophiolite is dominated by volcanic rocks with arc-like geochemical signatures, including basaltic andesites, dacites, and boninites; and by plutonic rocks that include dunite, wehrlite, gabbro, and quartz diorite (Hopson et al. 1981, 2008; Shervais and Kimbrough 1985; Giaramita et al. 1998; Evarts et al. 1999; Snow 2002; Shervais et al. 2004, 2005a, b; Shervais 2008). Basalts with MORB-like geochemistry are less common and typically form late eruptives overlying younger arc-like volcanics or dikes that cross-cut older diorites (Giaramita et al. 1998; Evarts et al. 1999; Snow 2002; Shervais et al. 2005a, b). Radiometric dates define a narrow age range for most of these remnants, between 172 and 161 Ma, although some remnants preserve ages as young as 145 Ma associated with continued calc-alkaline volcanism (Hopson et al. 1981, 2008; Shervais et al. 2005a; Mattinson and Hopson 2008). Radiolarian assemblages in chert imply minimum ages of Bathonian to early Kimmeridgian (Shervais et al. 2005a).

Models proposed for the origin of the CRO include (1) formation and drift of a Middle Jurassic equatorial midoceanic ridge and collision with the Cordilleran margin (e.g., Hopson et al. 1981, 2008), (2) formation in a backarc basin, behind a Middle Jurassic island arc that was sutured to the Cordilleran margin during the Late Jurassic Nevadan orogen (Schweickert et al. 1984; Godfrey and Klempner 1998; Ingersoll 2000; Godfrey and Dilek 2000), and (3) formation by fore-arc or intra-arc rifting above an east-dipping, proto-Franciscan subduction zone (Saleeby 1982; Shervais and Kimbrough 1985; Shervais 1990, 2001, 2008; Stern and Bloomer 1992; Evarts et al. 1999; Giaramita et al. 1998; Shervais et al. 2004, 2005a). The preponderance of evidence from the crustal section favors the third option—formation by fore-arc or intra-arc rifting above an active subduction zone—but the occurrence of late MORB-like basalts implies a

more complex scenario in which the SSZ ophiolite is overlain or intruded by oceanic basalts, possibly during a ridge–trench collision (Shervais et al. 2004, 2005a).

The distribution of peridotite sample locations studied here is shown in Fig. 2–1. These include the Grey Eagle mine near Chrome (Red Mountain), Black Diamond Ridge (north of the Stonyford volcanic complex), the Hyphus–Little Stony Creek block (south of the Stonyford volcanic complex), Del Puerto Canyon in the Diablo Range, and Cuesta Ridge in the Sur–Nacimiento block. Spinel lherzolite is the dominant lithology in the Black Diamond Ridge suite. In contrast, Grey Eagle (Chrome), Hyphus–Little Stony Creek, Del Puerto Canyon, and Cuesta Ridge are dominantly spinel harzburgite with subordinate dunite and orthopyroxenite.

The Del Puerto Canyon and Cuesta Ridge locales consist of an arc–like volcanic section, which includes arc tholeiite basalt and dacite, boninite, late basalt volcanism with MORB–like geochemistry, and ash–rich radiolarian cherts that overlie the volcanic sections, typical of the CRO. The Grey Eagle mine sits within a fairly homogenous harzburgite block that lacks a crustal section. The Black Diamond Ridge and Hyphus–Little Stony Creek blocks are associated with the Stonyford Volcanic Complex—an array of oceanic tholeiite, alkali basalt, and primitive arc basalt that appears to represent long–term interactions between the ocean island basalts derived from the subducting slab and depleted high Mg, Al, low–Ti basalts derived from the overlying mantle wedge (Shervais et al. 2005b). This interaction may have occurred in a slab–trench window.

Previous work

The petrology and major element phase chemistry of these same samples has been discussed by Choi et al. (2008b), along with the implications of the data with respect to sub-arc mantle processes. Their study divided CRO peridotites into three groups based on Cr# ($100 * Cr / [Cr + Al]$) in spinel and Mg# ($100 * Mg / [Mg + Fe]$) and minor element compositions in clinopyroxene. Group A = low spinel Cr# (11–27), low Mg# (91–93), and relatively high Al₂O₃ (~4–6 wt%), TiO₂ (~0.3 wt%), and Na₂O (~1 wt%); Group B = intermediate Cr# spinel (35–60), high Mg# (93–95), and very low Al₂O₃ (~2–3 wt%), TiO₂ (<0.08 wt%), and Na₂O (>0.2 wt%);

and Group C = high Cr# spinel (60–84), high Mg# (93.5–95.5), and very low Al₂O₃ (~0.8–2 wt %), TiO₂ (<0.1 wt%), and Na₂O (<0.2 wt%). Group A pyroxenes occur at Black Diamond Ridge and Cuesta Ridge locales. Groups B and C type locales are found at Hyphus–Little Stony Creek block, Grey Eagle Mine (Chrome), Cuesta Ridge, and Del Puerto Canyon. All Group A peridotites are spinel lherzolites or clinopyroxene–rich harzburgites, while the Group B and C peridotites include both spinel harzburgites and dunites but not lherzolites. Orthopyroxenite samples have mineral chemistries similar to the Group C peridotites. Choi et al. (2008b) also presented Sr isotope compositions of ultra–pure, acid leached clinopyroxene mineral separates. Five of the six peridotite samples analyzed have ⁸⁷Sr/⁸⁶Sr isotopic compositions of 0.7038 to 0.7041, including both lherzolites and harzburgites, which are higher than Pacific MORB (0.7021 to 0.7031) but within the range of primitive arc basalts. One lherzolite has clinopyroxene with ⁸⁷Sr/⁸⁶Sr = 0.7025—within the range of Pacific MORB. The single analyzed orthopyroxenite has ⁸⁷Sr/⁸⁶Sr = 0.70297. These data are consistent with the introduction of a fluid flux containing radiogenic Sr, derived from a subducting slab (Choi et al. 2008b).

Choi et al. (2008a) presented Sr, Nd, Hf, and Pb isotopic compositions for four peridotite samples from the Stonyford area (Black Diamond Ridge, Hyphus–Little Stony Creek). They conclude that the isotopic compositions reflect (1) a subduction component with elevated ⁸⁷Sr/⁸⁶Sr and ²⁰⁸Pb/²⁰⁴Pb ratios relative to MORB and (2) reaction with a melt component similar in composition to the Stonyford alkali basalts (Shervais et al. 2005b). They conclude that peridotites in the Stonyford area reflect subduction initiation along a large–offset transform fault, based on the variations in isotopic and phase compositions, and on the low two–pyroxene equilibration temperatures compared to abyssal peridotites.

Analytical methods

Nineteen samples from the suite studied by Choi et al. (2008b), along with two additional samples, were selected for trace element analysis. Over 100 pyroxene grains were analyzed using a Thermo–Finnigan Element 2 High–Resolution Double Focusing Magnetic Sector ICP–MS, in

conjunction with a New Wave Research 213 nm ND–YAG Laser Ablation system at the University of Notre Dame. This method provides many advantages over conventional secondary ion mass spectrometry (SIMS), chiefly, that a larger number of elements can be accurately quantified with a detection limit similar to that of SIMS, but with much shorter counting times (e.g., Denoyer 1991; Jarvis and Williams 1993; Longerich et al. 1993).

Nineteen elements were selected for analysis in this study, including the rare earth elements (La, Ce, Nd, Sm, Eu, Gd, Tb, Dy, Ho, Er, Tm, Yb, and Lu) plus Y, the high–field strength elements (Nb, Zr, and Hf), and the transition metals (Sc, V). Each pyroxene spot was ablated with the focused laser beam and aspirated into the radio frequency plasma torch using an argon carrier gas, where it was dissociated into molecules and ionized atoms. The ions are passed into vacuum via a skimmer cone interface, where a lens stack focuses the ion beam into the mass spectrometer. The ions are sorted by mass and detected using a scanning electron multiplier. Ti and Cr concentrations were taken from electron microprobe analyses, and converted to ppm.

To prevent the laser from penetrating through the samples, we prepared polished thick sections. Sample collections ranged in laser power (80–100%), beam size (50–100 μm), scanning speed (1–3 $\mu\text{m/s}$), and shape (spot, raster, and line). These parameters were adjusted so that analyses were confined to the host mineral; fractures and inclusions were avoided. Samples were counted for 60 s on background before the laser was turned on, followed by 180 s of sample collection during ablation. Raw counts were converted into final concentrations using the LAMTRACE data reduction software (Jackson et al. 1997) with CaO (wt%), determined by electron microprobe analysis (Choi et al. 2008b), as the internal standard. Ablation signal integration intervals were selected by carefully inspecting the time–resolved analysis to ensure that no inclusions were present in the analyzed volume, and to remove surface contamination by eliminating the first sequence of laser pulses. NIST glass 612 (Pearce et al. 1997) was used as the secondary calibration standard and run twice before and after sample collection.

Results

Average major and trace element compositions of pyroxene from the five locales under study are listed in Tables 2–1 (clinopyroxene) and 2–2 (orthopyroxene) (complete data for individual sample spots are available in the data repository). Clinopyroxene was analyzed in five lherzolites from Black Diamond Ridge, one harzburgite from Hyphus–Little Stony Creek, one harzburgite from Cuesta Ridge, and one orthopyroxenite dike from Del Puerto Canyon. Orthopyroxene was analyzed in five lherzolites from Black Diamond Ridge, 15 harzburgites from Hyphus–Little Stony Creek, Grey Eagle Mine, Del Puerto Canyon, and Cuesta Ridge, and in one orthopyroxenite dike from Del Puerto Canyon. The two new samples from Cuesta Ridge are clinopyroxene–rich harzburgites with low Cr# spinels, belonging to Group A. Because of their fundamental difference from the other samples, we discuss the Group A lherzolites of Black Diamond Ridge and harzburgites of Cuesta Ridge separately from the Group B and C harzburgites and pyroxenites of the other locales. One of the Cuesta Ridge harzburgites (CR89–1) is characterized by relatively Fe–rich mafic phases (Fo85 olivine, pyroxene Mg# ~87), and high CaO concentrations (2.46 wt%) in orthopyroxene compared to other Group A samples. This sample also contains alteration products that may have formed from plagioclase, suggesting an origin by melt infiltration and reequilibration (e.g., Seyler et al. 2004, 2007).

Petrography

The samples studied here fall into the three groups identified by Choi et al. (2008b), based on the Cr# in their accessory spinel phase. The Group A samples are all spinel lherzolites or clinopyroxene–rich harzburgites (~5 to 8% modal clinopyroxene), whereas the Group B samples mostly comprise spinel harzburgites, with two spinel lherzolites and one orthopyroxenite. The Group C samples include clinopyroxene–poor and clinopyroxene–free spinel harzburgites, dunites, chromitites, a wehrlite, and three orthopyroxenites.

Clinopyroxenes in the peridotites studied here, and those studied by Choi et al. (2008b) for which we have no trace element data, are diopsides with Wo ~47.1–49.5%, En ~46.5–50.8%

(Fig. 2-2), and $\text{Cr}_2\text{O}_3 = 0.34\text{--}1.24$ wt% (Table 2-1 and Choi et al. 2008b). Orthopyroxenes in these rocks have enstatites with $\text{Wo} \sim 0.8\text{--}2.6\%$, $\text{En} \sim 88.4\text{--}91.9\%$ (Fig. 2-2), and $\text{Cr}_2\text{O}_3 = 0.39\text{--}0.81$ wt% (Table 2-1 and Choi et al. 2008b). Pyroxenites and wehrlites are commonly slightly more Fe-rich (clinopyroxenes $\text{Wo} \sim 47.4\text{--}47.8\%$, $\text{En} \sim 48.2\text{--}49.2\%$; orthopyroxenes $\text{Wo} \sim 0.8\text{--}1.6\%$, $\text{En} \sim 85.7\text{--}90.2\%$). Exsolution lamellae, where present, are generally thin although some large enstatites contain blebby exsolution of diopside; there is no indication of inverted pigeonite (which would indicate equilibration pressures of ≤ 1.8 GPa pressure: Nickel and Brey 1984). Blebby exsolution of diopside from enstatite is seen in a few samples.

The Group A lherzolites are characterized by either protogranular textures with smooth, curved grain boundaries, rare 120° triple grain interfacial angles, and a range of grain sizes and shapes (i.e., xenoblastic granular) or porphyroclastic textures, with large highly strained porphyroclasts of olivine and orthopyroxene surrounded by a groundmass of smaller strain free neoblasts with common 120° triple grain interfacial angles (Mercier and Nicolas 1975; Pike and Schwarzman 1977). Many Group A lherzolites contain transitional textures, with areas of relict protogranular texture surrounded by more common porphyroclastic texture. Group A lherzolites are relatively coarse-grained compared to the other groups, with enstatite averaging ~ 4.5 to 3.0 mm and diopside averaging ~ 1.7 to 1.0 mm in size (Fig. 2-3,a-b). Olivine grain size is difficult to determine reliably because of the extensive serpentinization in many samples, but is typically on the same order as the enstatite or slightly smaller, $\sim 2\text{--}3$ mm across. The pyroxenes are distributed fairly evenly throughout most samples, as are Cr-spinel grains, which tend to be small ($0.5\text{--}0.9$ mm) and form holly leaf or flattened grains. Some samples preserve clusters of enstatite-diopside-spinel, which may represent the breakdown products of precursor garnet, or the product of melt reactions with precursor garnet (Fig. 2-3,a-b).

The Group B harzburgite textures range from xenoblastic granular-equant (protogranular) with curved grain boundaries, mild kink-banding in olivine, and a range in grain sizes, to equigranular mosaic textures with straight grain boundaries, common 120° triple grain

interfacial angles, and discrete euhedral to subhedral spinel octahedral, that resemble annealed textures. Pyroxenes in Group B harzburgites are somewhat finer-grained than Group A lherzolites, with enstatite averaging $\sim 2.6\text{--}1.6$ mm and diopside ranging from ~ 0.2 mm to 1.1 mm in size (Fig. 2–3,c–d). Spinel forms small (~ 0.6 mm) grains flattened along silicate grain boundaries, or more rarely as holly leaf forms at multiple grain boundaries. Olivine grain size ($\sim 3\text{--}4$ mm average) is slightly larger than the Group A lherzolites. Diopside forms both large discrete grains and small interstitial grains flattened along grain boundaries. Protogranular harzburgites may contain clusters of enstatite–diopside–spinel that represent the breakdown of precursor garnet; the most convincing cluster is found in sample SFV–301, which contains an ameboid-shaped spinel surrounded by diopside and enstatite (Fig. 2–3,c–d).

Group C harzburgites and dunites are characterized by large, undeformed olivine grains (average ~ 4 mm) with finer-grained enstatite ($\sim 1.6 \times 1.2$ mm) and rare diopside (~ 0.36 mm). Cr–spinel forms equant or subequant grains and rhombohedra, ~ 1 mm across, distributed throughout the samples along silicate grain boundaries or as inclusions in olivine. Textures include xenoblastic granular–equant, xenoblastic granular–tabular and secondary protogranular, which resembles primary protogranular but with spinel distributed throughout the sample (Fig. 2–3, e–f). Diopside forms both large discrete grains and small interstitial grains flattened along grain boundaries. The scarcity of diopside in many of these samples ($<1\%$ modally), and its distribution as tiny grains adjacent to enstatite, suggest that it may form by granule exsolution from enstatite in these samples. Alternately, it may represent vestiges of incompletely extracted partial melt. In contrast, other samples contain diopside that is clearly “primary” and in textural equilibrium with the surrounding enstatite and olivine (Fig. 2–3,e–f).

Group C also includes more unusual lithologies, including wehrlite and orthopyroxenite. The wehrlite is characterized by large subequant olivine grains in an equigranular mosaic texture with modally abundant Cr–spinel grains that form large ($\sim 1\text{--}2$ mm) octahedral and rhombohedral grains scattered throughout the sample on grain boundaries and as inclusions in olivine. Diopside

forms relatively large irregular grains at triple grain boundaries, suggesting incompletely extracted partial melt or the percolation of melt formed elsewhere through the sample. Group C orthopyroxenites have decussate textures with large enstatites and somewhat smaller interstitial diopsides. These samples are clearly the crystal fractionates from a magma that was saturated dominantly in orthopyroxene, as proposed by Choi et al. (2008b).

Major and trace element trends in pyroxene

Clinopyroxenes from Group A lherzolites are characterized by relatively high concentrations of Al, Ti, and Na compared to clinopyroxene from Group B harzburgite and Group C orthopyroxenite (Fig. 2–4). These trends are mimicked by the middle to heavy REE and the HFSE, which are enriched by factors of 2–4x in the HREE and 10–15x in the MREE, relative to the more depleted Group B–C clinopyroxenes. Orthopyroxene from Group A lherzolite are characterized by relatively high concentrations of Al compared to orthopyroxenes in the Group B–C harzburgites and orthopyroxenite, but show limited enrichments in Ti, V, and Na that reflect the relatively low partition coefficients for these elements relative to clinopyroxene (Fig. 2–4). These trends are again mimicked by the middle to heavy REE and the HFSE, which are only slightly enriched in Group A orthopyroxenes relative to Group B–C orthopyroxenes (Fig. 2–4).

In general, there is a moderate negative correlation between minor or trace element concentration and Cr# in pyroxene, consistent with progressive melt extraction from the more fertile (lower Cr#) peridotites. The low trace element concentrations in pyroxene from the orthopyroxenite dike, along with the high pyroxene Cr#, implies that the melts from which this dike crystallized were formed by relatively high degrees of partial melting, as discussed below.

Pyroxene trace element chemistry

Chondrite-normalized REE abundances for Group A lherzolite clinopyroxene show strongly depleted LREE concentrations and slightly hump-shaped MREE to HREE concentrations, with a slight crest at Dy–Ho (Fig. 2–5a), similar to clinopyroxene in abyssal

peridotites from normal ridge segments (Johnson et al. 1990; Johnson and Dick 1992; Seyler and Bonatti 1997). Despite their strong LREE depletion, Group A clinopyroxenes have overall concentrations at the upper end of the abyssal peridotite range, with HREE \sim 8–10x chondrite. In contrast, clinopyroxenes from Group B harzburgite and Group C orthopyroxenite have steep positive slopes on the chondrite-normalized REE diagram, with strongly depleted concentrations relative to the Group A clinopyroxenes (e.g., Yb \sim 0.8–1.2x chondrite; Fig. 2–5a). The more highly incompatible elements (La, Ce, and Nd) are below their detection limits in some analyses, and their concentrations can only be inferred by extrapolation. These strongly LREE–MREE depleted patterns and low concentration levels are characteristic of other ophiolite clinopyroxenes (Batanova et al. 1998; Batanova and Sobolev 2000; Bizimis et al. 2000), and they are also similar to clinopyroxenes from fore-arc peridotites retrieved by dredging (Parkinson and Pearce 1998).

Chondrite-normalized REE patterns for Group A orthopyroxenes have lower concentrations and steeper overall slopes that lack the pronounced curvature of the clinopyroxene analyses (Fig. 2–5b). Concentrations range from \sim 0.8–1x chondrite for Lu to \sim 0.1x chondrite for Ce— about one order of magnitude lower than clinopyroxene concentrations (Fig. 2–5b). One sample (CR89–1) exhibits a distinct spoon-shaped pattern, with elevated concentrations of La, Ce, and Nd relative to the MREE, that indicates later melt refertilization (e.g., Seyler et al. 2003, 2007). REE concentrations in the Group B–C orthopyroxenes are slightly lower than that in the Group A orthopyroxenes, with Lu \sim 0.2–0.6x chondrite, and La–Ce below detection in most samples. Two samples from Hyphus–Little Stony Creek have spoon-shaped patterns indicating later melt enrichment (Fig. 2–5b).

The distinct differences between Group A lherzolite pyroxene, and Groups B–C harzburgite and orthopyroxenite pyroxene, are graphically displayed by multi-element variation diagrams (spider diagrams), in which the trace elements are arranged in order of decreasing incompatibility from left to right, and normalized to the MORB-source mantle concentrations of Salters and Stracke (2004). Group A lherzolite clinopyroxenes have MREE to HREE

concentrations that are 3–7x DMM, while the LREE range from 0.1 to 1x DMM (Fig. 2–6a). They display small depletions in the moderately incompatible HFSE (Zr, Hf, Ti, and Y) relative to their adjacent REE, and a small but distinct enrichment in the more incompatible element Nb relative to La, but depleted relative to Ce. The greater depletion of Zr relative to Hf reflects experimental distribution coefficients that are higher for Hf than Zr in clinopyroxene, but their depletion relative to the adjacent REE cannot be attributed to simple melt depletion. The normally compatible elements Sc and V display slight depletions relative to the HREE, indicating that they behave as slightly incompatible elements in these pyroxenes. Group A lherzolite orthopyroxenes are complementary to their coexisting clinopyroxenes, with MREE–HREE concentrations 0.1–1x DMM, and distinct positive anomalies in Nb, Zr, and Hf relative to their adjacent REE indicating higher partition coefficients that are less incompatible than in clinopyroxene. Sc and V vary positively with HREE concentration, suggesting that they are slightly incompatible in orthopyroxene.

In contrast, Groups B–C clinopyroxene have MREE to HREE concentrations that range from 0.1 to 0.7x DMM and LREE concentrations ~0.01x DMM (Fig. 2–6,b–c). The highly incompatible elements Nb, Zr, and Hf are slightly enriched relative to their adjacent REE, whereas the moderately incompatible elements Ti and Y are slightly depleted. The compatible element Sc displays a strong positive anomaly relative to the adjacent HREE, indicating retention in the pyroxenes, while Cr and V show slight enrichments indicating moderate compatibility in pyroxene. Group B–C orthopyroxenes are similar to Group B–C clinopyroxenes but are more depleted: MREE to HREE concentrations range from 0.05 to 0.9x DMM, the LREE Ce ~0.05x DMM, and the incompatible elements of Nb, Zr, Hf, and Ti are all enriched relative to their adjacent REE. As in the clinopyroxene, Sc, V, and Cr exhibit large positive anomalies relative to their adjacent HREE consistent with partition coefficients near one (Fig. 2–6,b–c).

Discussion

Tectonic affinity

The origin of ophiolite complexes has remained controversial despite decades of research (e.g., Moores et al. 2000; Shervais 2001; Metcalf and Shervais 2008). Structural studies have emphasized evidence from sheet dike complexes that require continuous extension as supporting a mid-ocean ridge setting (e.g., Moores et al. 2000 and references therein). In contrast, geochemical and petrologic evidence supports formation of most ophiolites in a nascent or primitive island arc setting, commonly referred to as “supra-subduction zone” or SSZ (e.g., Shervais 2001; Metcalf and Shervais 2008, and references therein). All of these studies focus on the crustal rock assemblages and ignore the significance of the underlying mantle peridotite, which should resemble abyssal peridotites if formed in an ocean basin, or fore-arc peridotites if formed in an arc setting.

Distinguishing between abyssal and fore-arc peridotites offers another approach to ophiolite origin that looks beneath the crustal section into the underlying mantle tectonites. Choi et al. (2008a,b) concluded from major element phase chemistry and isotopic compositions, that Black Diamond Ridge lherzolites resemble abyssal peridotites, whereas all of the other locations studied represent fore-arc peridotites. Batanova and Sobolev (2000) found a similar dichotomy in the Troodos ophiolite peridotites using SIMS analyses of relic clinopyroxene. In this section, we use the trace element composition of CRO peridotite pyroxenes to constrain their tectonic affinity by comparing them to pyroxenes from abyssal and fore-arc peridotites (Johnson et al. 1990; Johnson and Dick 1992; Parkinson and Pearce 1998; Hellebrand et al. 1999, 2002; Miller et al. 2002; Niu 2004).

A compilation of data for abyssal and fore-arc peridotites show that clinopyroxene from global abyssal peridotites are enriched in Dy and Yb (>0.5 ppm) compared to clinopyroxene from global fore-arc (SSZ) peridotites, which are restricted to values of ≤ 0.4 ppm for both elements (Fig. 2-7a). These elements are well suited for distinguishing tectonic affinity because they are

unlikely to be substantially modified by processes, such as mantle metasomatism or the removal of small melt fractions, and in spinel lherzolites they are hosted almost exclusively in clinopyroxene (e.g., Kostopoulos 1991). Our data for clinopyroxene from the Group A lherzolites of Black Diamond Ridge are consistent with an abyssal origin ($Dy = 1.5\text{--}3.5$ ppm, $Yb = 1.0\text{--}2.0$ ppm) and span the less depleted end of the global abyssal peridotite array (Fig. 2–7a). In contrast, clinopyroxene from Group B harzburgite (Hyphus–Little Stony Creek, $Dy = 0.22$ ppm, $Yb = 0.34$ ppm) and Group C orthopyroxenite (Del Puerto, $Dy = 0.11$ ppm, $Yb = 0.13$ ppm) require a suprasubduction zone setting (Fig. 2–7a,inset).

Although we have no global database of comparable abyssal or fore–arc data for orthopyroxene, similar relationships are displayed. Figure 2–7b shows a distinct separation between Black Diamond Ridge and Cuesta Ridge orthopyroxenes, on one hand, and samples from other locales (Grey Eagle, Del Puerto Canyon, Hyphus–Little Stony Creek). Orthopyroxenes from Black Diamond Ridge and Cuesta Ridge have elevated Dy ($\sim 0.07\text{--}0.18$ ppm) and Yb ($\sim 0.08\text{--}0.31$ ppm) compared to orthopyroxene from other locations ($Dy \sim 0.01\text{--}0.024$ ppm; $Yb \sim 0.01\text{--}0.14$ ppm). Locations with coexisting clinopyroxene data suggest that the differences observed here can be related to tectonic setting, suggesting that the Black Diamond Ridge and Cuesta Ridge samples are abyssal in origin, whereas all others are SSZ in origin.

These conclusions are further supported by the overall chondrite–normalized REE patterns for these samples: clinopyroxenes from Black Diamond Ridge parallel pyroxenes from abyssal peridotites, whereas clinopyroxenes from Hyphus–Little Stony Creek have much lower concentrations and parallel fore–arc peridotite pyroxenes (Fig. 2–5). The advantages of the concentration–based approach discussed above, however, are that it may be applied to both clinopyroxene and orthopyroxene, and that it does not require concentration data for the highly incompatible (and highly depleted) LREE to be effective.

One significant result of this approach is the documentation of abyssal–type peridotite within the Cuesta Ridge mantle section. Prior work has indicated that Black Diamond Ridge was

the only locality studied to date in the CRO that contained abyssal-type peridotites (Choi et al. 2008a,b). This suggests that wider sampling of other CRO locales may reveal similar complexities. We note that at both locales, where abyssal-type Group A peridotite has been found, the crustal sections contain MORB-like lavas. At Cuesta Ridge these lavas form late flows and crosscutting dikes (Snow 2002; Shervais et al. 2004). At Stonyford, MORB-like lavas form most of the seamount, intercalated with alkali basalts and refractory arc basalts (Shervais et al. 2005b,c).

Clinopyroxene melt model results

Johnson et al. (1990), based on clinopyroxene REE concentrations, first demonstrated that abyssal peridotites must have formed by fractional melting processes. This conclusion has been further substantiated by subsequent studies (Johnson and Dick 1992; Seyler et al. 2001; Hellebrand et al. 2001, 2002). We have attempted to match our measured clinopyroxene patterns using the fractional melting equations derived by Gast (1968) and Shaw (1970), and modified by Johnson et al. (1990) for residual clinopyroxene. This type of model simulates removal of each melt increment from the residue, which leads to extreme light-REE depletions in the residue (Johnson et al. 1990; Hellebrand et al. 2002). Batch melting models cannot match the extremely depleted LREE patterns of the clinopyroxenes, and even critical melting models with < 1% retained melt porosity fail to reproduce the observed concentration patterns.

Our goal is to quantify the extent of melt extraction and the conditions under which melting occurred (dry versus wet, high or low pressure). Input parameters include the starting bulk composition (assumed for our models to be the depleted MORB-source mantle of Salters and Stracke 2004), modal proportions of minerals in the parent lherzolite, the proportions of these minerals entering the melt, and mineral-melt distribution coefficients determined by experimental studies (Table 2–3). For all of our models we used the initial spinel lherzolite mode of Johnson and Dick (1992). For high pressure melting models, we converted these modes to garnet lherzolite using the method of Hellebrand et al. (2002). Melting proportions differ among the

conditions tested: garnet facies melting (Walter 1998), dry melting in the spinel facies (Baker and Stolper 1994), and water undersaturated melting in the spinel facies (Gaetani and Grove 1998).

A substantial dataset now exists on mineral–liquid partition coefficients for the elements under consideration. We selected values that best represent wedge melting, namely temperatures of 1,200–1,300°C, pressures in the spinel or garnet peridotite stability fields, and liquid compositions consistent with sub–alkaline primary melts. For dry melting in the spinel or garnet peridotite fields, we used distribution coefficients of Johnson (1998) with some non–REE values from Green et al. (2000). For wet melting in the spinel peridotite field we used the distribution coefficients of Green et al. (2000) for clinopyroxene and garnet. Orthopyroxene distribution coefficients were calculated separately for lherzolites with low Cr# and high Na, and harzburgites with high Cr# and low Na, using the method of Witt–Eickschen and O’Neill (2005) and the clinopyroxene distribution coefficients of Johnson (1998) (Table 2–3).

We applied two models to the Group A lherzolite clinopyroxenes: dry melting in the spinel lherzolite facies and dry melting in the garnet lherzolite facies; in the latter case, clinopyroxene compositions are recalculated into the spinel facies using the algorithm of Johnson et al. (1990). In both cases, critical melting models with up to 1% retained melt porosity overestimate the LREE concentrations; in contrast, fractional melting models are more successful at capturing the observed patterns.

Group A lherzolite clinopyroxene concentrations are matched imprecisely by ~2–4% fractional melting in the spinel lherzolite field. These models capture the LREE depletion but do not capture the overall shape of the pattern (Fig. 2–8a). The agreement of the model to the data decreases as we approach the LREE. In particular, the modeled LREE are either too high for low degree of partial melts or too low for higher degree of partial melts. As discussed previously, starting from Nd to Lu, the normalized clinopyroxene concentrations display a humped pattern. This characteristic is not modeled with spinel lherzolite melting, which have smooth slopes in the heavy to middle–REE that range from slightly negative at low degrees of melting to strongly

positive at high degrees of melting; in all cases these slopes cut across normalized clinopyroxene data. In contrast, ~3% partial melting in the garnet lherzolite field models both the LREE depletion, and the hump-shaped pattern in the MREE observed in Group A clinopyroxene, when converted to spinel lherzolite modes using the method of Johnson et al. (1990) and Hellebrand et al. (2002) (Fig. 2–8b). HREE concentrations in clinopyroxene vary little at different extents of melting in this model, suggesting that the observed variation in HREE content may result from small amounts of garnet field melting (1–3%), followed by additional small fractions of melting in the spinel field.

Not all Group A clinopyroxenes require garnet field melting. Clinopyroxene from one sample (SFV–220) have low MREE and HREE concentrations and lack the hump-shaped MREE pattern (Fig. 2–8a). This sample may reflect ~4% melting in spinel field only. Nonetheless, its overall REE and HFSE concentrations are similar to the other Group A lherzolites. None of the melting models presented above reproduce the highly depleted concentration pattern observed in the Group B harzburgite clinopyroxene (the Group C clinopyroxene is from a pyroxenite dike and thus represents a cumulate, not a residue). Even at melt fractions of 15–20%, the MREE remain too high compared to the HREE (Fig. 2–8a).

The dry melting models presented above do not apply to hydrous melting in a supra-subduction zone environment, where the degree of melting reflects depression of the mantle solidus in addition to adiabatic upwelling above the solidus. In addition, the proportions in which phases enter the melt differ from dry melting, i.e., the proportion of enstatite entering the melt is enhanced relative to clinopyroxene, and the proportion of olivine decreases in response to the incongruent melting of enstatite (e.g., Gaetani and Grove 1998). As discussed by Bizimis et al. (2000), this means that residual clinopyroxene persists to higher melt fractions (up to 29% melt) and enstatite is depleted more rapidly. Choi et al. (2008b) noted that the modes of “Cpx–poor” and “Cpx–free” harzburgites in the CRO agree well with the mode calculated for “Cpx–out” using hydrous melt proportions, and are strikingly different from the mode calculated for “Cpx–

out” using dry melting proportions. This supports our assumption here of hydrous melting and validates the melting mode chosen to model it. However, hydrous fractional melting in the spinel field presents similar results to anhydrous fractional melting (Fig. 2–8c).

A two–stage model obtains better results with initial melting in the garnet field, followed by melting in the spinel field. We use the hydrous melting proportions of Gaetani and Grove (1998) for the spinel field melting, and non–modal fractional melting for both spinel and garnet field melting. Four cases were calculated, for 1, 3, 6, and 10% melting in the garnet field, although only the results for 6% are shown (Fig. 2–8d). Two–stage melting, with 6% fractional melting of DMM–source mantle in the garnet field, followed by 15–20% further fractional melting in the spinel field, explains the ultra–depleted REE patterns in Group B clinopyroxene. This corresponds to a total melting of 21–26% (garnet field plus spinel field). Under anhydrous melting conditions, clinopyroxene disappears from the residual peridotite assemblage after ~23% melting (Falloon et al. 1988; Kinzler and Grove 1992; Hirose and Kushiro 1993; Wasylenski et al. 2003). However, during hydrous melting, clinopyroxene can persist as a residual phase up to ~29% partial melting (e.g., Gaetani and Grove 1998; Bizimis et al. 2000). Therefore, the high apparent melt fractions observed in the strongly refractory but primary clinopyroxene–bearing CRO harzburgite can only be achieved at shallow depths by hydrous melting in the mantle wedge above a subduction zone.

Orthopyroxene melt model results

Group B and C harzburgites contained clinopyroxene that were too small to analyze confidently with the relatively large beam of the laser probe. As a result, we have trace element analyses in many orthopyroxenes from samples with no corresponding clinopyroxene analysis. While many of these phases have highly incompatible element concentrations that are below detection limits, the less incompatible elements (e.g., MREE–HREE) are sufficiently precise, which allows us to apply melting models to these orthopyroxenes and thus extend our understanding of melt extraction to a wider range of samples. Furthermore, we can calibrate these

results using samples that contain both pyroxenes, providing us with confidence in the results obtained with the samples that have analyzed only orthopyroxene.

In order to model these orthopyroxenes we cannot simply chose one set of orthopyroxene–liquid distribution coefficients. Pyroxenes from Group A lherzolites and Group B harzburgites differ by a factor of 10 in their clinopyroxene HREE concentrations, however, only by a factor of two in their orthopyroxene HREE concentrations. This results from the effects of both temperature and minor element concentrations on distribution coefficients, which impacts orthopyroxene more so than clinopyroxene because of the lower overall minor element content in orthopyroxene (e.g., Hill et al. 2000; Witt–Eickschen and O’Neill 2005). These issues have been addressed by Witt–Eickschen and O’Neill (2005), who used multi–element regressions among xenoliths with different equilibration temperatures to produce algorithms for calculating clinopyroxene–orthopyroxene distribution coefficients. These algorithms include effects for relative depletion (Cr#) and minor element content (Na), and allow for the calculation of orthopyroxene–liquid distribution coefficients that are consistent with distribution coefficients used for coexisting clinopyroxene (Witt–Eickschen and O’Neill 2005).

We calculated orthopyroxene–liquid distribution coefficients for Group A lherzolites using the high Na content of coexisting clinopyroxene and lower Cr# of coexisting spinel. We calculated orthopyroxene–liquid distribution coefficients for Group B and C harzburgites using the lower Na content of coexisting clinopyroxene and higher Cr# of coexisting spinel. For both we used the clinopyroxene–liquid distribution coefficients of Johnson (1998). In order to estimate the appropriate equilibration temperature, we used observed Cpx/Opx concentration ratios for the HREE in samples, where both phases coexist and varied the model temperature for each group (Group A and Groups B–C) to achieve a best fit with the calculated Cpx/Opx ratios. These temperatures (Group A = 950°C, Group B–C = 1,100°C) were then used in the Witt–Eickschen and O’Neill (2005) model to calculate the full range of distribution coefficients for each group. These temperatures are higher than the two–pyroxene temperatures calculated by Choi et al.

(2008a: 800–920°C Group A; 760–950°C Groups B–C), but are consistent with expected melting temperatures in the mantle wedge and with the integrative effects of laser beam analysis, which homogenizes low temperature unmixing fairly effectively. These parameters result in orthopyroxene–liquid distribution coefficients that are 1.2x higher for REE and 2x higher for the HFSE in the Group B–C harzburgites relative to the Group A lherzolites (Table 2–3). This means that for given fractions of melt extraction, Group A orthopyroxenes will have lower incompatible element concentrations than Group B–C orthopyroxenes for the same extent of melting.

Melting models for orthopyroxene of both groups are shown in Fig. 2–9. Group A lherzolite orthopyroxenes are modeled with ~1% dry melting in the spinel field and with 3% garnet field melting transformed to spinel field compositions. As seen with Group A clinopyroxene compositions, dry spinel field melting matches some samples relatively well but fails to capture the overall pattern of LREE depletion with limited HREE variation (Fig. 2–9a); in contrast, 3% melting in the garnet field appears to fit the data relatively well (Fig. 2–9b), consistent with our results for clinopyroxene melting models and with the occurrence of pyroxene–spinel clusters (precursor garnet?) in some samples. Group B–C orthopyroxenes are modeled by hydrous melting in the spinel field (Fig. 2–9c) and by a two–stage model with 6% garnet field melting followed by spinel field melting (Fig. 2–9d). As with the Group B clinopyroxene, hydrous melting in the spinel field alone does not match the observed patterns, but two–stage melting (garnet field–spinel field) works well, modeled by 6% garnet field melting followed by 15% melting in the spinel field.

One question that must be addressed before we conclude is whether the pyroxenes analyzed here represent primary enstatites or inverted pigeonites. None of the samples studied here preserve textures characteristic of inverted pigeonite, which are common in many large mafic intrusions. Pigeonite is not stable at pressures greater than about 1.8 GPa (e.g., Nickel and Brey 1984) and is not expected to be a primary phase in peridotites undergoing decompression melting from greater depths. Even at lower pressures (~1.5 GPa), where a small pigeonite field is

present at the liquidus, peridotite decompressing from higher pressures will contain primary enstatite, not pigeonite.

It is possible that in some samples with very low modal diopside (<1%), the diopside may have formed by exsolution from a “primary” low-Ca pyroxene. These samples are characterized by high Cr#’s in both pyroxenes and in spinel, indicating high degrees of partial melting (>23%). If we calculate the inferred “primary” low-Ca pyroxene from pyroxene modes, however, it is nearly identical in composition to the analyzed enstatite because the modal ratio of diopside/enstatite is extremely low in these samples. As a result, the inferred primary low-Ca pyroxene is enstatite, not pigeonitic in composition. In addition, our calculated partition coefficients for Group B–C orthopyroxenes are close to the experimentally determined values for enstatite (e.g., Johnson 1998), suggesting that these coefficients are valid despite the lack of diopside saturation in the primary assemblage of a few samples. James et al. (2002) have shown that when pyroxenes form from pigeonite inversion, the resulting diopside/enstatite partition coefficients will be much higher than the ratios calculated for primary phases; this is the opposite of what we observe in our Group B–C samples.

Overall, our results show that orthopyroxene can be used to calculate melting models in the absence of clinopyroxene data, provided data are available for a few Cpx–Opx pairs in order to calibrate the orthopyroxene distribution coefficients. The consistency achieved by our models for both pyroxenes supports extrapolation of these models to more refractory Cpx–free harzburgites formed by higher degrees of partial melting, which are common within ophiolites and fore–arc, supra–subduction–type peridotites.

Extent of melting calculated from Cr# in spinel

If possible, we would like to apply an independent method for confirming the extent of melting based on REE contents. Hellebrand et al. (2001) developed such a method for estimating the degree of melting in abyssal peridotites based on the Cr# in accessory spinel and its correlation with MREE–HREE concentrations in coexisting clinopyroxene. As discussed

previously, the concentrations of these moderately incompatible elements are controlled by the extent of melt extraction from the peridotite, and are little affected by later melt enrichment or metasomatism. Hellebrand et al. (2001) developed an empirical equation that describes the extent of melting (F) as a function of spinel $Cr\#$ ($F = 10 \ln(Cr\#) + 24$) using the MREE to HREE to calculate theoretical melt fractions for a range of abyssal peridotites.

Group A lherzolites have low $Cr\#$ s in spinel (10–30), while spinels in Group B–C harzburgites and dunites have higher $Cr\#$'s (30–85). Neodymium concentrations in Group A and B clinopyroxenes are highly correlated with the $Cr\#$ ratios of coexisting spinel (Fig. 2–10). Black Diamond Ridge samples plot near 3% melting in the garnet field. This figure includes data on Black Diamond Ridge samples from the study of Choi et al. (2008b), which are similar in their Nd concentrations and extent of melting. Sample SFV220, as discussed before, has a higher percent melt and lies off this trend. Sample SFV307, from Choi et al. (2008a), plots well off the melting trend, toward Group B clinopyroxenes. The Group B clinopyroxenes have higher melting percents and are also similar to the melting percents calculated with the REE modeling (e.g., 15–20% melting for the Stony Creek and Del Puerto Canyon harzburgites). Group B harzburgites from Burro Mountain and Del Puerto Canyon (Choi et al. 2008a) plot on the same melting trend, and again are similar to the melting percents and Nd concentrations of this study.

The two melting trends observed here correlate with either abyssal peridotites (Black Diamond Ridge, Cuesta Ridge) or with SSZ peridotites (Grey Eagle, Hyphus–Little Stony Creek, Del Puerto, and Burro Mountain). The abyssal peridotite trend reflects dry melting of a fertile MORB–source mantle. In contrast, the SSZ trend reflects hydrous melting of a more refractory source within the mantle wedge.

Melt refertilization in the mantle wedge

One of the salient characteristics of our study is that pyroxene from Group A lherzolites and Group B–C harzburgites exhibit slight enrichments in their LREE and more incompatible HFSE concentrations, relative to those expected from our melting models (Figs. 2–8, 2–9, 2–10).

These effects are muted for the Group A lherzolite pyroxenes, but significant for pyroxenes from the Group B–C harzburgites. These enrichments can only result from interaction between the depleted peridotites and an exotic magma formed deeper in the mantle (e.g., Johnson et al. 1990).

We modeled melt refertilization in CRO pyroxenes using the protocols formalized by Hellebrand et al. (2002). For Group A lherzolites, a residual pyroxene composition is calculated for 8% melting in the spinel field. This is enriched by a depleted melt formed by 20% melting in the spinel field, which is added incrementally to match the MREE–HREE abundance patterns (Table 2–4). The added melt is assumed to form 70% clinopyroxene and 30% olivine + orthopyroxene + spinel (Elthon 1992). The added pyroxene component is equilibrated with the residual pyroxene to obtain a single pyroxene composition. A similar procedure is followed for the Group B–C pyroxenes, except in this case the residual pyroxene composition is calculated for 6% melting in the garnet field followed by 15% melting in the spinel field, and then by addition of a depleted melt formed by 20% melting in the spinel field.

A range of model calculations shows that the observed concentration patterns and abundances of REE and HFSE in Group A clinopyroxenes are best matched by extremely small fractions of added melt—0.1 to 0.3% melt (Fig. 2–11a). This is consistent with the muted evidence for melt refertilization (e.g., fractionation of HFSE/REE ratios). Models with more or less melting to form the initial residual pyroxene have HREE concentrations that are too low or too high compared to those observed, and models that use a less depleted melt fraction result in too much enrichment of the more incompatible elements relative to the HREE. The Group B–C harzburgites are best matched by relatively small fractions of added melt (0.1–0.3%), but as noted above the starting pyroxene composition is much more depleted than in the Group A pyroxenes. The Group A orthopyroxene Cuesta Ridge sample CR89–1—which contains evidence for modal metasomatism—may contain up to 3% melt enrichment. We have modeled this enrichment by simple melt addition in Fig. 2–11, but the low silicate Mg#s suggest melt percolation and

reequilibrium which has affected the silicate major element phase chemistry more profoundly than the incompatible element budget.

Origin of the orthopyroxenite dikes

Orthopyroxenite dikes are common in many Coast Range ophiolite locations. Two distinct origins have been proposed for these dikes, which are commonly associated with dunite bodies: (1) the reaction of silicic aqueous fluids with olivine to form enstatite (e.g., Kelemen et al. 1992, 1997), and (2) the percolation of enstatite-saturated melts through fractures to form veins and dikes (e.g., Shervais 1979). Choi et al. (2008b) use the major element mineral chemistry of the phases to support an origin as frozen melts or cumulates from a depleted, boninitic magma. Our data support the same model: the LREE/HREE ratios of pyroxenes in the dike are too high to represent residual pyroxene or refractory olivine that has reacted with an aqueous fluid. In a volcanic system, where boninites occur, the crystallization of Opx-saturated, ultra-depleted boninitic magmas that fractionated in the mantle prior to eruption, probably accompanied by melt/mantle rock interaction, is to be expected. Using appropriate distribution coefficients, we can invert the trace element concentrations of pyroxenes from the dike to calculate the equilibrium melt. This melt has trace element patterns that are similar to depleted boninites from the SW Pacific, but at slightly lower concentrations. These data support the proposal of Choi et al. (2008b) that the orthopyroxenite dikes represent boninite cumulates, not silica metasomatism of olivine along fluid filled fractures.

Conclusions

The data presented in this study reaffirm the complexities of peridotite geochemistry in the mantle wedge above a subduction zone (Parkinson and Pearce 1998). Our data show that most Coast Range ophiolite locales are dominated (or consist) by highly refractory peridotite formed by > 20% polybaric hydrous fractional partial melting, beginning in the garnet stability field and ending in the spinel stability field. These rocks are largely clinopyroxene-poor harzburgites with

subordinate dunites. Clinopyroxene persists to relatively high melt fractions (~ 29%) as a result of hydrous melting proportions, whereas orthopyroxene contributes higher melt fractions, resulting in equilibrium melts that are more enriched in silica at high MgO concentrations than abyssal tholeiites. Subsequent melt enrichment is limited ($\leq 0.3\%$ added melt fractions) but may have a significant impact due to the low incompatible element concentrations in the highly refractory pyroxenes.

Abyssal-type peridotites are restricted to two locations, Black Diamond Ridge and Cuesta Ridge. The Black Diamond Ridge lherzolites form a distinct block that is physically separated from the more common SSZ peridotites that crop out south of the Stonyford volcanic complex, whereas the Cuesta Ridge Cpx-harzburgites are found within the same block as the more abundant SSZ peridotites. In both locales the abyssal-type peridotites formed by ~2–4% anhydrous melting in the garnet stability field, with or without small amounts (<3%) continued melting in the spinel stability field. Most samples show little evidence for refertilization ($\leq 0.1\%$ added melt), but one (CR89-1) has low Mg# silicates and possible plagioclase alteration products; this sample may have undergone up to 3% melt addition. These results are consistent with the conclusions of Choi et al. (2008a) based on major element phase chemistry and isotopic studies. However, whereas the major element phase chemistry allows estimates of total melt extraction, the trace element phase chemistry presented here allows us to rule out batch melting as a process, and to establish fractional melting (or critical melting with small, < 0.5% retained melt fractions) as the dominant process controlling the composition of these samples.

Our study also demonstrates that LA-ICP-MS analyses of orthopyroxene can be used effectively to distinguish tectonic settings of harzburgites and to calculate melt extraction and melt refertilization models in the absence of clinopyroxene data. However, care must be used in calculating Opx/melt distribution coefficients because these are sensitive to equilibration temperatures. This problem can be addressed if some Cpx-bearing samples are present by combining observed Cpx/Opx concentration ratios to models of Cpx/Opx partitioning and

adjusting the equilibration temperatures to match the HREE concentration ratios. This allows calculation of an internally consistent set of Cpx/melt and Opx/melt distribution coefficients that will yield the same results for either phase in fractional melting models.

Finally, detailed trace element analyses of pyroxenes from a pyroxenite dike show that these small dikes and veins represent cumulates from highly refractory, silica-rich melts similar in composition to boninites. These melts reflect high degrees of melting under hydrous conditions, during which orthopyroxene extraction is enhanced relative to clinopyroxene.

References

- Anders E, Grevesse N (1989) Abundances of the elements: meteoric and solar. *Geochim Cosmochim Acta* 53:197–214
- Arai S (1994) Characterization of spinel peridotites by olivine–spinel compositional relationships: review and interpretations. *Chem Geol* 113:191–204
- Baker MB, Stolper EM (1994) Determining the composition of high–pressure mantle melts using diamond aggregates. *Geochim Cosmochim Acta* 58:2811–2827
- Batanova VG, Sobolev AV (2000) Compositional heterogeneity in subduction–related mantle peridotites, Troodos massif, Cyprus. *Geology* 28:55–58
- Batanova VG, Suhr G, Sobolev AV (1998) Origin of geochemical heterogeneity in the mantle peridotites from the Bay of Islands ophiolite, Newfoundland, Canada: ion probe study of clinopyroxenes. *Geochim Cosmochim Acta* 62:853–866
- Bizimis M, Salters VJM, Bonatti E (2000) Trace and REE content of clinopyroxenes from supra–subduction zone peridotites. Implications for melting and enrichment processes in island arcs. *Chem Geol* 165:67–85
- Choi SH, Mukasa SB, Shervais JW (2008a) Initiation of Franciscan subduction along a large–offset fracture zone: evidence from mantle peridotites, Stonyford, California. *Geology* 36(8): 595–598

- Choi SH, Shervais JW, Mukasa SB (2008b) Supra-subduction and abyssal mantle peridotites of the Coast Range ophiolite, California. *Contrib Mineral Petrol* (in press)
- Denoyer ER (1991) Current trends in ICP-mass spectrometry. *At Spectrosc* 12:215–224
- Dick HJB (1989) Abyssal peridotites, very slow spreading ridges, andocean ridge magmatism. In: Saunders AJ, Norry MJ (eds) *Magmatism in the Oceanic Basins*. Geological Society of London Special Publication, vol 42, pp 71–105
- Dick HJB, Bullen T (1984) Chromian spinel as a petrogenetic indicator in abyssal and alpine-type peridotites and spatially associated lavas. *Contrib Mineral Petrol* 86:54–76
- Dick HJB, Fisher RL (1984) Mineralogic studies of the residues of mantle melting: abyssal and alpine type peridotites. In: Komprobst J (ed) *The mantle and crustal-mantle relationships—mineralogical, petrological, and geodynamic processes*, 3rd international Kimberlite conference, vol II. New York, NY, pp 295–308
- Elthon D (1992) Chemical trends in abyssal peridotites: refertilization of depleted oceanic mantle. *J Geophys Res* 97:9015–9025
- Evarts RC, Coleman RG, Schiffman P (1999) The Del Puerto ophiolite: petrology and tectonic setting. In: Wagner DL, Graham SA (eds) *Geologic field trips in northern California*. California Division of Mines and Geology Special Publication, vol 119, pp 136–149
- Falloon TJ, Green DH, Hatton CJ, Harris KL (1988) Anhydrous partial melting of a fertile and depleted peridotite from 2 to 30 Kb and application to basalt petrogenesis. *J Petrol* 29(6):1257–1282
- Gaetani GA, Grove TL (1998) The influence of water on melting of mantle peridotite. *Contrib Mineral Petrol* 131:323–346
- Gast PW (1968) Upper mantle chemistry and evolution of the Earth's crust. In: Phinney RA (ed) *The history of the Earth's crust, a symposium*. Princeton University Press, Princeton, NJ, pp 15–27

- Giaramita MI, MacPherson GJ, Phipps SP (1998) Petrologically diverse basalts from a fossil oceanic forearc in California: the Llanada and Black Mountain remnants of the Coast Range ophiolite. *Geol Soc Am Bull* 110:553–571
- Godfrey NJ, Dilek Y (2000) Mesozoic assimilation of oceanic crust and island arc into the North American continental margin in California and Nevada: insights from geophysical data. In: Dilek Y, Moores Eldridge M, Elthon D, Nicolas A (eds) *Ophiolites and oceanic crust: new insights from field studies and the Ocean Drilling Program*. Geological Society of America (GSA) Boulder, Special Paper 349, pp 365–382
- Godfrey NJ, Klemperer SL (1998) Ophiolite basement to a forearc basin and implications for continental growth; the Coast Range/Great Valley Ophiolite, California. *Tectonics* 17:558–570
- Green TH, Blundy JD, Adam J, Yaxley GM (2000) SIMS determination of trace element partition coefficients between garnet, cpx, and hydrous basaltic liquids at 2–7.5 GPa and 1080–1200°C. *Lithos* 53:165–187
- Hellebrand EW, Snow JE, Dick HJB, Devey CW, Hofmann AW (1999) Reactive crack flow in the oceanic mantle: an ion probe study on cpx from vein-bearing abyssal peridotites. *Ophiolite* 24:106–107
- Hellebrand E, Snow JE, Dick HJB, Hofmann AW (2001) Coupled major and trace elements as indicators of the extent of melting in mid-ocean-ridge peridotites. *Nature* 410:677–681
- Hellebrand E, Snow JE, Hoppe P, Hofmann AW (2002) Garnet-field melting and late-stage refertilization in ‘residual’ abyssal peridotites from the Central Indian Ridge. *J Petrol* 43(12): 2305–2338
- Hill E, Wood BJ, Blundy JD (2000) The effect of Ca-Tschermaks component on trace element partitioning between clinopyroxene and silicate melt. *Lithos* 53:203–215
- Hirose K, Kushiro I (1993) Partial melting of dry peridotites at high pressures: determination of compositions of melts segregated from peridotite using aggregates of diamond. *Earth Planet Sci Lett* 114:477–489

- Hopson CA, Mattinson JM, Pessagno EA (1981) Coast Range ophiolite, western California. In: Ernst WG (ed) *The Geotectonic Development of California*. Rubey, vol 1, pp 418–510
- Hopson CA, Mattinson JM, Pessagno EA, Luyendyk BP (2008), California Coast Range ophiolite: composite middle and late Jurassic oceanic lithosphere. In: Wright JE, Shervais JW (eds) *Ophiolites, arcs, and batholiths: a tribute to Cliff Hopson*. Geological Society of America Special Paper 438, pp 1–102
- Ingersoll RA (2000) Models for origin and emplacement of Jurassic ophiolites of northern California. In: Dilek Y, Moores E, Elthon D, Nicolas A (eds) *Ophiolites and oceanic crust*. Geological Society of America Special Publication, vol 349, pp 395–402
- Ishii T, Robinson PT, Maekawa H, Fiske R (1992) Petrological studies of peridotites from diapiric serpentinite seamounts in the Izu–Ogasawara–Mariana forearc, Leg 125. In: *Proceedings of the ocean drilling program, scientific results 125*. Texas A & M University, Ocean Drilling Program, College Station, TX, United States, pp 445–485
- Jackson S, Longrich H, Horn I (1997) The application of laser ablation microprobe–inductively coupled plasma–mass spectrometry (LA–ICP–MS) to in situ trace–element determinations in minerals. 4th Australian symposium on applied ICP–mass spectrometry, MacQuarie University, Sydney
- James OB, Floss C, McGee JJ (2002) Rare earth element variations resulting from inversion of pigeonite and subsolidus reequilibration in lunar ferroan anorthosites. *Geochim Cosmochim Acta* 65(7):1269–1284
- Jarvis KE, Williams JG (1993) Laser ablation inductively coupled plasma mass spectrometry (LA–ICP–MS): a rapid technique for the direct, quantitative determination of major, trace and rare–earth elements in geological samples. *Chem Geol* 106(3–4):251–262
- Johnson KTM (1998) Experimental determination of partition coefficients for rare earth and high–field–strength elements between clinopyroxene, garnet, and basaltic melt at high pressures. *Contrib Mineral Petrol* 133:60–68

- Johnson KTM, Dick HJB (1992) Open system melting and temporal and spatial variation of peridotite and basalt at the Atlantis II fracture zone. *J Geophys Res* 97:9219–9241
- Johnson KTM, Dick HJB, Shimizu N (1990) Melting in the oceanic upper mantle; an ion microprobe study of diopsides in abyssal peridotites. *J Geophys Res* 95:2661–2678
- Kelemen PB, Dick HJB, Quick JE (1992) Formation of harzburgite by pervasive melt/rock reaction in the upper mantle. *Nature* 358:635–641
- Kelemen PB, Hirth G, Shimizu N, Spiegelman M, Dick HJB (1997) A review of melt migration processes in the adiabatically upwelling mantle beneath oceanic spreading ridges. *Phil Trans R Soc Lond* 355:283–318
- Kinzler RJ, Grove TL (1992) Primary magmas of mid-ocean ridge basalts 2 applications. *J Geophys Res* 97(B5):6907–6926
- Kostopoulos DK (1991) Melting of the shallow upper mantle: a new perspective. *J Petrol* 32:671–699
- Longerich HP, Jackson SE, Fryer BJ, Strong DF (1993) The Laser ablation microprobe–inductively coupled plasma–mass spectrometer. *Geosci Can* 20:21–27
- Mattinson JM, Hopson CA (2008) New high-precision CA–TIMS UPb zircon plateau ages for the Point Sal and San Simeon ophiolite remnants, California Coast Ranges. In: Wright JE, Shervais JW (eds) *Ophiolites, arcs, and batholiths: a tribute to Cliff Hopson*: Geological Society of America Special Paper 438
- Mercier JCC, Nicolas A (1975) Textures and fabrics of upper-mantle peridotites as illustrated by xenoliths from basalts. *J Petrol* 16(2):454–487
- Metcalf RV, Shervais JW (2008) Supra-subduction zone (SSZ) ophiolites: is there really an “Ophiolite Conundrum”? In: Wright JE, Shervais JW (eds) *Ophiolites, arcs, and batholiths: a tribute to Cliff Hopson*. Geological Society of America Special Paper 438, pp 191–222
- Miller C, Thoni M, Wolfgang F, Schuster R, Melcher F, Meisel T, Zanetti A (2002) Geochemistry and tectonomagmatic affinity of the Yungbwa ophiolite, SW Tibet. *Lithos* 66:155–172

- Moore E, Kellogg LH, Dilek Y (2000) Tethyan ophiolites, mantle convection, and tectonic “historical contingency”: a resolution of the “ophiolite conundrum” In: Dilek Y, Moore E, Elthon D, Nicolas A (eds) Ophiolites and oceanic crust. Geological Society of America Special Publication, vol 349, pp 3–12
- Nickel KG, Brey G (1984) Subsolidus orthopyroxene–clinopyroxene systematics in the system CaO–Mg–SiO₂ to 60 Kbar: a reevaluation of the regular solution model. *Contrib Mineral Petrol* 87:35–42
- Niu Y (1997) Mantle melting and melt extraction processes beneath ocean ridges: evidence from abyssal peridotites. *J Petrol* 38:1047–1074
- Niu Y (2004) Bulk–rock major and trace element compositions of abyssal peridotites: implications for mantle melting, melt extraction and post–melting processes beneath mid–ocean ridges. *J Petrol* 45(12):2423–2458
- Niu Y, Hekinian R (1997) Basaltic liquids and harzburgitic residues in the Garrett transform: a case study of fast–spreading ridges. *Earth Planet Sci Lett* 146:243–258
- Niu Y, Langmuir CH, Kinzler RJ (1997) The origin of abyssal peridotites: a new perspective. *Earth Planet Sci Lett* 152:251–265
- Parkinson IJ, Pearce JA (1998) Peridotites of the Izu–Bonin–Mariana forearc (ODP Leg 125) evidence for mantle melting and melt–mantle interactions in a suprasubduction zone setting. *J Petrol* 39:1577–1618
- Parkinson IJ, Pearce JA, Thirwall MF, Johnson KTM, Ingram G (1992) Trace element geochemistry of peridotites from the Izu–Bonin–Mariana forearc, Leg 125. In: Fryer P, Pearce JA, Stokking LB (eds) Proceedings of the ODP Sci Results 125. Ocean Drilling Program, College Station, Texas, pp 487–506
- Pearce NJG, Perkins WT, Westgate JA, Gorton MJ, Jackson SE, Neal CR, Chenery SP (1997) A compilation of new and published major and trace element data for NIST SRM 610 and NIST SRM 612 glass reference materials. *Geostand Newsl* 21:115–144

- Pearce JA, Barker PF, Edwards SJ, Parkinson IJ, Leat PT (2000) Geochemistry and tectonic significance of peridotites from the south sandwich arc–basin system, South Atlantic. *Contrib Mineral Petrol* 139:36–53
- Pike JEN, Schwarzman EC (1977) Classification of textures in ultramafic xenoliths. *J Geol* 85(1): 49–61
- Saleeby JB (1982) Polygenetic ophiolite belt of the California Sierra Nevada: geochronological and tectonostratigraphic development. *J Geophys Res* B87:1803–1824
- Salters VJM, Stracke A (2004) Composition of the depleted mantle. *Geochem Geophys Geosyst* 5:Q05004. doi:10.1029/2003GC000597
- Schweickert RA, Bogen NL, Girty GH, Hanson RE, Merguerian C (1984) Timing and structural expression of the Nevadan Orogeny, Sierra Nevada, California. *Geol Soc Am Bull* 95:967–979
- Seyler M, Bonatti E (1997) Regional–scale melt–rock interaction in lherzolitic mantle in the Romanche Fracture Zone (Atlantic Ocean). *Earth Planet Sci Lett* 146:273–287
- Seyler M, Toplis MJ, Lorand JP, Luguet A, Cannat M (2001) Clinopyroxene microtextures reveal incompletely extracted melt in abyssal peridotites. *Geology* 29:155–158
- Seyler M, Cannat M, Mevel C (2003) Evidence for major–element heterogeneity in the mantle source of abyssal peridotites from the Southwest Indian Ridge (52 to 68 E). *Geochem Geophys Geosyst* 4(2):9101
- Seyler M, Lorand J–P, Toplis MJ, Godard G (2004) Asthenospheric metasomatism beneath the mid–ocean ridge: evidence from depleted abyssal peridotites. *Geology* 32(4):301–304
- Seyler M, Lorand J–P, Dick HJB, Drouin M (2007) Pervasive melt percolation reactions in ultra–depleted refractory harzburgites at the Mid–Atlantic Ridge, 15–208N: ODP Hole 1274A. *Contrib Mineral Petrol* 153:303–319
- Shaw DM (1970) Trace element fractionation during anatexis. *Geochim Cosmochim Acta* 34:237–243

- Shervais JW (1979) Ultramafic and mafic layers in the Alpine lherzolite massif at Balmuccia, N. W. Italy. Proceedings of the Second Symposium Ivrea–Verbano, *Memoria Scienza Geol. de Universite Padova*, vol 33, pp 133–145
- Shervais JW (1990) Island arc and ocean crust ophiolites: contrasts in the petrology, geochemistry, and tectonic style of ophiolite assemblages in the California Coast Ranges. In: Malpas J, Moores EM, Panayiotou A, Xenophontos C (eds) *Ophiolites: oceanic crustal analogues: proceedings of the symposium Troodos 1987*. Geological Survey Department, Nicosia, Cyprus, pp 507–520
- Shervais JW (2001) Birth, death, and resurrection: the life cycle of suprasubduction zone ophiolites. *Geochemistry, Geophysics, Geosystems*, vol. 2 (Paper number 2000GC000080), 20,925 words, 8 figures, 3 tables
- Shervais JW (2008) Tonalites, trondhjemites, and diorites of the Elder Creek ophiolite, California: low–pressure slab melting and reaction with the mantle wedge. In: Wright JE, Shervais JW (eds) *Ophiolites, arcs, and batholiths: a tribute to Cliff Hopson*. Geological Society of America Special Paper 438, pp 113–132
- Shervais JW, Kimbrough DL (1985) Geochemical evidence for the tectonic setting of the Coast Range ophiolite; a composite island arc–oceanic crust terrane in western California. *Geology (Boulder)* 13:35–38
- Shervais JW, Kimbrough DL, Renne P, Murchey B, Hanan BB (2004) Multistage origin of the Coast Range Ophiolite, California and Oregon: implications for the life cycle of suprasubduction zone ophiolites. *Int Geol Rev* 46:289–315
- Shervais JW, Murchey B, Kimbrough DL, Renne P, Hanan BB (2005a) Radioisotopic and biostratigraphic age relations in the Coast Range ophiolite, Northern California: implications for the tectonic evolution of the western Cordillera. *Geol Soc Am Bull* 117(5/6):633–653
- Shervais JW, Kolesar P, Andreasen K (2005b) Field and chemical study of serpentinization—Stonyford, California: chemical fluxes and mass balance. *Int Geol Rev* 47:1–23

- Shervais JW, Zoglman-Schuman MM, Hanan BB (2005c) The Stonyford volcanic complex: a forearc seamount in the northern California coast ranges. *J Petrol* 46(10):2091–2128
- Snow CA (2002) Geology of the Cuesta Ridge ophiolite remnant near San Luis Obispo, California: evidence for the tectonic setting and origin of the Coast Range Ophiolite [M.S. thesis]. Utah State University, 150 p
- Stern RJ, Bloomer SH (1992) Subduction zone infancy: examples from the Eocene Izu–Bonin–Mariana and Jurassic California. *Geol Soc Am Bull* 104:1621–1636
- Walter MJ (1998) Melting of garnet peridotite and the origin of komatiite and depleted lithosphere. *J Petrol* 39:29–60
- Wasylenki LE, Baker MB, Kent AJR, Stolper EM (2003) Near solidus melting of the shallow upper mantle: partial melting experiments on depleted peridotites. *J Petrol* 44:1163–1191
- Widom E, Kepezhinskas P, Defant M (2003) The nature of metasomatism in the sub–arc mantle wedge: evidence from Re–Os isotopes in Kamchatka peridotite xenoliths. *Chem Geol* 196:283–306
- Witt–Eickschen G, O’Neill HSC (2005) The effect of temperature on the equilibrium distribution of trace elements between clinopyroxene, orthopyroxene, olivine and spinel in upper mantle peridotite. *Chem Geol* 221:65–101

Table 2-1. Average major element (wt%) and trace element (ppm) compositions of clinopyroxene

Sample	SFV-14-1	SFV-14-2	SFV-220-1	SFV-306	SFV-308	CR112-1	SFV-222-1	DP-15
Rock Type	Spinel Lherzolite	Spinel Lherzolite	Spinel Lherzolite	Spinel Lherzolite	Spinel Lherzolite	Spinel Harzburgite	Spinel Harzburgite	Orthopyroxenite
Group	A	A	A	A	A	A	B	C
# Analysis	13	4	6	5	3	9	4	3
SiO ₂	50.08	51.50	49.93	51.28	51.31	52.05	51.70	54.15
TiO ₂	0.32	0.39	0.25	0.40	0.43	0.28	0.02	0.02
Al ₂ O ₃	5.71	5.64	5.79	6.15	5.88	5.58	1.96	0.50
Cr ₂ O ₃	0.75	0.82	1.24	0.89	0.89	0.99	0.67	0.42
V ₂ O ₃	-	0.06	-	0.04	0.04	-	-	0.01
FeO	2.41	2.33	2.28	2.59	2.38	2.52	2.47	2.52
MnO	0.10	0.08	0.08	0.08	0.08	0.08	0.10	0.11
MgO	16.02	15.46	15.67	15.59	15.32	15.75	18.01	17.72
CaO	22.22	22.83	21.71	22.66	22.58	22.28	23.58	24.44
Na ₂ O	0.80	0.92	1.17	0.95	1.05	0.65	0.05	0.16
K ₂ O	0.00	-	0.01	0.01	0.00	-	0.00	-
NiO	-	0.04	-	0.05	0.06	-	-	0.02
Total	98.41	100.07	98.12	100.68	100.02	100.18	98.56	100.07
Oliv-Fo	90.29	89.92	91.37	90.21	90.00	90.09	91.10	-
Pyx-Mg#	92.22	92.21	92.43	91.48	91.98	91.78	92.85	92.62
Pyx-Cr#	8.10	8.92	12.55	8.89	9.20	10.65	18.74	36.43
Wo	47.82	49.38	47.88	48.80	49.28	48.26	46.57	47.78
En	47.97	46.55	48.06	46.71	46.53	47.48	49.47	48.21
Fs	4.21	4.07	4.07	4.49	4.19	4.26	3.96	4.01
Trace Elements								
# Analysis	<u>3</u>	<u>6</u>	<u>5</u>		<u>4</u>		<u>2</u>	<u>5</u>
Sc	53.73	54.12	46.98	n.a.	51.00	n.a.	49.05	45.44
TiO ₂	0.10	0.38	0.22	n.a.	0.38	n.a.	0.03	0.02
Ti	619.48	2287.09	1322.50	n.a.	2246.63	n.a.	149.88	134.77
V	133.67	206.00	151.00	n.a.	189.00	n.a.	115.50	42.04
Y	18.07	15.12	10.80	n.a.	15.15	n.a.	1.86	0.65
Zr	5.50	4.85	3.31	n.a.	5.18	n.a.	0.07	0.18
Nb	0.02	0.03	0.04	n.a.	0.02	n.a.	0.02	0.01
La	0.03	0.01	0.05	n.a.	0.01	n.a.	-	-
Ce	0.31	0.29	0.26	n.a.	0.26	n.a.	-	0.01
Nd	1.74	1.63	0.98	n.a.	1.59	n.a.	-	0.03
Sm	1.29	1.15	0.68	n.a.	1.07	n.a.	0.01	0.02
Eu	0.58	0.53	0.32	n.a.	0.48	n.a.	-	0.01
Gd	1.66	1.54	0.94	n.a.	1.47	n.a.	0.06	0.05
Tb	0.43	0.38	0.24	n.a.	0.35	n.a.	0.02	0.01
Dy	3.24	2.79	1.79	n.a.	2.50	n.a.	0.23	0.11
Ho	0.73	0.61	0.41	n.a.	0.55	n.a.	0.07	0.03
Er	2.04	1.73	1.19	n.a.	1.56	n.a.	0.25	0.10
Tm	0.30	0.25	0.18	n.a.	0.23	n.a.	0.05	0.02
Yb	2.05	1.73	1.22	n.a.	1.57	n.a.	0.34	0.13
Lu	0.29	0.23	0.17	n.a.	0.21	n.a.	0.05	0.02
Hf	0.44	0.37	0.22	n.a.	0.34	n.a.	0.01	0.03
Spinel								
# Analysis	<u>5</u>	<u>3</u>	<u>4</u>	<u>3</u>	<u>1</u>	<u>8</u>	<u>7</u>	<u>2</u>
Sp-Mg#	74.79	74.81	72.13	75.71	74.34	72.51	59.22	19.93
Sp-Cr#	11.12	11.47	19.99	12.59	13.15	15.90	45.99	81.37

Table 2-3. Input parameters for melting models.

	<i>Distribution Coefficients^A</i>							<i>Source Composition^B</i>
	O/I	Opx/I ^C	Opx/I ^D	Opx/I ^E	Cpx/I	Gt/I	Sp/I	
La	0.00001	0.00009	0.00009	0.00048	0.0400	0.0030	0.0006	0.234
Ce	0.00001	0.00090	0.00025	0.00097	0.0700	0.0050	0.0006	0.772
Nd	0.00007	0.00900	0.00112	0.00343	0.1780	0.0520	0.0006	0.713
Sm	0.00070	0.02000	0.00357	0.00923	0.2930	0.2500	0.0006	0.27
Eu	0.00095	0.03000	0.00576	0.01302	0.3200	0.6000	0.0006	0.107
Gd	0.00150	0.03400	0.00770	0.01752	0.3400	1.2000	0.0010	0.395
Tb	0.00250	0.04500	0.01318	0.02761	0.3500	1.8000	0.0001	0.075
Dy	0.00400	0.06000	0.01865	0.03769	0.3800	2.2000	0.0015	0.531
Ho	0.00650	0.06500	0.02453	0.04893	0.3750	3.0000	0.0024	0.122
Er	0.00900	0.07000	0.03435	0.06233	0.3700	4.0000	0.0030	0.371
Tm	0.01500	0.08500	0.05181	0.08937	0.3850	5.2000	0.0036	0.06
Yb	0.02300	0.10000	0.06927	0.11640	0.4000	6.6000	0.0045	0.401
Lu	0.02500	0.11000	0.09082	0.15309	0.4000	7.2000	0.0050	0.063
	<i>Source modes^F</i>		<i>Melt Modes</i>					
	<i>Gt-per</i>	<i>Sp-per</i>	<i>Sp-per - Wet^G</i>	<i>Sp-per - Dry^H</i>	<i>Gt-per^I</i>			
Olivine	0.57	0.56	-0.25	-0.22	0.08			
Opx	0.21	0.25	0.51	0.38	-0.19			
Cpx	0.16	0.18	0.62	0.71	0.81			
Garnet	0.06	-	-	-	0.3			
Spinel	-	0.02	0.12	0.13	-			

^ADistribution coefficients of Johnson (1997); unless stated otherwise

^BDepleted MORB mantle composition of Salters and Stracke (2004)

^COrthopyroxene distribution coefficients; used in Group A clinopyroxene melting models

^DOrthopyroxene distribution coefficients calculated from the algorithm of Witt-Eickschena and O'Neill 2005; used in Group A orthopyroxene melting models

^EOrthopyroxene distribution coefficients calculated from the algorithm of Witt-Eickschena and O'Neill 2005; used in Group B and C orthopyroxene melting models

^FSp-per Source Mode from Johnson et al., (1990); Gt-per source mode calculated from equation in Johnson et al., (1990)

^GSp-per melt mode for SSZ from Gaetani and Grove

^HSp-per melt mode from Baker and Stolper (1994)

^IMelt Mode from Walter (1998)

Table 2-4. Melt refertilization model - Abyssal clinopyroxene.

	Initial cpx ^A	Melt ^B	Melt ^C	SFV308	SFV220-1	SFV14-2	SFV14-1
La	0.0000	0.1030	0.3004	0.0556	0.2222	0.0513	0.1410
Ce	0.0041	0.1135	0.3093	0.3342	0.3342	0.3692	0.4016
Nd	0.4129	1.2245	1.3868	2.2272	1.3773	2.2791	2.4404
Sm	1.3356	3.6059	3.6974	3.9741	2.5259	4.2519	4.7778
Eu	1.5589	4.1121	4.1879	4.4673	3.0093	4.9252	5.4206
Gd	1.7205	4.4235	4.4881	4.8228	3.0835	5.0759	5.4684
Tb	1.8107	4.4053	4.4627	4.6400	3.2000	5.0000	5.6933
Dy	2.0309	4.7089	4.7556	4.7137	3.3710	5.2448	6.1017
Ho	2.0057	4.3361	4.3836	4.5082	3.3770	4.9590	5.9836
Er	1.9801	3.9787	4.0245	4.1914	3.2075	4.6550	5.5067
Tm	2.0600	3.7283	3.7667	3.7500	3.0333	4.2167	5.0500
Yb	0.2104	3.4880	3.5204	0.3903	0.3032	0.4307	0.5105
Lu	2.0730	3.2984	3.3270	3.2540	2.6667	3.6825	4.6032
Ti	1.7763	2.8406	2.8709	2.8153	1.6573	2.8660	0.7763
Zr	0.2334	0.4140	0.4875	0.6521	0.4174	0.6106	0.6931
Y	2.1668	4.7732	4.8128	3.7224	2.6536	3.7143	4.4391
Nb	0.0000	0.1457	0.4205	0.0857	0.1714	0.1333	0.0952
Hf	1.5417	3.5457	3.6151	1.6985	1.0854	1.8442	2.2261

^ACalculated residual cpx composition of 8% fractional melting in Spinel field*

^BCalculated melt composition of 20% pooled melt with 0.1% melt added*

^CCalculated melt composition of 20% pooled melt with 0.3% melt added*

*All values normalized to DMM values of Salters and Stracke (2004)

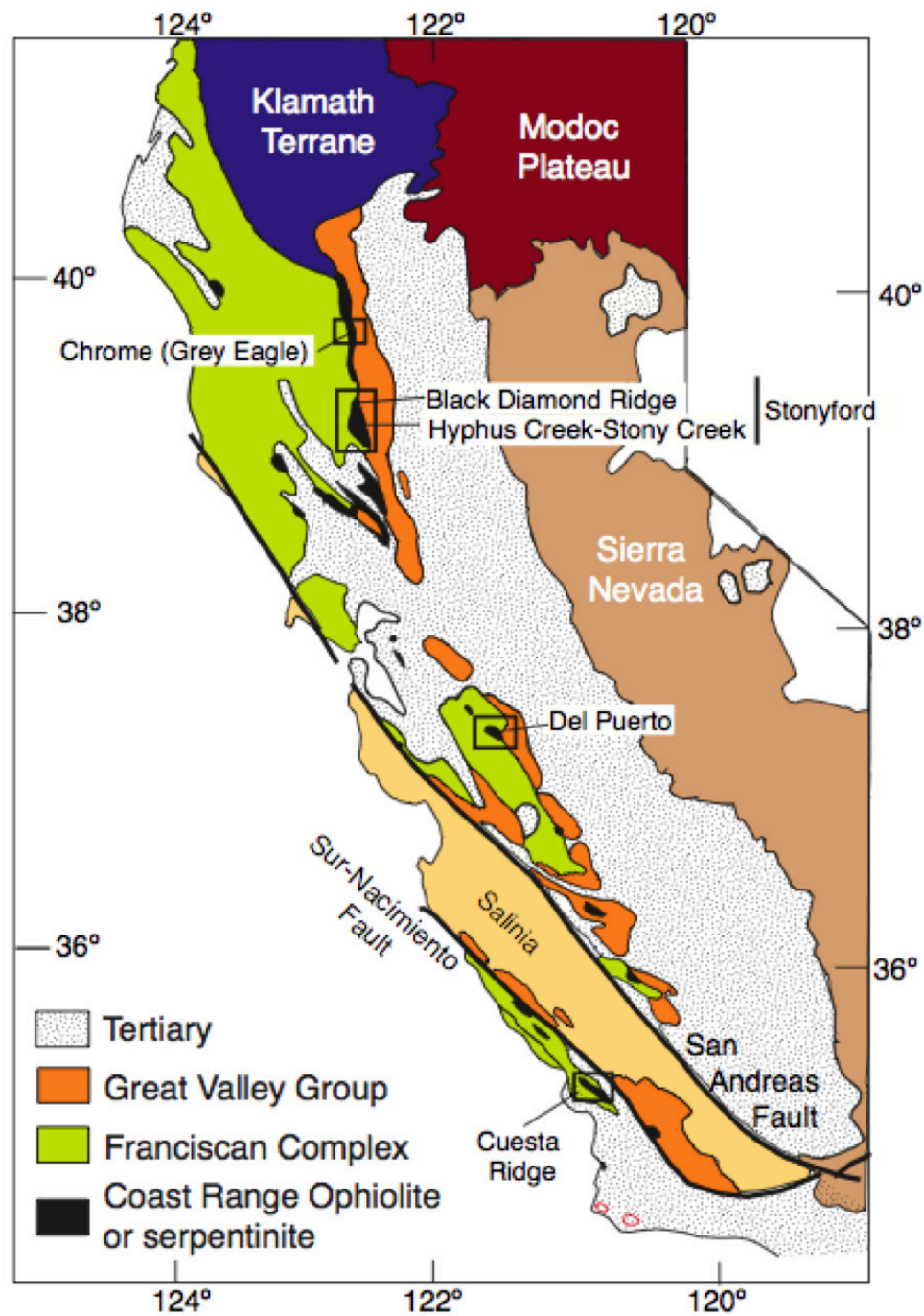


Figure 2-1. Location map showing distribution of the Coast Range ophiolite in California and the locations of sample suite studied here.

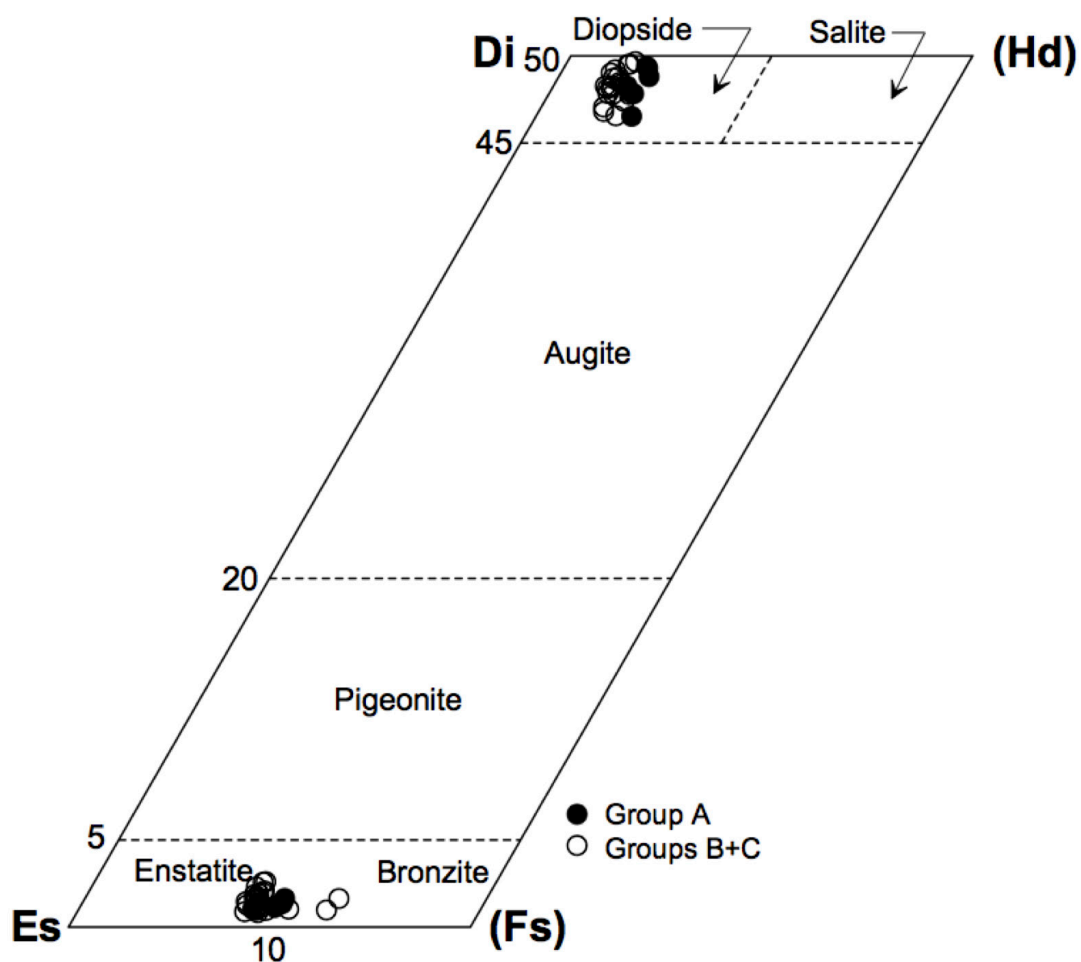


Figure 2-2. Pyroxene quadrilateral plot showing diopside and enstatite compositions in Group A (solid) and Group B–C (open) pyroxenes. The two bronzite analyses are from Group C orthopyroxenite dikes.

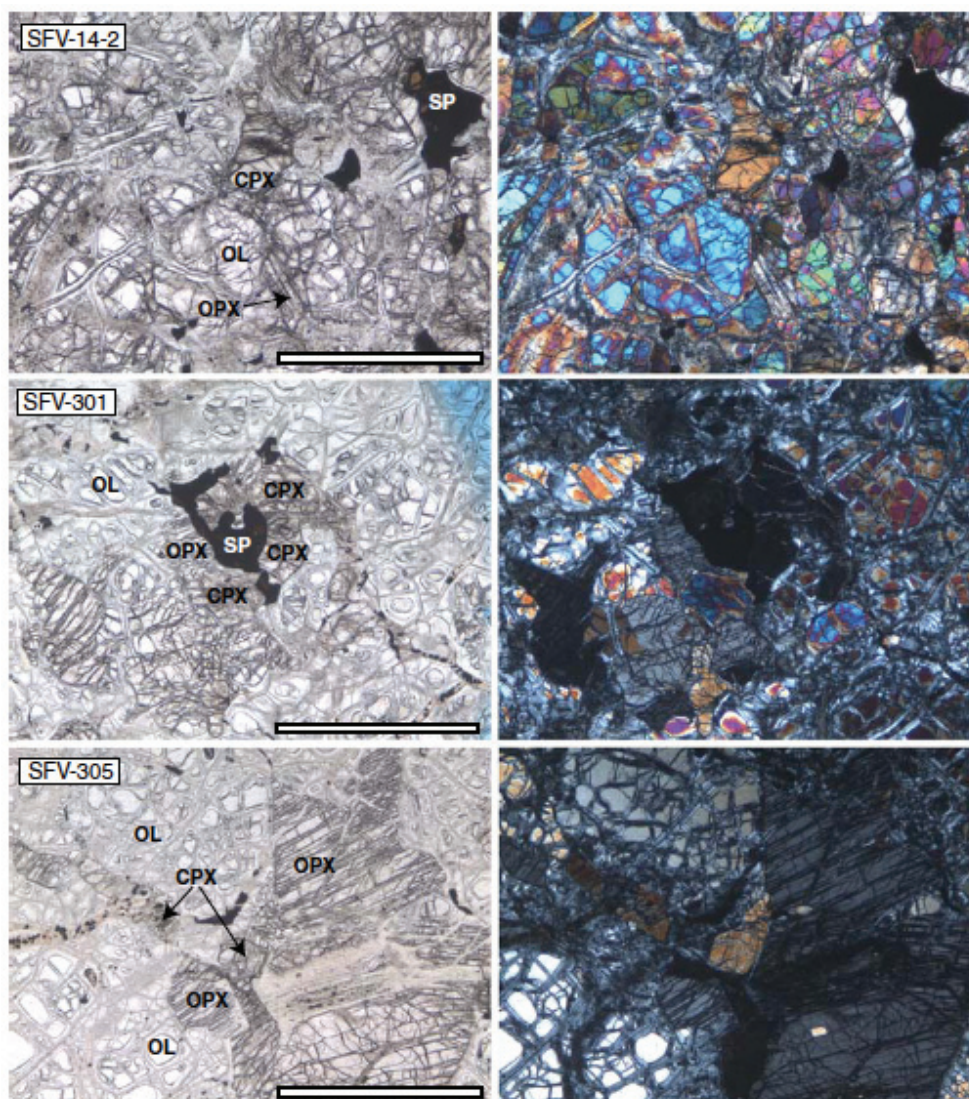


Figure 2-3. Photomicrographs of CRO peridotites. Group A protogranular lherzolite SFV-14-2 under plain light (a) and crossed polar textures (b); note smooth grain boundaries, lack of kink-banding or other deformational fabrics, and interstitial spinel that conforms to grain boundaries or triple junctions; Group B protogranular harzburgite SFV-301 under plain light (c) and crossed polars (d); pyroxene–spinel cluster ~1.5 mm across in center of view with large ameboid spinel. Group C secondary protogranular harzburgite SFV-305 under plain light (e) and crossed polars (f); note discrete diopside grains. Opx—orthopyroxene, Cpx—clinopyroxene, Ol—olivine, Sp—spinel. Bar scale = 1 mm.

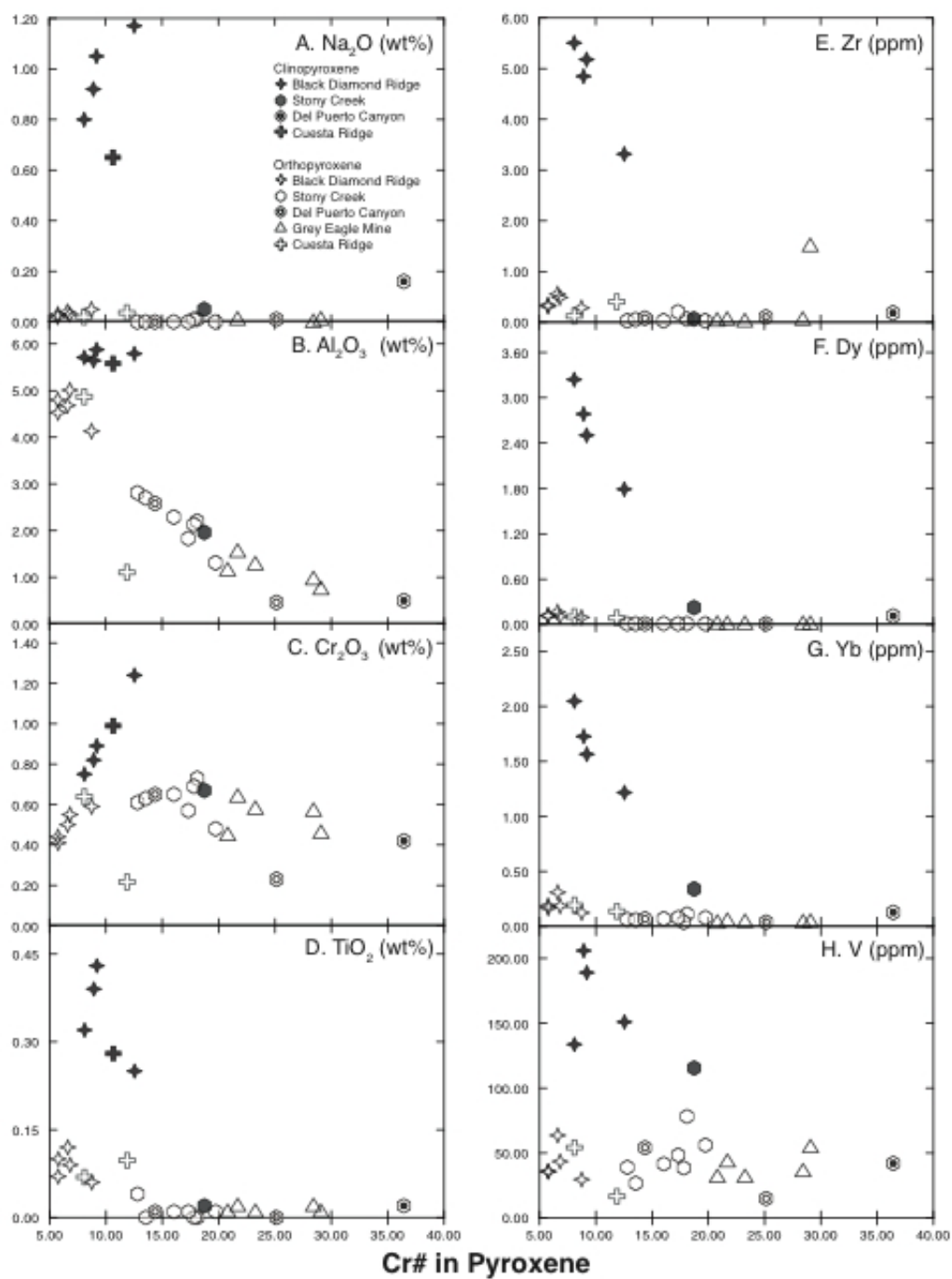


Figure 2-4. Minor and trace element variations in pyroxene as a function of Cr# in pyroxene; (a) Na₂O wt%, (b) Al₂O₃ wt%, (c) Cr₂O₃ wt%, (d) TiO₂ wt%, (e) Zr ppm, (f) Dy ppm, (g) Yb ppm, and (h) V ppm. Major element compositions are from the study of Choi et al. (2008b).

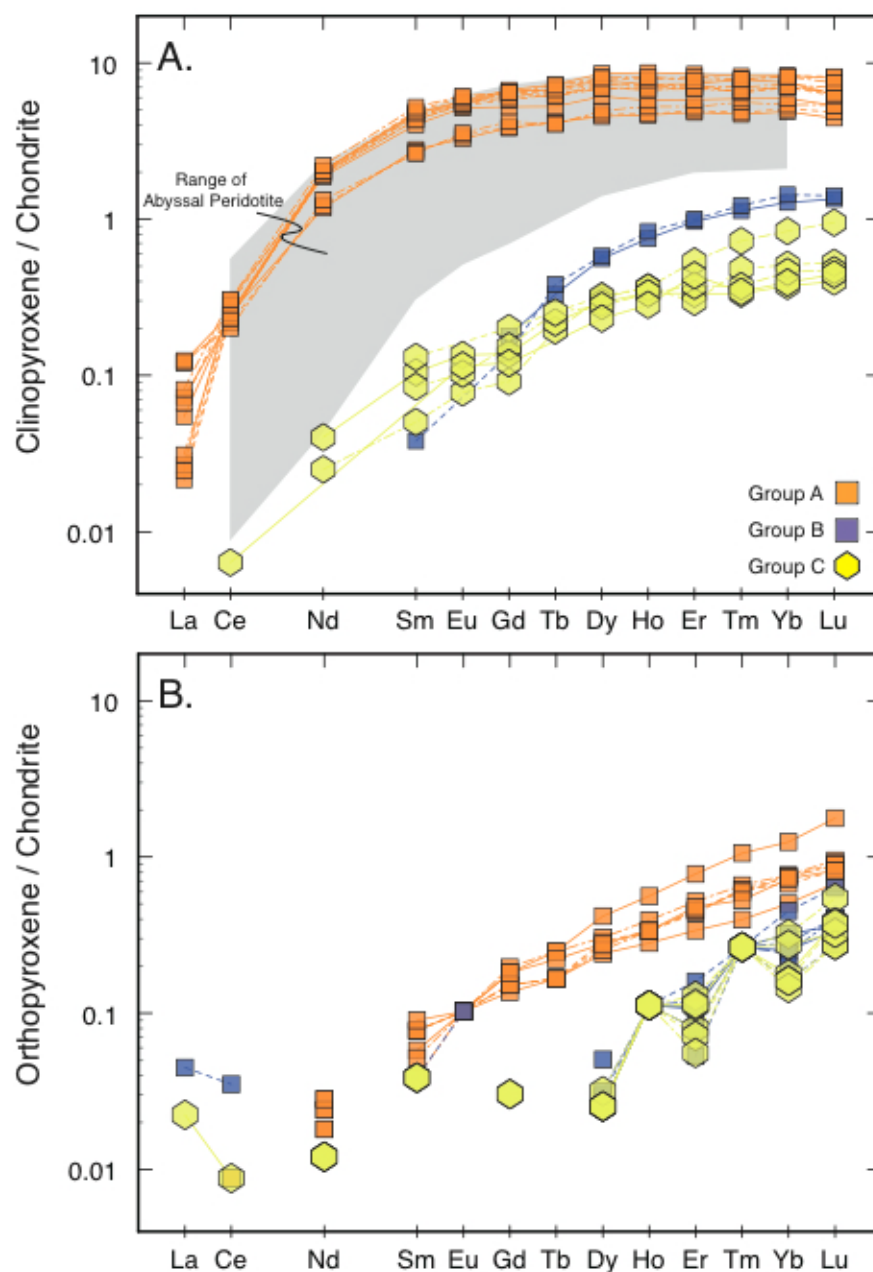


Figure 2-5. Chondrite-normalized REE concentrations for clinopyroxene in Group A lherzolites and Group B harzburgite. Field for abyssal clinopyroxenes (light gray) shown for comparison. The range of abyssal peridotites are from Johnson et al. (1990); Johnson and Dick (1992); Miller et al. (2002); and Niu (2004). Normalizing values from Anders and Grevesse (1989).

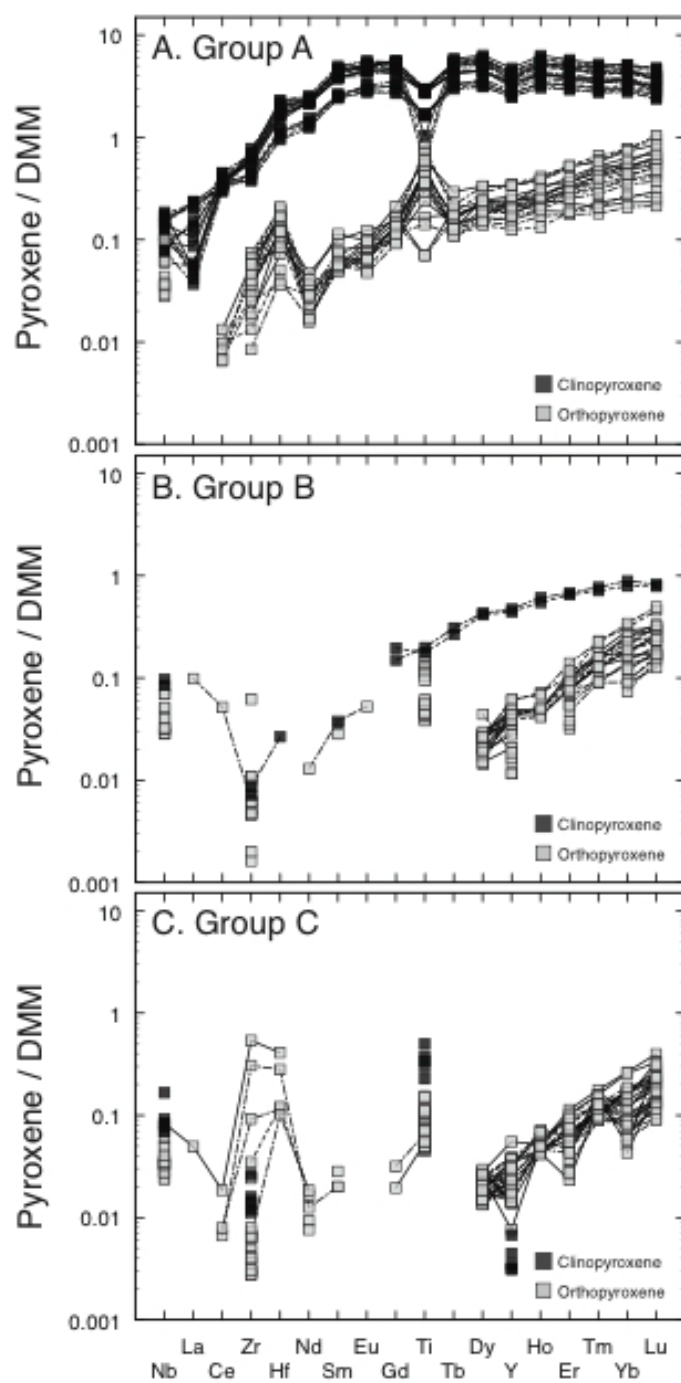


Figure 2-6. Multi-element variation diagram for Group A, Group B, and Group C clinopyroxene and orthopyroxene, normalized to the depleted MORB-source composition of Salters and Stracke (2004). Elements are arranged in order of decreasing incompatibility from left to right.

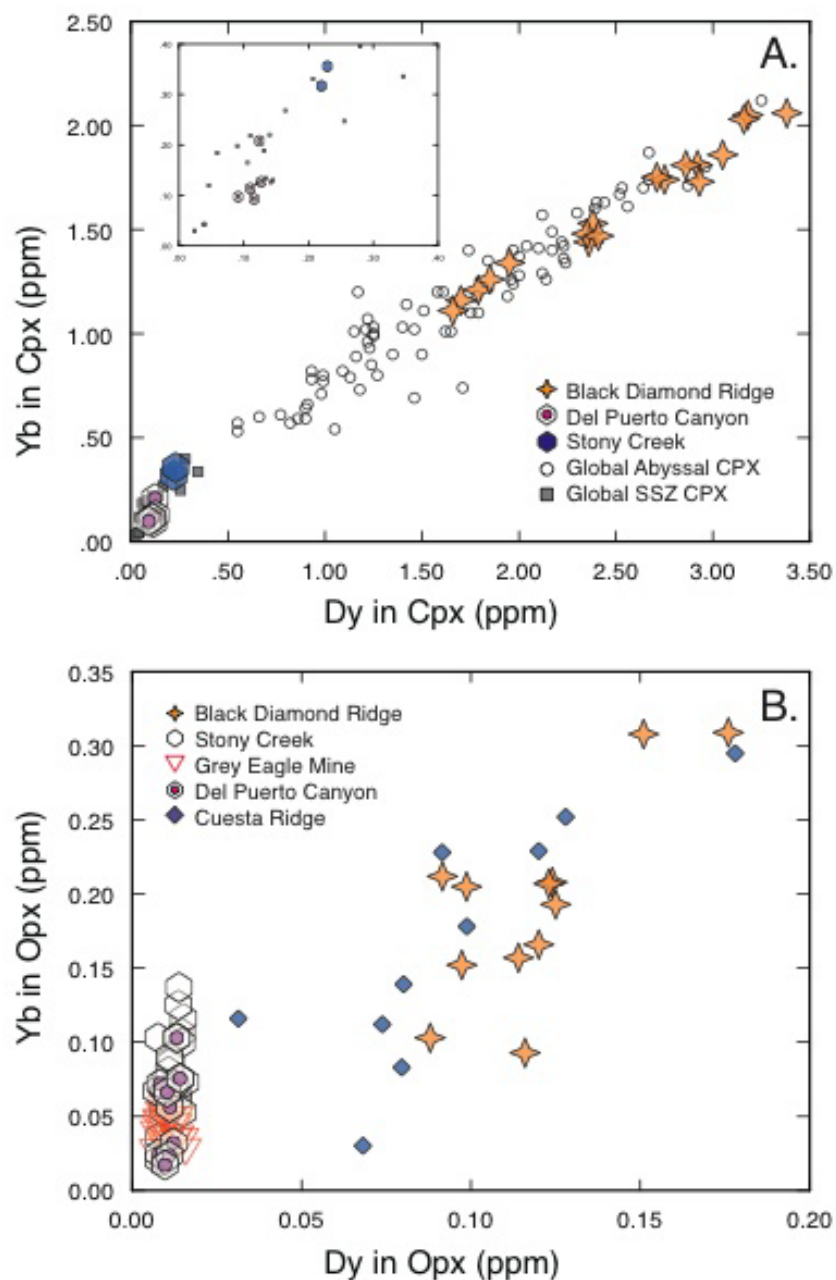


Figure 2-7. Correlation between Dy and Yb concentrations in a) clinopyroxene and b) orthopyroxene, showing the effects of tectonic setting on REE concentrations. Clinopyroxene data compared to database of global abyssal peridotites (Dick 1989; Johnson et al. 1990; Johnson and Dick 1992; Hellebrand et al. 2001, 2002; Miller et al. 2002; Niu 2004; Seyler et al. 2004 and global fore-arc/SSZ peridotites (Parkinson and Pearce 1998; Bizimis et al. 2000).

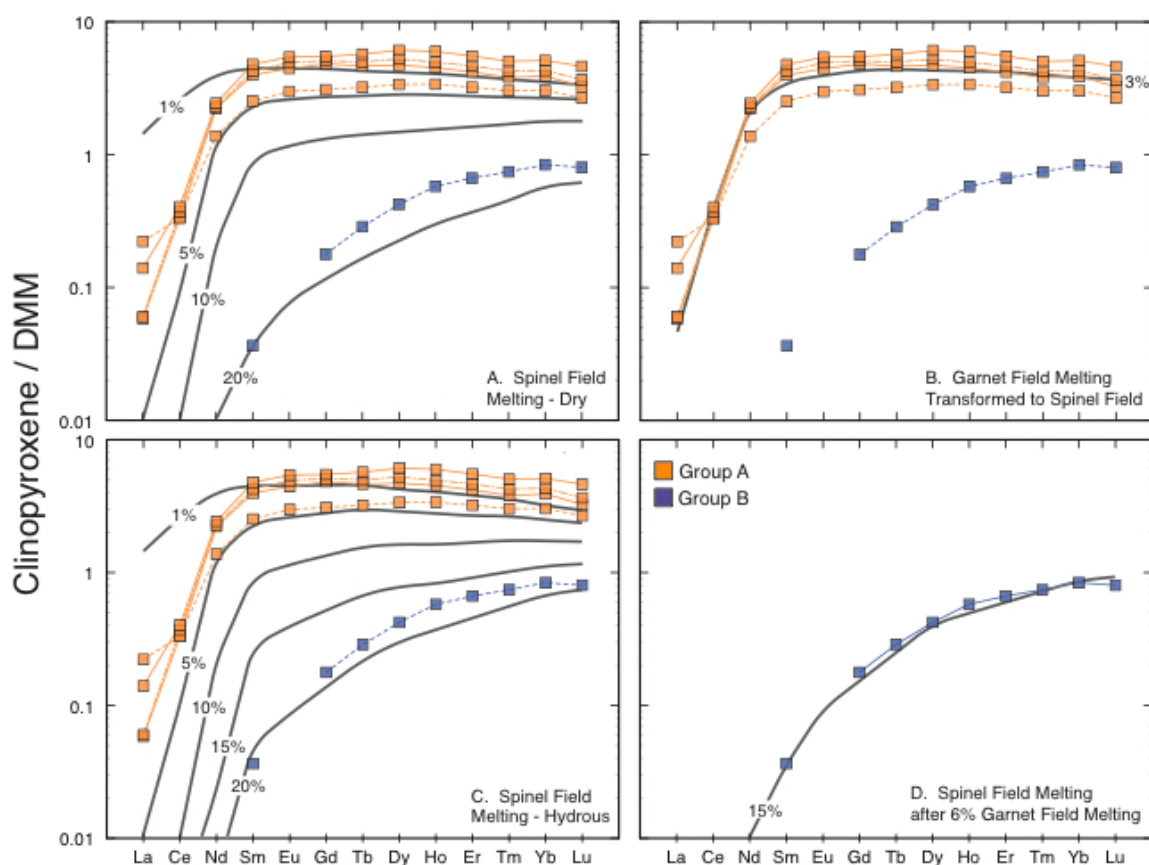


Figure 2-8. Melting models for clinopyroxene: a) dry fractional melting in the spinel field compared to Group A lherzolite clinopyroxenes, b) 3% dry fractional melting in the garnet field, recalculated to spinel field modes and compositions compared to Group A lherzolite clinopyroxenes, c) hydrous fractional melting in the spinel field compared to Group B harzburgite clinopyroxenes, d) 6% fractional melting in the garnet field followed by additional hydrous fractional melting in the spinel field compared to Group B harzburgite clinopyroxene. Best fit for Group A lherzolite clinopyroxenes requires 2–3% garnet field melting converted to spinel facies assemblage. Best fit for Group B harzburgite clinopyroxene is achieved with 6% garnet field melting followed by ~15% spinel field melting. The calculation method and parameters used in the model follow those of Johnson et al. (1990). The parameters are shown in Table 3.

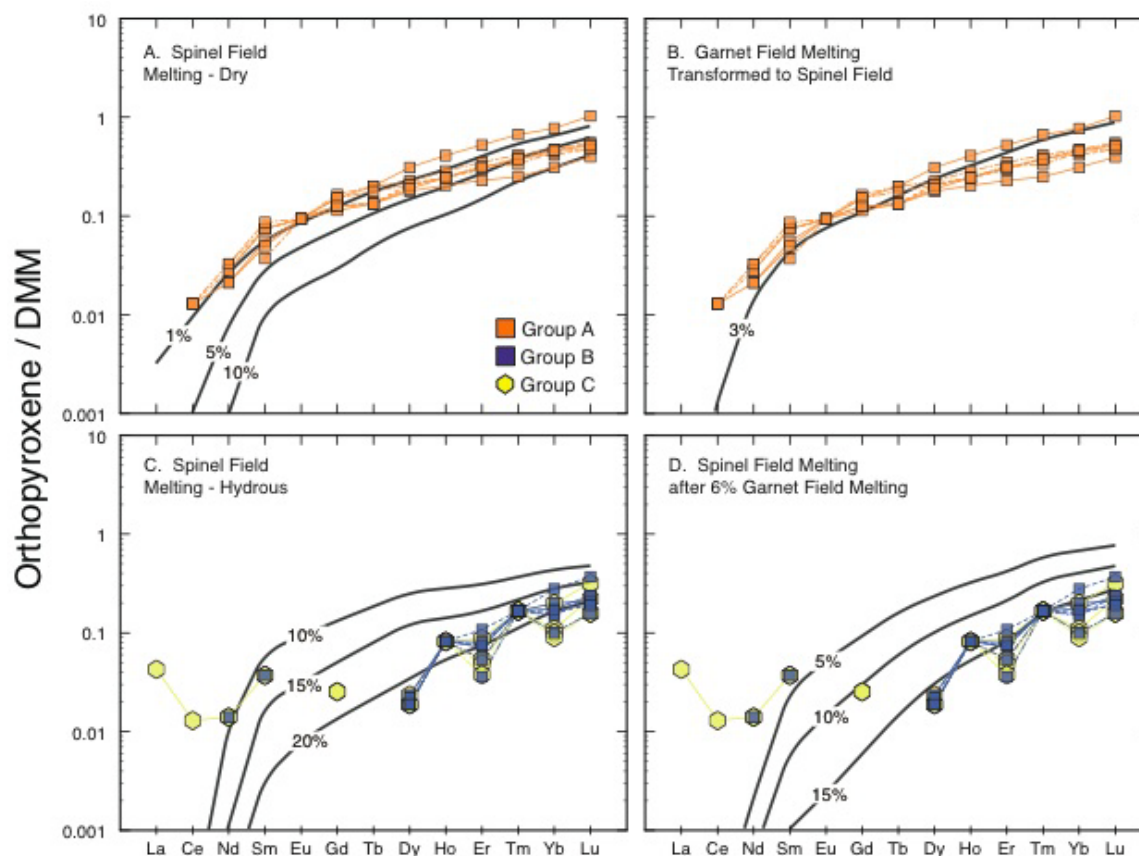


Figure 2-9. Melting models for orthopyroxene: a) dry melting in the spinel field compared to Group A lherzolite orthopyroxenes, b) 3% garnet field melting transformed to spinel field compositions compared to Group A lherzolite orthopyroxenes, c) hydrous melting in the spinel field compared to Groups B–C harzburgite orthopyroxenes, and d) 6% garnet field melting followed by spinel field melting compared to Groups B–C harzburgite orthopyroxenes. Best fit for Group A lherzolite orthopyroxene requires 2–3% garnet field melting converted to spinel facies assemblage. Best fit for Group B harzburgite orthopyroxene from Del Puerto, Grey Eagle, and Hyphus-Little Stony Creek achieved with 6% garnet field melting followed by ~15% spinel field melting; best fit for Group B harzburgite orthopyroxene from Cuesta Ridge achieved with 3% garnet field melting followed by ~10% spinel field melting.

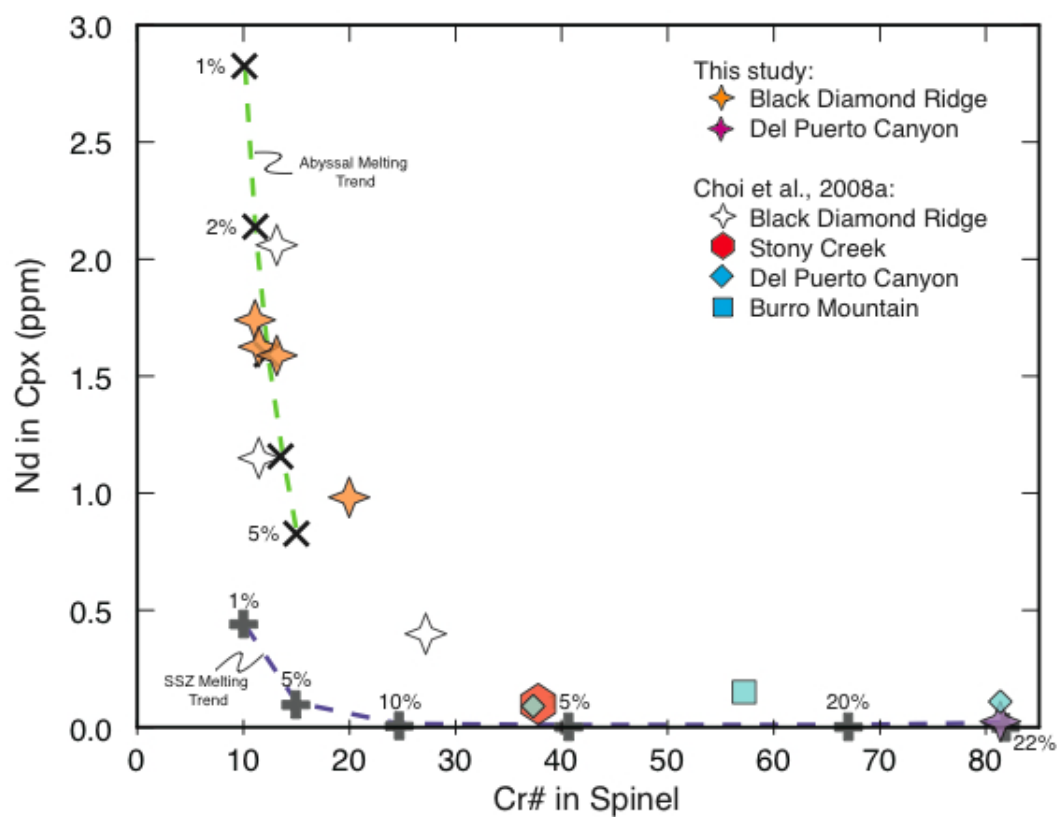


Figure 2-10. Comparison of Group A lherzolite melting trend (garnet field melting) and Groups B–C harzburgite melting trend, using Nd in clinopyroxene and Cr# in coexisting spinel.

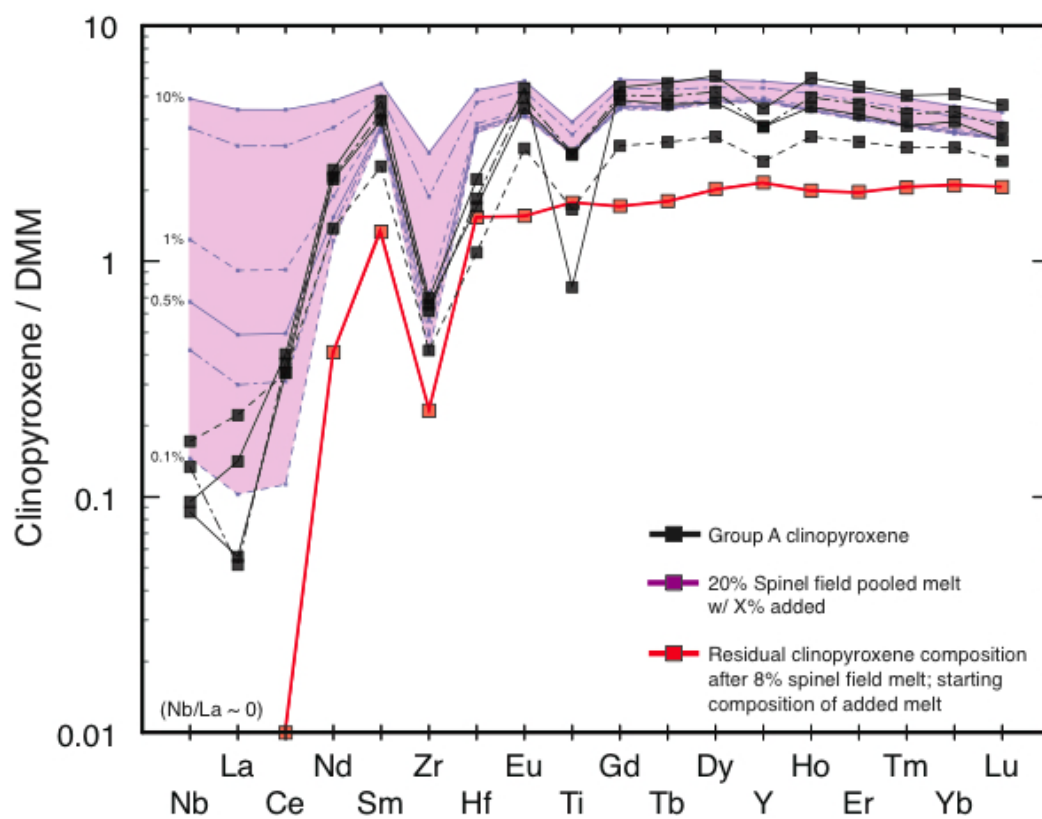


Figure 2-11. Effects of melt refertilization on model residual pyroxenes, compared to observed pyroxene concentrations. Model residual clinopyroxene (8% spinel field melting) with melt refertilization of 0.1 to 10%; added melt formed by 20% melting of MORB-source mantle.

MULTI-COMPONENT MIXING FOR YELLOWSTONE-SNAKE RIVER PLAIN BASALTS:
IMPLICATIONS FOR SUB-CONTINENTAL LITHOSPHERIC SOURCES AND THEIR
INTERACTION WITH THE YELLOWSTONE HOTSPOT¹

Abstract

New strontium, neodymium, and lead isotopic analyses of 25 basalts from the Yellowstone-Snake River volcanic province (YSRP) reflects heterogeneity in the age, composition, and thickness of the underlying subcontinental lithospheric mantle. These basalts span a 300 km transect of the craton margin – from the Western Idaho Shear Zone (which coincides with the $^{87}\text{Sr}/^{86}\text{Sr}$ 0.706 line) to the eastern Snake River Plain just west of Yellowstone. Results demonstrate that (1) low-K tholeiites erupted from the eastern, central, and western plain share similar isotopic signatures ($^{206}\text{Pb}/^{204}\text{Pb}=17.87\text{--}18.61$, $^{207}\text{Pb}/^{204}\text{Pb}=15.58\text{--}15.66$, $^{208}\text{Pb}/^{204}\text{Pb}=38.46\text{--}39.19$, $^{87}\text{Sr}/^{86}\text{Sr}=0.7060\text{--}0.7071$, and $^{143}\text{Nd}/^{144}\text{Nd}=0.51237\text{--}0.51253$), and vary systematically from west to east; (2) western plain high-K basalts have isotopic compositions that are intermediate between YSRP low-K tholeiites and early Columbia River basalts, but are similar to Boise River Group high-K basalts ($^{206}\text{Pb}/^{204}\text{Pb}=18.67\text{--}18.71$, $^{207}\text{Pb}/^{204}\text{Pb}=15.62\text{--}15.66$, $^{208}\text{Pb}/^{204}\text{Pb}=39.07\text{--}39.22$, $^{87}\text{Sr}/^{86}\text{Sr}=0.7050\text{--}0.7057$, and $^{143}\text{Nd}/^{144}\text{Nd}=0.51258\text{--}0.51261$); and (3) the Silver City basalt has a composition similar to the early Columbia River basalts (i.e., Steens-Imnaha: $^{206}\text{Pb}/^{204}\text{Pb}=19.06$, $^{207}\text{Pb}/^{204}\text{Pb}=15.586$, and $^{208}\text{Pb}/^{204}\text{Pb}=38.69$). We model these variations using a three-component mixing model that incorporates two lithospheric components (i.e., SCLM-1: older lithosphere, and SCLM-2: younger lithosphere) and a sublithospheric component, represented by the Yellowstone hotspot. This model shows that all YSRP tholeiites have > 96% sublithospheric component. Both the total lithospheric component and the ratio of older-to-younger SCLM varies systematically from west to east, such that basalts erupted closest

¹Manuscript submitted to Earth Planetary Science Letters
Co-authors: John W. Shervais, Barry B. Hanan

to Yellowstone have the highest total lithospheric component and the highest ratio of older-to-younger SCLM. The younger western SRP high-K basalts have the same ratio of older-to-younger lithosphere as the underlying western SRP low-K tholeiites, but with much lower total lithospheric component. This result supports models that call for lithospheric thinning prior to eruption of the high-K basalts.

Introduction

The Yellowstone–Snake River Plain (YSRP) volcanic province is the world’s premier example of a thermal anomaly (“hotspot”) that has been overridden by continental lithosphere (Pierce et al., 2002; Smith et al., 2009). Previous work on Snake River Plain basalts shows that this lithosphere varies in age (i.e., Mesozoic under Washington and Oregon, to Archean underneath Wyoming), thickness, and composition as a function of its distance from the cratonic margin (Hanan et al., 2008; Shervais and Hanan, 2008). Xenoliths found in some basalts show that parts of this lithosphere date back to the Archean (Leeman et al., 1985). The age progression of rhyolite eruptive centers implies a time transgressive onset of volcanism from west to east (Armstrong et al., 1975; Bonnicksen et al., 2008). In contrast, basaltic volcanism – which begins shortly after the end of rhyolite volcanism in each eruptive center – continues into the Holocene, long after these locations have moved away from the active thermal anomaly (Leeman, 1982a,b; Shervais et al., 2005; White et al., 2002; Shervais and Vetter, 2009).

New data from the Yellowstone seismic network (Smith et al., 2009) and the Earthscope Transportable Array (Williams et al., 2010) document a low-velocity seismic anomaly beneath Yellowstone that plunges steeply to the NW and extends to depths of at least 1000 km (James et al., 2011; Obrebski et al., 2010; Smith et al., 2009; Waite et al., 2006; Xue and Allen, 2007; Yuan and Dueker, 2005). The nature of this seismic anomaly continues to be hotly debated; recently proposed models include (1) a deep-seated mantle plume (Schmandt et al., 2012; Waite et al., 2006; Yuan and Dueker, 2005) that has broken through the subducting Farallon slab (Obrebski et al., 2010; Xue and Allen, 2007), (2) material from the lower mantle (but not from the core–mantle

boundary) that has squeezed through an east–west oriented propagating rift in the subducting Farallon plate to form the observed time–transgressive volcanism and “curtain” of low–velocity material beneath the SRP (James et al., 2011), or (3) shallow asthenosphere that has broken through the Farallon plate along a north–south oriented propagating fracture (Liu and Stegman, 2012). In all cases, however, partial melts from the decompressing sub–lithospheric mantle must interact with the overlying lithosphere before they can erupt (Hanan et al., 2008).

This study presents new Sr, Nd, and Pb isotopic analyses of two basalts from the WO–2 drill core at Idaho National Laboratory (INL), 20 volcanic vents located in the central and western Snake River Plain (18 low–K tholeiites and 4 alkali–rich basalt samples), and a single sample of basalt from the Owyhee Plateau that underlies the 16.66 Ma Silver City rhyolite along the craton margin. These samples span the entire length of the Snake River volcanic province and intercalate with previous sample sets from the eastern and western SRP (Hanan et al., 2008; Vetter and Shervais, 1992), Craters of the Moon (Putirka et al., 2009), and Yellowstone (Doe et al., 1982). The purpose of this study is twofold. First, we seek to refine models for lithospheric interaction (e.g., Hanan et al., 2008), in order to evaluate quantitatively the effect of variable lithospheric age, thickness, and composition. Our mixing model differs from that of Hanan et al. (2008) by including two lithospheric end–member components (an older component with low $^{206}\text{Pb}/^{204}\text{Pb}$ ratios, and a younger component with elevated $^{206}\text{Pb}/^{204}\text{Pb}$ ratios), in addition to a sublithospheric mantle component. This model factors in the distinct Archean/Paleoproterozoic provinces that underlie this region of southern Idaho, e.g., the Grouse Creek block (> 2.5 Ga), the Farmington Zone (< 2.5 Ga), the Selway terrane (< 2.5 Ga), and the Wyoming Craton (> 2.5 Ga). We test this model with new data and previously published results. Our second goal is to evaluate the unique origin of high–K basalts that occur in the western SRP (Shervais and Vetter, 2009), within the context of our model for lithospheric interaction, and the abrupt transition from low–K tholeiites to high–K alkali basalts.

Our new data, in conjunction with the 3–component model documents (1) a progressive west–to–east increase in the total lithospheric component, with the highest lithospheric component found in basalts from Yellowstone, (2) a progressive west–to–east increase in the ratio of older/younger subcontinental mantle lithosphere, and (3) that high–K basalts of the western SRP have a lower total lithospheric component compared to the underlying low–K tholeiites, but with the essentially the same ratio of older/younger SCLM, consistent with the delamination model proposed by Shervais and Vetter (2009).

Geologic Setting

The Neogene Yellowstone–Snake River Plain (YSRP) volcanic province is comprised of four distinct regions, i.e., the Eastern province, Central province, Western province, and the Owyhee Plateau (Fig. 3–1). These provinces transect the ancient cratonic boundary of North America delineated by the Western Idaho Shear Zone and $^{87/86}\text{Sr}$ 0.706 line (Fleck and Criss, 2004). Volcanism associated with the YSRP volcanic province was first manifested with widespread eruptions of the Columbia River Basalt Group ca. 17 Ma (e.g., Camp et al., 2003; Hooper et al., 2002; Shervais and Hanan, 2008). The Owyhee plateau is an eastern extension of these voluminous outpourings, and is coeval with the Steens/Imnaha eruptive period. The initial eruptive period in this region is represented by the 16.66 Ma Silver City rhyolite (Shervais and Hanan, 2008). Rhyolite volcanism continued under the Owyhee Plateau until about 8 Ma (Bonnichsen et al., 2008). The Bruneau–Jarbidge eruptive center formed circa 12.4 – 10.4 Ma at the eastern margin of the Owyhee Plateau, and represents the first event to lie on the Central–Eastern SRP hotspot track (Bonnichsen et al., 2008). The western SRP is comprised of a graben structure that lies at an oblique angle to North American plate motion and the eastern SRP NE–trend. This province contains Miocene rhyolites and basalts, Miocene–Pliocene lake sediments, and Pleistocene basalts that overlie lake sediments (Shervais et al., 2002; Wood and Clemens, 2002). Volcanic activity in the western SRP graben began at ~12 Ma, coeval with the Bruneau–

Jarbidge eruptive center and continued to ~200 ka (Bonnichsen et al., 2008; Vetter and Shervais, 1992; Wood and Clemens, 2002).

The eastern and central provinces form a low-relief swath through the surrounding Basin and Range province, and lies essentially parallel to absolute motion of North America (NUVEL 1A model of Gripp and Gordon, 2002). Central and eastern SRP volcanism consists of west-to-east time transgressive rhyolite caldera complexes (e.g., McDermitt, Owyhee-Humboldt, Bruneau-Jarbidge, Twin Falls, Picabo, Heise, and Yellowstone). Each center remained active for approximately 2 – 4 m.y., producing approximately 5,000 to 10,000 km³ of distinctive Snake River-type rhyolite (Bonnichsen et al., 2008; Branney et al., 2008; Leeman, 1982a,b; Morgan and McIntosh, 2005; Morgan et al., 1984; Nash et al., 2006; Pierce and Morgan, 1992). These eruptive centers were then mantled by up to 2 km of basalt (Christiansen, 2001; Smith and Braile, 1994). Basaltic volcanism persists long after the locus of rhyolite volcanism has moved to the northeast (Armstrong et al., 1975; Hughes et al., 2002; Shervais et al., 2005).

Sample and vent locations are listed in Table 3–1. Two samples are from the INL WO–2 drill-hole. This 1.52 km deep borehole penetrates 1.17 km of basalt and inter-bedded sediment (Shervais et al., 2006), and another 0.35 km of rhyolite tuff correlated with the Heise volcanic complex (ca. 4.45 Ma; Morgan and McIntosh, 2005). These samples are young basalts (< 500 ka) from the upper 130 m of core, and compliment the dataset produced by Hanan et al. (2008). Fourteen samples were collected from vents to the north and northeast of Twin Falls, Idaho (Fig. 3–1). This region represents the intersection of the eastern SRP plume track with structures related to the western SRP graben. Radiogenic ages are scarce, but vents generally range in age from ~20 ka to ~2 Ma (Shervais et al., 2005). Most vents are monogenetic, but many have two distinct eruptive phases with contrasting phenocryst assemblages and chemical compositions (Cooke, 1999; Matthews, 2000; Shervais et al., 2005). Basalts of the central SRP are thought to be underlain by rhyolite ash flows and lavas from the Twin Falls eruptive complex – a largely

occult eruptive center, evidenced by ash flows that emanate from a vent north of Twin Falls, and by post–caldera lava flows dated to 6.5 Ma (Bonnichsen and Godchaux, 2002).

Eight samples are located near Mountain Home, Idaho, and include four low–K tholeiitic basalts from plateau–forming shield volcanoes and four high–K transitional alkaline basalts (Shervais et al., 2002, 2005; Shervais and Vetter, 2009). The alkaline lavas erupted from two cinder cones (Union Buttes) and from a small shield volcano further west (Little Joe Butte). The transition from low–K tholeiite to high–K transitional alkaline basalts occurred ca. 800 ka, over a short time period (~ 200 ka; Shervais and Vetter, 2009). The Silver City locale is located near the Silver City range on the NW margin of the Owyhee Plateau, adjacent to the western Idaho suture zone (Fleck and Criss, 2004). This olivine tholeiite is overlain by Silver City rhyolite that is identical in age to the McDermitt rhyolite (16.66 Ma; Bonnichsen et al., 2008). This makes the Silver City basalt coeval with early Columbia River Group eruptions (i.e., Steens Mountain or Imnaha basalts) and suggests that volcanism in this region is part of the wider array of volcanic activity associated with inception of the YSRP volcanic system (Bonnichsen et al., 2008; Shervais and Hanan, 2008).

Methods

A subset of primitive YSRP tholeiites (6.5 – 10.5 wt% MgO), in addition to high–K basalts (> 1 wt%) was selected for isotope analysis. Samples were broken into smaller pieces (0.3 – 1 mm) with a stainless steel mortar and pestle. The rock chips were washed ultrasonically in 18–mega–ohm deionized water and then carefully hand picked under a binocular microscope to avoid any altered and/or fractured surfaces. The rock chips were washed in quartz–distilled 2.5 N HCl and 1 N HBr and rinsed with ultra–pure water before dissolution. Techniques for Pb, Sr, and Nd separation using anion exchange chromatography are described in Hanan et al. (2004, 2008). Lead and neodymium isotopic compositions were measured using the Nu Plasma 1700 at the Baylor Brooks Institute for Isotope Geology at San Diego State University, following the methods of Hanan et al. (2004). Neodymium isotope sample data are normalized to $^{146}\text{Nd}/^{144}\text{Nd} = 0.7219$,

to correct for in-run fractionation. The Nd isotope ratios were corrected for instrumental machine bias and drift by applying a discrimination factor determined by sample-standard bracketing (every 2 samples) with the SDSU AMES Nd standard with $^{143}\text{Nd}/^{144}\text{Nd} = 0.512130$. The measured value of La Jolla Nd at SDSU is 0.511844. Strontium analyses were performed at SIO-UCSD on a Sector-54 multi-collector thermal ionization mass spectrometer. All Sr isotope data are reported relative to NBS 987 standard (accepted $^{87}\text{Sr}/^{86}\text{Sr} = 0.71025$). The in-run mass discrimination for Pb was determined with NIST SRM 997 Tl with $^{205}\text{Tl}/^{203}\text{Tl} = 2.3889$ and NIST SRM 981 (Todt et al., 1996) using the method of White et al. (2000). The Pb isotope ratios were corrected for machine bias and drift by sample-standard bracketing, after correction for fractionation, with NIST SRM 981 (every 2 to 3 samples). The external reproducibility for $^{87}\text{Sr}/^{86}\text{Sr}$ and $^{143}\text{Nd}/^{144}\text{Nd}$ is 2 and 3 ppm respectively, and for $^{206}\text{Pb}/^{204}\text{Pb}$, $^{207}\text{Pb}/^{204}\text{Pb}$, and $^{208}\text{Pb}/^{204}\text{Pb}$ are 65, 98, and 130 ppm, respectively. Total procedural blanks were: <90 pg Pb, <200 pg Nd and < 250 pg Sr. No blank corrections were applied to the data because they are insignificant.

Results

Our new isotopic compositions are presented in Table 3-1. Basalts analyzed for this study are compared with previous SRP isotope studies (Hanan et al., 2008; Shervais and Vetter, 2009; Vetter and Shervais, 1992) and to compositions for the Columbia River Basalt Group (Camp and Hanan, 2008), Craters of the Moon (Putirka et al., 2009), and Yellowstone plateau basalts (Doe et al., 1982).

Isotopic Compositions of YSRP Basalts

Eastern SRP low-K tholeiites from the WO-2 drill core are depleted in $^{143}\text{Nd}/^{144}\text{Nd}$ and enriched in $^{87}\text{Sr}/^{86}\text{Sr}$, relative to Columbia River Group and WSRP high-K lavas (Fig. 3-2a), and are consistent with the isotopic compositions determined by Hanan et al. (2008) for the Nd-Sr-Pb isotope systems. Central SRP basalts have isotopic values that are generally consistent with eastern SRP basalts. They are, however, enriched in $^{208}\text{Pb}/^{204}\text{Pb}$ (~38.5 – 38.9) relative to eastern

SRP basalts, and define a trend that is intermediate between eastern SRP basalts and volcanic rocks from Craters of the Moon, e.g., ‘COM slope’ = 0.8115 ($r^2=0.804$), ‘CSRP slope’ = 0.8978 ($r^2=0.7355$), ‘ESRP slope’ = 0.3394 ($r^2=0.4204$; Fig. 3–2c). Bacon Butte has the most enriched $^{208}\text{Pb}/^{204}\text{Pb}$ composition (39.1) in our study; more enriched than the Craters of the Moon array.

Western SRP low–K tholeiites near Mountain Home, Idaho have isotopic compositions similar to central SRP basalts (Table 3–1). However, these basalts are more radiogenic in Pb and lie at the enriched end of the Pb–isotopic composition arrays, relative to eastern and central SRP basalts. Like the central SRP basalts described above, this array defines a steeper trend than for eastern SRP basalts (Fig. 3–2c), suggesting that western SRP is underlain by lithosphere that is similar in age and composition to that which underlies the central SRP, but distinct from the eastern SRP. High–K basalts from this region have isotopic signatures that are different from low–K tholeiites. They are enriched in $^{143}\text{Nd}/^{144}\text{Nd}$ and depleted in $^{87}\text{Sr}/^{86}\text{Sr}$ relative to the low–K tholeiites, and plot closer to the “bulk silicate earth” (BSE) composition of Zindler and Hart (1986; Fig. 3–2a). They are also enriched in $^{206}\text{Pb}/^{204}\text{Pb}$ relative to the tholeiitic basalts, and have $^{207}\text{Pb}/^{204}\text{Pb}$ and $^{208}\text{Pb}/^{204}\text{Pb}$ –isotope systematics similar to the high–K basalts of Smith Prairie (Boise River Group 2 of Vetter and Shervais, 1992; Fig. 3–2b,c). One western SRP low–K tholeiite (Eureka North) is isotopically similar to the alkali basalts.

Silver City basalt overlaps in Pb–isotope space with the early eruptive phases of the Columbia River flood basalt (Fig. 3–2b,c). This location has been previously linked to early eruptions from the Columbia River Basalt Group (e.g., Camp and Ross, 2004; Camp and Hanan, 2008; Shervais and Hanan, 2008). This new data supports this affinity, but narrows this association to the Imnaha eruptive period.

Isotopic Variations along the YSRP Track

A comparison of our new data to a compilation of isotopic data along the YSRP (e.g., Camp and Hanan, 2008; Carlson, 1984; Doe et al., 1982; Hanan et al., 2008; Hildreth et al., 1991; Vetter and Shervais, 1992; White et al., 2002) shows that the isotopic composition of basalts in

the YSRP vary as a function of their location, in particular their radial distance from Yellowstone. The Pb and Nd isotopic compositions of CRBG–SRP basalts display an abrupt transition from values typical of oceanic accreted terranes in the west to values indicative of interaction with SCLM in the east (e.g., Church, 1985; Hanan et al., 2008; Leeman et al., 1985; McCurry and Rodgers, 2009; Nash et al., 2006). This behavior is exhibited in Figure 3–3.

Overall, ϵ_{Nd} in basalts from Yellowstone to Twin Falls are generally ≤ -2 ; basalts from Twin Falls to Boise are ≤ 0 ; and basalts west of Boise are ≥ 8 epsilon units (Fig. 3–3a). Conversely, a decreasing $^{206}Pb/^{204}Pb$ trend is also observed. Basalts located within 100 km of the Yellowstone Plateau have $^{206}Pb/^{204}Pb$ compositions ≤ 17.5 ; intermediate $^{206}Pb/^{204}Pb$ ratios (17.7 – 18.5) from 200 – 400 km; and further west $^{206}Pb/^{204}Pb$ compositions are ≥ 18.5 (Fig. 3–3b). The locus of this abrupt change is the western Idaho shear zone, which represents the western limit of Laurentian cratonic mantle and the transition to accreted pre–Tertiary oceanic arcs underlain by oceanic mantle lithosphere (Fleck and Criss, 2004; Kistler and Peterman, 1978; Leeman et al., 1992).

The basalts analyzed for this study agree with the trends described above. INL and central plain tholeiites have low ϵ_{Nd} –3 to –5 and intermediate $^{206}Pb/^{204}Pb \sim 17.7 - 18.4$. Western plain low–K tholeiites, however, have ϵ_{Nd} –2 to –4 and $^{206}Pb/^{204}Pb \sim 18.2 - 18.6$ (Table 3–1). The Silver city basalt has similar $^{206}Pb/^{204}Pb$ to the younger oceanic accreted terranes of Oregon. In addition to the geographic variations discussed above, younger Mountain Home alkali basalts are characterized by lower $^{87}Sr/^{86}Sr$ and $^{207}Pb/^{204}Pb$ and higher ϵ_{Nd} and $^{206}Pb/^{204}Pb$, i.e., $^{206}Pb/^{204}Pb$ ranges from 18.6 – 18.7 and ϵ_{Nd} that approaches ≈ 0 epsilon units, compared to older low–K tholeiites (Fig. 3–2).

Discussion

Evidence for YSRP Cratonic Provinces

Evidence of a contrasting geochemical architecture across southern Idaho include: (1) exposures of Archean rocks (e.g., Chamberlain et al., 2003; Foster et al., 2006), (2) Archean–aged

crustal xenoliths in Neogene–Holocene mafic volcanic rocks (e.g., DuFrane et al., 2007; Leeman et al., 1985; Wolf et al., 2005), (3) geochronology of relic zircon grains in Cretaceous and Tertiary intrusive rocks (e.g., Egger et al., 2003; Gaschnig et al., 2007), (4) chemical and mineralogical features of YSRP rhyolites (Leeman et al., 1992; Nash et al., 2006), (5) Nd–, Sr–, Hf–, Pb– and O–isotopic characteristics of Mesozoic intrusions and Tertiary rhyolite (e.g. Farmer, 1988; King et al., 2004; Wright and Wooden, 1991), and (6) the radiogenic isotopic composition of YSRP basalts (e.g., Graham et al., 2009; Hanan et al., 1997, 2008; McCurry and Rodgers, 2009; Reid, 1995).

Foster et al. (2006) compiled these data to produce a new model of the Archean crustal structure, focused in part on the vicinity of the YSRP hotspot track. They showed that the eastern portion of the track is underlain by ≥ 2.5 Ga cratonic lithosphere of the Wyoming province, whereas the Archean/Paleoproterozoic Grouse Creek and Selway provinces underlie the central and western portions. The boundary between the Selway and Grouse Creek provinces is inferred to be near the Pioneer Mountains: accommodating recent identification of 2.6 – 2.7 Ga orthogneiss (Link et al., 2007; McCurry and Rodgers, 2009). The Wyoming province is separated from the Grouse Creek/Selway by a zone of 1.8 – 2.5 Ga Paleoproterozoic rocks defined as the “Farmington zone.”

The Farmington zone represents one of two fundamental boundaries in the YSRP and projects northward along the general trend of the Great Rift. This eastern boundary, however, is best defined by the major and trace element compositions of YSRP rhyolites. Rhyolites west of the Farmington zone have anhydrous phenocryst assemblages with eruption temperatures of 950 – 1100°C. Rhyolites east of the Farmington zone contain hydrous phenocrysts and cooler eruption temperatures 820 – 900°C (Cathey and Nash, 2009; Hughes and McCurry, 2002). The second fundamental boundary is the western Idaho shear zone (WISZ; $\sim 119^\circ$). East of this boundary, age corrected $^{87}\text{Sr}/^{86}\text{Sr}$ ratios are almost exclusively greater than 0.706 for basalts and greater than 0.7085 for rhyolites. West of this boundary, $^{87}\text{Sr}/^{86}\text{Sr}$ ratios for basalts (< 0.7045) and rhyolites ($<$

0.705) are consistently lower. Between is a transition zone characterized by $^{87}\text{Sr}/^{86}\text{Sr}$ ratios spanning 0.7035–0.706 for basalts and 0.705–0.708 for rhyolites (Leeman et al., 1992). Samples from the INL WO–2 drill core are located to the east of the Farmington Zone, CSRP and WSRP samples are located in between the Farmington Zone and WISZ, and the Silver City sample is located to the west of the WISZ (Fig. 3–1).

In the following sections, we model differences in isotopic composition with underlying SCLM sub–provinces and their effect on hotspot derived magmas.

Three–Component Mixing Model

Hanan et al. (2008) demonstrated that (1) small amounts of lithospheric contamination by low degree fractional melts will have a profound impact on the isotopic composition of any magma traversing southern Idaho lithosphere, and (2) that the age and composition of subcontinental lithospheric mantle varied systematically from west to east as a function of distance from the craton margin (or conversely, the distance from Yellowstone). The model of Hanan et al. (2008) was based on a series of binary mixtures between a sublithospheric component, similar in Pb–isotopes to an average Steens basalt composition, with fractional melts derived from heterogeneous Archean lithosphere, characterized by a Pb–isotopic composition represented by the ca. 2.8 Ga isochron for Beartooth Mountain igneous rocks (Wooden and Mueller, 1988). The Beartooth igneous rocks are a good proxy for Paleoproterozoic–Archean lithosphere because they represent the full range in Pb–isotope composition of the lithosphere sources that underlie the YSRP, including Archean gneiss xenoliths found in some eastern SRP basalts (Leeman et al., 1985). Through this model it was shown that the Yellowstone hotspot mixes with different compositions along the Beartooth mixing array, i.e., younger lithosphere in the west to older lithosphere near Yellowstone.

This gradient in the age and composition of the SCLM suggests that we need to consider two SCLM end–members, rather than a single SCLM component. To accommodate mixing of these two SCLM end–members with the sublithospheric component, we extend our model to

three components. The end-members we examine in this three component mixing model are: (1) old, Wyoming-like lithosphere (SCLM-1), located at the low $^{206}\text{Pb}/^{204}\text{Pb}$ end of the Beartooth Pb-Pb isotope array, (2) young, Mesozoic-like lithosphere (SCLM-2), located at the high $^{206}\text{Pb}/^{204}\text{Pb}$ end of the Beartooth array, and (3) a sublithospheric component, similar to an average Steens basalt composition.

Using basic principles described previously by Douglass and Schilling (2000), Hanan and Schilling (1997), Hanan et al. (2000), and Schilling et al. (1992) the mass fractions for each SRP sample can be calculated by using two isotope ratios at a time by applying the following equations (Schilling et al., 1992):

$$z_{depleted} = \frac{P_1}{(p_1 + p_2 + 1)}$$

$$z_{enriched} = \frac{P_2}{(p_1 + p_2 + 1)}$$

$$z_{plume} = (1 - z_1 - z_2) = \frac{1}{(p_1 + p_2 + 1)}$$

where z_1 = mass fraction of low SCLM-1 lithospheric component, z_2 = mass fraction of high SCLM-2 lithospheric component, and z_3 = mass fraction of sublithospheric magma component (equations A9 – A11 of Schilling et al., 1992). The variables p_1 and p_2 are calculated by:

$$P_{Pb-Pb} = \frac{x(y_2 - y_3) + y(x_3 - x_2) + x_2y_3 - y_2x_3}{n_1(x(y_1 - y_2) + y(x_2 - x_1) + y_2x_2 - y_1x_2)}$$

$$P_{Nd-Sr} = \frac{x(n_2y_2 - q_2y_3) + y(n_2x_3 - q_2x_2) + xy(q_2 - n_2) + q_2x_2y_3 - n_2y_2x_3}{x(n_1q_2y_1 - q_1n_2y_2) + y(n_1q_2x_2 - q_1n_2x_1) - xy(n_1q_2 - q_1n_2) - n_1q_2y_1x_2 + q_1n_2y_2x_1}$$

$$p_2 = \frac{n_1p_1(y_1 - y) + (y_3 - y)}{n_2(y - y_2)}$$

If the same denominator isotope pair was plotted (e.g., $^{206}\text{Pb}/^{204}\text{Pb}$ vs. $^{208}\text{Pb}/^{204}\text{Pb}$), equation $p_{1(\text{Pb-Pb})}$ was used to calculate p_1 ; if not (e.g., $^{143}\text{Nd}/^{144}\text{Nd}$ vs. $^{87}\text{Sr}/^{86}\text{Sr}$), equation $p_{1(\text{Nd-Sr})}$ was used to calculate p_1 , but need not be that specific isotope pair (i.e., all variations thereof between Pb–Nd–Sr): x_i and y_i represent end–member isotope ratios and x and y represent measured isotope values of our sample (equations A14 – A16 of Schilling et al., 1992). Lastly, calculated are the enrichment factors n_1 and n_2 , which represent the SCLM–1:Sublith and SCLM–2:Sublith trace element ratio of the components (e.g., Schilling et al., 1992).

Our three–component model allows for a more quantitative picture of the relative SCLM heterogeneity along the YSRP in time and space. The overriding constraint is that our basalts lie within the bounds of the ternary space formed by the three end–members. This model implies that the isotope composition of YSRP basalt is a function of the isotope composition of the end–members (Table 3–2) and the mass balance of the end–members in the mixture. This model (1) allows an evaluation of the assumption of the west–to–east age progression of the SCLM; (2) quantifies the total involvement of SCLM along the SRP; (3) identifies any abrupt changes in the proportion of SCLM; and (4) singles out any anomalies that might not be compatible with a sublithospheric source.

Selection of End–member Compositions

An average composition of Steens basalt (Hanan et al., 2008) was used as our sublithospheric end–member and represents the best estimate for the region (Table 3–2). The accreted oceanic terranes that underlie eastern Oregon and Washington have much less impact relative to the SCLM beneath the SRP, on the isotopic composition of sublithospheric magmas moving through them because of their younger mantle source age and mafic composition (e.g., Camp and Hanan, 2008). We assume that the Pb, Sr, and Nd isotope signature of the sublithospheric component has remained relatively constant since ca. 16.6 Ma (Hanan et al., 2008). Our sublithospheric end–member displays no signs of being contaminated and pass the lithosphere–asthenosphere test of Depaolo and Daley (2000). Lithospheric mantle can be

distinguished from the underlying asthenospheric mantle by utilizing La/Nb and Ba/Nb ratios. Low La/Nb and Ba/Nb (< 1.5 and < 30 , respectively) are representative of asthenosphere, while high La/Nb and Ba (> 1.5 and > 30 , respectively) are representative of lithosphere. The Steens samples, from which our sublithospheric end-member was derived from have asthenosphere-like values.

Lithosphere end-members were chosen to lie at the extremes of a regression of Beartooth Mountain igneous rocks (Wooden and Mueller, 1988), which on a $^{206}\text{Pb}/^{204}\text{Pb}$ vs. $^{207}\text{Pb}/^{204}\text{Pb}$ plot fits the line: $^{207}\text{Pb}/^{204}\text{Pb} = 0.1925 * (^{206}\text{Pb}/^{204}\text{Pb}) + 12.281$ ($r^2 = 0.993$). Increasing and decreasing $^{206}\text{Pb}/^{204}\text{Pb}$ compositions served as input into this equation, in order to find the isotopic composition of our components that best models our data. Other isotope paired arrays were also used to constrain end-member compositions, e.g., Pb vs. Nd, Pb vs. Sr, and Nd vs Sr. The goal was to find a common trace element and isotopic composition that provided the greatest consistency for the mass fractions. The two SCLM components span the range of Pb, Sr, and Nd isotope compositions required by the previous model and retain similar lithosphere/sublithosphere trace element ratios as the Hanan et al. (2008; Data Repository item 2008014) model, i.e., Pb SCLM/Sublith ratio ~ 100 , Sr SCLM/Sublith ratio ~ 10 , and Nd SCLM/Sublith ratio ~ 11 (Table 3-2).

Basement xenoliths that lie at the high $^{206}\text{Pb}/^{204}\text{Pb}$ end of the Beartooth regression are mostly found in the western plain (Leeman et al., 1985, 1992). This high $^{206}\text{Pb}/^{204}\text{Pb}$ SCLM-2 end-member represents “young,” < 2.5 Ga lithosphere, which in this area includes the Selway terrane; defined as a domain of 2.4 – 1.6 Ga Proterozoic basement that crops out in culminations in the Sevier thrust sheets north of the Grouse Creek block (Whitmeyer and Karlstrom, 2007) and possibly the Grouse Creek terrane; a complex mix of Archean and Paleoproterozoic rocks (Foster et al., 2006). Basement xenoliths with low $^{206}\text{Pb}/^{204}\text{Pb}$ ratios are found closer to Yellowstone in the eastern plain (Leeman et al., 1982). The low $^{206}\text{Pb}/^{204}\text{Pb}$ SCLM-1 end-member represents “older,” > 2.5 Ga lithosphere, which includes the Wyoming Craton and Medicine Hat terranes

that underlie this part of the YSRP. The isotopic composition of Pb in SRP rhyolites changes dramatically near the inferred craton edge and becomes progressively more radiogenic west of the craton Archean margin, consistent with lithosphere younging westward.

Three-Component Mixing Model: Results

The results of our 3-component mixing model are shown in Table 3-3. Hanan et al. (2008) showed a systematic east to west increase in the mass fraction of their sublithospheric component, i.e., Yellowstone ~95–98%, eastern SRP ~97–98.5%, and western SRP ~98–99%. Our new 3-component model confirms these trends, which are proposed to reflect west-to-east variations in the age, composition, and thickness of the underlying SCLM. This correlates to our model via an increase in lithospheric contribution as thicker and older cratonic lithosphere is encountered approaching Yellowstone.

Our hypothesis is that high mass fractions of the sublithosphere component correlate with low mass fractions of both lithosphere components. Figure 3-4 displays the mass fraction of both lithosphere components plotted against the mass fraction of the sublithosphere component. Samples from the WSRP (including Bruneau-Jarbidge, Boise River Group, and samples from this study) and Owyhee Plateau (Silver City) have high mass fractions of the sublithosphere component, i.e., greater than ~99%, and low mass fractions of both lithosphere components, i.e., less than ~0.5% SCLM-1 and ~1.5% SCLM-2. Central and Eastern SRP basalts (including COM, Wapi flow, INL, and samples from this study) have sublithosphere mass fractions that range from ~98% to 97%, intermediate SCLM-1 mass fractions; ranging from 0.5% to 1.0%, and intermediate to high SCLM-2 mass fractions; ~1.0% to 1.8%. Yellowstone basalts, however, have the lowest sublithosphere mass fraction; generally <97%, the highest observed SCLM-1 mass fractions; generally >2%, and similar SCLM-2 mass fractions as CSRP and ESRP tholeiites; i.e., 1.0% to 2.5% (Fig. 3-4a). Another observation is that the lithosphere components can be grouped based on their geographic location, i.e., WSRP, C-ESRP, and Yellowstone. Regressions of samples from each region demonstrate that they lie on different trends, with each

trend yielding high correlations, i.e., WSRP ($r^2 = 0.556$), C-ESRP ($r^2 = 0.790$), and Yellowstone ($r^2 = 0.871$) for SCLM-1 and WSRP ($r^2 = 0.948$), C-ESRP ($r^2 = 0.888$), and Yellowstone ($r^2 = 0.884$) for SCLM-2 (Fig. 3-4a,b).

If instead we add and ratio our lithosphere components, different interpretations of the lithosphere thickness and age are produced. We propose that the proportion of SCLM-1 + SCLM-2 (hereafter named ‘Total Lithosphere’) represents a proxy for effective lithospheric thickness, whereas the ratio of old SCLM-1 to young SCLM-2 (hereafter named ‘Lithosphere Ratio’) represents a proxy for the integrated age of the lithosphere and for compositional variations caused by lithospheric rejuvenation. In Figure 3-5, the following outcomes are observed when these parameters are viewed against distance from Yellowstone:

1. Tholeiitic basalts show a modest increase in Total Lithosphere component from west to east: 1.6–2.2% total lithosphere in the western SRP low-K basalts, 1.9–3.0% total lithosphere in the central SRP basalts, 1.8–3.8% in Craters of the Moon basalts, and 2.0–3.5% in basalts from the INL drill core WO-2 (Fig. 3-5a). In the central and eastern SRP, the mean total lithosphere content is just over 2%, suggesting that the thickness of the underlying lithosphere is relatively constant – consistent with recent calculations of lithospheric thickness based on effective elastic thickness in the western USA (Lowry and Pérez-Gussinyé, 2011).
2. Tholeiitic basalts show a systematic west-to-east increase in the Lithosphere Ratio (0.3 to 0.6 mass fraction). This factor of 2 increase is consistent with presumed variations in the age and composition of the underlying lithosphere, with older lithosphere becoming dominant towards Yellowstone (which is underlain by the Archean Wyoming province).
3. Yellowstone Plateau basalts average ~3.5% Total Lithosphere, and extends to a high of 9%, the highest observed in the YSRP province. This is consistent with the results of Lowry and Pérez-Gussinyé (2011), which show a sharp increase in lithospheric thickness just west of Yellowstone. Yellowstone basalts also have a Lithosphere ratio of ~0.9 to 1.9 (Fig. 3-5b). In

other words, Yellowstone basalts incorporate as much as up to 2.5 times more SCLM-1 (which we correlate with the Archean Wyoming province) than the younger SCLM-2.

4. Basalts of the Bruneau–Jarbidge eruptive center (BJEC), on the Owyhee Plateau, have ~1.2 to 2.9% Total Lithospheric, averaging ~1.8% or slightly less than the nearby western SRP basalts (Fig. 3–5a). The Lithosphere Ratio is ~0.25 – significantly less than western SRP basalts (~0.34 average). This area is proposed to be underlain by the Grouse Creek province, an Archean/Paleoproterozoic terrane that is distinct from the coeval Wyoming province which underlies Yellowstone (Foster et al., 2006).
5. The proportion of Total Lithosphere in western SRP basalts correlates with their age and composition. Older low–K tholeiites (>900 ka, $K_2O < 0.65\%$) have Total Lithosphere contents of ~1.9% – slightly higher than the average Total Lithosphere calculated for basalts of the Bruneau–Jarbidge eruptive center, but lower than that calculated for basalts of the central and eastern SRP. In contrast, the younger high–K basalts (<800 ka, $K_2O > 1.2\%$), both from this study and Vetter and Shervais (1992), have significantly lower Total Lithosphere (~1.0–1.6%) than either the underlying low–K tholeiites or Bruneau–Jarbidge basalts (Fig. 3–5a). Nonetheless, these high–K basalts have Lithosphere Ratios that are essentially identical to the underlying low–K tholeiites. This implies that both the older and younger basalts interacted with the same SCLM.
6. The Silver City basalt, which sits on the craton margin as defined by the Sr 0.706 line, involves <0.2% Total Lithospheric mantle (Fig. 3–5a) and has equally low (< 0.1%) SCLM-1 and SCLM-2 components. As a result, the calculated Lithosphere Ratio is sensitive to minor variations in the Pb isotope composition.

Post–Hotspot, WSRP high–K volcanism

Shervais and Vetter (2009) have recently reviewed the occurrence of high–K transitional alkaline basalt in the western SRP and adjacent region. The abrupt change from low–K tholeiitic basalt to high–K transitional alkaline basalt was first recognized by Vetter and Shervais (1992)

and later documented by Shervais et al. (2002) and White et al. (2002). This volcanism largely post-dates Lake Idaho deposits, but is coeval with basaltic volcanism in the eastern SRP (Amini et al., 1984; Shervais et al., 2002; Vetter and Shervais, 1992). Shervais and Vetter (2009) demonstrated that this transition occurred between approximately 700 ka and 900 ka. While some low-K basalts erupted during the transition period have isotopic compositions similar to the younger high-K basalts, all of the high-K basalts have distinct isotopic compositions, with lower $^{87}\text{Sr}/^{86}\text{Sr}$, higher ϵ_{Nd} and higher $^{206}\text{Pb}/^{204}\text{Pb}$ isotopic ratios than the western SRP low-K tholeiites (Fig. 3–2). The western SRP high-K basalts plot near Bulk Silicate Earth (BSE) in Figure 2a, and between the SRP basalt array and the Steens–Imnaha basalts in Figures 3–2b,c.

Two theories are advanced here in order to explain the occurrence of western SRP high-K volcanism. First, alkaline magmas are more likely to erupt during episodes of crustal extension, due to factors that govern the interaction of stress fields at magma-filled fracture tips (Takada, 1994). Fault scarps, with 2 to 9 m of throw, which crosscut shield volcanoes and associated basaltic flows, demonstrate extension within the western SRP graben (Shervais et al., 2002). The age of faulting cannot be determined precisely, but must be younger than ~ 1 Ma, based on the age of the basalt units cut by the faults. In one location, basalt is faulted against alluvial gravel of Canyon Creek, suggesting a late Pleistocene or Holocene age (Shervais et al., 2002). These faults may have played a role in allowing magma to intrude and transit through the crust. Alternatively, as discussed by Shervais and Vetter (2009), the limited time period over which this transition occurred requires that the SCLM was largely stripped away by delamination or a Rayleigh–Taylor instability, prior to eruption of the high-K basalts.

Our data and mixing model demonstrate that the western SRP high-K transitional basalts have a lower Total Lithosphere content than the slightly older low-K tholeiites they overlie (0.5–1.2% vs 1.2–2.2%), however, the SCLM ratio is approximately the same in both suites (~ 0.4 ; Fig. 3–4). This finding lends more credence to the delamination model more so than the extension model, for the fact that if the SCLM were intact during this eruptive period, it would have

superimposed its inherent isotopic composition on sublithospheric partial melts, and since potassic magmas are more naturally buoyant due to lower viscosity, the SCLM would have acted as a density filter.

Summary

The YSRP province is one of the youngest manifestations of hotspot volcanism erupting through continental lithosphere. The “standard model” has the Yellowstone plume impacting North American lithosphere around 17 Ma and partially melting to form the Columbia River flood basalt province, followed by initiation of NE trending time–transgressive volcanism (e.g., Pierce and Morgan, 1992; Pierce et al., 2002; Smith and Braile, 1994). Shervais and Hanan (2008) modified this model by showing that plume–tail volcanism did not commence until at least ~12 Ma, with the Bruneau–Jarbidge eruptive center. Nonetheless, the plume head–plume tail paradigm is generally accepted as the model that best explains the large volume of the initial flood basalts and the subsequent time–transgressive nature of the younger volcanics (Hill et al., 1992; Richards et al., 1989).

The structural architecture of lithosphere underlying the YSRP volcanic province is shown schematically in Figure 3–6. The Silver City basalt underlies 16.66 Ma rhyolite of the McDermitt caldera; therefore it must be considered an eastern extension of the “lower” Steens period of CRBG eruptions. These basalts have isotopic compositions that closely match that of the sublithospheric end–member and have negligible SCLM input (“16.5–10 Ma”; Fig. 3–6a). The rest of the basalts from this study are < 1 Ma. Western SRP basalts erupted through the hypothesized Grouse Creek block, which accounts for the increase in Total Lithosphere. The trend of Columbia River eruptive phases, Smith Prairie basalts, and western plain alkali basalts towards those of the Pb–isotope composition of the BJEC suggests that both suites interacted with similar age–thickness–composition lithosphere (e.g., Shervais and Vetter, 2009: “12–10 Ma”; Fig. 3–6a). Eruption of ‘plains–type’ basalt occurred in the CSRP and continued into the ESRP. Sublithospheric–derived magmas stalled in the middle crust and formed a series of sill–

like layered mafic intrusions (“8–4 Ma”; Fig. 3–6a). The sublithospheric component in these tholeiites are $\leq 98\%$, with an increasing west to east trend for the SCLM–1 component; reaching a maximum of $\sim 1.5\%$, excluding the Yellowstone Plateau. This region transects the ‘Farmington zone’ of Foster et al. (2006); therefore, both lithospheric end–members could be selectively tapped. Alternatively, this region of the YSRP is more complex than the east–west separation of Foster et al. (2006). The final resting place of the Yellowstone hotspot lies underneath the Yellowstone Plateau. Yellowstone basalts have the highest Total Lithosphere and highest SCLM ratio, reflecting interaction of plume–derived magmas with the Wyoming Craton (“ < 1 Ma”; Fig. 3–6a).

Figure 3–6b displays the channel eroded into the SCLM during passage of the hotspot, which has been imaged by seismic refraction (e.g., Peng and Humphreys, 1998; Schutt et al., 1998; Schutt and Humphreys, 2004; Stachnik et al., 2008; Yuan et al., 2010). In our plume–lithosphere interaction model, this confined channel acts as a reservoir for buoyant sublithospheric mantle material, which continues to flow westward beneath the SRP along a shoaling gradient in the SCLM (Shervais and Hanan, 2008). Teleseismic investigations (Humphreys et al., 2000) reveals an anisotropic mantle with a preferred northeast orientation of the olivine *a* axis, consistent with the strain expected for sublithospheric flow. This architecture accounts for both the continued basaltic volcanism millions of years after the North American continent overrode the Yellowstone hotspot, and how hotspot–derived magmas are able to retain their sublithospheric major and trace element chemistry, without being overprinted by the overlying SCLM.

Our work shows that low–K tholeiites have $> 96\%$ sublithospheric component, and display a west–to–east trend of increasing Total Lithosphere (which we correlate with lithospheric thickness), as well as an increasing SCLM ratio (which we correlate with variations in the age and composition of the underlying lithosphere). Young (< 1 Ma) high–K basalts of the western plain have $\geq 99\%$ sublithospheric component, resulting in isotope compositions that approach the

composition of the early Columbia River basalts (i.e., Steens–Imnaha). This work contributes to an already growing line of geochemical evidence that Snake River Plain basalts are derived from the interaction of a deep sublithospheric mantle and SCLM attached to the westwardly migrating North American continent. New Nd, Sr, and Pb isotopes, in conjunction with our 3–component mixing model, helped to construct a unified and consistent model for understanding the temporal–spatial–isotopic variations observed in Snake River Plain lavas.

References

- Amini, M.H., Mehnert, H.H., Obradovich, J.D., 1984. K–Ar ages of late cenozoic basalts from the western Snake River Plain. *Isochron/West* 41, 7–11.
- Armstrong, R.L., Leeman, W.P., Malde, H.E., 1975. K–Ar dating Quaternary and Neogene rocks of the Snake River Plain, Idaho. *Am. J. Science* 275, 225–251.
- Bonnichsen, B., Godchaux, M.M., 2002. Late Miocene, Pliocene, and Pleistocene geology of southwestern Idaho with emphasis on basalts in the Bruneau–Jarbridge, Twin Falls, and western Snake River Plain regions. In: Bonnichsen, B., White, C.M., McCurry, M. (Eds.), *Tectonic and magmatic evolution of the Snake River Plain volcanic province*. Idaho Geol. Surv. Bull. 30. Moscow, ID, United States, 233–312.
- Bonnichsen, B., Leeman, W.P., Honjo, N., McIntosh, W.C., Godchaux, M., 2008. Miocene silicic volcanism in southwestern Idaho: geochronology, geochemistry, and evolution of the central Snake River Plain. *Bull. Volcanol.* 70 (3), 315–342.
- Branney, M.J., Bonnichsen, B., Andrews, G.D.M., Ellis, B., Barry, T.L., McCurry, M., 2008. ‘Snake River (SR)–type’ volcanism at the Yellowstone hotspot track: distinctive products from unusual, high–temperature silicic super–eruptions. *Bull. Volcanol.* 70 (3), 293–314.
- Camp, V.E., Ross, M.E., Hanson, W.E., 2003. Genesis of flood basalts and Basin and Range volcanic rocks from Steens Mountain to the Malheur River Gorge, Oregon. *GSA Bulletin* 115, 105–128.

- Camp, V.E., Ross, M.E., 2004. Mantle dynamics and genesis of mafic magmatism in the intermontane Pacific Northwest. *J. Geophys. Res.* 109 (B08204).
- Camp, V.E., Hanan, B.B., 2008. A plume-triggered delamination origin for the Columbia River Basalt Group. *Geosphere* 4, 480–495.
- Carlson, R.W., 1984. Isotopic constraints on Columbia River flood basalt genesis and the nature of the subcontinental mantle. *Geochim. Cosmochim. Acta* 48, 2357–2372.
- Cathey, H.E., Nash, B.P., 2009. Pyroxene thermometry of rhyolite lavas of the Bruneau–Jarbidge eruptive center, central Snake River Plain. *J. Volcanol. Geotherm. Res.* 188, 173–185.
- Chamberlain, K.R., Frost, C.D., Frost, B.R., 2003. Early Archean to Mesoproterozoic evolution of the Wyoming Province: archean origins to modern lithospheric architecture. *Can. J. Earth Sci.* 40 (10), 1357–1374.
- Christiansen, R.L., 2001. The Quaternary and Pliocene Yellowstone plateau volcanic field of Wyoming, Idaho, and Montana. U.S. Geol. Surv. Professional Paper 729 G, 145 pp.
- Church, S.E., 1985. Genetic interpretation of lead–isotopic data from the Columbia River Basalt Group, Washington, and Idaho. *GSA Bulletin* 96, 676–690.
- Cooke, M.F., 1999. Geochemistry, volcanic stratigraphy, and hydrology of Neogene basalts, central Snake River Plain, Idaho. Thesis, University of South Carolina.
- DePaolo, D.J., Daley, E.E., 2000. Neodymium isotopes in basalts of the southwest Basin and Range and lithospheric thinning during extension. *Chem. Geol.* 169, 157–185.
- Doe, B.R., Leeman, W.P., Christiansen, R.L., Hedge, C.E., 1982. Lead and strontium isotopes and related trace elements as genetic tracers in the upper Cenozoic rhyolite–basalt association of the Yellowstone plateau volcanic field. *J. Geophys. Res.* 87, 4785–4806.
- Douglass, J., Schilling, J.G., 2000. Systematics of three–component, pseudo–binary mixing lines in 2D isotope ratio space representations and implications for mantle plume–ridge interaction. *Chem. Geol.* 163, 1–23.

- DuFrane, S.A., Vervoort, J.D., Leeman, W.P., Wolf, D.E., 2007. Hafnium isotope composition of Archean zircons from xenoliths of the Snake River Plain, Idaho. *Eos Trans. AGU* 88 (52), V43B–1375.
- Egger, A.E., Dumitru, T.A., Miller, E.L., Savage, C.F.I., Wooden, J.L., 2003. Timing and nature of Tertiary plutonism and extension in the Grouse Creek Mountains, Utah. *Int. Geol. Rev.* 45, 497–532.
- Farmer, G.L., 1988. Isotope geochemistry of Mesozoic and Tertiary igneous rocks in the Western United States and implications for the structure and composition of the deep continental lithosphere. In: Ernst, W.G. (Ed.), *Metamorphism and crustal evolution of the Western United States*. Prentice–Hall, Englewood Cliff, New Jersey, pp. 88–109.
- Fleck, R.J., Criss, R.E., 2004. Location, age, and tectonic significance of the western Idaho suture zone. *U.S. Geol. Surv. Open File Rep.* 2004–1039, 48 pp.
- Foster, D.A., Mueller, P.A., Mogk, D.W., Wooden, J.L., Vogel, J.J., 2006. Proterozoic evolution of the western margin of the Wyoming craton: implications for the tectonic and magmatic evolution of the northern Rocky Mountains. *Can. J. Earth Sci.* 43, 1601–1619.
- Gaschnig, R.M., Vervoort, J., Lewis, R.S., King, E., Valley, J., 2007. Multiple punctuated pulses of voluminous silicic magmatism in Idaho: in situ geochronology and isotope geochemistry of the Idaho Batholith. *Geol. Soc. Am.* 39 (6), 608 Abstracts with Programs.
- Graham, D.W., Reid, M.R., Jordan, B.T., Grunder, A.L., Leeman, W.P., Lupton, J.E., 2009. Mantle source provinces beneath the Northwestern USA delimited by helium isotopes in young basalts. *J. Volcanol. Geotherm. Res.* 188, 128–140.
- Gripp, A.E., Gordon, R.G., 2002. Young tracks of hotspots and current plate velocities. *Geophys. J. Int.* 150 (2), 321 – 361.
- Hanan, B.B., Schilling, J.G., 1997. The dynamic evolution of the Iceland mantle plume: the lead isotope perspective. *EPSL* 151, 43–60.

- Hanan, B.B., Vetter, S.K., Shervais, J.W., 1997. Basaltic volcanism in the eastern Snake River plain; lead, neodymium, strontium isotope constraints from the Idaho INEL WO-2 core site basalts, in *Abstracts with Programs – Geological Society of America*, p. 298
- Hanan, B.B., Blichert-Toft, J., Kingsley, R., Schilling, J.G., 2000. Depleted Iceland mantle plume geochemical signature. *Geochem. Geophys. Geosyst.* 1, doi:10.1029/1999GC000009.
- Hanan, B.B., Blichert-Toft, J., Pyle, D.G., Christie, D.M., 2004. Contrasting origins of the upper mantle revealed by hafnium and lead isotopes from the Southeast Indian Ridge. *Nature* 432, 91–94.
- Hanan, B.B., Shervais, J.W., Vetter, S.K., 2008. Yellowstone plume–continental lithosphere interaction beneath the Snake River Plain. *Geology* 36, 51–54.
- Hildreth, W., Halliday, A.N., Christiansen, R.L., 1991. Isotopic and chemical evidence concerning the genesis and contamination of basaltic and rhyolitic magma beneath the Yellowstone plateau volcanic field. *J. Pet.* 32, 63–138.
- Hill, R.I., Campbell, I.H., Davies, G.F., Griffiths, R.W., 1992. Mantle plumes and continental tectonics. *Science* 256, 186–193.
- Hooper, P.R., Binger, G.B., Lees, K.R., 2002. Ages of the Steens and Columbia river flood basalts and their relationship to extension–related calcalkaline volcanism in eastern Oregon. *GSA Bull.* 114, 43–50.
- Hughes, S.S., McCurry, M., 2002. Bulk major and trace element evidence for a time–space evolution of Snake River Plain rhyolites, Idaho. In: Bonnicksen, B., White, C.M., McCurry, M. (Eds.), *Tectonic and magmatic evolution of the Snake River Plain volcanic province*. Idaho Geol. Surv. Bull. 30, 161–171.
- Humphreys, E.D., Dueker, K.G., Schutt, D.L., Smith, R.B., 2000. Beneath Yellowstone: evaluating plume and nonplume models using teleseismic images of the upper mantle. *GSA Today* 10, 1–6.

- James, D.E., Fouch, M.J., Carlson, R.W., Roth, J.B., 2011. Slab fragmentation, edge flow and the origin of the Yellowstone hotspot track. *EPSL* 311 (1–2), 124–135.
- King, E.M., Valley, J.W., Stockli, D.F., Wright, J.E., 2004. Oxygen isotope trends of granitic magmatism in the Great Basin: location of the Precambrian craton boundary as reflected in zircons. *GSA Bull.* 116 (3–4), 451–462.
- Kistler, R.W., Peterman, Z.E., 1978. A study of regional variation of initial strontium isotopic composition of Mesozoic granitic rocks in California. *USGS Professional Paper* 1071, 17 p.
- Leeman, W.P., 1982a. Development of the Snake River Plain–Yellowstone Plateau province, Idaho and Wyoming: an overview and petrologic model. In: Bonnicksen, B., Breckenridge, R.M. (Eds.), *Cenozoic Geology of Idaho*. Idaho Bureau of Mines and Geology Bull. 26, 155–177.
- Leeman, W.P., 1982b. Evolved and hybrid lavas of the Snake River Plain, Idaho. In: Bonnicksen, B., Breckenridge, R.M. (Eds.), *Cenozoic Geology of Idaho*, 26. Idaho Bureau of Mines and Geology Bull. 26, 193–202.
- Leeman, W.P., Menzies, M.A., Matty, D.J., Embree, G.F., 1985. Strontium, neodymium and lead isotopic compositions of deep crustal xenoliths from the Snake River plain: evidence for Archean basement. *EPSL* 75, 354–368.
- Leeman, W.P., Oldow, J.S., Hart, W.K., 1992. Lithosphere–scale thrusting in the western U.S. Cordillera as constrained by Sr and Nd isotopic transitions in Neogene volcanic rocks. *Geology* 20, 63–66.
- Link, P.K., Durk, K.M., Fanning, C.M., 2007. SHRIMP U–Pb ages for Archean orthogneiss, Mesoproterozoic paragneiss, and Eocene Boulder Creek Pluton, Pioneer Mountains, south–central Idaho, part of the 2600 Ma Grouse Creek Block. *Geol. Soc. Am.* 39 (6), 613 Abstracts with Programs.
- Liu, L., Stegman, D.R., 2011. Segmentation of the Farallon slab. *EPSL* 311 (1–2), 1–10.

- Lowry, A.R., Pérez-Gussinyé, M., 2011. The role of crustal quartz in controlling Cordilleran deformation. *Nature* 471 (7338), 353–357.
- Matthews, S.M., 2000. Geology of Owinza Butte, Shoshone SE, and Star Lake quadrangles: Snake River Plain, southern Idaho. Thesis, University of South Carolina.
- McCurry, M., Rodgers, D.W., 2009. Mass transfer along the Yellowstone hot spot track I: petrologic constraints on the volume of mantle-derived magma. *J. Volcanol. Geotherm. Res.* 188, 86–98.
- Morgan, L.A., McIntosh, W.C., 2005. Timing and development of the Heise volcanic field, Snake River Plain, Idaho, western USA. *GSA Bull.* 117 (3–4), 288–306.
- Morgan, L.A., Doherty, D.J., Leeman, W.F., 1984. Ignimbrites of the eastern Snake Plain: evidence for major caldera-forming eruptions. *J. Geophys. Res.* 89 (B10), 8665–8678.
- Nash, B.P., Perkins, M.E., Christensen, J.N., Lee, D.C., Halliday, A.N., 2006. The Yellowstone hotspot in space and time: Nd and Hf isotopes in silicic magmas. *EPSL* 247 (1–2), 143–156.
- Obrebski, M., Allen, R.M., Xue, M., Hung, S-H., 2010. Slab-plume interaction beneath the Pacific Northwest. *Geophys. Res. Lett.* 37, L14305, doi:10.1029/2010GL043489
- Peng, X., Humphreys, E.D., 1998. Crustal velocity structure across the eastern Snake River Plain and the Yellowstone swell. *J. Geophys. Res.* 103 (B4), 7171–7186.
- Pierce, K.L., Morgan, L.A., 1992. The track of the Yellowstone hotspot: Volcanism, faulting, and uplift. In: Link, P.K., Kuntz, M.A., Platt L.B. (Eds.), *Regional geology of eastern Idaho and western Wyoming*. *Geol. Soc. Am. Memoir* 179, 1–53.
- Pierce, K.L., Morgan, L.A., Saltus, R.W., 2002. Yellowstone Plume Head: postulated tectonic relations to the Vancouver slab, continental boundaries, and climate. In: Bonnichsen, B., White, C.M., McCurry, M. (Eds.), *Tectonic and magmatic evolution of the Snake River Plain volcanic province, Idaho*. *Idaho Geol. Surv. Bull.* 30. Moscow, ID, United States, p. 5–33.

- Putirka, K.D., Kuntz, M., Unruh, D., Vaid, N., 2009. Magma evolution and ascent at the Craters of the Moon and neighboring volcanic fields, southern Idaho, USA: implications for the evolution of polygenetic and monogenetic volcanic fields. *J. Pet.* 50 (9), 1639–1665.
- Reid, M.R., 1995. Processes of mantle enrichment and magmatic differentiation in the eastern Snake River Plain: Th isotope evidence. *EPSL* 131 (3–4), 239–254.
- Richards, M., Duncan, R., Courtillot, V., 1989. Flood basalts and hot-spot tracks: plume heads and tails. *Science* 246, 103–107.
- Schilling, J.-G., Kingsley, R.H., Hanan, B.B., McCully, B.L., 1992. Nd–Sr–Pb isotopic variations along the Gulf of Aden: evidence for Afar mantle plume–continental lithosphere interaction. *J. Geophys. Res.* 97, 10927–10966.
- Schmandt, B., Dueker, K., Humphreys, E., Hansen, S., 2012. Hot mantle upwelling across the 660 beneath Yellowstone. *ESPL* 331–332, 224–236.
- Schutt, D.L., Humphreys, E.D., 2004. P and S wave velocity and VP/VS in the wake of the Yellowstone hot spot. *J. Geophys. Res.* 109, B01305
- Schutt, D., Humphreys, E.D., Dueker, K., 1998. Anisotropy of the Yellowstone Hot Spot Wake, Eastern Snake River Plain, Idaho. *Pure Appl. Geophys.* 151, 443–462.
- Shervais, J.W., Shroff, G., Vetter, S.K., Matthews, S., Hanan, B.B., McGee, J.J., 2002. Origin and evolution of the western Snake River Plain: implications from stratigraphy, faulting, and the geochemistry of basalts near Mountain Home, Idaho. In: Bonnicksen, B., White, C.M., McCurry, M. (Eds.), *Tectonic and Magmatic Evolution of the Snake River Plain Volcanic Province*. Idaho Geol. Surv. Bull. 30, 343–361.
- Shervais, J.W., Kauffman, J.D., Gillerman, V.S., Othberg, K.L., Vetter, S.K., Hobson, V.R., Zarnetske, M., Cooke, M.F., Matthews, S.H., Hanan, B.B., 2005. Basaltic volcanism of the Central and Western Snake River Plain: a guide to field relations between Twin Falls and Mountain Home, Idaho. In: Pederson, J., Dehler, C.M. (Eds.), *Guide to Field Trips in the Western United States*. Field Guide, vol. 6. Geol. Soc. Am., Boulder, Colorado, p. 27–52.

- Shervais, J.W., Vetter, S.K., Hanan, B.B., 2006. A layered mafic sill complex beneath the eastern Snake River Plain: evidence from cyclic geochemical variations in basalt. *Geology* 34, 365–368.
- Shervais, J.W., Hanan, B.B., 2008. Lithospheric topography, tilted plumes, and the track of the Snake River–Yellowstone hot spot. *Tectonics* 27 (TC5004).
- Shervais, J.W., Vetter, S.K., 2009. High-K alkali basalts of the western Snake River Plain (Idaho): abrupt transition from tholeiitic to mildly alkaline plume-derived basalts. *J. Volcanol. Geotherm. Res.* 188, 141–152.
- Smith, R.B., Jordan, M., Steinberger, B., Puskas, C.M., Farrell, J., Waite, G.P., Husen, S., Chang, W-L., O'Connell, R., 2009. Geodynamics of the Yellowstone hotspot and mantle plume: seismic and GPS imaging, kinematics, and mantle flow. *J. Volcanol. Geotherm. Res.* 188 (1–3), 26–56.
- Smith, R.B., Braile, L.W., 1994. The Yellowstone hotspot. *J. Volcanol. Geotherm. Res.* 61, 121–187.
- Stachnik, J.C., Dueker, K., Schutt, D.L., Yuan, H., 2008. Imaging Yellowstone plume–lithosphere interactions from inversion of ballistic and diffusive rayleigh wave dispersion and crustal thickness data. *Geochem. Geophys. Geosyst.* 9, Q06004. doi:10.1029/2008GC001992.
- Takada, A., 1994. The influence of regional stress and magmatic input on styles of monogenetic and polygenetic volcanism. *J. Geophys. Res.* 99, 13562–13573.
- Todt, W., Cliff, R.A., Hanser, A., Hofmann, A.W., 1996. Evaluation of ^{202}Pb – ^{205}Pb double spike for high-precision lead isotope analysis. *Earth Processes: Reading the Isotopic Code*, Geophysical Monograph 95.
- Vetter, S.K., Shervais, J.W., 1992. Continental Basalts of the Boise River Group near Smith Prairie. Idaho. *J. Geophys. Res.* 97, 9043–9061.
- White, C.M., Hart, W.K., Bonnicksen, B., Matthews, D., 2002. Geochemical and Sr-isotopic variations in western Snake River Plain basalts, Idaho. In: Bonnicksen, B., White, C.M.,

- McCurry, M. (Eds.), Tectonic and Magmatic Evolution of the Snake River Plain Volcanic Province. Idaho Geol. Surv. Bull. 30, 329–342.
- White, W.M., Albarede, F., Telouk, P., 2000. High-precision analysis of Pb isotope ratios by multi-collector ICP-MS. Chem. Geol. 167, 257–270.
- Waite, G.P., Smith, R.B., Allen, R.M., 2006. Vp and Vs structure of the Yellowstone hot spot from teleseismic tomography: evidence for an upper mantle plume. J. Geophys. Res. 111, B04303
- Whitmeyer, S.J., Karlstrom, K.E., 2007. Tectonic model for the Proterozoic growth of North America. Geosphere 3, 220–259.
- Williams, M.L., Fischer, M.L., Freymueller, J.T., Tikoff, B., Tréhu, A.M., and others, 2010. Unlocking the secrets of the North American continent: an EarthScope science plan for 2010–2020, 78 pp.
- Wolf, D.E., Leeman, W.P., Vervoort, J.D., 2005. U–PB zircon geochronology of crustal xenoliths confirms presence of Archean basement beneath the Central and Eastern Snake River Plain. Geological Society of America 37 (7), 60 Abstracts with Programs.
- Wood, S.H., Clemens, D.M., 2002. Geologic and tectonic history of the western Snake River Plain, Idaho and Oregon. In: Bonnichsen, B., White, C.M., McCurry, M. (Eds.), Tectonic and Magmatic Evolution of the Snake River Plain Volcanic Province. Idaho Geol. Surv. Bull. 30, 69–103.
- Wooden, J.L., Mueller, P.A., 1988. Pb, Sr, and Nd isotopic compositions of a suite of Late Archean, igneous rocks, eastern Beartooth Mountains: implications for crust–mantle evolution. EPSL 87, 59–72.
- Wright, J.E., Wooden, J.L., 1991. New Sr, Nd, and Pb isotopic data from plutons in the northern Great Basin; implications for crustal structure and granite petrogenesis in the hinterland of the sevier thrust belt. Geology 19 (5), 457–460.

- Xue, M., Allen, R.M., 2007. The fate of the Juan de Fuca plate: implications for a yellowstone plume head. *EPSL* 264, 266–276.
- Yuan, H., Dueker, K., 2005. Telesismic P–wave tomogram of the Yellowstone plume. *Geophys. Res. Lett.* 32, L07304
- Yuan, H., Dueker, K., Stachnik, J., 2010. Crustal structure and thickness along the Yellowstone hot spot track: evidence for lower crustal outflow from beneath the eastern snake river plain. *Geochem. Geophys. Geosyst.* 11:10.1029/2009GC002787.
- Zindler, A., Hart, S.R., 1986. Chemical geodynamics. *Annu. Rev. Planet. Earth Sci.* 14, 493–571.

Table 3-1. Sr-Nd-Pb isotopic values for eastern-, central-, western-SRP, and Owyhee Plateau basalts

Vent or Flow Group	Sample #	Sample Location		Vent Location		$^{143}\text{Nd}/^{144}\text{Nd}$	$^{87}\text{Sr}/^{86}\text{Sr}$	$^{206}\text{Pb}/^{204}\text{Pb}$	$^{207}\text{Pb}/^{204}\text{Pb}$	$^{208}\text{Pb}/^{204}\text{Pb}$	
		Lat. (°N)	Lon. (°W)	Lat. (°N)	Long. (°W)						
<u>Eastern SRP</u>											
	INL-1	WO2-90	43.580	112.876		N/A	0.512453	0.70613	18.145	15.622	38.558
	INL-2	WO2-431	43.580	112.876		N/A	0.512461	0.70656	18.201	15.630	38.530
<u>Central SRP</u>											
	Bacon Butte	99SRP-393	42.767	114.482	42.802	114.426	0.512391	0.70710	18.285	15.655	39.066
	Crater Butte	98SRP-177	42.895	114.323	42.955	114.275	0.512414	0.70662	18.079	15.615	38.523
	Dietrich Butte	98SRP-150	42.948	114.198	42.945	114.210	0.512387	0.70697	18.004	15.608	38.501
	Johnson Butte	97SRP-142	43.098	114.202	43.116	114.203	0.512374	0.70692	17.875	15.586	38.465
	Kimama Butte	99SRP-369	42.756	113.927	42.762	113.898	0.512369	0.70710	17.971	15.608	38.522
	Kinzie Butte	97SRP-134-1	43.094	114.333	43.089	114.332	0.512386	0.70673	18.010	15.606	38.478
	Kinzie Butte	98SRP-161	42.983	114.353	43.089	114.332	0.512452	0.70626	18.217	15.621	38.622
	Notch Butte	98SRP-211	42.880	114.450	42.884	114.417	0.512410	0.70680	18.137	15.621	38.672
	Owinza Butte	99SRP-335	42.843	114.166	42.869	114.061	0.512477	0.70629	18.403	15.650	38.803
	Rocky Butte	99SRP-321	42.768	114.183	42.731	114.077	0.512442	0.70628	18.250	15.630	38.729
	Shoshone	99SRP-179	42.982	114.304	43.184	114.351	0.512416	0.70694	18.392	15.652	38.854
	Sid Butte	99SRP-358	42.849	113.959	42.849	113.961	0.512429	0.70700	18.236	15.637	38.714
	Star Lake Butte	99SRP-327	42.808	114.157	42.804	114.155	0.512389	0.70657	18.082	15.618	38.573
	Wilson Butte	99SRP-372	42.780	113.954	42.784	114.214	0.512479	0.70614	18.421	15.655	38.895
<u>Western SRP low-K</u>											
	Crater Rings	96SRP-58-2	43.142	115.910	43.189	115.855	0.512428	0.70651	18.265	15.642	38.704
	Eureka Butte North	96SRP-28	43.177	115.589	43.169	115.570	0.512529	0.70605	18.611	15.664	39.193
	Lockman Butte East	96SRP-35	43.222	115.711	43.211	115.718	0.512448	0.70693	18.430	15.661	38.826
	Rattlesnake Springs	97SRP-106	43.055	115.801	43.125	115.794	0.512459	0.70646	18.386	15.641	38.713
<u>Western SRP high-K</u>											
	Little Joe Butte	97SRP-112	43.002	115.982	43.161	116.010	0.512580	0.70568	18.712	15.658	39.219
	Little Joe Butte	97SRP-122	43.092	115.991	43.161	116.010	0.512599	0.70577	18.703	15.654	39.206
	Union Butte East	96SRP-38-2	43.159	115.746	43.160	115.749	0.512610	0.70505	18.670	15.626	39.068
	Union Butte West	97SRP-111	43.147	115.765	43.157	115.770	0.512589	0.70552	18.667	15.651	39.181
<u>Owyhee Plateau</u>											
	Silver City/Reynolds	OWY-1	43.201	116.704		N/A	N/A		19.063	15.586	38.688

Table 3-2. End-member isotope ratios and elemental abundances used in 3-component mixing models

	SCLM-1	SCLM-2	Sublithosphere	SCLM/Sublith
Sr (ppm)	3000	3000	300	10
Nd (ppm)	154	154	14	11
Pb (ppm)	100	100	1.3	77
$^{87}\text{Sr}/^{86}\text{Sr}$	0.704	0.7451	0.7035	
$^{143}\text{Nd}/^{144}\text{Nd}$	0.5099	0.5099	0.5131	
$^{206}\text{Pb}/^{204}\text{Pb}$	13.8	19.2	19.4	
$^{207}\text{Pb}/^{204}\text{Pb}$	14.938	15.977	15.6	
$^{208}\text{Pb}/^{204}\text{Pb}$	35.68	48.32	38.7	

Table 3-3. Three-component mixing model results; mass fraction of end-members for YSRP samples

Vent or Flow Group	Sample #	Pb–Pb isotope system			Nd–Sr isotope system			
		SCLM–1	SCLM–2	Sublithosphere	SCLM–1	SCLM–2	Sublithosphere	
<u>Eastern SRP</u>								
	INL-1	WO2-90	0.0073	0.0148	0.9779	0.0157	0.0068	0.9775
	INL-2	WO2-431	0.0068	0.0147	0.9786	0.0142	0.0080	0.9778
<u>Central SRP</u>								
	Bacon Butte	99SRP-393	0.0066	0.0169	0.9765	0.0156	0.0097	0.9748
	Crater Butte	98SRP-177	0.0080	0.0154	0.9766	0.0159	0.0083	0.9758
	Dietrich Butte	98SRP-150	0.0089	0.0164	0.9747	0.0161	0.0093	0.9746
	Johnson Butte	97SRP-142	0.0100	0.0161	0.9740	0.0168	0.0092	0.9740
	Kimama Butte	99SRP-369	0.0095	0.0175	0.9730	0.0165	0.0097	0.9738
	Kinzie Butte 1	97SRP-134-1	0.0087	0.0158	0.9756	0.0168	0.0086	0.9746
	Kinzie Butte 2	98SRP-161	0.0063	0.0128	0.9810	0.0154	0.0072	0.9774
	Notch Butte	98SRP-211	0.0073	0.0148	0.9778	0.0156	0.0088	0.9756
	Owinza Butte	99SRP-335	0.0050	0.0128	0.9822	0.0143	0.0072	0.9785
	Rocky Butte	99SRP-321	0.0061	0.0134	0.9805	0.0157	0.0073	0.9770
	Shoshone	98SRP-179	0.0052	0.0134	0.9815	0.0150	0.0091	0.9759
	Sid Butte	98SRP-358	0.0066	0.0149	0.9785	0.0143	0.0093	0.9764
	Star Lake Butte	99SRP-327	0.0081	0.0159	0.9760	0.0171	0.0082	0.9747
	Wilson Butte	99SRP-372	0.0049	0.0131	0.9819	0.0146	0.0068	0.9786
<u>Western SRP low-K</u>								
	Crater Rings	96SRP-58-2	0.0064	0.0150	0.9786	0.0157	0.0079	0.9764
	Eureka Butte North	96SRP-28	0.0034	0.0105	0.9861	0.0129	0.0065	0.9806
	Lockman Butte East	96SRP-35	0.0050	0.0139	0.9812	0.0137	0.0090	0.9773
	Rattlesnake Springs	97SRP-106	0.0049	0.0119	0.9832	0.0145	0.0077	0.9777
<u>Western SRP high-K</u>								
	Little Joe Butte 1	97SRP-112	0.0026	0.0083	0.9891	0.0119	0.0054	0.9827
	Little Joe Butte 2	97SRP-122	0.0026	0.0080	0.9894	0.0109	0.0056	0.9834
	Union Butte East	96SRP-38-2	0.0026	0.0060	0.9914	0.0124	0.0038	0.9838
	Union Butte West	97SRP-111	0.0028	0.0082	0.9889	0.0120	0.0050	0.9830
<u>Owyhee Plateau</u>								
	Silver City/Reynolds	OWY-1	0.0009	0.0010	0.9982		N/A	

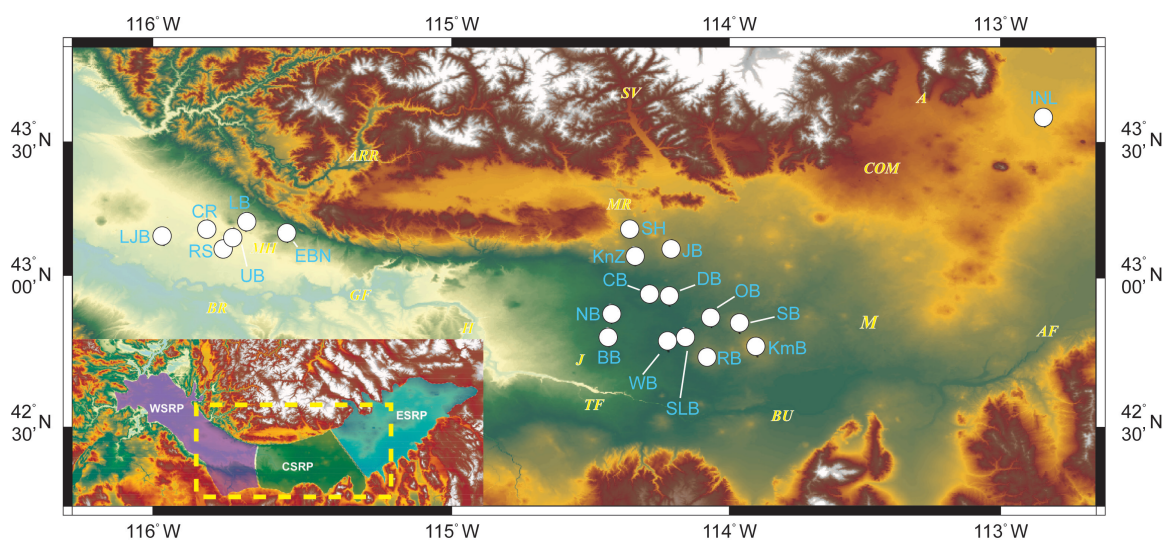


Figure 3-1. Digital elevation map of the Snake River Plain with western, central, and eastern provinces outlined (inset). Zoomed-in portion (yellow-dashed box) shows vent/sample locations analyzed for this study: BB = Bacon Butte, CB = Crater Butte, CR = Crater Rings, DB = Dietrich Butte, EBN = Eureka Butte North, INL = Idaho National Laboratory, JB = Johnson Butte, KmB = Kimama Butte, KzB = Kinzie Butte, LJB = Little Joe Butte, LB = Lockman Butte, NB = Notch Butte, OB = Owinza Butte, RS = Rattlesnake Springs, RB = Rocky Butte, SH = Shoshone, SB = Sid Butte, SLB = Star Lake Butte, UB = Union Buttes, WB = Wilson Butte. Silver City plots off the map (43.201N, -116.704W). Landmarks/towns for reference in the region include: American Falls (AF), Arco (A), Anderson Ranch Reservoir (ARR), Burley (BU), Bruneau (BR), Craters of the Moon (COM), Glens Ferry (GF), Hagerman (H), Jerome (J), Minidoka (M), Mountain Home (MH), Magic Reservoir (MR), Sun Valley (SV), and Twin Falls (TF).

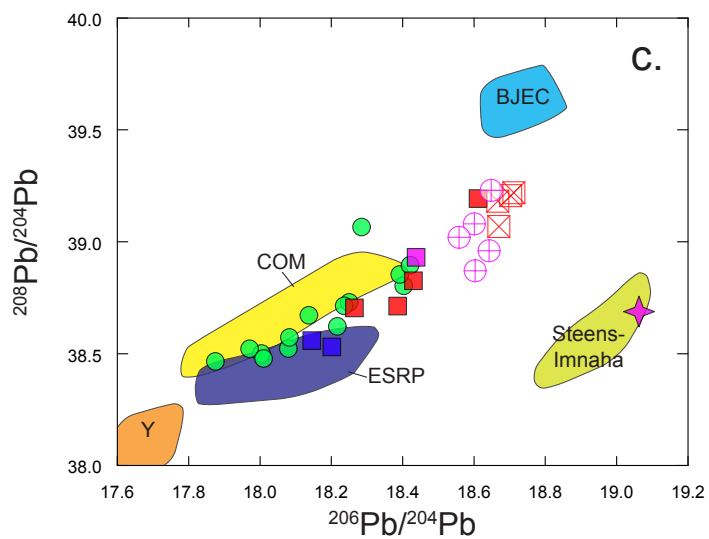
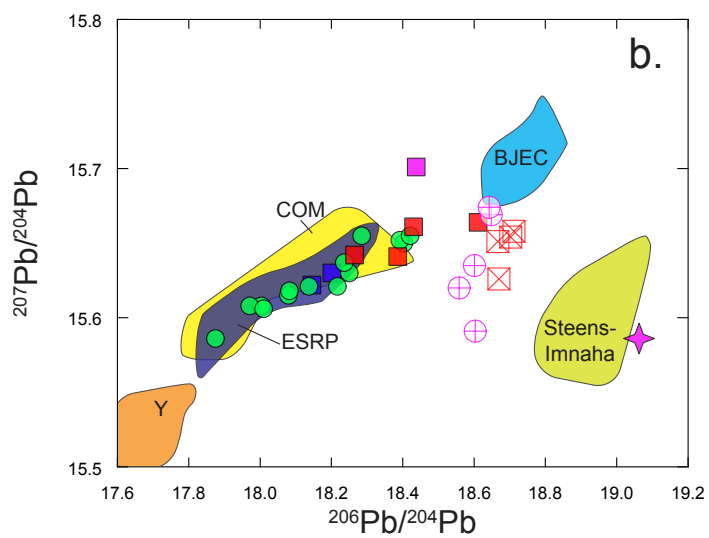
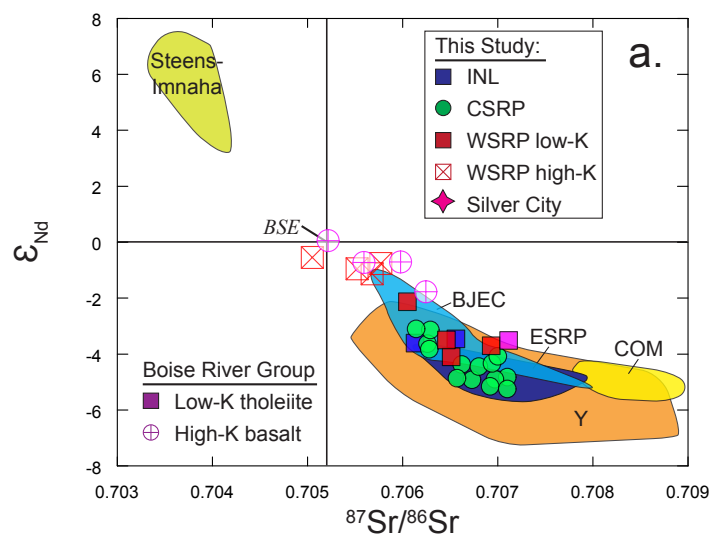


Figure 3-2. Isotopic compositions for basalts analyzed in this study. (a) ϵ_{Nd} vs. $^{87}Sr/^{86}Sr$, (b) $^{207}Pb/^{204}Pb$ vs. $^{206}Pb/^{204}Pb$, and (c) $^{208}Pb/^{204}Pb$ vs. $^{206}Pb/^{204}Pb$. The Nd isotopic results were converted to epsilon units using $\epsilon_{Nd} = [(^{143}Nd/^{144}Nd_{sample})/(^{143}Nd/^{144}Nd_{CHUR}) - 1] * 10000$, with $Nd_{CHUR} = 0.512638$. Samples from this study include: INL (blue square), Central plain (green circle), Western plain low-K tholeiite (red square), Western plain high-K basalt (red square with X), and Owyhee Plateau (pink star). Also shown for comparison are compositions from the Columbia River Basalt Groups (Steens + Imnaha; light green field); Craters of the Moon (COM; yellow field); Yellowstone basalts (Y; orange field); eastern SRP, represented by INL-WO2 and NPREE drillcore (ESRP; dark blue field); western plain, represented by the Bruneau-Jarvis Eruptive Center (BJEC; light blue field); and Smith Prairie basalts: low-K (pink square) and high-K (pink circle with cross). Data sources include: Columbia River Basalt groups (Camp and Hanan, 2008; GEOROC database); Craters of the Moon (Putirka et al., 2009); Yellowstone (Doe et al., 1982); eastern and western plain (Hanan et al., 2008); and Smith Prairie (Vetter and Shervais, 1992).

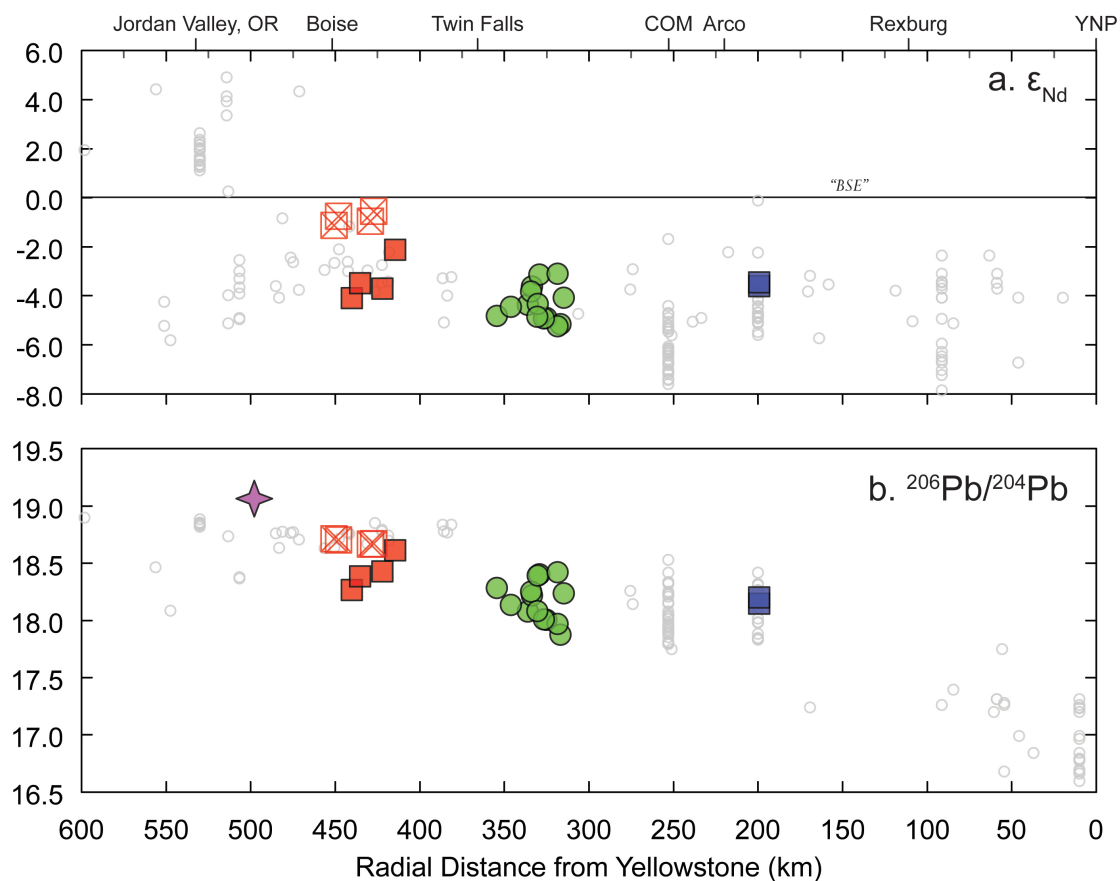


Figure 3-3. Radial Distance from Yellowstone (44.43N, 110.67W) vs. (a) ϵ_{Nd} and (b) $^{206}\text{Pb}/^{204}\text{Pb}$. From 0 to ~ 400 km lies continental lithosphere, with ϵ_{Nd} (-10 to -2) and $^{206}\text{Pb}/^{204}\text{Pb}$ shows an enrichment trend from 16.5 to 18.5. From approximately 550 km and further west lie Mesozoic accreted terranes and has ϵ_{Nd} (2 to 6) and $^{206}\text{Pb}/^{204}\text{Pb}$ (18.5 to 19.0). In between, from 400 to 550 km, lies transitional lithosphere with ϵ_{Nd} (-2 to 2) and $^{206}\text{Pb}/^{204}\text{Pb}$ similar to basalts that lie west. Sample notation same as Figure 2. Background data (grey squares) taken from GEOROC and NAVDAT databases.

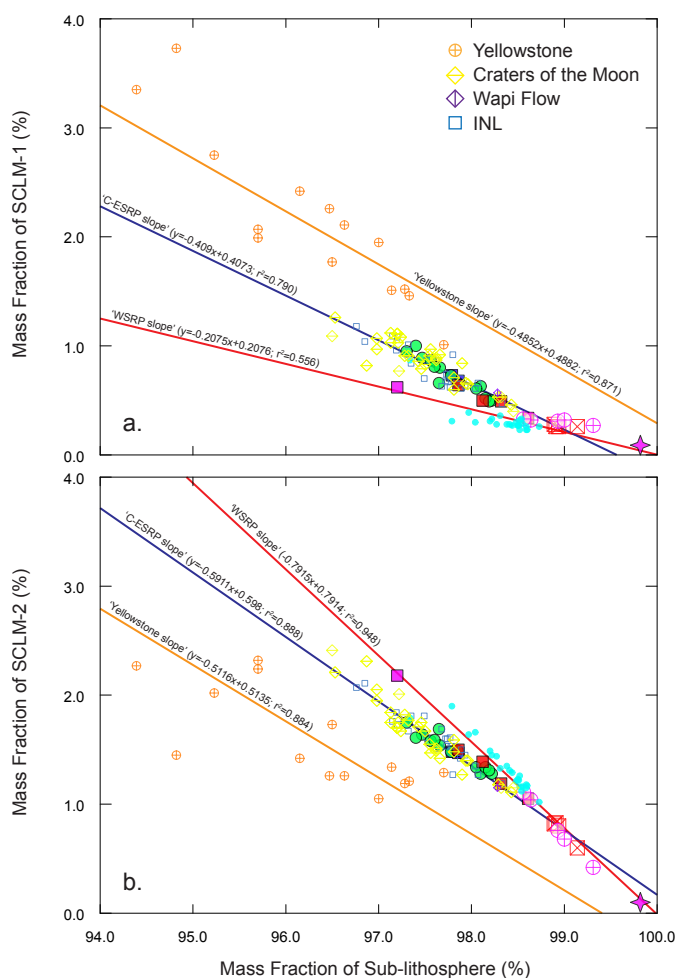


Figure 3-4. Mass fraction of (a) SCLM-1 (%) and (b) SCLM-2 (%) versus Sublithosphere mass fraction (%). Regressions of the SCLM-1 component demonstrate that WSRP samples lie on the trend of $\text{SCLM-1} = -0.2075 * (\text{sublithosphere mass fraction}) + 0.2076$ ($r^2 = 0.556$); Central and Eastern SRP samples lie on the trend of $\text{SCLM-1} = -0.409 * (\text{sublithosphere mass fraction}) + 0.4073$ ($r^2 = 0.790$); and Yellowstone samples lie on the trend of $\text{SCLM-1} = -0.4852 * (\text{sublithosphere mass fraction}) + 0.4882$ ($r^2 = 0.871$). Regressions of the SCLM-2 component demonstrate that WSRP samples lie on the trend of $\text{SCLM-2} = -0.7915 * (\text{sublithosphere mass fraction}) + 0.7914$ ($r^2 = 0.948$); Central and Eastern SRP samples lie on the trend of $\text{SCLM-2} = -0.5911 * (\text{sublithosphere mass fraction}) + 0.598$ ($r^2 = 0.888$); and Yellowstone samples lie on the trend of $\text{SCLM-2} = -0.5116 * (\text{sublithosphere mass fraction}) + 0.5135$ ($r^2 = 0.884$).

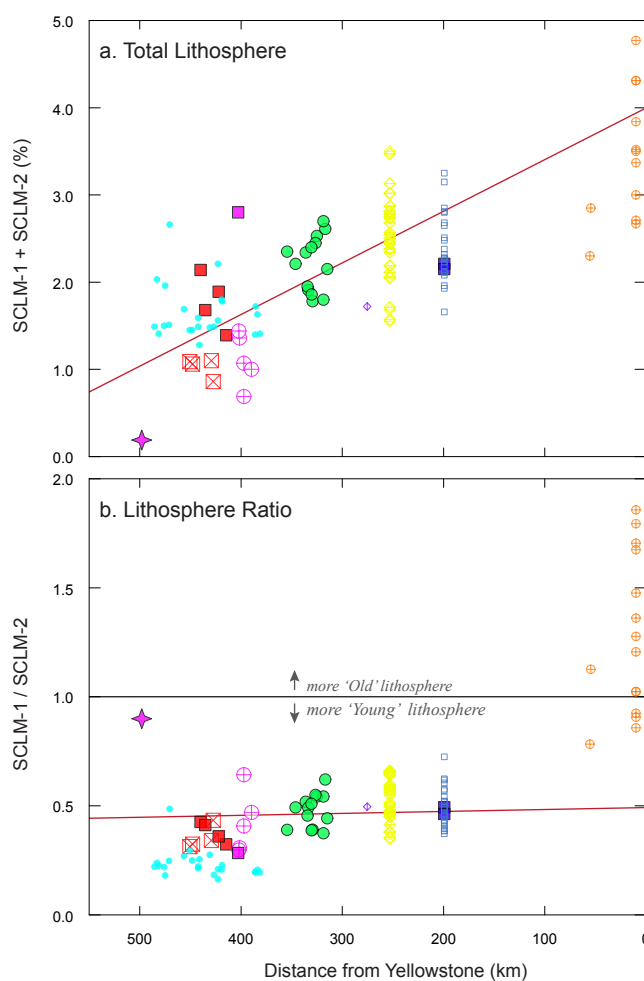


Figure 3-5. Radial distance from Yellowstone versus (a) Total Lithosphere (SCLM-1 + SCLM-2): an approximately 0.5% increase is observed for each region presented in this study, excluding the Owyhee Plateau, which has minimal SCLM involvement. Low-K tholeiites from the western plain average ~ 2% Total Lithosphere, while alkali basalts average ~ 1%. Central SRP basalts have a maximum of 3%. COM and INL basalts have varying amounts of SCLM, but are higher than central or western plain basalts. Yellowstone, at 6%, has the highest SCLM involvement. (b) Lithosphere Ratio (SCLM-1/SCLM-2): all basalts excluding Yellowstone have a ratio of < 1, which signifies involvement of more SCLM-2 type lithosphere relative to SCLM-1 type lithosphere. Red line denotes a linear regression of the samples analyzed for this study only.

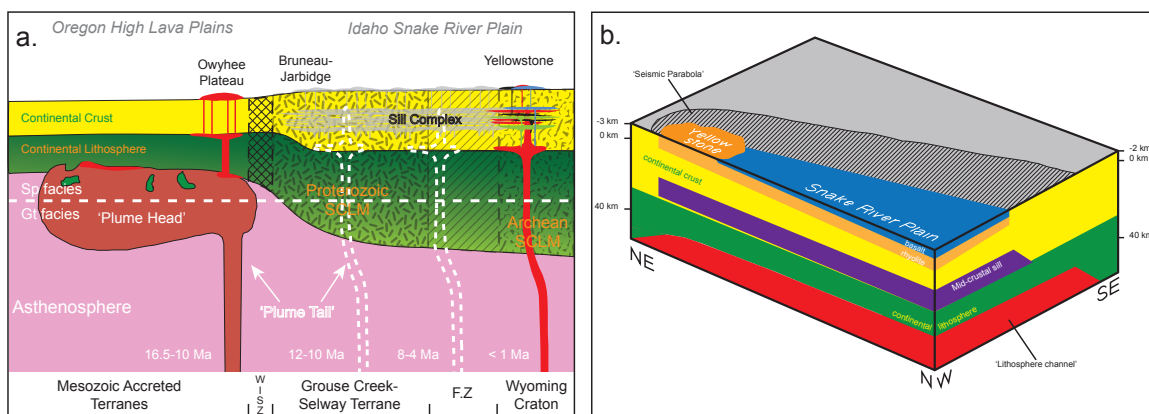


Figure 3-6. (a) SW-to-NE cross-section of the Snake River Plain, demonstrating 1) the east-west gradient in the SCLM, 2) the position of the hotspot at various points in time, i.e., 16.5–10 Ma, 12–10 Ma, 8–4 Ma, and < 1 Ma, 3) sub-crustal province boundaries, i.e., Mesozoic accreted terranes, Western Idaho Shear Zone (WISZ: Fleck and Criss, 2004), Grouse Creek/Selway Terrane, the Farmington Zone (FZ: Foster et al., 2006), and the Wyoming Craton, and 4) the interaction of the plume head and tail with North American lithosphere. (b) Schematic crustal cross-section of the Snake River Plain, demonstrating 1) the mid-crustal sill, 2) Tertiary and Quaternary basalt cover and underlying silicic volcanics, 3) the ‘seismic parabola (Anders and Sleep, 1992; Pierce and Morgan, 1992; Smith and Braile, 1994), and 4) the lithospheric channel (Schutt and Humphreys, 2004). Modelled after Peng and Humphreys (1998), Stachnik et al. (2008), and Putirka et al. (2009). See text for discussion.

CHAPTER 4

LATE PLIOCENE TO QUATERNARY BASALTS FROM THE WENDELL RASA TEST
WELL: ASSIMILATION–FRACTIONATION–RECHARGE PROCESSES OF
THE CENTRAL SNAKE RIVER PLAIN, IDAHO¹

Abstract

The Wendell RASA test well – a fully cored 340 m drill hole located near Wendell, Idaho – preserves at most three million years of volcanism within the central Snake River Plain. This investigation details the stratigraphy, paleomagnetism, lithology, and geochemistry from 52 lava flows and 2 major sediment horizons. Major element data define a limited range in composition, i.e., MgO approaching primitive compositions (i.e., ~ 10 wt%), potassium generally < 0.8 wt%, and tholeiitic iron enrichment trends, similar to lavas of the eastern Snake River Plain. Trace element concentrations are similar to ocean island basalts, with enriched LREE/HREE ratios like many Neogene volcanics of the western Cordillera, but with Ba and Pb enrichments. Based on these compositions, we define 11 flow groups, which include 5 fractionation cycles and 2 recharge cycles (possibly up to 4). When combined with paleomagnetic data, it is possible to suggest time spans of only a few decades or centuries for the emplacement of these groups, while other time breaks range up to many millennia. These cycles are inferred to represent fractionation and recharge of basaltic magma in a series of sill-like layered mafic intrusions located in the middle crust. Parent magmas were derived by partial melting of an E-MORB source mantle, in the relatively shallow spinel lherzolite facies. Lastly, we review the many potential recharge, fractionation, and assimilation processes that characterize much of Snake River Plain olivine tholeiite and ultimately conclude that the processes that control the eruptive history of basalt in the eastern province extend into the central province.

¹Manuscript submitted to *Bulletin of Volcanology*: in revision
Co-authors: John W. Shervais, Duane E. Champion

Introduction

The Yellowstone–Snake River Plain (YSRP) is a broad, flat, arcuate physiographic province that covers much of southern Idaho, culminating in the Yellowstone Plateau. Volcanic activity associated with this province links the voluminous ~ 17 Ma flood basalts of the Miocene Columbia River province in southeastern Oregon to Quaternary volcanic centers at Island Park and Yellowstone in Wyoming (e.g., Pierce et al. 2002; Smith and Braile 1993, 1994). ‘Plains–type’ basalt (Greeley 1982) erupted from numerous small shield volcanoes, and now forms an axial topographic volcanic high down the center of the eastern plain (e.g., Geist et al. 2002a,b; Hughes et al. 2002; Shervais et al. 2005). Petrologic studies have shown that this basalt is mostly olivine tholeiite, with relatively large ranges in major and trace element chemistry that requires some combination of fractional crystallization, crustal assimilation, and periodic recharge of the magma chamber via batch melts from the upper mantle (Miller and Hughes 2009).

Scientific and exploratory test wells and core holes, which help to unravel the subsurface geology, are rare in the Snake River Plain (Fig. 4–1). Over the last 25 years, an extensive shallow to intermediate drilling program in the eastern plain has been carried out at the Idaho National Laboratory (INL) site to study the local stratigraphy and groundwater flow (e.g., Champion et al. 2002, 2011; Geist et al. 2002a,b; Hanan et al. 2008; Hughes et al. 2002; Link and Mink 2002; Shervais et al. 2006a). The motives for these studies have been directed to understanding of the regional geochemistry, age relations, tectonic environment, and petrogenetic processes responsible for creating the volcanic rocks of the Snake River Plain. Results show that (1) the basaltic carapace ranges from < 100 m to 1100 m thick, (2) the rhyolite basement extends to depths in excess of 3 km, (3) sedimentary intercalations are subordinate to volcanic rocks, (4) younger basalts form a series of upward fractionation and recharge cycles that indicate fractionation in magma systems undergoing periodic recharge, (5) older basalts interacted with continental lithosphere, but later basalts interacted largely with crystallized portions of a layered magma system (Shervais et al. 2006a), and (6) Sr–Nd–Pb isotopes suggest small lithospheric

input ($\sim 1 - 5\%$) into a system dominated by plume-derived material similar in major and trace element composition to Hawaiian basalts (Hanan et al. 2008).

Studies concerning the stratigraphy and geochemistry of sub-surface lava flows from the Central Snake River Plain (CSRP) have never been completed before because, until recently, this region has not been sampled by coring (e.g., this study and Project Hotspot). The Wendell Regional-Aquifer Systems Analysis (RASA) hydrologic test well is a 342.3-meter test hole drilled near Wendell, Idaho and was part of the Snake River Plain regional aquifer study (Whitehead and Lindholm 1985). The main purpose for this drilling was to determine the subsurface geology and its controls on water movement in the 40-mile reach of the Snake River from Twin Falls to Bliss, and in particular, in the vicinity of Thousand Springs, the major discharge area for the Snake River aquifer of the eastern Snake River Plain. The hole penetrated an upper basalt unit from 0.3 – 122.8 m, an intermediate unconsolidated sedimentary unit from 122.8 – 179.8 m, a lower basalt unit from 179.8 – 327 m, and another sedimentary sequence from 327 m to total depth. These units were emplaced after activity ceased from the Twin Falls eruptive center (TFEC). The TFEC is a largely cryptic rhyolite eruptive center, attested by ash flows that emanate from a vent north of Twin Falls by post-caldera lava flows dated to 6.5 Ma (Bonnichsen and Godchaux 2002), and by an ovoid gravity anomaly (Shervais et al. 2011).

This study presents a detailed petrologic, paleomagnetic, and geochemical investigation of Wendell RASA basalts, and designed to assess the origin of basaltic magmas in the central SRP and their evolution through time. We touch on the same themes that were investigated for INL drill holes. The goals of this study are to (1) establish the nature and extent of chemical changes through time at a single location, where the physical, chemical, and isotopic characteristics of crust and mantle lithosphere are relatively fixed; (2) correlate lava flows and groups to paleomagnetic time-scales; (3) expand our knowledge of the crystal fractionation and magma recharge history of CSRP basalts, farther west of the INL site; (4) address how these

changes relate to current models of basaltic volcanism in the YSRP; and (5) illuminate the mantle and crustal processes of the central Snake River Plain.

Regional Setting

The CSRP is defined loosely as that part of the eastern Snake River Plain trend that lies between the Owyhee Plateau – a highland in SW Idaho, underlain by Miocene rhyolites, and the Great Rift – a north to northwest trending fissure that extends almost 100 km from Craters of the Moon National Monument on the north to the Wapi lava field on the south (Kuntz et al. 1982). The CSRP contains basalt, rhyolite, and lacustrine sediment (Armstrong et al. 1975; Pierce and Morgan 1992). To the west lies the northwest trending, normal fault–bounded western plain, while to the east lies the predominantly downwarped, not fault–bounded eastern plain.

The main regional geologic features include the pre–basaltic rocks of the highlands to the south and north of Twin Falls (e.g., Kauffman et al. 2011; Fig. 4–1 inset). The southern highlands, including the Cassia Mountains (South Hills), are underlain mainly by Miocene silicic volcanic rocks, erupted from the TFEC and flowed generally southward to cover earlier Tertiary volcanic rocks and Mesozoic and Paleozoic marine sediments. The Cassia Mountains and other parts of the southern highlands mark the separation between the Basin and Range Province and the YSRP province (Bonnichsen and Godchaux 2002). The northern highlands, including the Mount Bennett Hills, are underlain by Miocene silicic volcanic rocks similar to those in the southern highlands and, in turn, overlie older Tertiary volcanic rocks of the Challis Formation and granitic rocks of the Idaho batholith. The Mount Bennett Hills are bordered to the north by the Camas Prairie, a Pliocene–Pleistocene east–west oriented half–graben, in which there are abundant accumulations of late Pliocene and Pleistocene YSRP–type basalt and fluvial and lacustrine sediment (Bonnichsen and Godchaux 2002).

Locally, the area surrounding the Wendell test hole includes late Neogene to Quaternary basalts, which erupted from large shield volcanoes clustered along the axis of the plain (Fig. 4–1 inset). These shield volcanoes are presumed to overlie rhyolite from the Twin Falls eruptive

center (Bonnichsen and Godchaux 2002; Shervais et al. 2005), however, rhyolite was not intersected in this drill core. This area has been mapped in detail (Cooke et al. 2006a,b; Kauffman et al. 2005; Matthews et al. 2006a,b; Shervais et al. 2006b,c) and summarized on the Twin Falls 30' x 60' quadrangle geologic map (Kauffman et al. 2011). Older shield volcanoes have subdued topography and radial drainages with a thick cover of loess and well-developed soils (e.g., Flat Top Butte, Johnson Butte). Many of the older vents appear smaller than the younger vents because their flanks have been partially buried by younger lava flows (e.g., Skeleton Butte, Bacon Butte, Lincoln Butte). Flow surfaces from younger vents are characterized by extremely rugged, chaotic topography, with inflated flow fronts, collapsed flow interiors, ridges, and collapse pits (e.g., Owinza Butte, Rocky Butte, Notch Butte, Wilson Butte). These surfaces lack established drainages but thin loess is present in local depressions. The surfaces of flows from vents of intermediate age have nearly continuous loess mantles of variable thickness and well-developed soils, but lack well defined surface drainages (e.g., Crater Butte, Dietrich Butte: Shervais et al. 2005). Lava flows emanating from some of the buttes mentioned above were intersected in the Wendell RASA well.

Core Observations

Stratigraphy

Volcanic rocks intersected in the Wendell well include two major basalt units and two ash units. The upper basalt unit, identified as Snake River Group, is typical of Quaternary tholeiitic basalt of the ESRP and constitutes the first 123 meters of core (Fig. 4–2a). An older basalt unit, identified as Tertiary Idaho Group, was intersected from 179.8 to 327.1 m. Whitehead and Lindholm (1985) identified 25 lava flows in the Snake River Group section and 27 lava flows in the Idaho Group section (Fig. 4–1a), which range from approximately 1 to 13 m thick. Contacts between lava flows were identified using brecciated flow tops, sediment intervals, or where grayish–red purple basalt with bigger vesicles overlies less vesicular medium gray basalt. Two reddish–orange basaltic ash deposits are observed near the middle of the Idaho Group, at ~ 250

and ~ 260 meters below surface (mbs; Fig. 4–2a). The lower ash unit separates the upper Idaho member (180 to 260 m) from the lower Idaho member (260 to 327 m) and also occurs at a paleomagnetic reversal (Fig. 4–2b).

The Wendell well also intersects four sedimentary units. Two thin sediment horizons, less than three meters thick, are observed in the Snake River section at approximately 70 m (clayey sand) and 85 m (slightly compacted sand and clay). The largest sediment interval is 57–meters thick, observed from 122.8 to 179.8 m, and separates Snake River Group basalt from Idaho Group basalt (Fig. 4–2a). This package fines downward from gravel to clay (Whitehead and Lindholm 1985). Another significant sediment package, composed of fossiliferous claystone and sand and silt, underlies lower Idaho Group basalt, and makes up the bottom 15 m of the hole. Both packages are thought to be equivalent in age to the Glens Ferry Formation. The Glens Ferry Formation (4.5 to 1.0 Ma) is interpreted as flood plain, marsh, and lacustrine facies that accumulated on the eastern margin of Lake Idaho (Malde and Powers 1972; McDonald et al. 1996). Detrital zircon populations from the main body of the Glens Ferry Formation match those of the southwardly flowing Big and Little Wood rivers, which drain the Soldier and Pioneer Mountains (Link et al. 2002).

Paleomagnetic Methods

Wendell RASA drill–core was logged and sampled using the INL Lithologic Core Storage Library protocols described in Davis et al. (1997). Attempts were made to take at least seven paleomagnetic samples from each identified lava flow, using a drill press with a 1–inch diameter diamond core bit, and drilling at right angles to the vertical axis of the original core. The core plugs were trimmed to 2.2–cm (0.87 in) lengths, and the inclination, unoriented declination, and intensity of magnetizations were measured using a cryogenic magnetometer. Progressive alternating–field (AF) demagnetization using a commercial tumbling demagnetizer was performed on one sample from each core plug to remove any components of secondary magnetization. Mean inclination values for each lava flow and 95 percent confidence limits about

the mean value were calculated using the method of McFadden and Reid (1982). These inclination and polarity data obtained from successive lava flows in stratigraphic order allow us to assess whether these flows have similar or different remanent magnetizations.

Paleomagnetic Results

Paleomagnetic inclination and polarity measurements were conducted on hundreds of sub-samples taken from the Wendell RASA core. This study identified stratigraphic intervals that can be grouped as having similar polarity and inclination values or intervals with drastically different inclination values. Consistent inclination values reveal that lava flows and flow groups take months to perhaps decades to accumulate, otherwise the recorded paleomagnetic character of the lavas flows would have evolved to different values due to geomagnetic secular variation. This timeframe coupled with the range of rates for secular variation still results in single mean inclination/polarity values regardless the specific rate of secular variation. Thermal overprinting of YSRP basalts are rare and within the Wendell test well there are no lava flows 10's of meters thick overlying lava flows a few meters thick. Boundaries between the magnetic groups occur where flow bottoms and tops meet older or younger lava flows, and also typically within sedimentary interbeds that separate lava flows. The time break across each of these boundaries is at least hundreds of years long, and possibly much longer. Other than the 57 meters of sediment observed between Snake River and Idaho Group basalts, there are no thick sediment horizons in between individual flows, which would likely represent much longer hiatuses in volcanism, e.g., tens to hundreds of thousands of years. The identification of these groups of lava flows and the time breaks between them is entirely independent of chemistry, and thus an important and independent confirmation of groupings based on chemistry (see discussion).

Most of the surface of the central Snake River Plain is covered with normal magnetic polarity basalts, erupted during the C1n Brunhes Normal Polarity Chron, dated to less than 781 ka (Gradstein et al. 2005). Lava flows within the Snake River Group are thought to be less than 400 ka in age, based on inclination correlation to nearby surface outcrops and $^{40}\text{Ar}/^{39}\text{Ar}$ dating by

Tauxe et al. (2004). Overall, there are seven inclination intervals in the Wendell well: five within the Snake River section and two within the Idaho Group section. Within the Snake River Group there are three steep intervals, separated by two shallow intervals. The first shallow inclination interval (24.3 to 35.3 mbs) is composed of 13 lava flows, with an inclination range of 54° to 62°, and a mean inclination of 59°. The second shallow inclination interval (85.3 to 88.4 mbs) is composed of 4 lava flows and overlies a sediment interbed. Inclination ranges from 49° to 56°, with a mean inclination of 52° (Fig. 4–2b).

Upper Idaho Group lava flows have reversed magnetic polarity, with nearly constant reversed inclination, and slightly steepening from -68° to -71° . The lower Idaho Group has normal polarity, averaging $67.0^\circ \pm 1.1^\circ$ (Fig. 4–2b). There are two plausible scenarios to explain the chronostratigraphy for this section. The first scenario argues for a young timeframe for this section. The reversed upper Idaho member represents a century or less part of the upper Matuyama Reversed Polarity Chron (C1r.2r), and the normal polarity lower Idaho Group member represents a century or less part of the C2n Olduvai Subchron. This timeframe puts the base of the lower Idaho Group at approximately 2.0 Ma. The second scenario argues for an older timeframe for these basalts. The reversed polarity upper Idaho member again represents a century or less part of the Matuyama Reversed Polarity Chron, and does not occur during the Jaramillo or Olduvai Normal Polarity Subchrons. This makes the base of the upper Idaho Group at approximately 2.6 Ma. The normal polarity lower Idaho member now represents a century or less part of the C2An Gauss Normal Polarity Chron, and does not occur during the Kaena or Mammoth Reversed Polarity Subchrons. Thus the base of the lower Idaho Group is as old as 3.6 Ma.

Confirmation of either of these scenarios will be achieved by age dating of the ash units and conispiral gastropods and carbonized plant fragments present in the slightly cemented siltstone near the bottom of the hole. This has yet to be accomplished.

Lithology

Snake River Plain basaltic lavas are dominantly diktytaxitic olivine tholeiites (e.g., Hughes et al. 2002). In thin section, many Wendell RASA lavas are composed of primarily olivine, plagioclase and Fe–Ti oxides. Overall textures range from cumulophyric to diktytaxitic/intersertal to intergranular and hypidiomorphic to allotriomorphic. Olivine ranges from subhedral to anhedral in some sections of the core, but becomes more altered further down in the well, sometimes to completion. Olivine and plagioclase are coarser grained (up to 4 mm across) in the lower Idaho Group section.

In hand sample, the upper part of the Snake River basalt group ranges from very vesicular to vesicular and is distinctively grayish–red purple. The central part is generally much less vesicular and is mostly gray. The lower part is more crystalline, gray in color, and has a more sugary texture. Basalt of this group is typically more vesicular than Idaho Group basalt. Some pervasive features from this section include plagioclase–rich/olivine–poor horizons, which may represent flow breakouts or inflated lava flows (Mary Hodges pers. comm.; Fig. 4–2c); also the tops of the transitions to younger basalt flows are more aphanitic and vesicular. Other features include amygdules (vesicles filled with secondary minerals, e.g., calcite, pyrite, or zeolites), vesicle sheets or segregation zones (~ 51.8 mbs; Fig. 4–2d), and vesicle pipes (~ 100.5 mbs; Fig. 4–2e).

The top 30 m of the upper Idaho Group basalt is a very cindery, scoriaceous zone with high hydraulic conductivity that includes agglutinate and ropey features (Fig. 4–2f). Below this zone, basalt is crystalline with few fractures and vesicles (Whitehead and Lindholm 1985). Throughout much of this part of the core, basalt has a sugary texture with varying degrees of alteration, i.e., secondary mineralization of calcite and clay. Whitehead and Lindholm (1985) also recognized fluorite and ‘serpentinized material’ in their characterization of this core. The ash units overlie oxidized basalt (Fig. 4–2g). Scoriaceous basalt clasts were identified within the matrix of the 250 mbs ash unit. Massive lava flows that underlie the lower ash unit, most likely

represents a ponded flow or lava lake: autoliths (interpreted as remobilized spatter) are observed throughout this section (Fig. 4–2h).

Analytical Methods

All 62 basalt samples from the 52 lava flows, in addition to the basaltic ash unit, were analyzed for whole rock major and trace elements. Samples for major element analysis were first crushed in a Gyral Grinder Shatterbox, inside a tungsten carbide vessel and ground again in an agate mortar and pestle. Following grinding, sample powders were ignited at 800 °C for 24 hours then mixed with 6 grams of a Claisse flux, with a composition of 35% Li–tetraborate and 65% Li–metaborate. Six drops of lithium iodide were added as a releasing agent. That combination was heated using the Claisse–Fluxy fusion machine to convert the mixtures to glass beads and analyzed on the MagiX Pro XRF instrument at California State University, Fresno.

Rare earth and other trace element concentrations were measured using the Perkin–Elmer 6000 Inductively Coupled Plasma Mass Spectroscopy at Centenary College, Shreveport, Louisiana. Approximately 60 mg of each sample was first dissolved in 2ml HF and 3 ml HNO₃ for three hours: watch glasses prevented evaporation. After the target time was reached, watch glasses were removed and ran to dryness. After HF/HNO₃ dissolution and dry down, another 3 ml HNO₃ was added and left at 50°C overnight, then dried down at 90°C. After this second dry–down, another 3 ml HNO₃ was added and dried down immediately. The sample was brought into solution with 2–3 ml of 50% HNO₃ and 5% HNO₃ to 50 ml. This analytical protocol was modified from Jenner et al. (1990) and Neal (2001). Table 4–1 demonstrates that the ICP instrument at Centenary College was able to reproduce USGS standard W–2 within accepted standard deviation values.

Geochemical Results

Major Elements

Wendell RASA lavas are sub-alkaline, tholeiitic basalt (Le Bas et al. 1986), with Snake River Group basalts slightly more alkali-rich than Idaho Group basalts (Fig. 4-3). Whole-rock major element compositions are listed in Table 4-2 (Snake River Group) and Table 4-3 (Idaho Group). Idaho Group and Snake River Group basalts have similar compositional ranges, e.g., SiO₂ ranges from 46 – 49 wt%, Al₂O₃ = 12 – 16 wt%, FeO_t = 12 – 16 wt%, MgO = 7 – 10 wt%, CaO = 9 – 11 wt%, and K₂O ≤ 0.8 wt%. Loss on ignition (LOI) is generally low for both groups; however, some samples within the Idaho Group have high LOI (up to 2.3%). Overall, Wendell RASA lavas define smooth to diffuse increasing and decreasing trends on MgO-variation plots (Fig. 4-4, a-h). Titanium, iron, potassium, and phosphorous generally increases with decreasing MgO, while silica, aluminum, and calcium generally decreases with decreasing MgO. These major element compositions and trends are typical of ESRP tholeiitic basalts and similar to those from other eastern SRP drill cores, e.g., WO2 and NPPE (Shervais et al. 2006a), Test Area North (Geist et al. 2002a,b), and USGS-132 (Miller and Hughes 2009). They are, however, higher in Fe than similar basalts of the eastern Snake River Plain, but less Fe-rich than typical ferrobasalts often found in the western SRP (Fig. 4-4d).

Trace Elements

Overall, Wendell RASA lavas have trace element trends similar to basalts from the ESRP (Fig. 4-4i-o). Trace element compositions are listed in Table 4-2 (Snake River Group) and Table 4-3 (Idaho Group). Although similar in general, the Snake River Group and Idaho Group do vary in some trace elements, e.g., Snake River Group basalts have higher Rb (Fig. 4-4j), Sr (Fig. 4-4k), Ba (Fig. 4-4m), and Hf (Fig. 4-4n) than Idaho Group basalts. These similarities and differences are best displayed on Primitive Mantle normalized (Taylor and McLennan 1985) multi-element variation diagrams (Fig. 4-5). Snake River and Idaho Group basalts display progressive incompatible element enrichment (Fig. 4-5). Idaho Group basalts are HREE-

enriched compared to Snake River Group basalts. Snake River Group basalts have a steep REE pattern, with HREE 2 to 10x PM and LREE 10 to 20x PM (Fig. 4–5a). Idaho Group basalts have a flatter REE pattern, with HREE 8 to 20x PM and LREE 10 to 20x PM (Fig. 4–5b). Both suites display similar incompatible element compositions, i.e., Ba, Pb, and Rb, up to 100x, 50x, and 30x PM, respectively, and compatible element compositions, i.e., Sc and V, up to 3x PM for both.

Discussion

Stratigraphic Trends

Several distinct depth–correlated trends are observed on plots of element concentration versus depth (Fig. 4–6). Within the Snake River Group, there are a series of near surface lavas that have higher SiO₂ (49.0 wt%) than the rest of the core, which averages approximately 48.0 wt % (Fig. 4–6b). Potassium, in general, increases from ~ 0.1 to ~ 0.5 wt% up–section (Fig. 4–6d). Chromium exhibits an overall decrease up–section, but within the Idaho Group section, below the 250–mbs ash horizon, decreases from 350 to 200 ppm: above this horizon, chromium decreases from 400 to 250 ppm (Fig. 4–6f).

Increasing and decreasing trends for MgO (Fig. 4–6b) and TiO₂ (Fig. 4–6e) up–section help define 11 flow groups [or individual lava flows grouped based on similar major and trace element compositions or similar paleomagnetic inclination]. Flow groups are numbered from top to bottom: Flow Group 1 (3.1 – 13.6 m; 4 flows), Flow Group 2 (27.3 – 32.4 m; 5 flows), Flow Group 3 (36.2 – 54.6 m; 5 flows), Flow Group 4 (59.7 – 85.8 m; 4 flows), Flow Group 5 (74.8 – 116.1 m; 11 flows), Flow Group 6 (187.7 – 196.8 m; 2 flows), Flow Group 7 (211.9 – 227.9 m; 4 flows), Flow Group 8 (229.9 – 242.4 m; 4 flows), Flow Group 9 (252.9 – 262.9 m; 6 flows), Flow Group 10 (266.4 – 285.9 m; 10 flows), and Flow Group 11 (293.3 – 322.4 m; 7 flows). Flow Groups 4 and 5 are the only flow groups that interleave with each other. This finding is of particular interest because no other SRP drill core exhibits this behavior. Lava flows in drill core are packaged together to represent an eruption from one vent or plumbing system. This interpretation shows that possibly two vents or plumbing systems were concurrently active. Other

interpretations of this stratigraphy are unsatisfactory because the 3 lava flows that overlie flow 16b continue the fractionation trend observed for the lower part of Flow Group 4. The 3 lava flows that comprise the upper part of Flow Group 5 continue the fractionation trend observed in the lower part of Flow Group 5. In other proposed scenarios these trends would be considered coincidences.

These 11 flow groups are classified as fractionation (decreasing MgO/increasing TiO₂ up-section), recharge (increasing MgO/decreasing TiO₂ up-section), or neither. This includes 5 fractionation trends (4, 5, 7, 8, and 10), 2 recharge trends (3, 11), and 3 groups that do neither (1, 2, and 9). Flow Group 6 is a possible recharge trend, however, there were only 2 flows available for sampling, but is consistent with the titanium data. It should be noted that flow 16, although composed of two flow units (a and b), belongs to two different flow groups, 5 and 4, respectively. This determination was made by compositions observed in Table 4-2 (especially FeO_t and TiO₂) and by the depth-chemistry trends observed in Figure 4-6.

Idaho Group basalts have a La/Lu ratio that ranges from 30 to 60, while Snake River Group basalts range from 50 to 80 (Fig. 4-6g). This ratio should remain more or less constant during simple fractional crystallization; wide ranges represent either variations in the extent of partial melting of a garnet-bearing source, or the assimilation of crustal lithologies during fractionation. The occurrence of flow groups with limited La/Lu ranges (i.e., Flow Groups 1, 2, 6, 7, 10, and 11) is consistent with fractionation, whereas flow groups with wide ranges (i.e., Flow Groups 5, 8, 9, and one sample each from Flow Groups 3 and 4) must reflect assimilation or melting effects. The chromium trends add further confirmation for these divisions and define 5 major fractionation cycles: 2 within the Idaho Group, and 3 in the Snake River Group (Fig. 4-6f).

Correlation of Paleomagnetic and Geochemical Cycles

This study presents a unique opportunity to correlate and merge geochemical and paleomagnetic measurements to define flow groups that are both chemically related and erupted within a relatively short time span (e.g., Champion et al. 2011). Figure 4-6 compares each of our

11 flow groups with the depth–corresponding inclination data by juxtaposing paleomagnetic data, alongside chemical data, plus a generalized stratigraphy of the Wendell well, and the mean inclination value for our proposed boundaries. This figure also presents an enhanced interpretation of the fractionation–recharge stratigraphy.

In order to preserve consistent inclination values, lava flows must erupt within a time period of only months to decades, with a maximum of approximately a century; eruptions that last longer than a century generally will not preserve the same paleomagnetic inclination. Time breaks between flow groups are inferred to represent at least a couple of hundred of years and possibly much longer. Significant hiatuses in volcanism, revealed by thick sediment packages or polarity reversals, are inferred to last thousands to tens of thousands of years.

Based on geochemistry, the Snake River Group was divided into 5 flow groups. Flow Groups 1 and 2 are clearly separated by different paleomagnetic mean inclination values, whereas the chemical data are less clear, i.e., similar MgO–content but distinct in SiO₂. Flow Group 1 with mean inclination of 74° and Flow Group 2 with mean inclination of 59° are time independent of each other by at least centuries. These two units, therefore, are manifestations of two separate batches of lava coming to the surface at two different times. Flow Groups 3 and 4 have a boundary at about 58 meters, which is in the middle of a consistent (77±1°) normal polarity interval, probably emplaced over a short time span, i.e., only a few years to decades. Flow Group 3, based on chemistry is a recharge cycle, however, the very top of Flow Group 3 occurs within lavas having a mean inclination value of 71±3°, which is different than the rest of Group 3 lava flows and could represent a hiatus of a century or two. Paleomagnetic data suggests that Flow Groups 4 and 3 together represent a fractionation–recharge episode of limited time duration. The mean inclination value of 76±3° for the top part of Flow Group 5 could also possibly be paleomagnetically associated with the short time interval of Flow Groups 3 and 4, but the chemistry plots do not suggest any associated trends. Additionally, based on stratigraphy, it is separated from the top part of Flow Group 4 by a sedimentary interbed at 73.5 mbs, and is thus

time independent, and only coincidentally similar in mean inclination value. The upper part of Flow Group 5 is separated from its lower part, by the lower part of Flow Group 4. The lower part of Flow Group 4 has a mean inclination value of $52\pm 6^\circ$, and completely different from both the lower Flow Group 5 mean inclination of $75\pm 1^\circ$, and the upper part of Flow Group 5 mean inclination of $76\pm 3^\circ$. The timeframe to move from 75° to 52° has to be viewed as at least several centuries, but could be thousands to tens of thousands of years. Similarly, the timeframe to move from 52° back to 76° is an additional several centuries to many thousands of years. Therefore, the overall timeframe from the bottom of Flow Group 5 to the top of Flow Group 4 has to be considered close to a thousand years, but possibly very much longer.

Idaho Group basalts were divided into 6 flow groups. Flow Groups 6 and 7 are separate parts of a consistent reversed inclination interval of $-71\pm 1^\circ$, lasting no longer than a century. Flow Groups 8 and 9 have a mean inclination of $-68\pm 2^\circ$; however, Flow Group 9 is separated from Flow Groups 6, 7, and 8 by the 250 mbs ash unit. Two lines of evidence support the conclusion that Flow Groups 9 through 6 erupted in only a century or so: 1) the consistent steep reversed inclinations, and 2) the “ash” between Flow Groups 8 and 9 may be an indication of an instantaneous event. If that were the case then Flow Group 9 to 8 would be considered a recharge period, followed by fractionation and weak recharge (i.e., Flow Groups 8 to 6). On the other hand, if the “ash” between Flow Groups 8 and 9 is on a surface of long enduring time, then the Flow Group 8 to 6 sequence represents fractionation followed by weak recharge and Flow Group 9 is an earlier unrelated event. The reversal in polarity between Flow Groups 9 and 10 is an indication that they are separated by at least several thousands of years of time, if not tens of thousands of years. Flow Groups 10 and 11 are separated based on chemistry into a recharge cycle, followed by a fractionation cycle. However, they record a consistent mean normal polarity inclination value ($67\pm 1^\circ$). These two flow groups occur within an approximately 50-meter thick package of massive basalt, which based on paleomagnetism represents a single eruption cycle requiring at most a few decades to erupt and emplace. It is difficult to imagine that the

fractionation/recharge cycles of Flow Group 10 and 11, respectively, can form during this “brief” time–frame. It seems more likely that these two cycles erupted from different vents; each with its own plumbing system that erupted unrelated lavas during near simultaneous eruptions. This conclusion goes beyond the focus of this study, but presents an attractive opportunity to study lava flow emplacement and magma differentiation on “brief” geologic time–scales.

Petrologic Models for Wendell RASA basalts

The major and trace element composition, in conjunction with the depth–correlated variations detailed above imply the superposition of several different processes that operated throughout the volcanic history of the area intersected by the Wendell well and the CSRP as a whole. Some of the mechanisms that can operate within continental basalt systems include fractional crystallization (FC), bulk mixing, and assimilation paired with FC (AFC). We investigate each of these processes using the “FC–AFC–FCA–mixing” excel spreadsheet of Ersoy and Helvacı (2010). In these models we display the Rb versus K/Rb ratio. Rubidium is a highly incompatible element and its bulk partition coefficient is smaller than potassium, therefore, differentiation processes dominated by crystal fractionation will result in an increase of the Rb concentration in the remaining melt (Ersoy and Helvacı 2010).

Previous workers have suggested that the dominant process controlling the evolution of YSRP olivine tholeiite is low–pressure fractional crystallization of olivine and plagioclase, with a groundmass of minor apatite and spinel (e.g., Geist et al. 2002; Leeman 1982a,b). We model fractional crystallization of a parent magma – flow 51a (9.31 wt% MgO). Results are shown in Figure 4–7a (green line). It could be argued that fractional crystallization does play a role in the formation of only two lower Idaho Group samples (flows 35 and 52e) but requires greater than 60% crystallization. Overall, fractional crystallization is inconsistent with the limited range in major element and compatible trace element concentrations and if one were to argue for FC alone, then multiple parent magmas would need to be generated to produce a series of FC curves.

Wendell RASA basalts have relatively high phosphorus and titanium compositions, as observed in Figure 4–4 and in Tables 4–1 and 4–2. This observation is similar to other drill core and surface flows (e.g., Geist et al. 2002a,b; Shervais et al. 2006a). In order to account for this enrichment, we mixed a high P/Ti end–member with flow 51a, via two–component bulk mixing. In this scenario, the starting composition approaches the composition of the assimilate. Again, using flow 51a as a parent composition, we mixed with an average composition for Graveyard Point intrusive rocks (GPI: White 2007). The chilled margins of the Graveyard Point Intrusion (6 – 8 Ma) has a composition intermediate between high–alumina olivine tholeiites from the northwestern margin of the Basin and Range province and the more evolved olivine tholeiites typical of the younger (< 3 Ma) SRP basalts (White 2007). This pluton is a good model for shallow sub–volcanic magma chambers in the YSRP. Similar to the results for fractional crystallization, this scenario might be plausible for some samples but does not produce a unique mixing solution for all samples. Results show that bulk mixing of GPI intrusive rocks is possible for flows 21a and 52c; however, the amount of mixing needed ranges as high as 50%, which is considered to be very unrealistic (Fig. 4–7a – yellow line). Although not shown, other end–members were tested, i.e., evolved Crater of the Moon composition (McCurry et al. 2008) and an average YSRP rhyolite composition, however, these models could not replicate the range in K/Rb. Therefore, bulk mixing of the most logical crustal rocks observed in this region cannot replicate Wendell RASA basalt compositions, and therefore not viable within the CSRP.

Much of the chemical complexity shown by Wendell RASA basalts might be accounted for if crystallization were accompanied by assimilation, e.g., AFC. To further test AFC in the central plain, we assimilated the average GPI intrusive rock (gabbro) composition used for the bulk mixing model, while fractionating our parent composition (flow 51a). One important variable in these calculations is the “r” value, which represents the ratio of assimilated material to crystallized material (DePaolo 1981). An “r” value of 0 represents fractional crystallization, while an “r” value of 1 represents bulk mixing. AFC of gabbro agrees very well with the observed

compositions from Wendell RASA, when “ r ” ranges from 0.1 to 0.3 and modeled with 10% increments of fraction of melt remaining (Fig. 4–7a – red lines). These results are consistent with the hypothesis of Shervais et al. (2006a) for the partial assimilation of previously intruded mafic magmas by later YSRP basalts.

Another scenario we tested was treating flow 51a as a primary magma and generating a series of parent magmas through bulk mixing, which then undergoes further FC or AFC. A primary magma is defined as a partial melt of a mantle source, while a parent magma is defined as the most magnesian liquid that can be inferred from a given rock suite in the crust. In Figure 4–7b, we first mix flow 51a (parent magma) with gabbro from the Graveyard Point Intrusion, and then fractionate primary magmas created along the mixing trend. Up to 20% bulk assimilation captures the range of K/Rb observed in Wendell lavas. Fractional crystallization trends were generated from 10% and 20% bulk mixing values. These trends again require high amounts of crystallization to reach observed Rb compositions from Wendell lavas. In Figure 4–7c, again we first mix flow 51a (parent magma) with gabbro from the Graveyard Point Intrusion, but now apply further AFC of GPI gabbro from primary compositions. High amounts of AFC are required to reach Wendell RASA compositions. These last two models represent extreme scenarios for CSRP basalt petrogenesis.

These models are not meant to reproduce the exact paths followed by Wendell RASA lavas, which is not possible without knowing the true assimilant and all parent magma compositions, but only to constrain the types of processes involved and their relative importance in controlling observed chemical trends. Two conclusions are noted with these models. First, fractional crystallization remains a possibility, but each suite would then require separate parent magmas: this may or may not happen after bulk mixing with gabbro. Second, parent magmas may result from source variation, source melting, or AFC of a single primary magma. We test source variation and partial melting in the next section.

Mantle Origin of CSRP Magmas

The chemical systematics of continental basalts may reflect different degrees of partial melting of similar source regions or partial melting of source regions that differ significantly in their trace element characteristics. In this section we model the effect of variations in the amount of partial melting with different mantle source compositions. In order to model these variations, a series of non-modal batch melting models featuring spinel (~ 1.5 to 2.0 GPa) or garnet (~ 2.0 to 3.0 GPa) lherzolite assemblages were constructed with chemical compositions that reflect the source regions of primitive mantle (PM: Taylor and McLennan 1985), normal mid-ocean ridge basalt (N-MORB: Salters and Stracke 2004), and enriched mid-ocean ridge basalt (E-MORB: Mertz et al. 2001). Input parameters (Table 4-4) for this model include the starting source composition, modal proportions of minerals in the parent lherzolite (source mode), and the proportions of those minerals entering the melt (melt mode). Mineral-melt distribution coefficients were compiled from the Earthref.org website (e.g., McKenzie and O'Nions, 1995 and references therein). Non-modal batch melting yields results similar to pooled fractional melts, but at slightly higher melt fractions.

Models involving a garnet lherzolite source for N-MORB, E-MORB, or PM, although not shown, show no similarity to either Snake River Group or Idaho Group trace element compositions. Garnet facies melting results in compositions that are HREE depleted and LREE enriched; thus are LREE/HREE enriched at small melt fractions. In addition, REE patterns crossover between Ho and Er, where small and large fractional melts have the same composition. These features allow us to rule out batch melting of a garnet lherzolite as the source of Wendell RASA basalts.

Models involving spinel facies melting are able to reproduce observed Wendell RASA normalized trace element compositions (Fig. 4-8). Starting with a primitive mantle source, the REE pattern is flat to depleted whereas the observed compositions display a slope. Partial melting matches the spread in HREE for both Snake River and Idaho Group basalts, but at low percent

partial melts (1%) overestimate the HREE and the more incompatible elements (Rb, Pb, Ba, Th) and underestimate the LREE. Higher percent partial melts (20%) underestimate all elements except the HREE (Fig. 4–8,a–d). Similar results are observed if instead an N–MORB mantle source was used. The range in HREE is captured, but again, have a flat to depleted trend. Low percent melts underestimate the LREE and other trace elements, while higher percent partial melts are uniformly depleted in all elements (Fig. 4–8,b–e).

Melting of an E–MORB mantle source in the spinel lherzolite facies best reproduces Wendell RASA compositions. Melt fractions that best reproduce Snake River and Idaho Group compositions range from 5 – 15%; similar to those calculated for other YSRP basalt (i.e., Shervais and Vetter 2009). These models capture all trace element characteristics, i.e., HREE depletion, LREE enrichment, and enriched HFSE (Fig. 4–8, c–f). The melt models do not capture enriched compositions in Ba and Pb. This characteristic among recent lavas in western US mafic igneous rocks has been attributed to contributions from the continental lithosphere that experienced subduction metasomatism (e.g., Fitton et al. 1991). The fit of the model melts derived from an E–MORB source to the observed data is remarkably good, especially considering that the composition of the E–MORB source was calculated to model oceanic island basalts, not continental tholeiites (Mertz et al. 2001). Partial melting of this enriched source is not only required for Wendell RASA lavas, but is an important mantle source in YSRP basalt genesis (e.g., Hanan et al. 2008; Shervais and Vetter 2009).

Enriched Mantle Source = Mantle Plume?

It has been debated that this enriched mantle source represents a deep–seated mantle plume, i.e., the Yellowstone hotspot. Geochemical support for the plume model comes from recent studies of major and trace element chemistry (e.g., Christiansen and McCurry 2008; Shervais et al. 2006a; Vetter and Shervais 1992), and radiogenic isotopes (Hanan et al. 2008) and helium isotopes (Graham et al. 2009). We further investigate the plume model by examining

diagnostic trace element ratios of depleted (MORB) and enriched (Hawaii) sources, compared with Wendell RASA basalts.

The derivation from an enriched source is best observed by co-variation of Th/Yb versus Ta/Yb (Fig. 4-9a). These ratios allow for an evaluation of source composition by diminishing the effects of fractionation due to crystallization and partial melting (e.g., Hughes et al. 2002; Pearce 1983). Enriched sources (represented by ocean island basalts, i.e., Hawaii) are high in both Th/Yb and Ta/Yb (i.e., > 0.3 , respectively), while depleted sources (represented by MORB) are low (i.e., < 0.3 , respectively). Wendell RASA basalts plot within the “enriched sources” field. The vector “W” (within-plate enrichment), defines the overall trend in Wendell RASA basalts. An enriched source in the YSRP, according to non-plume centered models, could include heterogeneous enriched sub-continental mantle (e.g., Leeman and Vitaliano 1976; Menzies et al. 1983; Hanan et al. 1997), with the caveat that isotopic and other chemical data also suggests crustal contamination as another process in some YSRP and Yellowstone basalts (Hildreth et al. 1991; Leeman 1982c). The latter process would correspond to the “C” (crustal contamination) vector, which the Wendell core does not show, however, the overall spread may be related to variable source hybridization due to a combination of subduction zone and within-plate processes (vectors “S” and “W”: Hughes et al. 2002).

Another diagnostic ratio which can further assess the enriched versus depleted source issue is Zr/Nb versus Y/Nb (Shervais and Vetter 2009). Depleted components will have high Zr/Nb and Y/Nb, while enriched components will have low ratios because Nb is more incompatible than either Zr or Y. Figure 4-9b compares an enriched source (ocean island basalt, i.e., Hawaii), with a depleted source (compilation of global MORB geochemistry). In this plot, the two trends intersect at low ratios (i.e., $Y/Nb \sim 1$ and $Zr/Nb \sim 3$). Wendell RASA basalts define a trend with a wide range of Zr/Nb but a more limited spread in Y/Nb. Idaho Group basalts have $Y/Nb \sim 2$ and Zr/Nb that ranges from 11 – 15 and Snake River Group basalts have $Y/Nb \sim 1$ and Zr/Nb that ranges from 8 – 14. The overall trend, however, of Wendell RASA core overlaps the Hawaiian

trend (Fig. 4–9b). Snake River Group basalts do plot closer to the intersection of MORB and Hawaii basalts. The Wendell RASA low–K tholeiitic basalts represent mixing with a depleted end–member composition similar to that involved in the Hawaiian plume; note that this depleted end–member component is not typical zero–age Pacific–like MORB source asthenosphere.

Crustal and Mantle Processes of the central SRP

Significant variations in both the crustal and lithosphere structure have been documented within the eastern Snake River Plain (e.g., Braile et al. 1982; Dueker and Humphreys 1990; Humphreys and Dueker 1994; Humphreys et al. 2000; Peng and Humphreys 1998; Saltzer and Humphreys 1997; Sparlin et al. 1982). A relatively high velocity layer in the middle crust has been interpreted as a mid–crustal sill complex. This complex measures approximately 10–km–thick by 90–km–wide, with seismic velocities (~ 6.5 km/s) intermediate between mafic lower crust and the more felsic intermediate crust. This mafic “sill” is inferred to represent basaltic melts that were intruded into the crust; where magmas rose buoyantly and collected at their level of neutral buoyancy.

Evidence of a mafic sill complex underlying the CSRP is provided by regional seismic refraction studies, which indicate that the sediment and volcanic fill are underlain by material in the intermediate crust having appropriate velocity and density of diabase or gabbro intrusive rocks, and not material typical of granite (Hill and Pakiser 1967; Yuan et al. 2010). In addition, the Graveyard Point Intrusion, located near the Oregon–Idaho boarder ~ 100 km west of Boise, represents such an exposed mafic intrusive complex (White 2007). Lastly, cumulate gabbro xenoliths (ol + cpx + plag + Fe–Ti oxide) are noted in some lava flows emanating from CSRP vents (i.e., Sid Butte: Matthews et al. 2006b).

The petrologic models presented in this study are consistent with the above observations. We infer partial melting of an enriched mantle source at pressures of approximately 10 – 20 kbar, in the spinel lherzolite facies, because the slope of the rare earth element patterns rule out garnet–bearing sources. Fractionation occurred largely within the mid–crustal sill complex, which

exposed fractionating magma to previously injected gabbroic dikes from earlier intrusive episodes, similar in composition to Graveyard Point intrusive rocks. Further evidence of the influence of a central YSRP sill complex comes from the stratigraphic cyclic trends, which resulted from mixing between chemically primitive and evolved compositions. The upward fractionation sequences are inferred to represent fractionation cycles identified in layered intrusions. Reversed intervals document the progressive influx of new magma batches (e.g., Shervais et al. 2006a). This recharge of an evolved magma with new primitive melt is the most important factor in forming the repetitive cycles that are characteristic of layered mafic intrusions. The Graveyard Point Intrusion provides the only example of the evolved compositions necessary to mix with more primitive magmas to produce the observed trends.

The gradational transitions imply that the influx of new magma batches occurred over a period of time, and did not completely overwhelm residual magma from the previous fractionation cycle. In this scenario magma is assumed to be extracted into a homogeneous batch, until this magma collects into some part of the lower–middle crust and fractionates extensively prior to continued ascent and eruption (e.g., Hughes et al. 2002). In contrast, abrupt transitions from evolved to primitive compositions imply a complete turnover in the magma supply, consistent with observations in many layered intrusions for a return to phase assemblages and compositions that are as primitive as the basal cumulates in the underlying cycle. Alternatively, abrupt reversals may represent tapping of a new magma storage chamber, or non–uniform distribution of the erupted lava.

Conclusions

The data and models presented in this study provide our best look at the construction and evolution of the central Snake River Plain through time at a single geographic location. Late Pliocene and Pleistocene basalts of the central Snake River Plain sampled by this drill core represent eruptions from volcanoes similar to those observed on the surface today. The

geochemical and paleomagnetic data, alongside petrologic models define very clear relationships for central SRP basalts:

(1) Wendell RASA basalts present similar major and trace element compositions to basalts from the eastern plain.

(2) The merger of chemical and paleomagnetic data enhances the flow unit divisions and gives confidence to our divisions based on chemistry.

(3) The lavas from this study form a series of upward fractionation cycles and reversed cycles that represent fractionation of individual magma batches and progressive recharge of a crustal magma chamber. Each cycle may have originated from single volcanoes, or alternatively, individual volcanoes may include more than one fractionation–recharge cycle.

(4) The preservation of these chemical cycles is inferred to represent fractionation and recharge of basaltic magma in a series of sill–like layered mafic intrusions located in the middle crust.

(5) Fractionation was accompanied by assimilation of crustal material, but this crust could not be the ancient cratonic crust that underlies this region. Our models indicate the dominant assimilant was previously intruded mafic rocks.

(6) Trace element ratios indicate that the parent magmas of Wendell RASA basalts came from an enriched mantle source, similar to Hawaiian plume basalts.

Future drilling projects (i.e., Project Hotspot – www.icdp-online.org) will further address how continental hotspots construct and interact with North American lithosphere and how this interaction affects the geochemical evolution of mantle–derived magmas within the central Snake River Plain.

References

Armstrong RL, Leeman WP, Malde HE, (1975) K–Ar dating, Quaternary and Neogene volcanic rocks of the Snake River Plain, Idaho. *Am J Sci* 275:225–251

- Bonnichsen B, Godchaux M, (2002) Late Miocene, Pliocene, and Pleistocene geology of southwestern Idaho with emphasis on basalts in the Bruneau–Jarbridge, Twin Falls, and western Snake River plain regions. In: Bonnichsen, White, McCurry (eds) Tectonic and magmatic evolution of the Snake River Plain volcanic province. Idaho Geol Surv Bull 30. Moscow, ID, United States, pp. 233–312
- Braile LW, Smith RB, Ansorge J, Baker MR, Sparlin MA, Prodehl C, Schilly MM, Healy JH, Mueller S, Olsen KH (1982) The Yellowstone–Snake River plain seismic profiling experiment; crustal structure of the eastern Snake River plain. *J Geophys Res* 87:2597–2609
- Champion DE, Lanphere MA, Anderson SR, Kuntz MA (2002) Accumulation and subsidence of the Pleistocene basaltic lava flows of the eastern Snake River Plain, Idaho. In: Link PK, Mink LL (eds) Geology, hydrogeology, and environmental remediation: Idaho National Engineering and Environmental Laboratory, eastern Snake River plain, Idaho. Special Paper 353, Geol Soc Am. Boulder, CO, United States, pp. 175–192
- Champion DE, Hodges MKV, Davis LC, Lanphere MA (2011) Paleomagnetic correlation of surface and subsurface basaltic lava flows and flow groups in the southern part of the Idaho National Laboratory, Idaho, with paleomagnetic data tables for drill cores. USGS Scientific Investigations Report 2011–5049. 34 p., 1 pl. (DOE/ID 22214)
- Christiansen EH, McCurry M (2008) Contrasting origins of Cenozoic silicic volcanic rocks from the western Cordillera of the United States. *Bull Volcanol* 70: 251–267
- Cooke MF, Shervais JW, Kauffman JD, Othberg KL (2006a) Geologic Map of the Dietrich Butte Quadrangle, Lincoln County, Idaho: Idaho Geological Survey, Moscow Idaho, DWM–63 scale 1:24,000
- Cooke MF, Shervais JW, Kauffman JD, Othberg KL (2006b) Geologic Map of the Dietrich Quadrangle, Lincoln County, Idaho: Idaho Geological Survey, Moscow Idaho, DWM–66 scale 1:24,000

- Davis LC, Hannula SR, Bowers B (1997) Procedures for use of, and drill cores and cuttings available for study at, the Lithologic Core Storage Library, Idaho National Engineering Laboratory, Idaho: U.S. Geological Survey Open-File Report 97-124 (DOE/ID-22135), 31p
- DePaolo DJ (1981) A neodymium and strontium isotopic study of the Mesozoic calc-alkaline granitic batholiths of the Sierra Nevada and Peninsula Ranges, California. *J Geophys Res* 86:10470-10488
- Dueker K, Humphreys E (1990) Upper mantle velocity structure of the Great Basin. *Geophys Res Lett* 17:1327-1330
- Ersoy Y, Helvaci C (2010) FC-AFC-FCA and mixing modeler: A Microsoft Excel spreadsheet program for modeling geochemical differentiation of magma by crystal fractionation, crustal assimilation and mixing. *Computers and Geosciences* 36:383-390
- Fitton JG, James D, Leeman WP (1991) Basic magmatism associated with Late Cenozoic extension in the western United States: Compositional variations in space and time. *J Geophys Res* 96:13693-13711.
- Geist D, Teasdale R, Sims E, Hughes S (2002a) Subsurface volcanology at TAN and controls on groundwater flow. *GSA Special Paper* 353:45-59
- Geist D, Sims E, Hughes S (2002b) Open-system evolution of a single cycle of Snake River Plain magmatism. *GSA Special Paper* 353:193-204
- Geist DJ, Sims EN, Hughes SS, McCurry M (2002) Open-system evolution of a single episode of Snake River Plain magmatism. In: Link PK, Mink LL (eds) *Geology, hydrogeology, and environmental remediation; Idaho National Engineering and Environmental Laboratory, eastern Snake River plain, Idaho*. Geol Soc Am. Boulder, CO, United States
- Gradstein FM, Ogg JG, Smith AG (2005) *A Geologic Time Scale 2004*. Cambridge University Press

- Graham DW, Reid MR, Jordan BT, Grunder AL, Leeman WP, Lupton JE (2009) Mantle source provinces beneath the northwestern USA delimited by Helium isotopes in young basalts. *J Volcanol Geotherm Res* 188:128–140
- Greeley R (1982) The Snake River Plain, Idaho: representative of a new category of volcanism. *J Geophys Res* 87 (B4):2705–2712
- Hanan BB, Vetter SK, Shervais JW (1997) Basaltic volcanism in the eastern Snake River plain; lead, neodymium, strontium isotope constraints from the Idaho INEL WO–2 core site basalts, in *Abstracts with Programs – Geological Society of America*, p. 298
- Hanan BB, Shervais JW, Vetter SK (2008) Yellowstone plume–continental lithosphere interaction beneath the Snake River Plain. *Geology* 36:51–54
- Hildreth W, Halliday AN, Christiansen RL (1991) Isotopic and chemical evidence concerning the genesis and contamination of basaltic and rhyolitic magma beneath the Yellowstone Plateau Volcanic Field. *J Pet* 32:63–138
- Hill DP, Pakiser LC (1967) Seismic–Refraction Study of Crustal Structure between the Nevada Test Site and Boise, Idaho. *Geol Soc Am Bull* 78:685–704
- Hughes SS, McCurry M, Geist DJ (2002) Geochemical correlations and implications for the magmatic evolution of basalt flow groups at the Idaho National Engineering and Environmental Laboratory. In: Link PK, Mink LL (eds) *Geology, hydrogeology, and environmental remediation; Idaho National Engineering and Environmental Laboratory, eastern Snake River plain, Idaho*. *Geol Soc Am Special Paper* 353:151–173
- Humphreys ED, Dueker KG (1994) Physical state of the western U.S. upper mantle. *J Geophys Res* 99:9625–9650
- Humphreys ED, Dueker KG, Schutt DL, Smith RB (2000) Beneath Yellowstone: evaluating plume and nonplume models using teleseismic images of the upper mantle. *GSA Today* 10:1–6

- Jenner GA, Longerich HP, Jackson SE, Fryer BJ (1990) ICP–MS – A powerful too for high–precision trace–element analysis in Earth Science: Evidence from analysis of selected U.S.G.S. reference samples. *Chem Geol* 83:133–148
- Kauffman JD, Othberg KL, Shervais JW, Matthews SH (2005) Geologic Map of the Shoshone Quadrangle, Lincoln County, Idaho: Idaho Geological Survey, Moscow Idaho; DWM–44, Scale: 1:24000
- Kauffman JD, Othberg KL, Gillerman VS, Garwood DL (2011) Geologic Map of the Twin Falls 30 x 60 minute quadrangle, Idaho: Idaho Geological Survey, Moscow, Idaho, Digital Web Map DWM–43–M, 1:100,000
- Kuntz MA, Champion DE, Spiker EC, Lefebvre RH, McBroome LA (1982) The Great Rift and the evolution of the Craters of the Moon lava field, Idaho. In: Bonnicksen B, Breckenridge R M (eds) *The Great Rift and the Evolution of the Craters of the Moon Lava Field, Idaho*, Idaho Bur Mines Geol Bull, 26: 423–437
- Le Bas MJ, Le Maitre RW, Streckeisen AL, Zanettin B (1986) A Chemical Classification of Volcanic Rocks Based on the Total Alkali–Silica Diagram. *J Pet* 27:745–750
- Leeman WP, Vitaliano CJ (1976) Petrology of McKinney Basalt, Snake River Plain, Idaho. *Geol Soc Am Bull* 87:1777–1792
- Leeman WP (1982a) Olivine tholeiitic basalts of the Snake River Plain, Idaho. In: Bonnicksen B, Breckenridge R M (eds) *Cenozoic geology of Idaho*. Idaho Bureau of Mines and Geology Bull 26:181–191
- Leeman WP (1982b) Development of the Snake River Plain–Yellowstone Plateau Province, Idaho and Wyoming: An overview and petrologic model. In: Bonnicksen B, Breckenridge R M (eds) *Cenozoic geology of Idaho*. Idaho Bureau of Mines and Geology Bull 26:155–177
- Leeman WP (1982c) Evolved and hybrid lavas from the Snake River Plain, Idaho. In: Bonnicksen B, Breckenridge R M (eds) *Cenozoic geology of Idaho*. Idaho Bureau of Mines and Geology Bull 26:193–202

- Link PK, Mink L, (2002) Geology, hydrogeology, and environmental remediation; Idaho National Engineering and Environmental Laboratory, eastern Snake River plain, Idaho. Geol Soc Am Special Paper 353
- Link PK, McDonald HG, Fanning CM, Godfrey AE (2002) Detrital zircon evidence for Pleistocene drainage reversal at Hagerman Fossil Beds National Monument, central Snake River Plain, Idaho. In: Bonnichsen B, White CM, McCurry M (eds) Tectonic and Magmatic Evolution of the Snake River Plain Volcanic Province. Idaho Geol Surv Bull 30:105–119
- Malde HE, Powers HA (1972) Geologic map of the Glens Ferry–Hagerman area, west central Snake River Plain, Idaho. U.S. Geological Survey, Miscellaneous Investigations Map I-696, Scale 1:48,000
- Matthews SH, Shervais JW, Kauffman JD, Othberg KL (2006a) Geologic Map of the Shoshone SE Quadrangle, Jerome and Lincoln Counties, Idaho: Idaho Geological Survey, Moscow Idaho, DWM-62 scale 1:24,000
- Matthews SH, Shervais JW, Kauffman JD, Othberg KL (2006b) Geologic Map of the Star Lake Quadrangle, Jerome and Lincoln Counties, Idaho: Idaho Geological Survey, Moscow Idaho, DWM-67 scale 1:24,000
- McCurry M, Hayden K, Morse L, Mertzman S (2008) Genesis of post-hotspot, A-type rhyolite of the Eastern Snake River Plain volcanic field by extreme fractional crystallization of olivine tholeiite. Bull Volcanol 70:361–383
- McDonald GH, Link PK, Lee DE (1996) An overview of the geology and paleontology of the Pliocene Glens Ferry Formation, Hagerman Fossil Beds National Monument. Northwest Geology 26:16–45
- McFadden PL, Reid AB (1982) Analysis of paleomagnetic inclination data. Geophys J Royal Astro Soc 69:307–319
- McKenzie D, O'Nions RK (1995) The source regions of ocean island basalts. J Pet 36:133–159

- Menzies MA, Leeman WP, Hawkesworth CJ (1983) Isotope geochemistry of Cenozoic volcanic rocks reveals mantle heterogeneity below western USA. *Nature* 303:205–209
- Mertz DF, Weinrich AJ, Sharp WD, Renne PR (2001) Alkaline intrusions in a near-trench setting, Franciscan Complex, California; constraints from geochemistry, petrology, and $^{40}\text{Ar}/^{39}\text{Ar}$ chronology. *Am J Sci* 301:877–911
- Miller ML, Hughes SS (2009) Mixing primitive and evolved olivine tholeiite magmas in the Eastern Snake River Plain, Idaho. *J Volcanol Geotherm Res* 188:153–161
- Neal CR (2001) The interior of the Moon: The presence of garnet in the primitive, deep lunar mantle. *J Geophys Res* 106:27865–27885
- Pearce JA (1983) Role of the sub-continental lithosphere in magma genesis at active continental margins. In Hawkesworth CJ, Norrey MJ (eds) *Continental Basalts and Mantle Xenoliths*: Cheshire, U.K., Shiva Publishing Ltd., p. 230–249
- Peng X, Humphreys ED (1998) Crustal velocity structure across the eastern Snake River Plain and the Yellowstone swell. *J Geophys Res* 103:7171–7186
- Pierce KL, Morgan LA (1992) The Track of the Yellowstone Hotspot: Volcanism, Faulting, and Uplift. In Link PK, Kuntz MA, Platt LB (eds) *Regional Geology of Eastern Idaho and Western Wyoming*. *Geol Soc Am Memoir* 179:1–53
- Pierce KL, Morgan LA, Saltus RW (2002) Yellowstone Plume Head: Postulated Tectonic Relations to the Vancouver Slab, Continental Boundaries, and Climate. In: Bonnichsen B, White CM, McCurry M (eds) *Tectonic and Magmatic Evolution of the Snake River Plain Volcanic Province*. *Idaho Geol Surv Bull* 30:5–33
- Saltzer RL, Humphreys ED (1997) Upper Mantle P Wave Velocity Structure of the Eastern Snake River Plain and its relationship to geodynamic models of the region. *J Geophys Res* 102:11829–11841

- Shervais JW, Vetter SK (2009) High-K alkali basalts of the Western Snake River Plain (Idaho): Abrupt transition from tholeiitic to mildly alkaline plume-derived basalts. *J Volcanol Geotherm Res* 188:141–152
- Shervais JW, Kauffman JD, Gillerman VS, Othberg KL, Vetter SK, Hobson VR, Zarnetske M, Cooke MF, Matthews SH, Hanan BB (2005) Basaltic Volcanism of the Central and Western Snake River Plain: A Guide to Field Relations Between Twin Falls and Mountain Home, Idaho. In: Pederson J, Dehler CM (eds) *Guide to Field trips in the western United States*, Field Guide volume 6, Geol Soc Am, Boulder Colorado, p. 27–52
- Shervais JW, Vetter SK, Hanan BB (2006a) A Layered Mafic Sill Complex beneath the Eastern Snake River Plain: Evidence from Cyclic Geochemical Variations in Basalt. *Geology* 34:365–368
- Shervais JW, Cooke MF, Kauffman JD, Othberg KL (2006b) *Geologic Map of the Owinza Quadrangle, Lincoln County, Idaho*, Idaho Geological Survey, Moscow Idaho: Idaho Geological Survey, Moscow Idaho, DWM–64 scale 1:24,000
- Shervais JW, Cooke MF, Kauffman JD, Othberg KL (2006b) *Geologic Map of the Owinza Butte Quadrangle, Jerome and Lincoln Counties, Idaho*: Idaho Geological Survey, Moscow Idaho, DWM–65 scale 1:24,000
- Shervais JW, Evans JP, Christiansen EJ, Schmitt DR, Kessler JA, Potter KE, Jean MM, Sant CJ, Freeman TG (2011) Project Hotspot – The Snake River Scientific Drilling Project. *Geothermal Resources Council Transactions* 35:995–1003
- Smith RB, Braile LW (1993) Topographic signature, space–time evolution, and physical properties of the Yellowstone–Snake River Plain volcanic system: the Yellowstone hotspot. In: Snoke AW, Steidtmann JR, Roberts SM (eds) *Geology of Wyoming*. Geological Survey of Wyoming Memoir 5:694–754
- Smith RB, Braile LW (1994) The Yellowstone hotspot. *J Volcanol Geotherm Res* 61:121–187.

- Sparlin MA, Braile LW, Smith RB (1982) Crustal structure of the eastern snake river plain determined from ray trace modeling of seismic refraction data. *J Geophys Res* 87:2619–2633
- Taylor SR, McLennan SM (1985) *The Continental Crust: its Composition and Evolution*. Oxford, Blackwell Scientific Publications, 312 pp
- Tauxe L, Luskin C, Selkin P, Gans P, Calvert A (2004) Paleomagnetic results from the Snake River Plain: Contribution to the time-averaged field global database. *Geochem Geophys Geosyst* 5:Q08H13, doi:10.1029/2003GC000661
- Vetter SK, Shervais JW (1992) Continental Basalts of the Boise River Group near Smith Prairie, Idaho. *J Geophys Res* 97:9043–9061
- White CM (2007) The Graveyard Point Intrusion: an Example of Extreme Differentiation of Snake River Plain Basalt in a Shallow Crustal Pluton. *J Pet* 48:303–325
- Whitehead RL, Lindholm GF (1985) Results of Geohydrologic test drilling in the Eastern Snake River Plain, Gooding County, Idaho. US Geological Survey, Water-Resources Investigations Report 84-4294
- Yuan H, Dueker K, Stachnik J (2010) Crustal structure and thickness along the Yellowstone hot spot track: Evidence for lower crustal outflow from beneath the eastern Snake River Plain. *Geochem Geophys Geosyst*. doi:11:10.1029/2009GC002787

Table 4-1. ICP-MS precision; comparison with USGS standard W-2

Atomic Number	Element	W-2 recommended values	W-2 measured values	Standard deviation
21	Sc	36 ± 1.1	38.1	1.3
23	V	260 ± 12	296.8	13.4
24	Cr	92 ± 4.4	115.2	2.8
37	Rb	21 ± 1.1	21.8	0.2
38	Sr	190 ± 3.0	222.2	3.5
39	Y	23 ± 1.6	17.2	0.6
40	Zr	100 ± 4.0	90.2	5.1
41	Nb	7.9	7.0	0.3
56	Ba	170 ± 11	187.6	4.7
57	La	10 ± 0.59	11.9	0.5
58	Ce	23 ± 1.5	26.0	1.3
59	Pr		3.4	0.1
60	Nd	13 ± 1.0	14.6	0.1
62	Sm	3.3 ± 0.13	3.7	0.1
63	Eu	1.0 ± 0.86	1.3	0.02
64	Gd		4.1	0.1
65	Tb	0.63	0.7	0.02
66	Dy	3.6 ± 0.8	4.6	0.2
67	Ho	0.76	0.9	0.02
68	Er	2.5	2.6	0.1
69	Tm	0.38	0.4	0.01
70	Yb	2.1 ± 0.2	2.4	0.1
71	Lu	0.33	0.3	0.02
72	Hf	2.6 ± 0.18	2.7	0.1
73	Ta	0.5	0.5	0.01
90	Th	2.4 ± 0.1	2.3	0.1
92	U	0.53	0.6	0.02

Table 4-2. Snake River Group bulk-rock elemental analyses. Major oxides in wt%; trace elements and REE in ppm.

Group	Flow #	1	2	3a	3b	4	5	6a	6b	7	8a	8b	9	10	11	12	13	14	16b	15a	15b	16a	17	18	19	20	21a	21b	22	23		
	Average	3.1	5.5	7.7	13.5	27.4	29.4	31.2	31.5	32.3	36.3	38.9	48.8	52.2	54.6	59.7	61.8	67.3	85.8	74.8	75.5	79.6	94.2	96.4	98.1	100.3	107.0	109.4	112.3	116.1		
Depth (m)																																
Major Elements																																
SiO ₂	65.9	65.3	65.7	65.2	65.9	65.9	65.4	65.1	65.5	65.9	65.5	65.2	65.5	65.5	65.4	65.9	65.5	65.2	65.5	65.1	65.6	65.2	65.9	65.3	65.9	65.9	65.9	65.9	65.9	65.9	65.9	65.9
TiO ₂	2.82	2.86	2.98	2.84	2.80	2.85	2.80	2.85	2.88	2.89	2.80	2.87	2.88	2.89	2.89	2.87	2.90	2.91	2.92	2.91	2.92	2.93	2.92	2.91	2.90	2.90	2.92	2.92	2.92	2.92	2.92	2.92
Al ₂ O ₃	14.83	14.63	14.53	14.54	15.27	15.12	15.53	15.33	15.36	15.35	15.03	14.55	14.65	14.58	14.68	14.68	14.56	14.68	14.68	14.56	14.57	14.57	14.42	14.34	14.42	14.40	14.49	14.49	14.48	14.43	14.35	
FeO	14.7	14.75	14.98	14.77	13.62	13.78	13.33	13.48	13.52	13.93	13.99	14.99	14.97	15.01	14.93	15.02	14.70	15.99	15.15	16.42	16.34	16.17	16.10	15.59	15.39	15.29	15.41	15.54	15.54	15.44	15.50	
MnO	8.17	8.18	8.18	8.15	8.08	8.08	8.18	8.18	8.18	8.07	8.18	8.18	8.18	8.18	8.18	8.18	8.18	8.18	8.18	8.18	8.18	8.18	8.18	8.18	8.18	8.18	8.18	8.18	8.18	8.18	8.18	
MgO	8.0	8.16	8.15	8.15	8.05	8.17	7.95	8.04	7.82	8.28	8.34	8.34	8.34	8.34	8.34	8.34	8.34	8.34	8.34	8.34	8.34	8.34	8.34	8.34	8.34	8.34	8.34	8.34	8.34	8.34	8.34	
CaO	9.35	9.37	9.44	9.19	9.69	9.60	9.7	9.62	9.69	9.75	9.65	9.69	9.73	9.68	9.73	9.67	9.67	9.67	9.67	9.67	9.67	9.67	9.67	9.67	9.66	9.54	9.51	9.52	9.60	9.48		
Na ₂ O	2.01	1.99	1.88	2.19	1.87	1.84	1.89	1.88	1.88	1.86	1.84	1.76	1.81	1.84	1.83	1.82	1.79	1.82	1.81	1.89	1.88	1.91	1.79	1.84	1.91	1.83	1.83	1.84	1.83	1.81		
K ₂ O	0.52	0.52	0.52	0.52	0.52	0.52	0.52	0.52	0.52	0.52	0.52	0.52	0.52	0.52	0.52	0.52	0.52	0.52	0.52	0.52	0.52	0.52	0.52	0.52	0.52	0.52	0.52	0.52	0.52	0.52	0.52	
P ₂ O ₅	0.72	0.87	0.76	0.86	0.41	0.41	0.41	0.41	0.41	0.41	0.41	0.41	0.41	0.41	0.41	0.41	0.41	0.41	0.41	0.41	0.41	0.41	0.41	0.41	0.41	0.41	0.41	0.41	0.41	0.41	0.41	
LOI	-0.72	-0.87	-0.76	-0.86	-0.36	-0.45	-0.45	-0.38	-0.44	-0.49	-0.57	-0.65	-0.65	-0.67	-0.69	-0.74	-0.63	-0.47	-0.56	-0.68	-0.73	-0.65	-0.68	-0.32	-0.44	-0.44	-0.61	-0.61	-0.67	-0.64		
Mg#	51.9	52.3	50.7	52.2	52.9	52.9	51.9	52.1	52.5	52.9	52.5	52.1	52.5	52.5	52.5	52.9	52.5	52.1	52.5	52.1	52.5	52.9	52.5	52.1	52.5	52.5	52.5	52.5	52.5	52.5	52.5	
Ca#	240.6	237.0	225.8	245.5	247.4	246.9	233.6	235.5	234.2	238.5	252.8	233.4	233.3	233.0	233.0	233.1	234.1	232.4	232.4	233.0	233.4	233.2	232.6	232.6	232.6	231.9	232.0	232.0	232.0	232.0	232.0	
K	4309	4255	4579	4326	3582	3671	3581	3653	3747	2837	2602	3006	3332	3354	3345	3345	3355	3274	3510	4437	4156	4000	4156	4156	4156	4156	4156	4156	4156	4156	4156	
P	2693	2710	2845	2747	1798	1844	1754	1792	1792	1790	1753	2221	2350	2506	2448	2448	2485	2281	1974	3499	3299	3262	3443	3452	2414	2395	2383	2343	2405	2412		
Trace Elements																																
La	28.1	25.9	30.3	28.8	22.0	19.9	21.8	23.8	24.5	24.5	11.2	12.2	23.9	24.5	27.5	23.0	23.1	23.1	14.4	20.8	23.6	28.7	19.1	15.7	16.4	15.1	17.3	14.5	21.4	18.2		
Ce	61.4	56.4	65.9	63.04	47.7	44.5	48.9	51.6	49.8	50.0	30.4	30.8	53.8	55.2	61.5	52.0	54.9	54.4	35.4	70.2	61.5	69.8	47.5	40.1	41.4	41.3	43.0	39.7	50.7	44.5		
Pr	8.2	7.5	8.8	8.5	6.3	5.9	6.5	6.8	7.1	7.1	3.7	4.1	7.2	7.4	8.3	6.7	6.9	4.1	4.6	8.3	6.8	8.1	5.9	5.1	5.1	5.1	4.9	5.3	4.5	6.9	5.6	
Nd	34.7	33.1	37.3	36.2	27.1	26.3	27.9	29.1	30.7	30.7	16.3	19.2	31.7	32.6	36.2	30.1	30.5	21.1	21.1	36.2	29.1	31.2	26.6	22.7	22.8	21.9	24.5	19.5	31.9	24.7	23.0	
Sm	2.7	2.6	2.9	2.8	2.1	2.0	2.1	2.2	2.3	2.3	1.3	1.7	2.5	2.6	2.9	2.4	2.3	1.7	1.8	2.6	2.1	2.4	2.2	1.8	1.9	1.8	2.1	1.5	2.5	2.03	1.9	
Eu	10.1	9.5	11.3	10.9	8.6	7.7	8.5	9.1	9.2	4.5	5.5	9.5	9.6	10.8	10.8	9.1	7.3	5.9	5.9	9.1	7.8	8.1	6.8	5.6	5.5	5.5	6.4	4.7	8.1	5.8	5.8	
Gd	1.4	1.3	1.6	1.5	1.2	1.1	1.2	1.3	1.3	0.6	0.7	1.3	1.3	1.5	1.7	1.4	1.2	1.1	1.0	1.2	1.1	1.1	0.9	0.8	0.8	0.8	0.8	0.8	0.6	1.2	0.9	
Tb	1.6	1.4	1.8	1.7	1.4	1.2	1.4	1.5	1.5	0.7	0.8	1.5	1.5	1.7	1.7	1.4	1.2	1.1	1.1	1.2	1.1	1.1	1.0	0.9	0.9	0.9	0.9	0.7	1.3	0.9	0.9	
Dy	4.5	4.2	4.9	4.7	3.9	3.6	3.7	4.2	4.4	1.8	2.6	4.1	4.1	4.6	4.6	3.9	3.2	2.6	2.6	3.5	3.2	3.2	3.2	2.9	2.3	2.3	2.2	2.7	1.8	3.7	2.7	
Ho	0.6	0.5	0.7	0.6	0.5	0.5	0.5	0.5	0.5	0.2	0.3	0.5	0.5	0.5	0.6	0.5	0.4	0.4	0.4	0.4	0.4	0.4	0.4	0.3	0.3	0.3	0.3	0.3	0.3	0.3	0.3	
Tm	0.6	0.5	0.6	0.6	0.5	0.5	0.5	0.5	0.5	0.2	0.3	0.5	0.5	0.5	0.6	0.5	0.4	0.4	0.4	0.4	0.4	0.4	0.4	0.4	0.3	0.3	0.3	0.3	0.3	0.3	0.3	
Y	31.4	27.4	34.2	34.2	20.4	18.9	22.8	24.1	24.1	34.7	33.6	35.4	34.1	31.5	32.7	30.8	30.1	22.8	22.8	25.1	34.1	31.3	38.1	31.3	33.9	37.9	18.3	37.3	26.7	30.3	26.7	
Zr	15.9	14.2	16.3	14.2	12.9	11.3	12.6	14.6	14.3	13.3	8.6	9.8	14.7	12.5	14.7	12.5	10.7	11.7	10.5	11.4	13.2	12.4	14.0	11.4	14.0	11.2	12.8	7.3	12.5	10.3	10.3	
Hf	37.5	27.4	39.4	28.9	21.7	20.6	23.6	26.3	26.3	33.4	31.3	34.4	34.4	31.3	34.4	31.3	27.4	28.9	28.9	32.9	47.3	47.3	37.0	35.7	47.9	30.9	43.7	19.7	42.5	27.7	27.7	
Nb	282.5	248.9	291.7	274.02	220.3	201.6	217.02	245.7	237.4	202.2	157.5	206.9	82.03	312.2	284.6	298.3	183.1	183.1	183.1	323.1	377.5	338.4	329.5	346.01	273.03	311.1	325.5	306.1	247.5	247.5	247.5	
Sr	25.4	21.4	26.1	24.2	19.6	17.04	18.4	25.8	19.7	21.9	12.03	26.9	9.01	32.6	26.9	21.9	21.9	18.3	18.3	34.3	47.5	33.5	22.7	20.4	20.4	20.4	30.1	17.2	30.2	17.8		
Th	63.2	56.2	66.9	62.2	54.8	52.3	56.9	63.9	64.4	44.4	45.5	63.6	18.3	18.3	18.3	5.5	6.2	4.3	4.3	7.1	7.5	7.7	7.2	7.4	6.2	69.4	69.4	63.9	58.01	58.01		
Ta	1.6	1.3	1.6	1.4	1.2	1.1	1.03	1.1	1.1	1.5	1.5	0.5	1.8	1.8	1.8	1.6	1.3	1.1	0.9	1.9	2.5	2.01	2.1	2.1	2.1	1.9	1.1	1.8	1.1	1.1		
Pb	1.8	1.4	1.8	1.0	1.6	1.1	1.1	1.1	1.1	1.3	1.0	1.02	0.6	1.3	0.6	1.3	1.2	1.0	0.8	1.3	1.7	1.7	1.7	1.7	1.7	1.4	1.7	0.8	1.7	1.4	1.4	
U	292.7	287.8	313.8	288.4	200.02	179.9	200.3	285.7	314.9	311.1	203.8	423.6	296.7	106.4	317.8	208.3	208.3	208.3	208.3	342.4	339.5	297.3	291.9	291.9	380.6	319.4	364.1	341.6	334.2	334.2	334.2	
NI	177.9	117.3	90.3	104.9	90.4	108.9	87.5	125.7	125.7	125.7	202.2	275.7	131.4	49.2	130.5	100.8	333.03	333.03	99.8	72.3	72.3	72.3	72.3	72.3	72.3	95						

Table 4-3. Idaho Group bulk-rock elemental analyses. Major oxides in wt%; trace elements and REE in ppm.

Flow #	6						7						8						9						10						11					
	25	26	27	28	29	30	31	32	33a	33b	34	35	36	37	38	40	41	43	44	45	47	48	49	50a	50b	50c	51a	51b	52a	52b	52c	52d	52e	52f		
Major Elements¹																																				
SiO ₂	47.41	47.50	46.98	47.36	47.34	47.32	46.46	46.25	46.81	46.72	46.51	47.35	47.03	47.11	46.96	46.98	46.51	46.91	46.57	46.76	46.95	46.73	46.66	46.77	46.74	46.99	47.01	46.74	47.08	47.08	46.93	46.86	46.1			
TiO ₂	2.45	2.55	2.68	2.42	2.37	2.44	2.84	2.61	2.67	2.82	2.44	2.60	2.67	2.82	2.44	2.44	2.44	2.64	2.64	2.67	2.84	2.66	2.56	2.56	2.15	2.18	2.34	2.26	2.26	2.26	2.56	2.4				
Al ₂ O ₃	15.93	14.29	14.73	14.30	14.13	14.13	14.91	14.53	14.30	14.45	15.75	15.03	15.29	15.32	15.64	14.96	13.98	14.82	15.54	14.27	15.23	15.83	14.79	14.78	13.7	13.81	14.26	13.79	13.86	14.79	15.7	15.2				
FeO	0.17	0.17	0.18	0.17	0.15	0.15	0.18	0.17	0.17	0.16	0.18	0.13	0.18	0.18	0.19	0.17	0.17	0.18	0.2	0.18	0.18	0.19	0.17	0.17	0.17	0.17	0.16	0.17	0.16	0.17	0.17	0.17				
MnO	0.17	0.17	0.18	0.17	0.15	0.15	0.18	0.17	0.17	0.16	0.18	0.13	0.18	0.18	0.19	0.17	0.17	0.18	0.2	0.18	0.18	0.19	0.17	0.17	0.17	0.17	0.16	0.17	0.16	0.17	0.17	0.17				
CaO	10.16	10.08	10.19	10.07	10.00	9.83	10.20	10.76	10.08	10.12	3.74	9.75	9.36	9.58	9.44	9.39	11.25	10.53	11.19	10.65	10.19	10.29	9.89	9.83	10.32	10.35	10.24	10.33	10.35	9.77	10.6	10.6				
Na ₂ O	1.72	1.73	1.65	1.75	1.69	1.66	1.66	1.63	1.73	1.64	1.65	1.85	1.74	1.89	1.88	1.88	1.64	1.69	1.69	1.64	1.65	1.78	1.78	1.8	1.67	1.72	1.71	1.67	1.69	1.81	1.7	1.7				
K ₂ O	0.36	0.39	0.43	0.40	0.37	0.37	0.42	0.38	0.42	0.42	0.35	0.51	0.52	0.52	0.59	0.49	0.43	0.56	0.56	0.43	0.56	0.44	0.43	0.43	0.35	0.37	0.4	0.38	0.38	0.43	0.38	0.38				
LOI	-0.36	0.01	0.28	-0.09	0.15	2.29	-0.21	0.16	-0.48	1.44	6.95	-0.03	3.9	-0.18	0.02	-0.44	-0.41	0.24	-0.35	-0.2	-0.03	-0.23	-0.34	-0.66	-0.69	-0.74	-0.6	-0.56	0.83	0.39	0.12	1.29	-0.3			
Mg#	53.9	52.2	51.7	52.5	55.0	55.6	53.2	54.7	53.2	55.7	36.0	48.2	51.4	48.9	48.6	51.5	53.2	50.1	46.7	52.5	48.4	47.0	53.0	53.1	57.4	56.8	55.4	56.8	56.8	53.1	52.4	52.4				
Cr#	289.2	262.1	253.1	276.7	311.9	316.0	379.8	403.1	398.4	391.2	72.7	214.5	238.0	219.1	199.5	229.6	227.1	209.9	236.3	230.1	229.5	237.7	269.5	271.7	262.0	340.3	353.7	316.5	346.9	348.1	270.2	247				
Ni	116.4	110.6	106.0	121.8	137.2	141.1	160.1	166.0	160.0	160.0	183.3	220.2	237.9	244.5	241.2	248.0	183.3	188.0	203.5	203.5	220.2	237.9	244.5	241.2	187.2	153.7	161.7	172.9	167.2	165.9	182.2	171				
P	1588	1714	1877	1735	1651	1603	2146	2321	2481	2538	2801	2205	2374	2274	2501	2338	1180	2038	2305	1981	2202	2366	1925	1877	1872	1537	1617	1729	1672	1659	182.2	171				
Trace Elements²																																				
La	14.8	19.9	31.2	22.9	27.7	27.7	27.7	25.6	28.3	26.1	33.2	21.02	19.1	22.1	31.4	19.4	25.3	24.7	21.7	16.2	25.9	16.2	25.9	12.8	18.9	19.7	17.0	15.5	21.9	18.4	18.4	18.4	18.4			
Ce	4.53	6.82	10.4	7.4	8.4	8.4	7.5	7.4	8.3	9.1	9.3	6.8	7.5	8.3	9.1	6.8	7.5	8.3	7.8	6.2	7.5	6.2	7.5	4.04	5.6	5.6	4.7	4.7	5.6	5.6	5.6	5.6	5.6	5.6	5.6	
Nd	22.9	31.4	46.1	33.8	36.2	36.2	36.2	32.7	36.2	43.7	29.2	28.3	32.7	46.5	30.3	32.7	46.5	30.3	23.8	33.9	33.9	33.9	33.9	19.5	26.4	27.3	23.9	20.2	30.3	25.4	25.4	25.4	25.4	25.4	25.4	
Sm	1.6	2.7	3.3	2.2	2.6	2.6	2.6	2.4	2.6	2.9	2.1	1.7	2.1	2.5	2.9	2.5	2.5	2.9	3.9	2.5	2.8	2.5	2.9	2.8	4.9	2.3	4.3	2.1	3.02	2.5	2.3	2.3	2.3	2.3	2.3	
Gd	6.3	8.0	12.3	8.8	6.7	7.8	7.08	5.9	8.8	6.3	4.2	3.2	4.2	5.2	6.3	5.2	5.2	6.3	12.4	5.2	5.2	5.2	5.2	10.2	5.9	7.2	6.6	6.1	7.8	6.6	6.1	7.8	6.6	6.1	7.8	
Tb	0.9	1.2	1.9	1.3	1.1	1.1	1.02	0.74	1.2	0.6	0.4	0.3	0.4	0.5	0.6	0.4	0.4	0.5	2.00	0.4	0.4	0.4	0.4	0.8	0.8	1.2	1.2	1.1	0.8	1.3	1.3	1.3	1.3	1.3		
Ho	1.1	1.5	2.3	1.6	1.1	1.1	1.2	0.8	1.4	0.8	0.5	0.4	0.5	0.6	0.7	0.5	0.5	0.6	1.7	0.5	0.5	0.5	0.5	1.02	1.0	1.4	1.4	1.4	1.02	1.6	1.5	1.4	1.02	1.6	1.5	
Er	3.2	4.1	6.4	4.6	3.4	3.6	3.3	2.3	4.5	3.2	2.1	1.6	2.1	2.5	3.6	2.5	2.5	3.6	5.1	2.5	2.5	2.5	2.5	3.3	3.3	4.2	4.2	3.3	3.3	4.5	4.5	4.5	4.5	4.5		
Tm	0.4	0.5	0.9	0.6	0.4	0.4	0.4	0.3	0.6	0.4	0.2	0.2	0.2	0.2	0.3	0.2	0.2	0.3	0.8	0.2	0.2	0.2	0.2	0.4	0.4	0.6	0.6	0.4	0.6	0.6	0.6	0.6	0.6	0.6		
Lu	2.8	3.6	5.8	4.2	2.9	3.1	2.8	1.9	3.4	2.5	1.7	1.3	1.7	2.1	2.8	1.7	1.7	2.1	4.8	1.7	1.7	1.7	1.7	2.9	2.9	3.9	3.9	2.9	2.9	4.2	4.2	4.2	4.2	4.2	4.2	
Yb	2.8	3.6	5.8	4.2	2.9	3.1	2.8	1.9	3.4	2.5	1.7	1.3	1.7	2.1	2.8	1.7	1.7	2.1	4.8	1.7	1.7	1.7	1.7	2.9	2.9	3.9	3.9	2.9	2.9	4.2	4.2	4.2	4.2	4.2	4.2	
Sc	6.9	8.9	6.9	9.6	2.3	2.3	10.2	7.61	2.7	4.7	4.7	4.7	4.7	4.7	4.7	4.7	4.7	4.7	6.03	8.4	6.1	8.6	8.3	7.6	11.9	5.6	6.7	7.4	2.2	3.1	8.2	9.3	9.3	9.3	9.3	9.3
Sr	232.8	274.1	343.9	255.9	227.6	227.6	356.8	284.7	289.4	289.4	289.4	289.4	289.4	289.4	289.4	289.4	289.4	289.4	316.9	273.9	258.7	264.0	264.0	208.9	235.9	282.3	222.1	143.7	271.1	238	238	238	238	238		
Zr	158.9	205.1	273.4	197.0	156.2	156.2	310.6	233.9	227.9	227.9	227.9	227.9	227.9	227.9	227.9	227.9	227.9	227.9	231.6	228.8	195.7	254.4	260.9	176.4	278.4	147.5	178.5	183.4	168.9	154.9	204.2	181	181	181	181	181
Nb	12.1	15.6	20.8	15.1	11.9	11.9	23.7	17.8	18.2	20.2	13.4	10.2	13.4	16.4	14.4	14.4	14.4	16.6	23.8	14.3	20.4	18.4	17.2	14.4	22.5	11.8	14.0	14.8	13.4	12.5	16.6	16.1	16.1	16.1	16.1	
Hf	4.0	5.3	7.2	4.9	3.5	3.5	5.5	4.0	4.5	5.0	3.2	2.4	3.2	4.0	3.6	3.6	3.6	4.2	5.8	3.9	5.0	4.5	4.2	3.6	4.9	2.7	4.5	4.6	4.2	3.9	5.0	5.0	5.0	5.0	5.0	
Ta	0.8	1.00	1.5	0.9	0.8	0.8	1.5	1.2	1.4	1.6	1.4	0.9	1.0	1.03	1.6	0.9	1.0	1.03	1.6	0.9	1.3	1.2	1.3	0.9	1.5	0.8	0.9	0.9	0.8	1.1	1.0	1.0	1.0	1.0	1.0	1.0
Th	0.8	1.0	1.5	0.9	0.8	0.8	1.5	1.2	1.4	1.6	1.4	0.9	1.0	1.03	1.6	0.9	1.0	1.03	1.6	0.9	1.3	1.2	1.3	0.9	1.5	0.8	0.9	0.9	0.8	1.1	1.0	1.0	1.0	1.0	1.0	1.0
U	0.3	0.4	0.5	0.4	0.3	0.3	0.4	0.3	0.4	0.4	0.3	0.2	0.3	0.3	0.4	0.3	0.3	0.4	0.5	0.3	0.4	0.4	0.3	0.4	0.3	0.4	0.4	0.3	0.4	0.4	0.3	0.4	0.3	0.4	0.3	0.4
V	0.3	0.4	0.5	0.4	0.3	0.3	0.4	0.3	0.4	0.4	0.3	0.2	0.3	0.3	0.4	0.3	0.3	0.4	0.5	0.3	0.4	0.4	0.3	0.4	0.3	0.4	0.4	0.3	0.4	0.4	0.3	0.4	0.3	0.4	0.3	0.4
Ni	347.5	445.3	305.8	421.3	313.3	313.3	313.3	313.3	313.3	313.3	313.3	313.3	313.3	313.3	313.3	313.3	313.3	313.3	313.3	313.3	313.3	313.3	313.3	313.3	313.3	313.3	313.3	313.3	313.3	313.3	313.3	313.3	313.3	313.3	313.3	

¹measured by Neqpy Fluorescence
²measured by ICP-MS

Table 4-4. Input parameters for Snake River Plain batch melt models

Source Composition						
	Primitive Mantle ^a	N-MORB ^b	E-MORB ^c			
La	0.55	0.234	1.8			
Ce	1.4	0.772	4.02			
Nd	1.08	0.713	2.49			
Sm	0.35	0.27	0.73			
Eu	0.13	0.107	0.24			
Gd	0.46	0.395	0.83			
Tb	0.08	0.08	0.14			
Dy	0.57	0.531	0.85			
Ho	0.13	0.122	0.18			
Er	0.37	0.371	0.49			
Tm	0.06	0.06	0.07			
Yb	0.37	0.401	0.42			
Lu	0.06	0.063	0.06			
K	200	60	548			
Sr	20	9.8	70			
Y	3.45	4.07	4.38			
Sc	12	16.3	12.87			
Ti	1020	790	2098			
Zr	8.51	7.94	19.34			
Hf	0.25	0.2	0.57			
Nb	0.54	0.21	2.85			
Ta	0.03	0.0138	0.15			
Th	0.07	0.014	0.19			
Rb	0.62	0.088	0.062			
Ba	6.5	1.2	0.65			
U	0.018	0.0047	0.05			
P	61	40.7	61			
		Ol	Opx	Cpx	Sp	Gt
Source Mode						
Spinel Lherzolite		63	19	16	2	0
Garnet Lherzolite		66	14	16	0	4
Melt Mode						
Spinel Lherzolite		10	20	68	2	0
Garnet Lherzolite		5	5	40	0	50

^a McKenzie and O'Nions (1995)^b Salters and Stracke (2004)^c Mertz et al (2001)

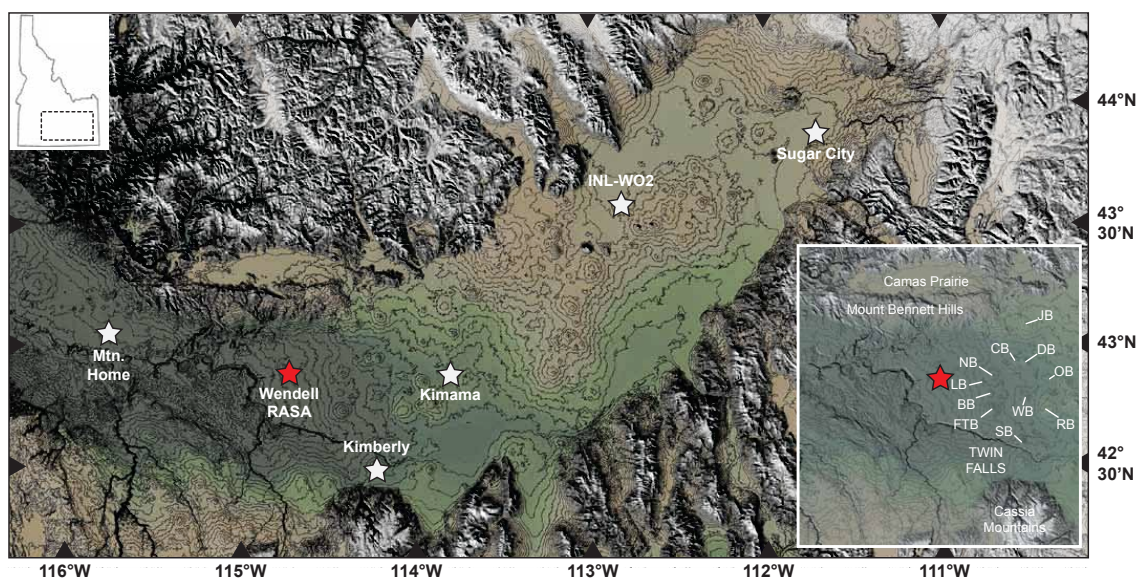


Figure 4-1. Snake River Plain location map; approximate location of the Wendell RASA drill hole is denoted with the red star. Other fully cored deep drill holes in the YSRP province include Sugar City (0.7 km), INL–WO2 (1.52 km), Project Hotspot – Kimama (1.91 km), Project Hotspot – Kimberly (1.96 km), and Mountain Home (1.3 km). Inset shows the location of the Wendell RASA drill hole (red star) in relation to CSRP regional features, including the Camas Prairie, Mount Bennett Hills, and the Cassia Mountains. Nearby volcanic vents includes Bacon Butte (BB), Crater Butte (CB), Dietrich Butte (DB), Flat Top Butte (FTB), Johnson Butte (JB), Lincoln Butte (LB), Notch Butte (NB), Owinza Butte (OB), Rocky Butte (RB), Skeleton Butte (SB), and Wilson Butte (WB).

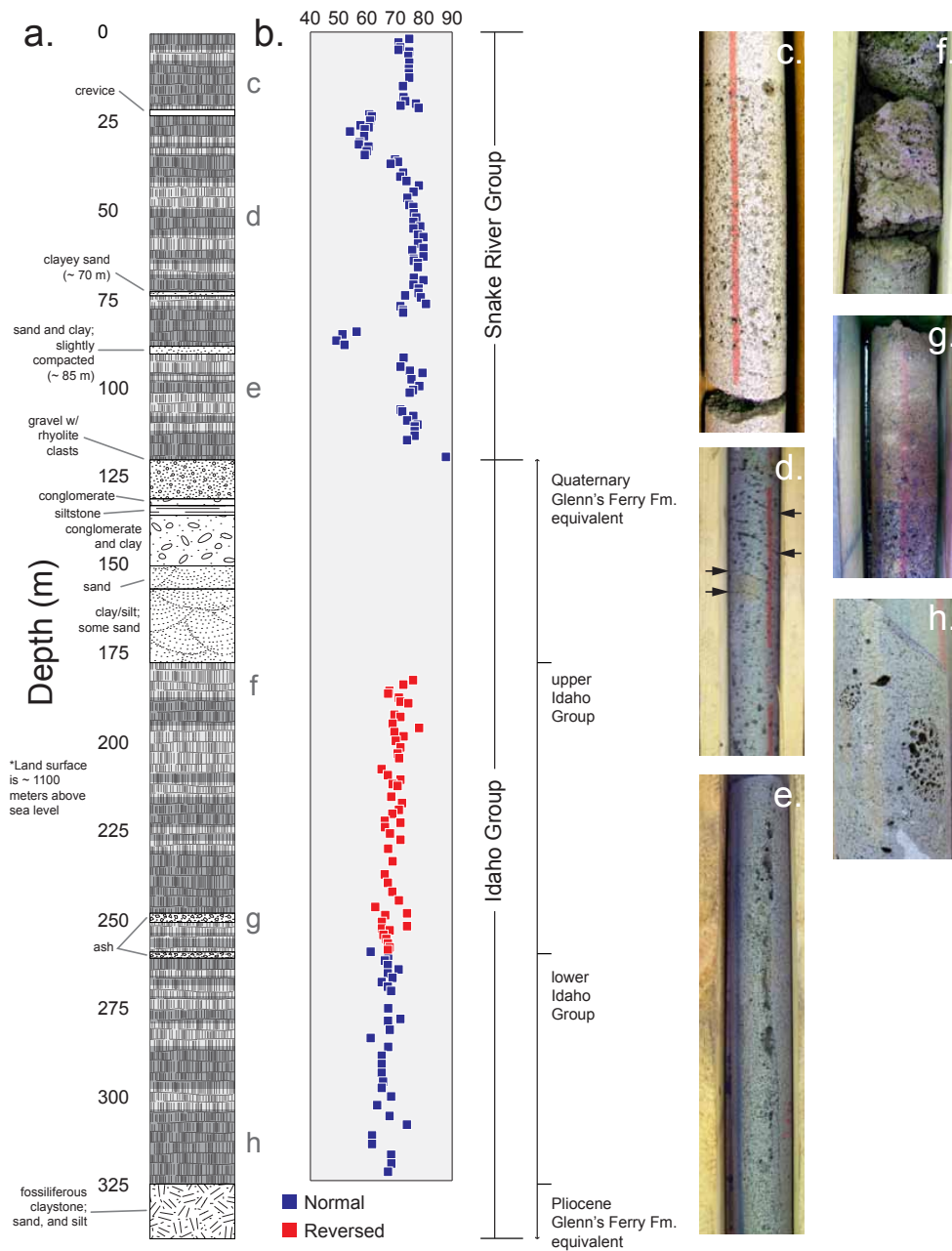


Figure 4-2. (a) Lithologic log of Wendell RASA test hole 7S-15E-12CBA1 (modified from Whitehead and Lindholm 1985). (b) Paleomagnetic inclination results. Alternating shades of grey denote individual lava flows. Volcanic features observed within the Snake River Group section include (c) flow breakouts, (d) vesicle sheets or 'segregation zones,' and (e) vesicle pipes. Volcanic features observed within the Idaho Group section include (f) ropey/agglutinate features, (g) basaltic ash, and (h) autoliths/remobilized spatter.

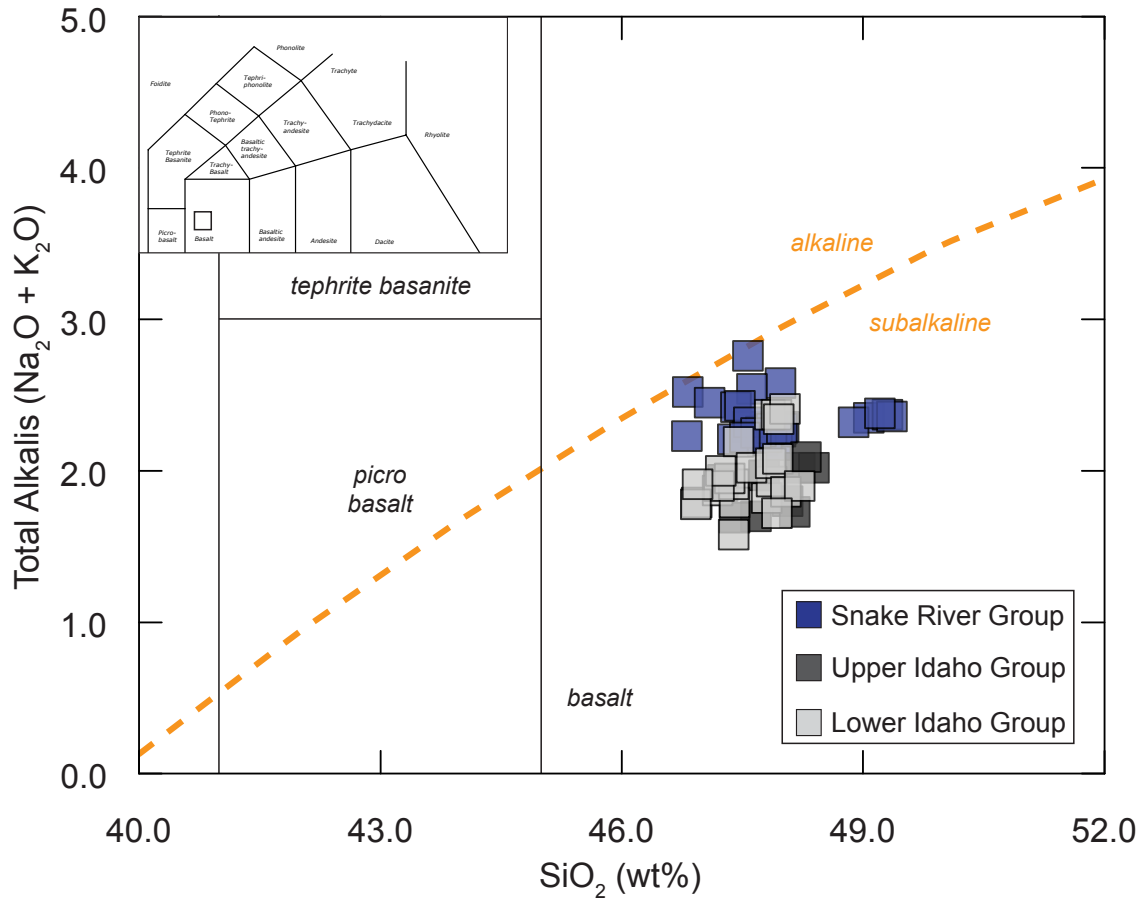


Figure 4-3. Classification of Wendell RASA lavas based on Total Alkalis (Na₂O + K₂O) vs. SiO₂ from Le Bas et al. (1986). Inset displays the entire Le Bas diagram, with approximate area of Wendell RASA lavas shown in black square. All flows analyzed in this study plot in the basalt field. Orange-dashed line shows the separation between alkaline and subalkaline rocks. All flows plot in the subalkaline field; however, Snake River Group basalts (blue squares) are more alkaline than Idaho Group basalts (grey squares).

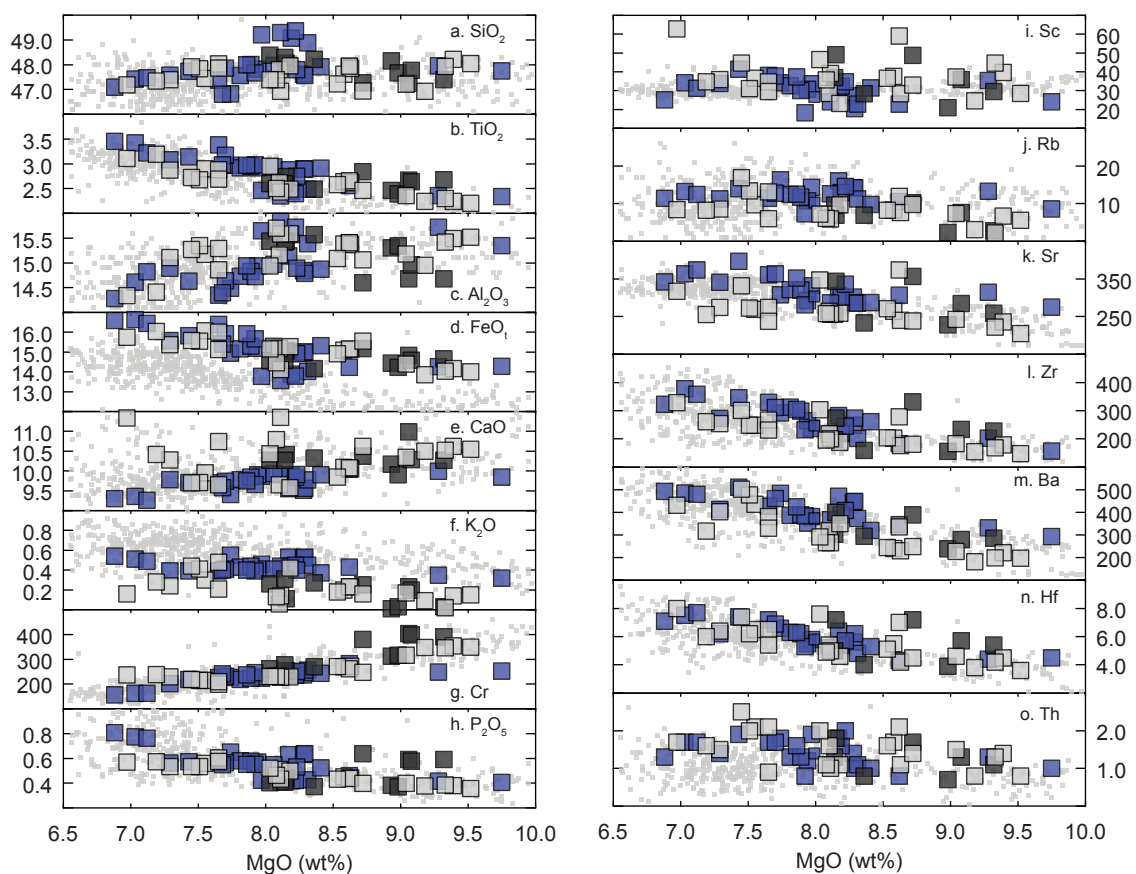


Figure 4-4. Major and trace element compositions of Wendell RASA basalts plotted against MgO (wt%). (a) SiO_2 (wt%); (b) TiO_2 (wt%); (c) Al_2O_3 (wt%); (d) FeO_t (wt%); (e) CaO (wt%); (f) K_2O (wt%); (g) Cr (ppm); (h) P_2O_5 (wt%); (i) Sc (ppm); (j) Rb (ppm); (k) Sr (ppm); (l) Zr (ppm); (m) Ba (ppm); (n) Hf (ppm); (o) Th (ppm). Wendell RASA major and trace element concentrations are similar to other ESRP olivine tholeiites (Hughes et al. 2002; small grey squares). Sample notation same as Figure 3.

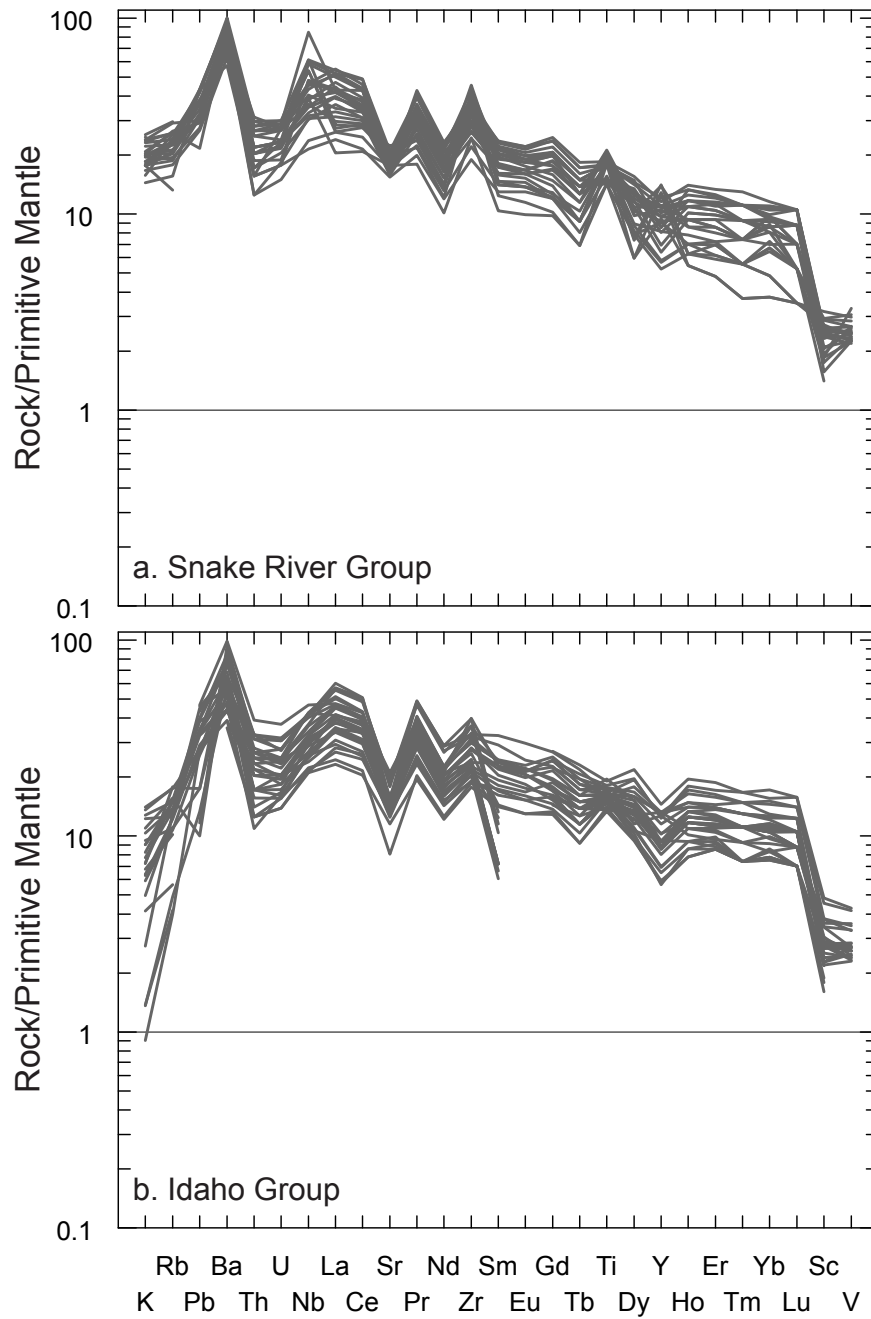


Figure 4-5. Primitive Mantle normalized (Taylor and McLennan 1985) multi-element spider diagrams for (a) Snake River Group and (b) Idaho Group basalts. Trace elements are arranged in order of decreasing compatibility from right to left.

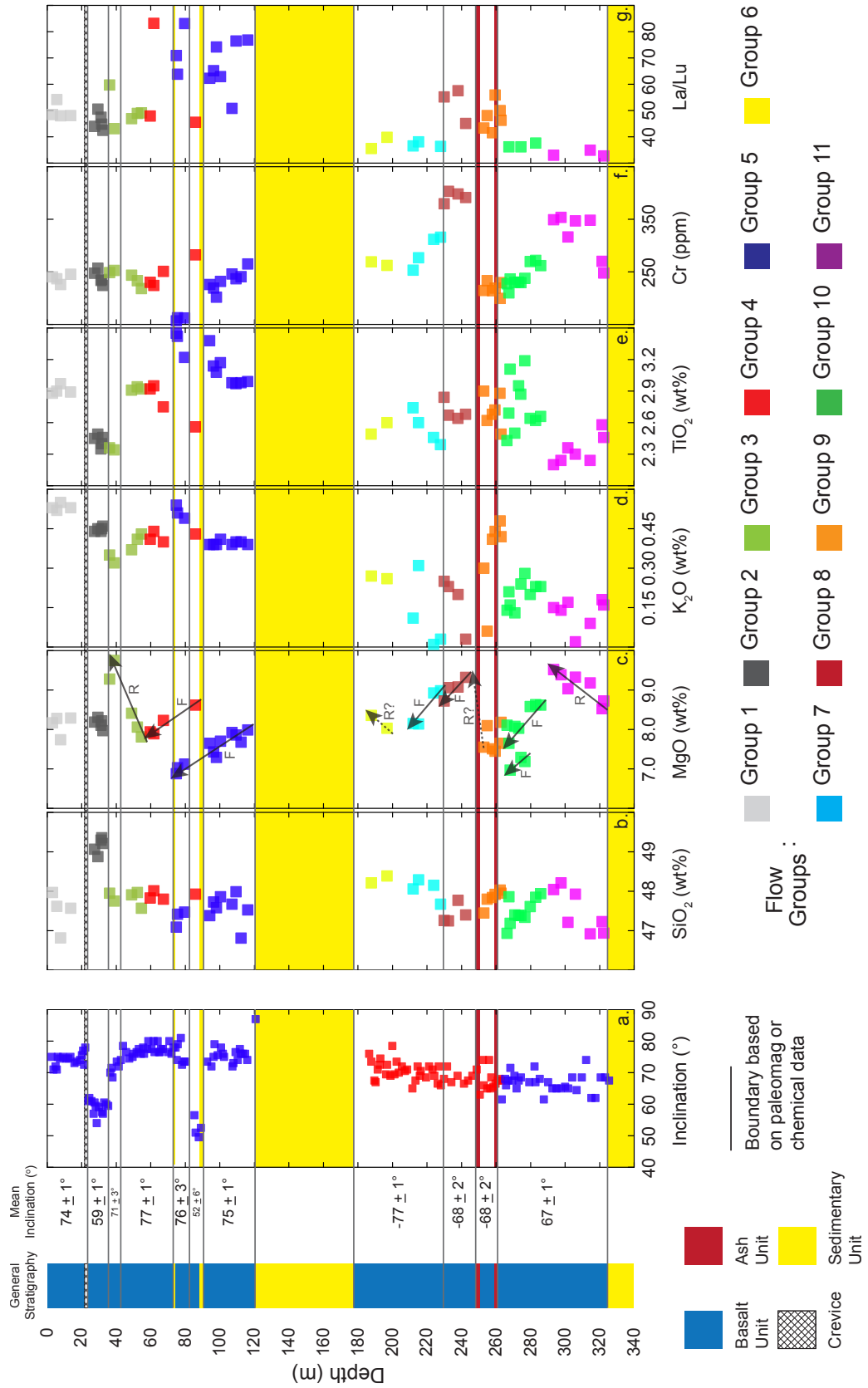


Figure 4-6. Comparison between a generalized stratigraphic column, paleomagnetic inclination data, and the chemical composition of Wendell RASA basalts, as a function of depth below surface (in meters). (a) Paleomagnetic inclination data (same as Figure 2b). The stratigraphic column has been further annotated with mean inclination values and 95 percent confidence levels for proposed boundaries between inclination/Flow Groups. Wendell RASA major and trace element data define distinct chemical trends, i.e., (b) SiO₂ is pretty much constant from top to bottom; (c) MgO ranges from 7.0 – 10.0 wt% and displays many increasing and decreasing trends with depth; (d) K₂O displays an enrichment from 0.1 wt% at the bottom to 0.5 wt% at the top; (e) TiO₂ trends are anti-correlated with MgO-trends; (f) Cr₂O₃ displays a general decreasing trend, from as high as 350 ppm at the bottom and to approximately 225 ppm at the top; and (g) La/Lu displays the more primitive nature of Snake River Group basalts compared to Idaho Group basalts, i.e., ~ 50 – 80 vs. ~ 30 – 60. These geochemical trends allow us to identify 11 flow groups: Group 1 (light grey), Group 2 (dark grey), Group 3 (light green), Group 4 (red), Group 5 (dark blue), Group 6 (yellow), Group 7 (light blue), Group 8 (dark red), Group 9 (orange), Group 10 (green), and Group 11 (purple). Figure 6c is further annotated with our interpretation of the fractionation (F) and recharge (R) cycles. Flow groups 4, 5, 7, 8, and 10 are interpreted as fractionation cycles, Flow groups 3 and 11 are interpreted as recharge cycles, with possibly two additional recharge cycles (6, in between 8 and 9), and Flow Groups 1 and 2 do neither.

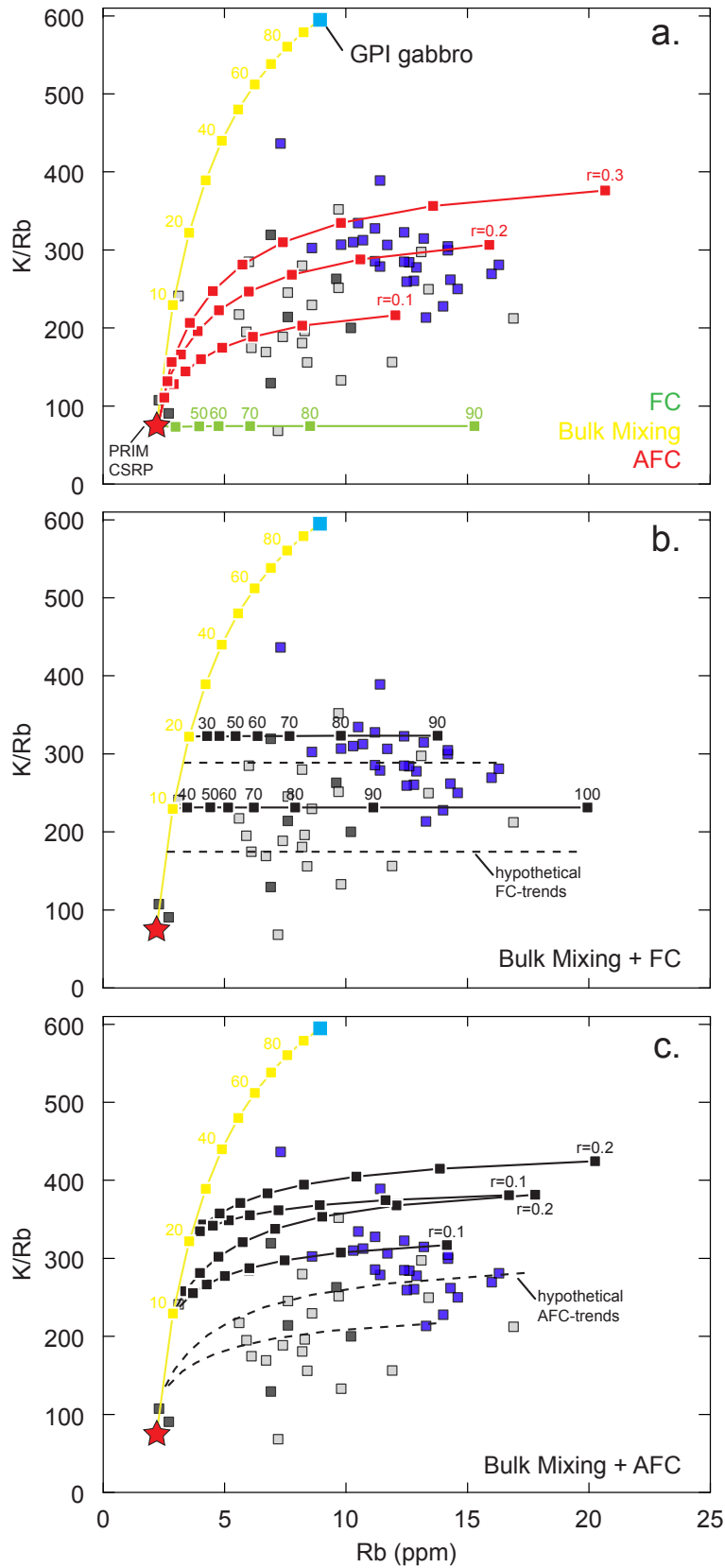


Figure 4-7. Crystallization, mixing, and assimilation models for Wendell RASA basalts. (a) Fractional crystallization (green; numbers shown in percent crystallization), bulk mixing of an average Graveyard Point gabbro composition (yellow; numbers shown in percent assimilated), and AFC (red) of an average Graveyard Point gabbro composition; 'r' ranges from 0.1 to 0.3 and modeled in 10% increments of fraction of melt remaining. (b) Bulk mixing plus fractional crystallization. FC trends calculated from 10% and 20% assimilated gabbro; values for FC trends shown in percent crystallization. (c) Bulk mixing plus AFC. AFC trends calculated from 10% and 20% assimilated gabbro; r calculated at 0.1 and 0.2 and modeled in 10% increments of fraction of melt remaining.

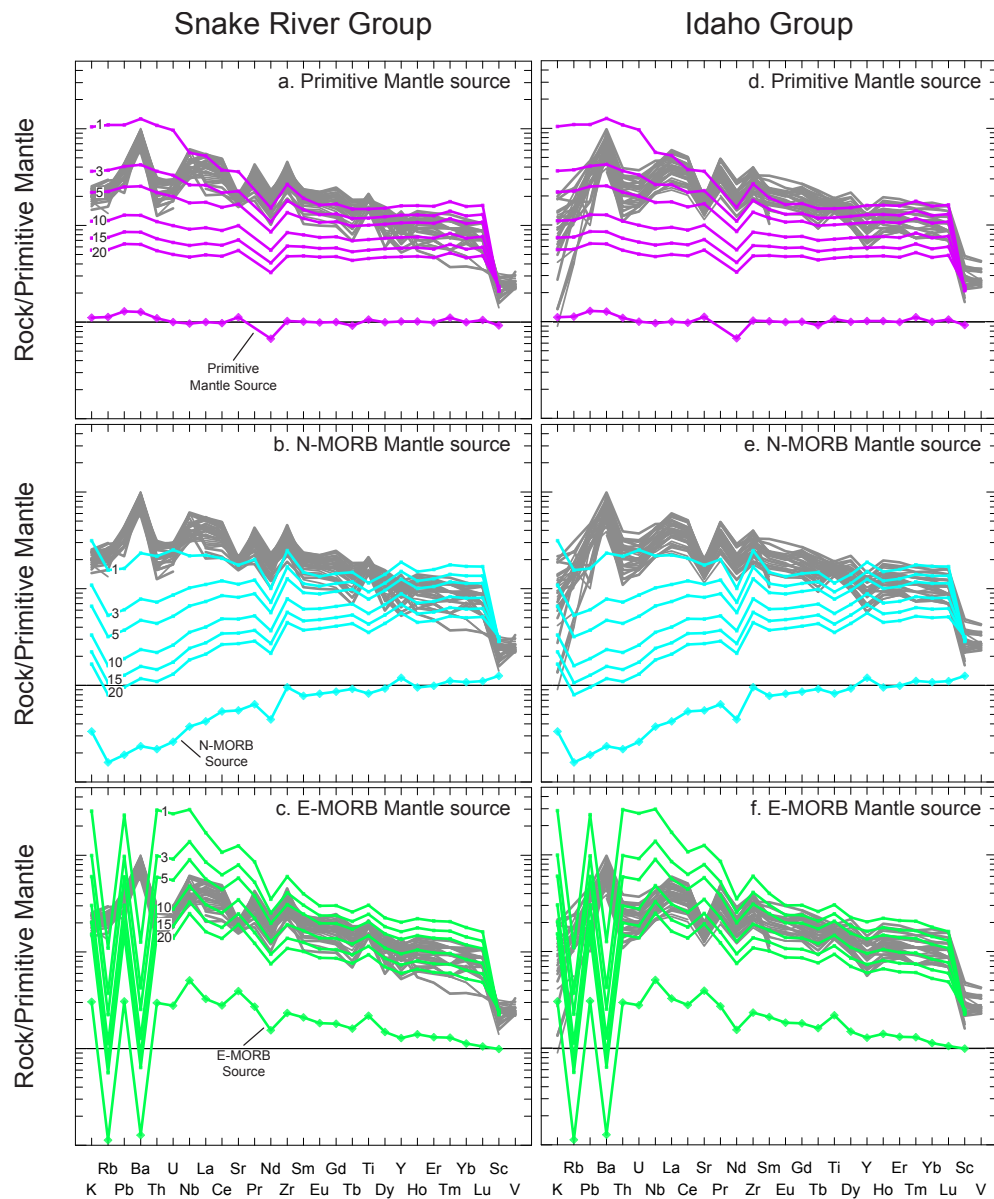


Figure 4-8. Partial melting models from 1% to 20%, for different mantle sources, e.g., primitive mantle source (Taylor and McLennan 1985), N-MORB mantle source (Salters and Stracke 2004), and E-MORB mantle source (Mertz et al. 2001) in the spinel lherzolite facies. Snake River Group partial melt models: (a) primitive mantle source, (b) N-MORB mantle source, (c) E-MORB mantle source. Idaho Group partial melt models: (d) primitive mantle source, (e) N-MORB mantle source, (f) E-MORB mantle source. Normalized to Primitive Mantle of Taylor and McLennan (1985).

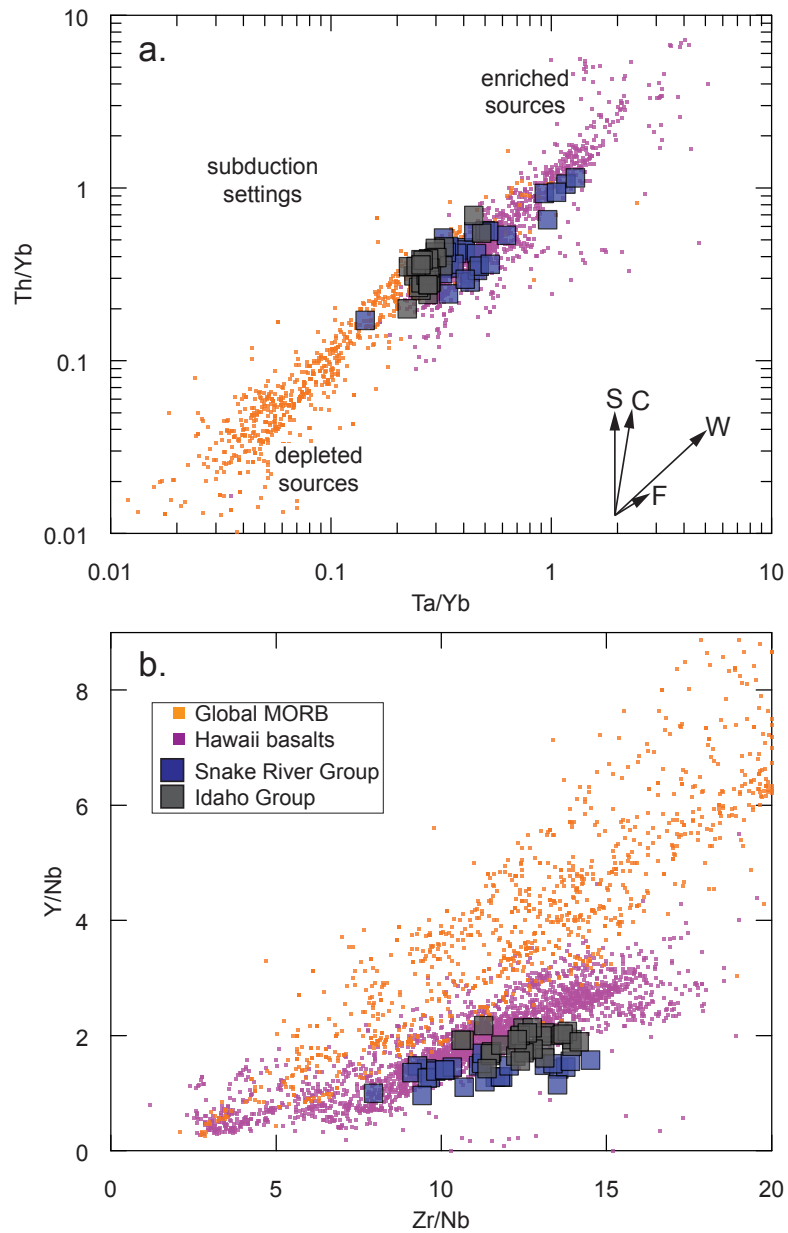


Figure 4-9. (a) Co-variation of Th/Yb vs. Ta/Yb for Wendell RASA basalts. Vectors represent relative contributions of modification: S—subduction zone mantle enrichment, C—crustal contamination, W—within plate mantle enrichment, and f—fractional crystallization (after Pearce 1983). (b) Co-variation of Zr/Nb vs. Y/Nb. Wendell RASA basalts overlap in composition and trends for Hawaiian basalts. These basalts are compared to compositions from MORB (a depleted source) and Hawaii (an enriched source).

CHAPTER 5

SUMMARY AND CONCLUSIONS

Four original research projects were presented for this dissertation. This research examined the construction and life cycle of oceanic and continental lithosphere and pushed the frontiers of the scientific knowledge of two important tectonic elements within the US Cordillera. The hypotheses advanced for the Coast Range Ophiolite (CRO) and Snake River Plain (SRP) have been tested before; however, the methods employed for this dissertation provided the ground-breaking evolution needed to advance these theories. This was aided by applying standard and innovative algorithms to model CRO and SRP geochemical variations.

Research into the Coast Range Ophiolite reaffirmed the complexities of peridotite geochemistry in the mantle wedge above a subduction zone. This project was the first to use the laser ablation method for study of this ophiolite. For this research, the fractional melting equations of Johnson et al. (1990) was employed to study the residual clinopyroxene and orthopyroxene found in CRO ultramafic rocks. Results from this modeling showed that abyssal-type peridotite (Black Diamond Ridge and Cuesta Ridge) formed by approximately 2–4% anhydrous melting in the garnet stability field, with or without small amounts (< 3%) of continued melting in the spinel stability field. Fore-arc type peridotite (Stony Creek, Del Puerto Canyon, Grey Eagle Mine), however, are dominated (or consist of) by highly refractory peridotite formed by > 20% polybaric hydrous fractional partial melting in the spinel stability field, after 6% partial melting in the garnet stability field. These models could not account for the observed fluid mobile element enrichment, e.g., B ~10–600x DMM, Pb ~1–70x DMM, and Li ~1–10x DMM. Other fluid mobile elements (Rb, Be, Ba, Th) were also present above detection limits in many samples. I modeled this enrichment through a newly derived equation, which showed that fluid mobile elements were added to a DMM source in the 10's to 100's of ppm range. This fluid-enriched mantle source region represents the source region of island arc magmas. Using non-

modal batch or pooled fractional melting equations, magmas derived from our FME-enriched source display a similar composition to magmas generated at subduction zones.

The Coast Range Ophiolite preserves evidence for five stages of magmatic development: stage 1 – Birth, stage 2 – Youth, stage 3 – Maturity, stage 4 – Death, and stage 5 – Resurrection (Shervais et al., 2004; Metcalf and Shervais, 2008). These stages follow the Pacific intra-oceanic subduction zone model (Stern and Bloomer, 1992; Bloomer et al., 1995; Shervais, 2001). The geochemical compositions and models presented for this part of my dissertation captures these stages. First, subduction initiates along a transform margin, juxtaposing young, thin (hotter) oceanic lithosphere against older, thicker (cooler, more dense) oceanic lithosphere. Initiation of a new subduction margin generates fore-arc oceanic crust in a nascent subduction zone by extension and magmatism in response to slab sinking and hinge rollback. This is followed by stabilization of an island-arc crust by continued subduction. Rifting and reconfiguration of the arc generates fore-arc oceanic crust by spreading in a narrow back-arc basin in response to continued hinge rollback. Lastly, back-arc basin widens as hinge rollback continues.

Research into the Snake River Plain revealed the intricacies of how magmas are formed in continental settings. The main goal of this research was to examine how basalts were derived from the interaction between westwardly migrating North American continental lithosphere and the Yellowstone Hotspot. Temporal (early vs. late) and spatial (western vs. eastern) isotopic variations of YSRP basalts were modeled by using basic principles previously described by Schilling et al. (1992), Hanan and Schilling (1997), Douglass and Schilling (2000), and Hanan et al. (2000). This model allowed derivation of the mass fraction of each component for each sample. This model showed that low-K tholeiites are more polluted with sub-continental lithospheric mantle (SCLM), have < 98% “Plume” component, and display an increasing west to east trend for the “Old” SCLM component and a decreasing west to east trend for the “Young” SCLM component. Younger lavas (< 1 Ma) in the western plain have the highest “Plume” component ($\geq 99\%$) and are less polluted with SCLM material, resulting in isotope compositions

that approach the composition of the Yellowstone Plume. Additionally, by applying the fractional crystallization (FC) and assimilation–fractional crystallization (AFC) equations of Rayleigh (1896) and DePaolo (1981), respectively, it was shown that basalts intersected in the Wendell RASA drill core formed mostly by AFC processes, i.e., fractionation and recharge of basaltic magma in a series of sill–like layered mafic intrusions located in the middle crust.

The “standard model” has the Yellowstone–Snake River hotspot impacting North American lithosphere around 17 Ma under northern Nevada (McDermitt caldera) and melting to form a plume head–flood basalt province (Columbia River Basalt Group), followed by the initiation of NE time–transgressive volcanism, from its initial position under the McDermitt caldera to its final position under the Yellowstone caldera (e.g., Smith and Braile, 1994; Pierce and Morgan, 1992; Pierce et al., 2002). The plume head–plume tail paradigm (Richards et al., 1989; Hill et al., 1992) is generally accepted as the model that best explains the large volume of the initial flood basalts and the subsequent time–transgressive nature of the younger volcanics. To this model, my research incorporates the three–dimensional chemical and structural architecture of the province that gives rise to the temporal, spatial, and geochemical variations observed in Snake River Plain basalts.

References

- Bloomer SH, Taylor B, MacLeod CJ, Stern RJ, Fryer P, Hawkins JW, Johnson L (1995) Early arc volcanism and the ophiolite problem: A perspective from drilling in the western Pacific, in Taylor, B., and Natland, J., eds., *Active Margins and Marginal Basins of the Western Pacific*. American Geophysical Union Geophysical Monograph 88:1–30
- DePaolo D (1981) Trace element and isotopic effects of combined wallrock assimilation and fractional crystallization. *EPSL* 53:189–202

- Douglass J, Schilling JG (2000) Systematics of three–component, pseudo–binary mixing lines in 2D isotope ratio space representations and implications for mantle plume–ridge interaction. *Chem Geol* 163:1–23
- Hanan BB, Blichert–Toft J, Kingsley R, Schilling JG (2000) Depleted Iceland mantle plume geochemical signature: Artifact of multicomponent mixing? *Geochem Geophys Geosyst* 1: 1003, doi:10.1029/1999GC000009
- Hanan BB, Schilling JG (1997) The dynamic evolution of the Iceland mantle plume: the lead isotope perspective. *EPSL* 151:43–60
- Hill RI, Campbell IH, Davies GF, Griffiths RW (1992) Mantle plumes and continental tectonics. *Science* 256:18–193
- Johnson KTM, Dick HJB, Shimizu N (1990) Melting in the oceanic upper mantle; an ion microprobe study of diopsides in abyssal peridotites. *J Geophys Res* 95:2661–2678
- Metcalfe RV, Shervais JW (2008) Suprasubduction–zone ophiolites: Is there really an ophiolite conundrum?, in Wright, J.E., and Shervais, J.W., eds., *Ophiolites, Arcs, and Batholiths: A Tribute to Cliff Hopson*. *Geol Soc Am Special Paper* 438:191–222
- Pierce KL, Morgan LA (1992) The track of the Yellowstone hotspot: Volcanism, faulting, and uplift, in, *Regional geology of eastern Idaho and western Wyoming*. *Geol Soc Am Memoir* 179:1–53
- Pierce KL, Morgan LA, Saltus RW (2002) Yellowstone Plume Head: Postulated Tectonic Relations to the Vancouver Slab, Continental Boundaries, and Climate, in, Bonnichsen, B., White, C. and McCurry, M., eds., *Tectonic and magmatic evolution of the Snake River Plain volcanic province, Idaho*. *Geological Survey Bulletin* 30. Moscow, ID, United States, p. 5–33.
- Rayleigh JWS (1896) Theoretical considerations respecting the separation of gases by diffusion and similar processes. *Philos Mag* 42:493–498
- Richards M, Duncan R, Courtillot V (1989) Flood basalts and hot–spot tracks: Plume heads and tails. *Science* 246:103–107

- Schilling JG, Kingsley RH, Hanan BB, McCully BL (1992) Nd–Sr–Pb isotopic variations along the Gulf of Aden: evidence for Afar mantle plume–continental lithosphere interaction. *J Geophys Res* 97:10927–10966
- Shervais JW (2001) Birth, death, and resurrection: The life cycle of suprasubduction zone ophiolites. *Geochemistry Geophysics Geosystems* 2, doi: 10.1029/2000GC000080.
- Shervais JW, Kimbrough DL, Renne P, Hanan BB, Murchey B, Snow CA, Zoglman–Schuman MM, Beaman J (2004) Multi–Stage Origin of the Coast Range Ophiolite, California: Implications for the Life Cycle of Supra–Subduction Zone Ophiolites. *Int Geol Rev* 46:289–315
- Stern RJ, Bloomer SH (1992) Subduction zone infancy; examples from the Eocene Izu–Bonin–Mariana and Jurassic California arcs. *Geol Soc Am Bulletin* 104(12):1621–1636
- Smith RB, Braile LW (1994) The Yellowstone hotspot. *J Volcanol Geotherm Res* 61:121–187

APPENDICIES

APPENDIX A
INSIDE THE SUBDUCTION FACTORY: MODELING FLUID MOBILE
ELEMENT ENRICHMENT IN THE MANTLE WEDGE
ABOVE A SUBDUCTION ZONE¹

¹Manuscript submitted to *Geochimica et Cosmochimica Acta*: in revision
Co-authors: John W. Shervais

Abstract

Enrichment of the mantle wedge above subduction zones with fluid mobile elements is thought to represent a fundamental process in the origin of arc magmas. This “subduction factory” is typically modelled as a mass balance of inputs (from the subducted slab) and outputs (arc volcanics). We present here a new method to model fluid mobile elements, based on the composition of peridotites associated with supra-subduction ophiolites, which form by melt extraction and fluid enrichment in the mantle wedge above nascent subduction zones.

The Coast Range ophiolite (CRO), California, is a Jurassic supra-subduction zone ophiolite that preserves mantle lithologies formed in response to hydrous melting. We use high-precision laser ablation ICP-MS analyses of relic pyroxenes from these peridotites to document fluid mobile element (FME) concentrations, along with a suite of non-fluid mobile elements that includes rare earth and high-field strength elements. In the CRO, fluid-mobile elements are enriched by factors of up to 100x DMM, whereas fluid immobile elements are progressively depleted by melt extraction. The high concentrations of fluid mobile elements in supra-subduction peridotite pyroxene can be attributed to a flux of aqueous fluid or fluid-rich melt phase derived from the subducting slab. To model this enrichment, we derive a new algorithm that calculates the concentration of fluid mobile elements added to the source:

$$C_{wr,add} = [C_{cpx-obs} / [(D_{cpx} / (D_{bulk} - PF)) * [1 - (PF / D_{bulk})^{(1/P)}]] - C_{0,wr}]$$

where $C_{wr,add}$ = concentration of FME added to mantle wedge during a given melt increment, $C_{cpx-obs}$ = concentration of observed pyroxene, D_{cpx} and D_{bulk} = mineral and bulk partition coefficients, P = melt proportion, and F = melt fraction required to model the observed MREE-HREE concentrations. Application of this algorithm to CRO peridotites shows that fluid influx must be continuous with open system melting, which allows us to calculate FME concentrations for small melt increments. Addition of the calculated FME concentrations to depleted MORB

mantle (DMM) asthenosphere or refractory arc mantle (RAM) results in pooled magmas that match primitive arc tholeiites and boninites.

Introduction

The question of the geochemical flux through the mantle wedge during subduction is critical to our understanding of arc volcanism, and forms an important aspect of the global geochemical flux (Peacock, 1990; Plank and Langmuir, 1998; Tatsumi and Kogiso, 2003). These processes may be inferred indirectly in active subduction systems by measuring inputs and outputs, but this approach does not permit direct observation of the dynamic processes within the mantle wedge source of arc magmas. Direct observation of the mantle wedge is possible, however, by studying outcrops of mantle peridotite that underlie ophiolites formed in fore-arc settings (Pearce et al., 1984; Pearce, 2003; Shervais, 2001; Metcalf and Shervais, 2008). This mantle reflects the processes that have affected it through time, including melt extraction, fluid phase enrichment, and melt refertilization, which have been frozen in place by cooling and emplacement. A primary advantage of this approach is the fact that large tracts of mantle wedge peridotite are commonly exposed at the base of many supra-subduction ophiolites, allowing us to examine, in situ, their petrology, geochemistry, and structure on longer length scales than is currently possible in any active system (Batanova et al., 1998; Batanova and Sobolev, 2000; Bizimis et al., 2000; Nicolas and Boudier, 2000; LeMee et al., 2004; Barth et al., 2008; Choi et al., 2008a; Choi et al., 2008b; Jean et al., 2010).

The origin and evolution of MORB-source asthenosphere versus that of the mantle wedge source of island arc volcanics represent fundamental questions concerning the geochemical evolution of the Earth. It has been concluded that mid-ocean ridges are composed of dominantly spinel lherzolites formed by fractional melting under dry conditions, from which relatively small melt fractions (~5–15%) have been extracted. These contain pyroxenes with strongly depleted light-REE, relative to what would be expected from batch melting, and essentially flat middle-to heavy-REE (Johnson et al., 1990; Hellebrand et al., 2002). Observed

variations towards enriched compositions in MORB are explained as mixing with plume-type mantle from ridge-centered hotspots or from passive heterogeneities created by ancient mantle plumes (Schilling et al., 1983; Dosso et al., 1993; Niu et al., 1996; Hanan and Schilling, 1997; Hanan et al., 2000; Warren et al., 2009). In contrast, the starting point for arc volcanism is a wedge of asthenosphere that overlies subduction zones, similar to that from which MORBs are derived (Batanova et al., 1998), and modified by partial melts of the descending slab or by fluids emanating from the subducting slab (Tatsumi and Eggins, 1995; Plank and Langmuir, 1998; Elliott, 2003; Tatsumi, 2005). Partial melts of this metasomatised mantle wedge leads to arc volcanics that are enriched in large ion lithophile elements (e.g., Cs, Rb, K, Ba, Pb, Sr, La, Ce) and depleted in high-field strength elements (e.g., Ta, Nb, Zr, Ti).

Previous efforts to model this “subduction factory” have relied on box models that compare the mass balance of inputs (subducting oceanic crust + sediment) to the outputs (island arc volcanic rocks), in order to calculate the flux through the mantle wedge, using a range of assumptions about fluid volumes and compositions (Ayers, 1998; Plank and Langmuir, 1998; Scambelluri et al., 2001; Hacker et al., 2003; McDade et al., 2003; Kimura et al., 2009). Ozawa and Shimizu (1995) present a different mass balance approach, modelling open system behavior in the mantle wedge using ordinary differential equations and an assumed incompatible element enriched component to calculate melting and flux in the mantle wedge. Their approach uses the composition of amphibole in the peridotites to calculate their flux composition, and therefore is limited to amphibole-bearing peridotite (Ozawa and Shimizu 1995; Ohara et al., 2002; Yoshikawa and Ozawa, 2007; Morishita et al., 2011). There is no amphibole-bearing peridotite within the Coast Range ophiolite.

The focus of this study are the fluid-mobile elements (e.g., Li, B, Be, Rb, Th, Pb), which are characteristically enriched in arc lavas. Fluid-mobile elements (FME) are preferentially partitioned into fluid phases during metamorphic dehydration reactions, and into melt during anatexis (Kessel et al., 2005). Estimates of the FME content of primitive mantle (McDonough

and Sun, 1995; Lyubetskaya and Korenaga, 2007;) and depleted mantle (Salters and Stracke, 2004) imply very low abundances in whole rock samples and major mantle phases (around 1 ppm for Li and B), consistent with C1–chondrite (Anders and Grevesse, 1989). Beryllium data are scarce and concentrations are extremely low in primitive mantle, e.g., 0.054 ppm (McDonough and Sun, 1995) or 0.068 ppm (Lyubetskaya and Korenaga, 2007) and 0.025 in depleted mantle (Anders and Grevesse, 1989). Fluids emanating from the subducting lithosphere enrich the overlying mantle in these lithophile elements derived from the subducting oceanic crust and its carapace of pelagic sediment, and lead to the eruption of volcanic rocks that are compositionally distinct from MORB (Plank and Langmuir, 1998; Scambelluri et al., 2001).

The Coast Range ophiolite of California is a supra–subduction zone ophiolite in the US Cordillera underlain by peridotites that formed in the mantle wedge (Choi et al., 2008a; Choi et al., 2008b). Jean et al. (2010) presented trace element systematics of the rare earth, high–field strength, and transition elements to model the amount of hydrous partial melting that occurred within the mantle wedge. In this study we extend the work of Jean et al. (2010) to the FME using newly acquired in situ laser ablation ICP–MS analyses of clinopyroxene. Our approach models the active processes that occur within the dynamic mantle wedge, and the total addition of material to the mantle wedge source region. It can be applied to any refractory mantle peridotite that has been modified by melt extraction and/or metasomatism, and requires no preconceived fluid flux composition.

Regional Setting

The Coast Range Ophiolite, California, forms a discontinuous belt of ultramafic, mafic, and minor felsic igneous rocks approximately 700 km–long, that extends from the southern edge of the Klamath Mountains to the western Transverse Ranges (Fig. A–1: Hopson et al., 1981, 2008; Shervais and Kimbrough, 1985). This ophiolite consists largely of crustal rocks, including both plutonic rocks (i.e., gabbros and diorites) and volcanic or hypabyssal rocks (i.e., boninites, basalts, basaltic andesites, and dacites) (Giarmita et al., 1998; Shervais et al., 2004, 2005a, 2005b;

Hopson et al., 2008; Shervais, 2008). It has been dated to between 165–172 Ma using U–Pb zircon (Kimbrough in Shervais et al., 2005a; Hopson et al., 2008; Mattinson and Hopson, 2008) and $^{39}\text{Ar}/^{40}\text{Ar}$ on basaltic glass (Renne in Shervais et al., 2005a), and as middle to early late Jurassic (Bajocian through Kimmeridgian) using radiolarian assemblages (Murchev in Shervais et al., 2005a). Detailed mapping in the northern Coast Ranges suggests that the ophiolite formed over a proto–Franciscan subduction zone, which may have nucleated on a pre–existing fracture zone (Choi et al., 2008b; Shervais et al., 2011; Shervais and Choi, 2012). Geochemical studies of the crustal assemblages have shown that almost all locales represent supra–subduction zone magmatism, including the Stonyford volcanic complex, which contains arc volcanics intercalated with ocean island basalts (Shervais and Kimbrough, 1985; Shervais, 1990, 2001; Shervais et al., 2004, 2005a, 2005b).

Coast Range ophiolite crustal rocks are underlain in most locales by serpentinized or partially serpentinized peridotites (Shervais et al., 2004b; Choi et al., 2008a, 2008b; Jean et al., 2010). In the northern Coast Ranges the serpentinized peridotites are commonly associated with a serpentinite matrix melange, comprising blocks of massive peridotite and exotic blocks of igneous and metamorphic rocks in a matrix of sheared serpentinite (Hopson and Pessagno 2005; Shervais et al., 2011). In the central and southern Coast Ranges, massive peridotite and sheared serpentinite crop out below crustal rocks of the ophiolite, but primary contact relationships are obscure. Peridotite of undetermined provenance is also found within the Franciscan complex (e.g., Coleman, 2003).

The distribution of peridotite sample locations studied here is shown in Figure A–1. Locations examined for this study include the Grey Eagle Mine near Chrome (Red Mountain), Black Diamond Ridge (north of the Stonyford volcanic complex), Hyphus–Little Stony Creek block (south of the Stonyford volcanic complex), Del Puerto Canyon in the Diablo Range, and Burro Mountain and Cuesta Ridge in the Sur–Nacimiento block. These peridotites are divided into three groups based on their spinel Cr# [$\text{Cr}/(\text{Cr}+\text{Al})$] and their minor and trace element

concentrations in pyroxene (Choi et al., 2008b). Group A samples (Black Diamond Ridge and Cuesta Ridge) are spinel lherzolites or clinopyroxene-rich harzburgites (~ 5 to 8% modal clinopyroxene). Group B samples (Burro Mountain and Stony Creek) are mostly comprised of spinel harzburgites, with two spinel lherzolites and one orthopyroxenite. Group C samples (Del Puerto Canyon and Grey Eagle Mine) include clinopyroxene-poor and clinopyroxene-free spinel harzburgite, dunite, chromitite, wehrlite, and orthopyroxenite.

Detailed petrologic, isotopic, and geochemical studies of these peridotites have documented conclusively that they either formed in a supra-subduction zone setting (Groups B and C) or represent abyssal-like peridotites (Group A) that were modified by subduction zone processes (Choi et al., 2008a, 2008b; Jean et al., 2010; Shervais et al., 2011). Thus, we may use these samples as analogues for the mantle wedge above a subduction zone, in order to document how FME become enriched in the source region of arc volcanics.

Analytical Methods

Peridotite samples were analyzed using a Thermo-Finnigan Element 2 High-Resolution Double Focusing Magnetic Sector ICP-MS, in conjunction with a New Wave Research 213 nm Nd-YAG Laser Ablation system at the Midwest Isotope and Trace Element Research Analytical Center (MITERAC) at the University of Notre Dame. Analytical methods similar to those used by Kent and Ungerer (2006) and Jean et al. (2010) were adopted for this study. We prepared polished thick sections, which were cleaned using the protocol of Marschall and Ludwig (2004) to minimize surface contamination of boron and other fluid mobile elements. Prior to the acquisition protocol, each area was rastered with a pre-ablation mode using lower power and repetition rate (i.e., a power output of 60%, equivalent to a fluence of ~6 J/cm²; repetition rate of 5Hz). Five pulses at this setting removed the outer surface of the pyroxene grain under analysis; if a crack or inclusion was exposed after this protocol a new location was chosen. The protocol for trace element analyses used a beam diameter of 40 to 60 μm at 80% laser power (equivalent to a fluence of 16 J/cm²) and a repetition rate of 10Hz. Data acquisition consisted of a maximum of 60

s (normally less than 30 s) on background before the laser was turned on, followed by a maximum of 180 s (normally less than 60 s) of sample collection during the lasering interval. Analyses carried out on lines/rasters versus spots produced essentially identical results, suggesting that signal strength is not attenuated by pit depth.

The NIST 612 glass standard was used as the external calibration standard, with CaO (wt %) determined by electron microprobe analysis (Choi et al., 2008b) as the internal standard. The NIST 612 standard was analyzed twice before and after trace element acquisition, with a laser set-up identical to that used for data acquisition. Data reduction and concentration determinations were obtained using the GLITTER[®] laser ablation software, developed by the ARC National Key Centre for Geochemical Evolution and Metallogeny of Continents (GEMOC) and CSIRO Exploration and Mining. Ablation signal integration intervals were selected by carefully inspecting the time-resolved analysis to ensure that no inclusions were present in the analyzed volume, and to remove surface contamination by eliminating the first sequence of laser pulses.

Table A-1 compares the preferred values for the NIST 612 standard (Pearce et al., 1997) to an average of replicate standard compositions measured during this study (N=80). In addition, we show the average 1σ error, percent relative uncertainty and detection limits for replicate analyses of this standard. Our measured values for the NIST 612 standard fall into the range of accepted values for the NIST 612 standard with percent relative uncertainty of < 0.1% for most elements (Table A-1). Individual laser ablation analyses of this standard are presented in electronic annex EA-1.

Results

Table A-2 presents the average clinopyroxene composition, 1σ error, detection limits, and the observed ranges for each peridotite locale. The 1σ error and detection limits for our peridotite samples are generally lower than those for the NIST 612 standard. Note that each analysis has its own detection limit, based on counting statistics, and that only analyses which exceed the detection limit are reported and used in the averages. The ranges in detection limit for each

element in Table A–2 are based on the analyses that exceed detection limits; if none of the data for a given element exceed detection limits, the range is for all analysis. Complete data are presented in electronic annex EA–2. Samples that had fluid mobile elements below detection limits or anomalously high concentrations were not included in the results or discussion sections.

When normalized to depleted–MORB mantle (DMM: Salters and Stracke, 2004) Group A peridotites, recognized by their low spinel Cr# (<30), clinopyroxenes with flat MREE–HREE patterns, modest LREE depletion, B ~10–600x DMM, Pb ~1–70x DMM, and Li ~1–8x DMM (Fig. A–2a). Group B peridotites have intermediate spinel Cr#s (30–60) and clinopyroxenes that are LREE–MREE depleted, with B ~10–400x DMM, Pb ~2–20x DMM, and Li ~3–10x DMM (Fig. A–2b). Group C peridotites have high Cr# spinel (>60), and their clinopyroxenes are more depleted in LREE and MREE than those of Group B, but have similar FME concentrations: B ~11–90x, Pb ~2–40x, and Li ~1–10x DMM (Fig. A–2c). Other FME (Rb, Be, Ba, Th) were also present above detection limits in many samples (Table A–2 and Fig. A–2). The high field strength elements (Nb, Zr, Hf, Ti) all have concentrations similar to the LREE–MREE in each sample.

Discussion

It is generally acknowledged that the starting point for the “subduction factory” is a wedge of asthenosphere similar to that from which mid–ocean ridge basalts are derived (Stolper and Newman, 1994; Parkinson and Pearce, 1998). This wedge is subjected to metasomatic enrichment by fluids emanating from the subducting lithosphere, which includes DMM, altered oceanic crust, and accumulated sediments. If the subducted lithosphere is still young and hot, the overlying mantle wedge can also be enriched by slab–derived melts (Peacock, 1990). The chemical and isotopic composition of the MORB–source mantle asthenosphere has been well defined over the last three decades, giving us a fairly clear starting point for modelling the subduction–induced enrichment of the supra–subduction mantle wedge (Zindler and Hart, 1986; Salters and Zindler, 1995; Salters, 1996; Hanan and Schilling, 1997).

In this section, we derive a new method for evaluating FME enrichment and then apply this method to evaluating FME enrichments in the CRO peridotites. For these models, we used the mean for each element, excluding high-concentration outliers that could represent contamination or alteration for each peridotite locale (Table A-2).

Modelling Fluid Mobile Element Addition – Theory

The concentration of trace elements in refractory pyroxene formed during anhydrous partial melting was previously modelled by Johnson et al. (1990), using a modified non-modal fractional melting equation:

$$C_{\text{cpx,model}} = C_{0,\text{wr}} * [D_{\text{cpx}} / (D_{\text{bulk}} - PF)] * [1 - (PF / D_{\text{bulk}})]^{(1/P)} \quad (1)$$

where $C_{\text{cpx,model}}$ = modelled concentration of any trace element in refractory pyroxene, $C_{0,\text{wr}}$ = concentration of the trace element in the source peridotite whole rock, D_{cpx} and D_{bulk} = pyroxene/melt and bulk rock/melt distribution coefficients, respectively, P = melting proportions, and F = fraction of melting. Equation (1) consists of three parts: the initial concentration term [$C_{0,\text{wr}}$], the distribution term [$D_{\text{cpx}} / (D_{\text{bulk}} - PF)$], and the melting function [$1 - (PF / D_{\text{bulk}})]^{(1/P)}$. The melting function is the same for modelling whole rock and mineral melting; the distribution term partitions the calculated refractory whole rock composition into the refractory pyroxene fraction.

Jean et al. (2010) applied this equation to trace element analyses from pyroxenes (clino- and ortho-) in peridotites of the Coast Range ophiolite. Figure A-3 shows average clinopyroxene concentrations for each locale, along with the spinel melt model and the garnet + spinel melt model. Starting with the DMM-source composition of Salters and Stracke (2004), Group A peridotites (abyssal) can be modelled with small melt fractions (<5%), mostly in the spinel peridotite field. In contrast, Group B and C peridotites (Burro Mtn., Del Puerto Canyon, Stony Creek) require up to 8% melting in the garnet field, followed by up to 20% melting in the spinel field. The resulting compositions are extremely refractory and appear to represent the refractory residue of boninite extraction. Group B and C peridotites have mineral modes and trace element

signatures that reflect hydrous melting, and none of these samples show evidence for later metasomatism (i.e., no modal amphibole or feldspar). Despite their extremely refractory compatible element compositions, the high FME concentrations, which we document here, exceed that of the assumed depleted MORB–source mantle, primitive mantle concentrations, and melt model concentrations. This implies that the excess concentration of fluid mobile elements can be attributed to a flux of aqueous fluid or fluid–rich melt phase derived from the subducting slab. This aqueous flux contributes high concentrations of fluid mobile elements to the mantle wedge and may contain a dissolved silicate melt phase as well. Because the “hot zone” of the mantle wedge where melts originate lies outside the stability field of hydrous phases such as hornblende or phlogopite, aqueous fluid forms a separate phase within the wedge until it dissolves into newly generated silicate melt.

We start our derivation by adding the excess concentrations to an initial whole rock composition ($C_{0,wr}$) and then melt the resulting “fluid–enriched” composition. This requires a modified form of equation (1). The mass balance of this system can be expressed as:

$$C_{cpx,obs} - C_{cpx,model} = C_{cpx,added} \quad (2)$$

where $C_{cpx,added}$ represents the concentration of an element in pyroxene which can be attributed to fluid mobile element enrichment. We can rearrange equation (2) to get:

$$C_{cpx,obs} = C_{cpx,added} + C_{cpx,model} \quad (3)$$

The term $C_{cpx,model}$ is simply the result of equation (1). The term $C_{cpx,added}$ can be modelled by an analogous equation:

$$C_{cpx,added} = C_{wr,add} * [D_{cpx} / (D_{bulk} - PF)] * [1 - (PF / D_{bulk})]^{(1/P)} \quad (4)$$

The term $C_{wr,add}$ reflects the concentration of fluid mobile (or other) incompatible element added to the source composition during melting. Equations (1) and (4) can be combined into one expression using equation (3):

$$C_{cpx,obs} = [C_{0,wr}] * [D_{cpx} / (D_{bulk} - PF)] * [1 - (PF / D_{bulk})]^{(1/P)} + [C_{wr,add}] * [D_{cpx} / (D_{bulk} - PF)] * [1 - (PF / D_{bulk})]^{(1/P)} \quad (5)$$

Combining terms:

$$C_{cpx,obs} = [C_{0,wr} + C_{wr,add}] * [D_{cpx} / (D_{bulk} - PF)] * [1 - (PF / D_{bulk})]^{(1/P)} \quad (6)$$

Solving for $[C_{wr,add}]$ yields:

$$C_{wr,add} = [C_{cpx,obs} / [[D_{cpx} / (D_{bulk} - PF)] * [1 - (PF / D_{bulk})]^{(1/P)}]] - [C_{0,wr}] \quad (7)$$

Equation (7) represents an independent determination of the subduction component added to the mantle wedge that requires no assumptions about model inputs. The observed refractory pyroxene composition is determined analytically and is not model dependent. The melt proportions and melt fractions are those calculated for elements that are not enriched by the subduction flux (e.g., the middle to heavy REE), which results in good fits to the observed pyroxene compositions (Fig. A–3: Choi et al., 2008, 2008b; Jean et al., 2010). $C_{0,wr}$ may be the same whole rock source composition used in these MREE–HREE based models – which is taken to be DMM (Salters and Stracke, 2004); alternatively, we can use a whole rock composition calculated to represent the refractory arc mantle (RAM) source. In both cases, a result may be calculated for each chemical element of interest.

Modelling Fluid Mobile Element Addition – Application

We test this model using new laser ablation ICP–MS data for the fluid mobile elements. Results from the partial melt models (Fig. A–3) were used to calculate $C_{cpx,model}$ for each locale. The results from equation (7) serve as input into equations (4) and (3), which functions as a check

on the observed concentrations in the refractory clinopyroxene. Because the melt fraction is the same as those used for the melt extraction models (equation 1), the calculated concentrations ($C_{\text{cpx,model}}$) for the rare earth and high field strength elements should match approximately the observed concentrations ($C_{\text{cpx,obs}}$), i.e., $C_i^{\text{melt model}}/C_i^{\text{sample}} \sim 1$. Moreover, both $C_{\text{wr,add}}$ and $C_{\text{cpx,added}}$ for these elements should be effectively zero; negative values represent uncertainties in the model and are generally small, i.e., < 0.1 ppm. The $C_{\text{cpx,model}}$ for most of the fluid mobile elements are effectively zero; therefore any enrichment observed in our samples must be due solely to fluid addition.

In our calculations we applied melting modes appropriate for hydrous melting of peridotite, distinguishing between deeper garnet–field melting and shallower spinel–field melting, which may follow earlier garnet–field melting (Gaetani and Grove, 1998; Walters, 1998). Partition coefficients were chosen to be internally consistent for partial melting of peridotites under garnet–field and spinel field conditions (e.g., Brenan et al., 1998; Johnson, 1998; Green et al., 2000; Witt–Eickschen and O’Neil, 2005; Adam and Green, 2006). Previous work has shown that critical melting (in which a portion of the melt is retained in the residual assemblage) is limited (e.g., Johnson et al., 1990), but we include it in our model because it will have profound influence on results where it occurs. In our calculations, we treat retained melt as a phase with partition coefficients of 1.0 for all elements. Furthermore, all modes are presented as mass fractions, not volume percents, to simplify calculations: this results in spinel and garnet modes slightly higher than their volumetric modes. Details of our model are spelled out in Appendix 1 and 2, and a worksheet with model calculations is offered in electronic annex EA–3.

Using melt models presented in Figure A–3, which are based on the less incompatible and generally fluid–immobile middle and heavy REE, fluid–mobile elements are enriched relative to their model abundances by factors of 10^5 to 10^{43} greater than model concentrations (Fig. A–4). This is true even when we use distribution coefficients determined for hydrous melting of mantle peridotites (Green et al., 2000; Gaetani et al., 2003; McDade et al., 2003; Fumagalli and Poli,

2005; Kessel et al., 2005). Minor enrichments are also seen in some highly incompatible high field strength elements as well (e.g., Zr, Hf, Nb), which must reflect enrichment by a melt phase.

In equation (7), the initial concentration term $C_{0,wr}$ could represent two end-member situations: first, that fluid mobile elements are added to the DMM source prior to melting, and second, that fluid mobile elements are added continuously during melting, so that their current concentrations reflect equilibration with the last effective melt fraction (refractory mantle source). Note that the concentration of FME in both potential source regions are very low ($\ll 1$ ppm); thus, the $C_{wr,add}$ calculated from equation (7) depends almost entirely on the observed concentrations in pyroxene ($C_{cpx,obs}$), the bulk distribution coefficients for each element (D), and the melt fraction (F).

In the first case, $C_{0,wr}$ represents a DMM source and the $C_{wr,add}$ determined by equation (7) represents the total addition of material to the mantle wedge source region. Our results suggest that this model is not valid, because the added concentrations required are orders of magnitude higher than expected, e.g., B $\sim 10^{5-7}$, Sr $\sim 10^{4-6}$, Pb $\sim 10^{7-11}$, Th $\sim 10^{20-24}$, and Ba $\sim 10^{33-43}$ ppm. These values are unrealistic because the FME are extremely incompatible and are thus concentrated in the first melt fractions. Successive melting events will progressively deplete the source, which is not capable of retaining FME concentrations sufficiently high to produce the observed pyroxenes with the amount of melting required by the middle to heavy REE.

In the second case, we use the penultimate melt fraction in the melting models as our starting composition, and calculate the composition of the fluid component added to the system during the last melting increment (taken to be 0.5% melting – this can be adjusted in our model spreadsheet). This “refractory arc mantle” (RAM) source reflects the effects of previous melt extraction from the DMM source. The results of these calculations are shown in Table A–3 and Figure A–4. Figure A–4 compares the average measured clinopyroxene compositions for each locality to calculated $C_{cpx,add}$ compositions for this melt model. The calculated concentrations of $C_{wr,add}$ for the ultimate melt fraction from a refractory source region range from B $\sim 2-4$ ppm, Li

~2–4 ppm, Ba ~1000 ppm, Th ~0.01–0.04 ppm, and Pb ~0.1–0.6 ppm – concentrations that are 10's to 100's of times higher than DMM source compositions (Table A–4). These results represent the concentrations of fluid mobile elements that are added to the source during any given increment of melting, and which are added continuously as melting proceeds; they are also consistent with simple fluid mobile element partitioning using fluid–mineral partition coefficients (Green et al., 2000; Gaetani et al., 2003; McDade et al., 2003; Fumagalli and Poli, 2005; Kessel et al., 2005).

These results confirm previous models which predict that melting in the mantle wedge above a subduction zone is an open system process in which slab–derived components are continually enriched in the wedge as melt fractions are extracted (e.g., Tatsumi and Eggins, 1995; Ozawa and Shimizu, 1995). The question arises, however, if the enrichments of FME we calculate here are sufficient to produce the observed concentrations in primitive arc volcanic rocks.

Modelling Fluid Mobile Elements in Arc Volcanics

These results may be used to calculate the composition of the fluid–enriched mantle source region. We use the fluid–enriched source ($C_{0,wr} + C_{wr,add}$) to calculate the compositions of island arc magmas derived by partial melting, using non–modal batch or pooled fractional melting equations (Rollinson, 1993). We have modelled arc volcanism using two approaches: one assumes a MORB–mantle (DMM) starting composition with incremental fluid mobile element enrichment; the other assumes a more refractory source composition (RAM: refractory arc mantle = MORB–source mantle after melt extraction in the garnet stability field or garnet + spinel field melting) with incremental fluid mobile element enrichment. We add the calculated FME concentration for the final 0.5% melt extraction to (1) the DMM source and (2) the RAM source for that location, based on source composition after garnet–field melting or, in some cases, garnet + spinel melting.

Figure A–5 displays DMM–normalized model arc magma compositions (calculated by assuming an additional 10% batch or pooled fractional melting of the FME–enriched source), compared to primitive arc volcanic rocks (arc tholeiites with $\text{SiO}_2 < 58.0$ wt %) and Izu–Bonin boninites, taken from the Georoc database (Kuroda et al., 1978; Shiraki et al., 1980; Jenner et al., 1987; Arculus et al., 1992; Gill et al., 1992; Pearce et al., 1992; Matsumoto et al., 1993; Taylor et al., 1994; Hochstaedter et al., 2000; Münker, 2000). This figure shows that pooled magmas are equivalent to primitive arc volcanics in their trace element characteristics. It further shows that magmas derived from the calculated FME–enriched RAM source are generally equivalent to boninites, or are transitional between boninite and arc tholeiite.

Conclusions

The data presented here demonstrates that essentially all fluid mobile elements (Li, B, Be, Rb, Th, Pb) present in island arc volcanic rocks had their source in the subducting slab, and that these elements must be added more or less continuously during melting in order to maintain the high concentrations observed in the sub–arc peridotites and in the volcanic rocks derived from them.

The algorithm we derive for calculating FME enrichments in otherwise refractory peridotites can be applied to any peridotite that formed as a refractory residue in the mantle wedge below an island arc complex. Such peridotites are common in ophiolites (e.g., Batanova et al., 1998; Batanova and Sobolev, 2000; Bizimis et al., 2000; LeMee et al., 2004; Barth et al., 2008; Choi et al., 2008a; Choi et al., 2008b; Jean et al., 2010), and are also found as xenoliths in arc volcanoes (e.g., Ionov, 2010; Soustelle et al., 2010) and even as clasts in forearc mudvolcanoes (Fryer et al., 2000; D’antonio and Kristensen, 2004). New instrumentation makes determining a large suite of trace elements in single pyroxene grains possible, but because of the extremely refractory nature of many of these peridotites, extreme care must be used in sample preparation and analysis.

Appendix 1. Application of the Fluid Addition Equation to Fractional Melting

Equation (7) can be solved for the addition of multiple fluid mobile elements (or even melt components) to the mantle wedge, as represented by subduction zone peridotites, using the attached Excel spreadsheet (electronic annex EA-3) and the appropriate partitioning and melting coefficients. To facilitate these calculations, we present a spreadsheet that allows the investigator to solve for 30 elements simultaneously, in a two-step process that fixes first, the amount of melt extraction, and second, the FME addition to the sample. We have selected partition coefficients and melting proportions appropriate to hydrous melting that we have found to produce internally consistent results, but these may be modified by the user to any values they prefer.

Details of the Model Calculator:

We use the fractional melting equation (1) as a basis for these calculations because it has been shown repeatedly that batch melting rarely, if ever, successfully reproduces peridotite pyroxene compositions. Values that may be modified by the user include:

Starting composition: We use the depleted MORB-source (DMM) of Salters and Stracke (2004) as our starting composition. The user may also use a refractory arc source (RAM) in subsequent calculations, derived by melting DMM. The user may also substitute their preferred mantle source.

Partition coefficients: We use coefficients from hydrous melting experiments in both the spinel and garnet peridotite facies. The sources are listed in the references below, and in the spreadsheet.

Modal mineralogy – initial: For all of our models we used the initial spinel lherzolite mode of Johnson and Dick (1992) and Adam and Green (2006). For high pressure melting models, we converted these modes to garnet lherzolite using the method of Hellebrand et al. (2002). Note that

these modes are expressed in terms of mass fractions, not volume, to facilitate calculations. This affects mainly the garnet and spinel proportions, because their density is greater than other silicate phases.

Melting proportions: There is a large range of experimentally determined melting proportions in the literature, mostly for anhydrous melting. We use the hydrous experiments of Walter (1998) for spinel peridotite melting modes, and Gaetani and Grove (1998) for garnet melting modes. The melting modes are expressed in mass fractions, and may be set by the user to other values.

Critical melting: Critical melting refers to a melting process in which a portion of the melt formed is retained in the source, and participates in subsequent melt fractions. Johnson et al. (1990) documented that little or no melt retention occurs in abyssal peridotites. Jean et al. (2010) documented the same result for many supra-subduction peridotites. Nonetheless, we include it here using the simple procedure of designating retained melt as a phase in the source with partition coefficients for all elements of 1.0, and a melt mode of 1.0. The mass fraction of retained melt is a variable that may be set; however, most solutions require this to be $\ll 1$.

Depth of Melting (Garnet vs Spinel facies): Our spreadsheet calculator is designed for spinel field-only melting and garnet + spinel field melting. Note that the latter may be used for garnet field-only melting by leaving the melt fractions for spinel-field melting at zero. Jean et al. (2010) found that most supra-subduction peridotites require some garnet-field melting to acquire their steep MREE-HREE depletions, followed by spinel-field melting to lower the overall concentrations.

Application: To apply the calculator, the user first adjusts the melt fractions (F) and (if desired) retained melt fraction in order to obtain a close fit between the MREE-HREE in the model to the observed pyroxene. This represents the total melt extraction. Examination of the tables and the multi-element chart show the solutions for all elements that exceed their model abundances (by

melt extraction) and must therefore have been added to the source after melting. In the example provided, it can be seen in the REE plot that the MREE–HREE pattern cannot be matched by spinel–only melting. The best–fit model requires 8% garnet field melting followed by 15% spinel field melting. The LREE are enriched over model values, indicating either fluid or melt addition to the source. Examination of the multi–element plot provided shows that HFSE are also well matched by the model, but the fluid mobile elements exceed their calculated model abundances by several orders of magnitude. In many cases, the calculated concentration of FME’s is effectively zero.

Appendix 2. Instructions for Using the Fluid Addition Calculator and Estimating Fluid Input into a Subduction Zone

Background: The results from this exercise represents (1) the total addition of material to the mantle wedge source region and may be calculated for each element of interest and (2) an independent determination of the subduction component that requires few assumptions and has been substantially supported by previous studies. Input parameters include the starting bulk composition (columns AD and AE; assumed for our models to be the depleted MORB–source mantle of Salters and Stracke, 2004), modal proportions of minerals in the parent lherzolite (cells Q10 – V11), and the proportions of these minerals entering the melt (cells Q14 – V15). For all of our models we used the initial spinel lherzolite mode of Johnson and Dick (1992) and Adam and Green (2006). For high pressure melting models, we converted these modes to garnet lherzolite using the method of Hellebrand et al. (2002).

Input: A substantial dataset now exists on mineral–liquid partition coefficients for the elements under consideration. The mineral–melt distribution coefficients included in this calculator (listed in columns D–L) were determined by experimental studies and best represent the wedge melting environment, namely temperatures of 1,200–1,300°C, pressures in the spinel or garnet peridotite stability fields, and liquid compositions consistent with sub–alkaline primary melts. These

distribution coefficients are set; however, if the user feels more comfortable with other values from other studies, feel free to substitute. Similarly for the “Source Mode” and “Melt Mode” for garnet and spinel. The first input values are in cells AG8 (percent melt for Spinel Facies), AI8 (percent melt for Garnet Facies), and AK8 (percent melt for Spinel Facies after Garnet Facies melting); cell AJ8 is linked to AI8 and AL8 is linked to AK8. The observed composition of your clinopyroxene goes into gray column AN. It is not necessary to analyze all elements in the spreadsheet.

Output: Output values are in blue columns. Columns AG–AL were calculated using the non modal fractional melting equation of Johnson et al. (1990). These values are based on the percent melt, mineral–melt distribution coefficients, and Source and Melt Modes. Red columns AR–AU are also output from the equations detailed in this paper, which allows you to calculate the amount of fluid added to your source. Column AR (equation 7 in manuscript) is the concentration added to the whole rock; column AS (equation 4 in manuscript) is the concentration added to the clinopyroxene; column AT is the addition of columns AK and AS and should reproduce the clinopyroxene composition in column AN; column AT is final whole rock concentration after partial melting and fluid addition (addition of columns AL and AR).

Excel Settings: In this workbook some equations may be solved simultaneously by numerical methods. Please make certain that under Excel – Preferences – Calculations, that “Iterative” calculations are allowed, otherwise Excel will report a “Circular reference” error.

REE Chart: This plot shows the rare–earth elements normalized to C1–chondrite of McDonough and Sun (1995). In blue diamonds are the normalized clinopyroxene compositions. In yellow circles are the normalized compositions for partial melting in the spinel field. In red squares are the normalized compositions for partial melting beginning in the garnet field and continuing into the spinel field. This chart will be created automatically. The example provided shows that both

melting strategies have similar compositions for the heavy-REE, but separate in the middle to light-REE. The goal is to match the heavy-REE and middle-REE to the data.

All Elements Chart: This plot shows all elements normalized to depleted MORB-mantle of Salters and Stracke (2004); same color scheme as REE Chart. The goal is to match REE and check whether this model matches other elements. If not, then fluid must have been added to your source.

References

- Adam J. and Green T. (2006) Trace element partitioning between mica- and amphibole-bearing garnet lherzolite and hydrous basanitic melt: 1. Experimental results and the investigation of controls on partitioning behavior. *Contrib. Min. Pet.* **152**, 1–17.
- Anders E. and Grevesse N. (1989) Abundances of the elements: Meteoric and solar. *Geochim. Cosmochim. Acta* **53**, 197–214.
- Arculus R.J., Pearce J.A., Murton B.J. and Van Der Laan S.R. (1992) Igneous Stratigraphy And Major-Element Geochemistry Of Holes 786a And 786b. *Proc. Ocean Drill. Prog. Scient. Results* **125**, 143–169.
- Ayers J. (1998) Trace element modeling of aqueous fluid-peridotite interaction in the mantle wedge of subduction zones. *Contrib. Min. Pet.* **132**, 390–404.
- Barth M.G., Mason P.R.D., Davies G.R. and Drury M.R. (2008) The Othris Ophiolite, Greece; a snapshot of subduction initiation at a mid-ocean ridge. *Lithos* **100**, 234–254.
- Batanova V.G. and Sobolev A.V. (2000) Compositional heterogeneity in subduction-related mantle peridotites, Troodos Massif, Cyprus. *Geology* **28**, 55–58.
- Batanova V.G., Suhr G. and Sobolev A.V. (1998) Origin of geochemical heterogeneity in the mantle peridotites from the Bay of Islands Ophiolite, Newfoundland, Canada; ion probe study of clinopyroxenes. *Geochim. Cosmochim. Acta* **62**, 853–866.

- Bizimis M., Salters V.J.M. and Bonatti E. (2000) Trace and REE content of clinopyroxenes from supra-subduction zone peridotites; implications for melting and enrichment processes in island arcs. *Chem. Geol.* **165**, 67–85.
- Brenan J.M., Ryerson F.J. and Shaw H.F. (1998) The role of aqueous fluids in the slab-to-mantle transfer of boron, beryllium, and lithium during subduction: Experiments and models. *Geochim. Cosmochim. Acta* **62**, 3337–3347.
- Canil D. (1999) Vanadium partitioning between orthopyroxene, spinel and silicate melt and the redox states of mantle source regions for primary magmas. *Geochim. Cosmochim. Acta* **63**(3–4), 557–572.
- Choi S.H., Mukasa S.B. and Shervais J.W. (2008a) Initiation of Franciscan subduction along a large-offset fracture zone; evidence from mantle peridotites, Stonyford, California. *Geology* **36**, 595–598.
- Choi S.H., Shervais J.W. and Mukasa S.B. (2008b) Supra-subduction and abyssal mantle peridotites of the Coast Range Ophiolite, California. *Contrib. Min. Pet.* **156**, 551–576.
- D'antonio M. and Kristensen M.B. (2004) Serpentine and brucite of ultramafic clasts from the South Chamorro Seamount (Ocean Drilling Program Leg 195, Site 1200): inferences for the serpentinization of the Mariana forearc mantle. *Min. Mag.* **68**(6), 887–904.
- Dosso L., Bougault H. and Joron J-L. (1993) Geochemical morphology of the North Mid-Atlantic Ridge, 10°–24°N: Trace element-isotope complementarity. *EPSL* **120**, 443–462.
- Elkins L., Gaetani G. and Sims K. (2008) Partitioning of U and Th during garnet pyroxenite partial melting: Constraints on the source of alkaline ocean island basalts. *EPSL* **265**, 270–286.
- Elliott T.R. (2003) Tracers of the slab, in *Inside the Subduction Factory*, Geophys. Monogr. Ser., vol. 138, edited by J. Eiler, pp. 23–45, AGU, Washington, D. C.
- Fryer, P., Lockwood, JP, Becker, N., Phipps, S, Todd, C, 2000, Significance of serpentine mud volcanism in convergent margins. In Dilek, Y., Moores, E.M., Elthon, D., Nicolas, A. (Eds.),

- Ophiolites and Oceanic Crust: New Insights from Field Studies and the Ocean Drilling Program. *Geol. Soc. Am. Special Paper* **349**, 35–51.
- Fumagalli P. and Poli S. (2005) Experimentally determined phase relations in hydrous peridotites to 6.5 GPa and their consequences on the dynamics of subduction zones. *J. Pet.* **46**, 555–578.
- Gaetani G.A. and Grove T.L. (1998) The influence of water on melting of mantle peridotite. *Contrib. Min. Pet.* **131**, 323–346.
- Gaetani G.A., Kent A.J.R., Grove T.L., Hutcheon I.D. and Stolper E.M. (2003) Mineral/melt partitioning of trace elements during hydrous peridotite partial melting. *Contrib. Min. Pet.* **145**, 391–405.
- Giaramita M.I., MacPherson G.J. and Phipps S.P. (1998) Petrologically diverse basalts from a fossil oceanic fore-arc in California: The Llanada and Black Mountain remnants of the Coast Range ophiolite. *Geol. Soc. Am. Bull.* **110**, 553–571.
- Gill J.B., Seales C., Thompson P., Hochstaedter A.G. and Dunlap C. (1992) Petrology And Geochemistry Of Pliocene–Pleistocene Volcanic Rocks From The Izu Arc Leg 126. *Proc. Ocean Drill. Prog., Scient. Results* **126**, 383–404.
- Green T.H., Blundy J.D., Adam J. and Yaxley G.M. (2000) SIMS determination of trace element partition coefficients between garnet, clinopyroxene and hydrous basaltic liquids at 2–7.5 GPa and 1080–1200 degrees C. *Lithos* **53**, 165–187.
- Hacker B.R., Abers G.A. and Peacock S.M. (2003) Subduction factory, 1, Theoretical mineralogy, densities, seismic wave speeds, and H₂O contents. *J. Geophys. Res.* **108**(B1), 2029, doi: 10.1029/2001JB001127.
- Hanan B.B., Blichert-Toft J., Christie D.M. and Albarède F. (2000) Ultra-depleted hafnium isotopes from Australian–Antarctic Discordance MORB. *J. Conf. Abstr.* **5**, 478.
- Hanan B.B. and Schilling J–G. (1997) The dynamic evolution of the Iceland mantle plume; the lead isotope perspective. *EPSL* **151**, 43–60.

- Hart S.R. and Dunn T. (1993) Experimental cpx/melt partitioning of 24 trace elements. *Contrib. Min. Pet.* **113**, 1–8.
- Hauri E.H., Wagner T.P. and Grove T.L. (1994) Experimental and natural partitioning of Th, U, Pb and other trace elements between garnet, clinopyroxene and basaltic melts. *Chem. Geol.* **117**, 149–166.
- Hellebrand E., Snow J.E., Hoppe P. and Hofmann A.W. (2002) Garnet–field melting and late–stage refertilization in "residual" abyssal peridotites from the Central Indian Ridge. *J. Pet.* **43**, 2305–2338.
- Hochstaedter A.G., Gill J.B., Taylor B., Ishizuka O., Yuasa M. and Morita S. (2000) Across–Arc Geochemical Trends In The Izu– Bonin Arc: Constraints On Source Composition And Mantle Melting. *J. Geophys. Res.* **B105**, 495–512.
- Hopson C.A. and Pessagno E.A. (2005) Tehama–Colusa Serpentinite Mélange: A Remnant of Franciscan Jurassic Oceanic Lithosphere, Northern California. *Int. Geol. Rev.* **47**(1), 65–100.
- Hopson C.A., Mattinson J.M. and Pessagno E.A. (1981) Coast Range ophiolite, western California. In: Ernst, W.G. (Ed.), *The geotectonic development of California*, Rubey Volume I, pp. 418–510.
- Hopson C.A., Mattinson J.M., Pessagno E.A. and Luyendyk B.P. (2008) California Coast Range ophiolite: Composite Middle and Late Jurassic oceanic lithosphere. In: Wright, J.E., Shervais, J.W. (Eds.), *Ophiolites, Arcs, and Batholiths. Geol. Soc. Am. Special Paper* **438**, p. 1102.
- Horn I., Foley S.F., Jackson S.E. and Jenner G.A. (1994) Experimentally determined partitioning of high field strength– and selected transition elements between spinel and basaltic melt. *Chem. Geol.* **117**, 193–218.
- Ionov D.A. (2010) Petrology of Mantle Wedge Lithosphere: New Data on Supra–Subduction Zone Peridotite Xenoliths from the Andesitic Avacha Volcano, Kamchatka. *J. Pet.* **51**, 327–361.

- Jean M.M., Shervais J.W., Choi S.H. and Mukasa S.B. (2010) Melt Extraction and Melt Refertilization in Mantle Peridotite of the Coast Range Ophiolite: An LA–ICP–MS Study. *Contrib. Min. Pet.* **159**, 113–136.
- Jenner G.A., Cawood P.A., Rautenschlein M. and Matthey D.P. (1987) Composition Of Back–Arc Basin Volcanics, Valu Fa Ridge, Lau Basin: Evidence For A Slab–Derived Component In Their Source. *J. Volcanol. Geotherm. Res.* **32**, 209–222.
- Johnson K.T.M., Dick H.J.B. and Shimizu N. (1990) Melting in the oceanic upper mantle; an ion microprobe study of diopsides in abyssal peridotites. *J. Geophys. Res.* **95**, 2661–2678.
- Johnson K.T.M. (1998) Experimental determination of partition coefficients for rare earth and high–field–strength elements between clinopyroxene, garnet, and basaltic melt at high pressures. *Contrib. Min. Pet.* **133**, 60–68.
- Kent A.J.R. and Ungerer C.A. (2006) Analysis of light lithophile elements (Li, Be, B) by laser ablation ICP–MS: Comparison between magnetic sector and quadrupole ICP–MS. *Am. Mineral.* **91**, 1401–1411.
- Kessel R., Schmidt M.W., Ulmer P. and Pettke T. (2005) Trace element signature of subduction zone fluids, melts, and supercritical liquids at 120–180 km depth. *Nature* **437**, 724–727.
- Kimura J.-I., Hacker B.R., van Keken P.E., Kawabata H., Yoshida T. and Stern R.J. (2009) Arc Basalt Simulator version 2, a simulation for slab dehydration and fluid–fluxed mantle melting for arc basalts: Modeling scheme and application, *Geochem. Geophys. Geosyst.* **10**, Q09004, doi:10.1029/623 2008GC002217.
- Klemme S., Blundy J.D. (2002) Experimental constraints on major and trace element partitioning during partial melting of eclogite. *Geochim. Cosmochim. Acta* **66**, 3109–3123.
- Kuroda N., Shiraki K. and Urano H. (1978) Boninite as a Possible Calc–Alkaline Primary Magma. *Bull. Volcanol.* **41**, 563–575.
- LeMee L., Girardeau J. and Monnier C. (2004) Mantle segmentation along the Oman ophiolite fossil mid–ocean ridge. *Nature (London)* **432**, 167–172.

- Lyubetskaya T. and Korenaga J. (2007) Chemical composition of Earth's primitive mantle and its variance: 1. Method and results. *J. Geophys. Res.* **112**, 1–21.
- Mallman G. and O'Neill H St.C (2009) The Crystal/Melt Partitioning of V during Mantle Melting as a Function of Oxygen Fugacity Compared with some other Elements (Al, P, Ca, Sc, Ti, Cr, Fe, Ga, Y, Zr and Nb). *J. Pet.* **50**(9), 1765–1794.
- Marschall H.R. and Ludwig T. (2004) The low-boron contest: minimizing surface contamination and analysing boron concentrations at the ng/g-level by secondary ion mass spectrometry. *Contrib. Min. Pet.* **81**, 265–278.
- Matsumoto A., Mizugaki K., Tamanyu S., Ono K., Kitahara T., Shinada S. and Sasada M. (1993) The Hata Basalts: Early Products of Taga Volcano, Izu Peninsula – Geology And K–Ar Ages in and around the Tanna Basin Shizuoka Japan. *Bull. Volcanol. (Soc. Japan Ser. 2)* **38**, 1–13.
- Mattinson J.M. and Hopson C.A. (2008) New high-precision CA–TIMS U–Pb zircon plateau ages for the Point Sal and San Simeon ophiolite remnants, California Coast Ranges, in Wright, J.E., and Shervais, J.W., eds., Ophiolites, Arcs, and Batholiths. *Geol. Soc. Am. Special Paper* **438**, 103–112.
- McDade P., Blundy J.D. and Wood B.J. (2003) Trace element partitioning between mantle wedge peridotite and hydrous MgO-rich melt. *Am Min* **88**, 1825–1831.
- McDonough W.F. and Sun S.S. (1995) The composition of the Earth. *Chem. Geol.* **120**, 223–253.
- Metcalf, R.V., and Shervais, J.W., 2008, Supra-Subduction Zone (SSZ) Ophiolites: Is There Really An "Ophiolite Conundrum"? In: Wright, J.E., Shervais, J.W. (Eds.), Ophiolites, Arcs, and Batholiths: A Tribute to Cliff Hopson. *Geol. Soc. Am. Special Paper* **438**, 191–222.
- Morishita T., Dilek Y., Shallo M., Tamura A. and Arai S. (2011) Insight into the uppermost mantle section of a maturing arc: The Eastern Mirdita ophiolite, Albania. *Lithos* **124**, 215–226.
- Münker C. (2000) The Isotope And Trace Element Budget Of The Cambrian Devil River Arc System New Zealand: Identification Of Four Source Components. *J. Pet.* **41**, 759–788.

- Nicolas A. and Boudier F. (2000) Large mantle upwellings and related variations in crustal thickness in the Oman ophiolite. In: Dilek, Y., Moores Eldridge, M., Elthon, D., Nicolas, A. (Eds.), *Ophiolites and oceanic crust; new insights from field studies and the Ocean Drilling Program. Geol. Soc. Am. Boulder, CO, United States.*
- Niu Y., Waggoner D.G., Sinton J.M. and Mahoney J.J. (1996) Mantle source heterogeneity and melting processes beneath seafloor spreading centers: the East Pacific Rise, 18°–19°S. *J. Geophys. Res.* **101**, 27711–27733.
- Ohara Y., Stern R.J., Ishii T., Yurimoto H. and Yamazaki T. (2002) Peridotites from the Mariana Trough: first look at the mantle beneath an active back–arc basin. *Contrib. Min. Pet.* **143**, 1–18.
- Ozawa K. and Shimizu N. (1995) Open–system melting in the upper mantle: Constraints from the Hayachine–Miyamori ophiolite, northeastern Japan. *J. Geophys. Res.* **100**, 22315–22335.
- Ozawa K. (2001) Mass balance equations for open magmatic systems: trace element behavior and its application to open system melting in the upper mantle. *J. Geophys. Res.* **106**, 13407–13434.
- Parkinson I.J. and Pearce J.A. (1998) Peridotites from the Izu–Bonin–Mariana forearc (ODP Leg 125); evidence for mantle melting and melt–mantle interaction in a supra–subduction zone setting. *J. Pet.* **39**, 1577–1618.
- Peacock S.M. (1990) Fluid processes in subduction zones. *Science* **248**, 329–337.
- Pearce J.A., Van Der Laan S.R., Arculus R.J., Murton B.J., Ishii T., Peate D.W. and Parkinson I.J. (1992) Boninite and Harzburgite from Leg 125 (Bonin–Mariana Forearc): A Case Study of Magma Genesis During the Initial Stages of Subduction. *Proc. Ocean Drill. Prog., Scient. Results* **125**, 623–659.
- Pearce J.A. (2003) Suprasubduction zone ophiolites: the search for modern analogues, in: Dilek, Y., Newcomb, S. (Eds.), *Ophiolite concept and the Evolution of Geologic Thought. Geol. Soc. Am. Special Paper* **373**, 269–294.

- Pearce J.A., Lippard S.J. and Roberts S. (1984) Characteristics and tectonic significance of supra-subduction zone ophiolites. In: Kokelaar, B.P., Howells, M.F. (Eds.), *Marginal basin geology*, Geological Society Special Publications, Keele, United Kingdom, pp. 74–94.
- Pearce N.J.G., Perkins W.T., Westgate J.A., Gorton M.P., Jackson S.E., Neal C.R. and Chenerly S.P. (1997) A Compilation of New and Published Major and Trace Element Data for NIST SRM 610 and NIST SRM 612 Glass Reference Materials. *Geostand. Newslett.* **21**, 115–144
- Plank T. and Langmuir C.H. (1998) The chemical composition of subducting sediment and its consequences for the crust and mantle. In: Albarede, F., Blichert-Toft, J., Staudigel, H., White, W.M. (Eds.), *Geochemical Earth Reference Model (GERM)*. *Chem. Geol.* **145**(3–4), 325–394.
- Rollinson H. (1993) *Using geochemical data: evaluation, presentation, interpretation*. Pearson Education Limited, Harlow UK.
- Salters V.J.M. and Stracke A. (2004) Composition of the depleted mantle. *Geochem. Geophys. Geosyst.* **5**, Q05004. doi:10.1029/2003GC000597.
- Salters V.J.M. (1996) The generation of mid-ocean ridge basalts from the Hf and Nd isotope perspective. *EPSL* **141**, 109–123.
- Salters V.J.M. and Zindler A. (1995) Extreme $^{176}\text{Hf}/^{177}\text{Hf}$ in the sub-oceanic mantle. *EPSL* **129**, 13–30.
- Savov I.P., Ryan J.G., D'Antonio M., Kelley K. and Mattie P. (2005) Geochemistry of serpentinitized peridotites from the Mariana Forearc Conical Seamount, ODP Leg 125: Implications for the elemental recycling at subduction zones. *Geochem. Geophys. Geosyst.* **6**, Q04J15, doi:10.1029/2004GC000777
- Scambelluri M., Bottazzi P., Trommsdorff V., Vannucci R., Hermann J., Gomez P.M.T. and Lopez S.V.V. (2001) Incompatible element-rich fluids released by antigorite breakdown in deeply subducted mantle. *EPSL* **192**, 457–470.

- Schilling J-G., Zajac M., Evans R., Johnston T., White W., Devine J.O. and Kingsley R. (1983) Petrologic and geochemical variations along the mid-Atlantic Ridge from 29°N to 73°N. *Am. J. Sci.* **283**, 510–586.
- Shervais J.W. (1990) Island arc and ocean crust ophiolites: contrasts in the petrology, geochemistry, and tectonic style of ophiolite assemblages in the California coast ranges. Ophiolites: Oceanic Crustal Analogues. Malpas J.C., Moores E.M., Panayiotou A., Xenophontos C. (Eds.), The Geological Survey Department, Nicosia, Cyprus, pp. 507–520.
- Shervais J.W. (2001) Birth, Death, and Resurrection: The Life Cycle of Suprasubduction Zone Ophiolites, *Geochem. Geophys. Geosyst.* **2**.
- Shervais J.W. (2006) Significance of Subduction-related Accretionary Complexes in Early Earth Processes, in Uwe Reimold and Roger Gibson, editors, Early Earth Processes. *Geol. Soc. Am. Special Paper* **405**, 173–192.
- Shervais J.W. (2008) Tonalites, Trondhjemites, and Diorites of the Elder Creek Ophiolite, California: Low Pressure Slab Melting and Reaction with the Mantle Wedge. In Wright J.E., Shervais, J.W. (Eds.), Ophiolites, Arcs, and Batholiths: A Tribute to Cliff Hopson. *Geol. Soc. Am. Special Paper* **438**, p. 113–132.
- Shervais J.W. and Kimbrough D.L. (1985) Geochemical evidence for the tectonic setting of the Coast Range Ophiolite: A composite island arc-oceanic crust terrane in western California. *Geology* **13**, 35–38.
- Shervais J.W., Kimbrough D.L., Renne P. Murchey B. and Hanan B.B. (2004) Multi-stage Origin of the Coast Range Ophiolite, California and Oregon: Implications for the Life Cycle of Supra-subduction Zone Ophiolites. *Int. Geol. Rev.* **46**, 289–315.
- Shervais J.W., Murchey B., Kimbrough D.L., Renne P. and Hanan B.B. (2005a) Radioisotopic and Biostratigraphic Age Relations in the Coast Range Ophiolite, Northern California: Implications for the Tectonic Evolution of the Western Cordillera. *Geol. Soc. Am. Bull.* **117** (5/6), 633–653.

- Shervais J.W., Zoglman–Schuman M.M. and Hanan B.B. (2005b) The Stonyford Volcanic Complex: A Forearc Seamount in the Northern California Coast Ranges. *J. Pet.* **46**(10), 2091–2128.
- Shervais J.W., Choi S.H., Sharp W.D., Ross J., Zoglman–Schuman M.M. and Mukasa S.B. (2011) Serpentinite Matrix Mélange: Implications of Mixed Provenance for Mélange Formation. In: Wakabayashi, J., Dilek, Y. (Eds.), *Melanges: Processes of Formation and Societal Significance. Geol. Soc. Am. Special Paper* **480**, 1–38.
- Shiraki K., Kuroda N., Urano H. and Maruyama S. (1980) Clinoenstatite In Boninites From The Bonin Islands, Japan. *Nature* **285**, 31–32.
- Soustelle V., Tommasi A., Demouchy S. and Ionov D.A. (2010) Deformation and Fluid–Rock Interaction in the Supra–subduction Mantle: Microstructures and Water Contents in Peridotite Xenoliths from the Avacha Volcano, Kamchatka. *J. Pet.* **51**, 363–394.
- Stern R.J., Kohut E., Bloomer S.H., Leybourne M., Fouch M. and Vervoort J. (2006) Subduction factory processes beneath the Guguan cross– chain, Mariana Arc: no role for sediments, are serpentinites important? *Contrib. Min. Pet.* **151**, 202–221.
- Stolper E.M. and Newman S. (1994) The role of water in the petrogenesis of Mariana Trough magmas. *EPSL* **121**, 293–325.
- Tatsumi Y. (2005) The subduction factory; how it operates in the evolving Earth. *Geology* **15**, 4–10.
- Tatsumi Y. and Eggins S. (1995) *Subduction zone magmatism*. Blackwell Science, Cambridge, MA, United States.
- Tatsumi Y. and Kogiso T. (2003) The subduction factory: Its role in the evolution of the Earth's crust and mantle. In: Larter, R.D., Leat, P.T. (Eds.), *Intra–oceanic subduction systems: tectonic and magmatic processes*. London, Geological Society Special Publication 219, pp. 55–80.

- Taylor R.N., Nesbitt R.W., Vidal P., Harmon R.S., Auvray B. and Croudace I.W. (1994) Mineralogy Chemistry And Genesis Of The Boninite Series Volcanics Chichijima Bonin Islands Japan. *J. Pet.* **35**, 577–617.
- Walter M.J. (1998) Melting of garnet peridotite and the origin of komatiite and depleted lithosphere. *J. Pet.* **39**, 29–60.
- Warren J.M., Shimizu N., Sakaguchi C., Dick H.J.B. and Nakamura E. (2009) An assessment of upper mantle heterogeneity based on abyssal peridotite isotopic compositions. *J. Geophys. Res.* **114**, B12203, doi:10.1029/2008JB006186.
- Witt-Eickschen G. and O’Neil H.S.C. (2005) The effect of temperature on the equilibrium distribution of trace elements between clinopyroxene, orthopyroxene, olivine and spinel in upper mantle peridotite. *Chem. Geol.* **221**, 65–101.
- Yoshikawa M. and Ozawa K. (2007) Rb–Sr and Sm–Nd isotopic systematics of the Hayachine–Miyamori ophiolitic complex: Melt generation process in the mantle wedge beneath an Ordovician island arc. *Gondwana Res.* **11**, 234–246.
- Zindler A. and Hart S.R. (1986) Chemical geodynamics. *Ann. Rev. Earth Planet. Sci.* **14**, 493–571.

Table A-1. Mean Error and Detection Limits of NIST 612 Glass Standard

Atomic Number	Element	Preferred Values ^b	Concentrations from this study ^c			
			Measured values	1 σ Error	r.s.e (%)	Minimum Detection Limits (99% Confidence)
3	Li	41.54 \pm 2.87	41.42	4.41	0.29	3.14
4	Be	37.73 \pm 2.41	37.71	3.59	0.05	0.90
5	B	34.73 \pm 3.21	34.82	5.79	-0.26	1.07
21	Sc	41.05 \pm 4.09	41.02	2.02	0.07	2.79
23	V	39.22 \pm 3.76	39.24	1.71	-0.05	0.23
37	Rb	31.63 \pm 0.59	31.61	1.52	0.06	0.28
38	Sr	76.15 \pm 2.29	76.15	2.79	0.01	0.17
39	Y	38.25 \pm 2.14	38.26	1.54	-0.02	0.08
40	Zr	35.99 \pm 1.25	35.94	2.20	0.13	1.31
41	Nb	38.06 \pm 0.86	38.06	1.53	-0.002	0.04
56	Ba	37.74 \pm 1.26	37.66	2.85	0.22	1.81
57	La	35.77 \pm 2.15	35.77	1.36	0.003	0.04
58	Ce	38.35 \pm 1.64	38.37	1.51	-0.05	0.04
59	Pr	37.16 \pm 0.93	37.16	1.37	-0.01	0.02
60	Nd	35.24 \pm 2.44	35.27	1.59	-0.08	0.18
62	Sm	36.72 \pm 2.63	36.76	1.77	-0.11	0.13
63	Eu	34.44 \pm 1.59	34.43	1.30	0.04	0.20
64	Gd	36.95 \pm 1.06	36.99	2.03	-0.12	0.35
65	Tb	35.92 \pm 2.68	35.92	1.34	-0.004	0.04
66	Dy	35.97 \pm 0.82	35.99	1.63	-0.06	0.08
67	Ho	37.87 \pm 1.09	37.87	1.44	-0.01	0.02
68	Er	37.43 \pm 1.50	37.43	1.66	-0.01	0.10
69	Tm	37.55 \pm 1.25	37.56	1.41	-0.02	0.03
70	Yb	39.95 \pm 2.86	39.95	1.78	-0.01	0.11
71	Lu	37.71 \pm 1.95	37.72	1.47	-0.02	0.03
72	Hf	34.77 \pm 3.65	34.75	1.55	0.06	0.11
82	Pb	38.96 \pm 1.84	38.99	2.03	-0.08	0.06
90	Th	37.23 \pm 0.72	37.25	1.49	-0.06	0.01

(a) All values in ppm

(b) Values from Table 9 of Pearce et al. (1997)

(c) N = 80

Table A-2. Mean trace element compositions, 1σ error, detection limits, and ranges for Coast Range Ophiolite clinopyroxene

	Black Diamond Ridge (n=42)				Cuesta Ridge (n=6)				Stony Creek (n=31)				Burro Mountain (n=20)				Del Puerto Canyon (n=19)			
	Cpx Range	Detection Limits (99% confidence)	Cpx (1 σ)	Cpx Range	Detection Limits (99% confidence)	Cpx (1 σ)	Cpx Range	Detection Limits (99% confidence)	Cpx (1 σ)	Cpx Range	Detection Limits (99% confidence)	Cpx (1 σ)	Cpx Range	Detection Limits (99% confidence)	Cpx (1 σ)	Cpx Range	Detection Limits (99% confidence)	Cpx (1 σ)	Cpx Range	
B	1.97 (0.54)	0.42		0.78–4.13	0.59		0.86–1.79	0.79		0.54–9.38	0.74		1.33–7.95	0.49		0.92–5.34	0.71		0.75–5.71	
Li	2.11 (0.43)	0.25		0.73–4.17	n.a.		n.a.	0.69		0.37–4.56	0.77		2.15–6.46	n.a.		n.a.	n.a.		n.a.	
Rb	0.87 (0.09)	0.16		0.66–0.89	n.a.		n.a.	0.04		0.10–0.10	n.a.		n.a.	n.a.		n.a.	n.a.		n.a.	
K	0.37 (0.03)	0.07		0.33–0.41	0.01		0.01–0.01	0.04		0.01–0.10	1.07		n.a.	n.a.		n.a.	n.a.		n.a.	
Th	0.005 (0.004)	0.002		0.002–0.042	0.01		0.01–0.05	0.04		0.001–0.01	0.02		0.002–0.02	0.02		0.001–0.05	0.02		0.001–0.05	
Pa	b.d. (n.a.)	n.a.		n.a.	n.a.		n.a.	n.a.		n.a.	n.a.		n.a.	n.a.		n.a.	n.a.		n.a.	
Sr	0.51 (0.02)	0.01		0.02–1.67	0.08		0.05–0.28	0.04		0.01–0.75	0.04		0.03–0.14	0.01		0.05–0.84	0.01		0.05–0.84	
Y	4.11 (0.19)	0.09		2.57–4.89	0.24		1.19–24.28	0.11		0.07–0.88	0.07		0.52–8.77	0.06		0.29–0.56	0.06		0.29–0.56	
Nb	0.06 (0.02)	0.01		0.01–0.46	0.02		0.03–0.03	0.01		0.01–0.18	0.02		0.06–0.14	0.01		0.01–0.09	0.01		0.01–0.09	
Zr	4.43 (0.53)	0.53		1.40–7.65	0.83		0.86–9.99	0.06		0.06–0.07	n.a.		n.a.	n.a.		0.08–0.11	0.01		0.08–0.11	
Hf	0.34 (0.07)	0.06		0.14–0.55	0.06		0.15–0.48	0.07		0.01–0.23	0.04		0.04–0.08	0.05		0.05–0.05	0.05		0.05–0.05	
Ti	2015	n.a.		1488–2588	1777		1119–2529	142		26–6782	261		n.a.	n.a.		119–121	n.a.		119–121	
Cr	6492	n.a.		5135–8469	5580		4010–6782	5117		4801–8282	5859		n.a.	n.a.		2904–5176	n.a.		2904–5176	
Sc	57.7 (2.66)	0.53		39.9–92.9	1.60		58.5–63.8	0.96		47.4–74.6	46.8 (1.96)		38.3–55.8	0.42		45.1–64.0	0.36		45.1–64.0	
V	0.64 (0.1)	0.01		0.01–0.664	0.23		0.56–0.917	0.14		0.06–0.23	0.09		0.02–0.1	0.09		0.02–0.09	0.09		0.02–0.09	
La	0.54 (0.02)	0.01		0.37–0.73	0.05		0.37–0.4	0.01		0.004–0.01	0.02		0.02–0.03	0.01		0.01–0.04	0.01		0.01–0.04	
Ce	0.28 (0.03)	0.02		0.10–0.42	0.05		0.17–0.19	0.01		0.004–0.01	0.01		0.01–0.01	0.01		n.a.	n.a.		n.a.	
Pr	0.13 (0.02)	0.02		0.07–0.20	0.02		0.04–0.52	0.01		n.a.	n.a.		n.a.	n.a.		n.a.	n.a.		n.a.	
Nd	1.40 (0.14)	0.10		0.60–2.76	0.19		0.41–3.22	0.08		0.01–0.15	0.03		0.09–0.09	0.03		0.03–0.03	0.03		0.03–0.03	
Sm	0.09 (0.12)	0.07		0.47–1.53	0.15		0.34–1.35	0.04		0.004–0.004	0.01		0.13–0.13	0.01		0.01–0.01	0.01		0.01–0.01	
Eu	0.44 (0.06)	0.09		0.22–0.63	0.13		0.25–0.53	0.01		0.05–0.42	0.11		0.13–0.13	0.01		0.04–0.07	0.01		0.04–0.07	
Gd	1.22 (0.16)	0.19		0.86 (0.21)	0.41		0.57–1.44	0.14		0.02–0.03	0.01		0.26–0.54	0.02		0.02–0.03	0.02		0.02–0.03	
Tb	0.34 (0.03)	0.02		0.20–0.51	0.04		0.19–0.34	0.01		0.02–0.03	0.01		0.02–0.03	0.01		0.02–0.03	0.01		0.02–0.03	
Dy	2.59 (0.16)	0.04		1.46–4.31	0.09		0.87–2.16	0.05		0.02–0.36	0.03		0.26–0.54	0.02		0.09–0.26	0.02		0.09–0.26	
Ho	0.66 (0.04)	0.01		0.35–0.89	0.02		0.20–0.53	0.01		0.01–0.12	0.01		0.01–0.12	0.01		0.02–0.07	0.01		0.02–0.07	
Er	0.52 (0.12)	0.05		0.35–2.57	0.10		0.35–1.56	0.07		0.02–0.41	0.05		0.19–0.44	0.03		0.01–0.25	0.03		0.01–0.25	
Tm	0.05 (0.01)	0.02		0.02–0.16	0.02		0.02–0.1	0.01		0.01–0.01	0.01		0.01–0.01	0.01		0.01–0.01	0.01		0.01–0.01	
Yb	1.66 (0.14)	0.07		0.90–3.66	0.12		0.68–1.55	0.06		0.05–0.72	0.06		0.17–0.53	0.04		0.10–0.35	0.04		0.10–0.35	
Lu	0.23 (0.02)	0.02		0.10–0.52	0.03		0.12–0.22	0.01		0.01–0.14	0.01		0.01–0.14	0.01		0.02–0.06	0.01		0.02–0.06	
Y	14.57 (0.58)	0.04		9.56–25.66	0.10		5.02–11.89	0.07		0.11–	0.63		1.61–3.07	0.03		0.73–1.68	0.03		0.73–1.68	

(a) all values in ppm

(b) calculated ppm values from EMP weight percent data (Choi et al., 2006b; Jean unpublished data)

b.d. = below detection

n.a. = not available

*Errors and detection limits are calculated on a sample-by-sample basis. Bold values in Shervais and Jean-EA-2 were used to complete this table.

Table A-3. Results from fluid addition calculation at 0.5% melt increment of RAM source

	Abysal			Stony Creek			Burro Mountain			Del Puerto Canyon		
	Ccpx, model	Cwr,add	Ccpx,add	Ccpx, model	Cwr,add	Ccpx,add	Ccpx, model	Cwr,add	Ccpx,add	Ccpx, model	Cwr,add	Ccpx,add
B	0.006	1.56	1.92	0.000	3.21	3.96	0.000	3.41	4.21	0.000	2.09	2.58
Li	0.561	1.75	1.55	0.326	3.32	2.94	0.404	3.28	2.90	0.331	3.31	2.93
Rb	0.000	136.2	0.87	0.000	15.7	0.10	0.000	u.n.	u.n.	0.000	u.n.	u.n.
Ba	0.000	995.8	1.39	0.000	86.2	0.12	0.000	2801.2	3.90	0.000	210.7	0.29
Th	0.000	0.03	0.01	0.000	0.04	0.01	0.000	0.01	0.00	0.000	0.01	0.00
Be	0.001	u.n.	u.n.	0.000	u.n.	u.n.	0.000	u.n.	u.n.	0.000	u.n.	u.n.
Pb	0.000	0.56	0.46	0.000	0.23	0.19	0.000	0.10	0.08	0.000	0.41	0.34
Sr	5.841	0.23	0.90	0.000	0.10	0.40	0.003	0.82	3.15	0.000	0.16	0.62
Nb	0.232	-0.03	-0.12	0.000	0.01	0.06	0.001	0.02	0.09	0.000	0.01	0.04
Zr	9.709	-1.15	-3.62	0.018	0.02	0.05	0.179	u.n.	u.n.	0.016	0.03	0.10
Hf	0.397	0.00	-0.01	0.006	0.03	0.12	0.031	0.01	0.04	0.006	0.00	0.02
Ti	1695	112	317	262	-13	-36	596	-56	-157	281	-21	-59
Cr	2940	2729	3045	4009	1623	1811	3712	2459	2745	4127	1143	1276
Sc	34.2	12.5	25.9	35.4	14.7	30.6	36.5	8.0	16.6	36.6	12.4	25.7
V	292.1	-8.4	-30.9	300.1	4.1	14.7	323.2	-17.5	-64.0	320.7	-9.0	-33.0
La	0.120	0.00	-0.01	0.000	0.00	0.01	0.000	u.n.	u.n.	0.000	0.00	0.01
Ce	0.827	-0.06	-0.26	0.000	0.00	0.01	0.003	0.00	0.02	0.000	0.01	0.02
Pr	0.152	0.01	0.03	0.000	0.00	0.01	0.001	0.00	0.01	0.000	u.n.	u.n.
Nd	0.888	0.17	0.71	0.000	u.n.	u.n.	0.006	u.n.	u.n.	0.000	0.00	0.02
Sm	0.759	0.06	0.30	0.015	0.02	0.09	0.080	0.01	0.04	0.016	0.00	0.02
Eu	0.287	0.04	0.19	0.009	0.00	0.00	0.036	u.n.	u.n.	0.009	0.00	0.00
Gd	1.147	0.04	0.17	0.058	0.03	0.14	0.165	0.01	0.03	0.052	0.01	0.03
Tb	0.262	0.02	0.10	0.025	0.00	0.01	0.051	0.00	0.02	0.021	0.00	0.01
Dy	1.810	0.20	0.88	0.286	0.02	0.07	0.444	0.03	0.13	0.226	0.01	0.03
Ho	0.404	0.04	0.18	0.074	0.01	0.02	0.109	0.01	0.04	0.059	0.00	0.01
Er	1.172	0.13	0.51	0.240	0.03	0.12	0.335	0.02	0.09	0.192	0.02	0.06
Tm	0.181	0.02	0.06	0.040	0.01	0.03	0.057	0.00	0.01	0.033	0.00	0.01
Yb	1.095	0.18	0.58	0.354	0.04	0.13	0.430	0.02	0.05	0.296	0.01	0.04
Lu	0.175	0.02	0.06	0.054	0.01	0.03	0.066	0.00	0.00	0.045	0.00	0.01
Y	13.871	0.35	1.49	2.838	0.00	0.00	4.251	-0.02	-0.07	2.375	-0.03	-0.13

u.n. = undefined: element was below detection limit, therefore could not model FME enrichment

Table A-4. Fluid-mobile element composition of fluid added to the mantle wedge

	DMM	Abyssal	SSZ		
	S&S 2004	Cwr,add	Cwr,add AVG	Cwr,add MIN	Cwr,add MAX
B	0.06	1.56	2.90	2.09	3.41
Li	0.7	1.75	3.30	3.28	3.32
Rb	0.088	136.2	15.7	15.7	15.7
Ba	1.2	996	1033	86	2801
Th	0.014	0.03	0.02	0.01	0.04
Pb	0.023	0.56	0.25	0.10	0.41
Sr	9.8	0.23	0.36	0.10	0.82

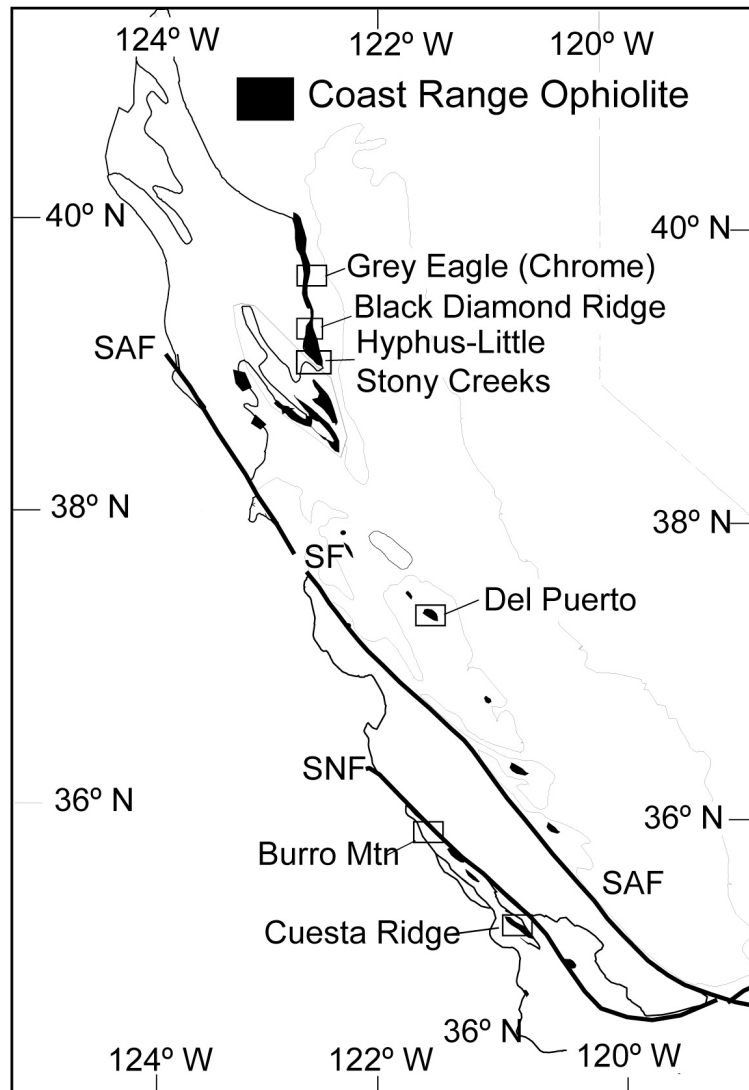


Figure A-1. Geologic sketch map of California showing the location of Coast Range ophiolite localities sampled as part of this project. SF: San Francisco, SAF: San Andreas fault, SNF: Sur-Nacimiento fault.

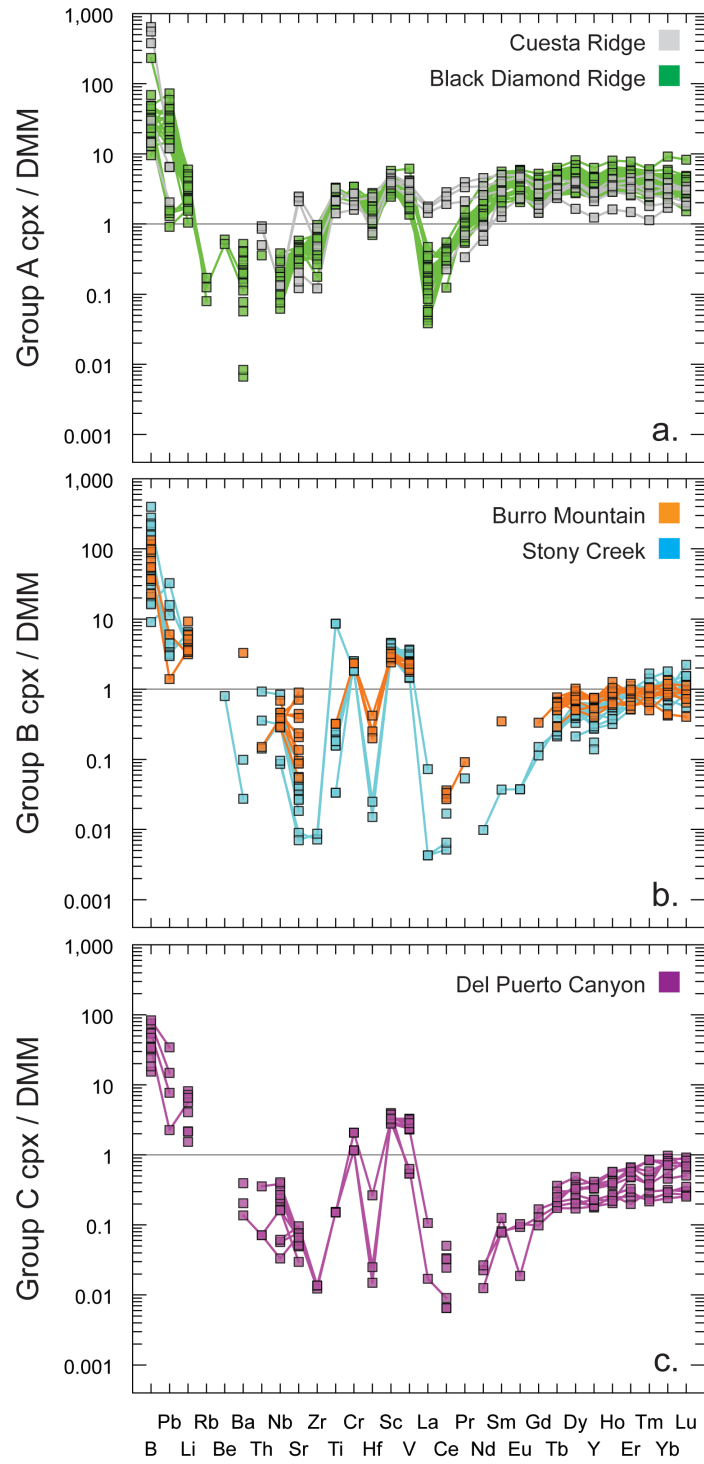


Figure A-2. Trace element concentrations in clinopyroxenes from five supra-subduction ophiolite bodies (Coast Range ophiolite, California, USA) analysed by laser ablation ICP-MS. All data normalized to the depleted MORB mantle (DMM) of Salters and Stracke (2004). (a) Group A samples – abyssal-like lherzolites with low Cr/Al ratios in spinel, (b) Group B samples – depleted harzburgites with intermediate Cr/Al ratios in spinel, and (c) Group C samples – ultra-depleted harzburgites with high Cr/Al ratios in spinel.

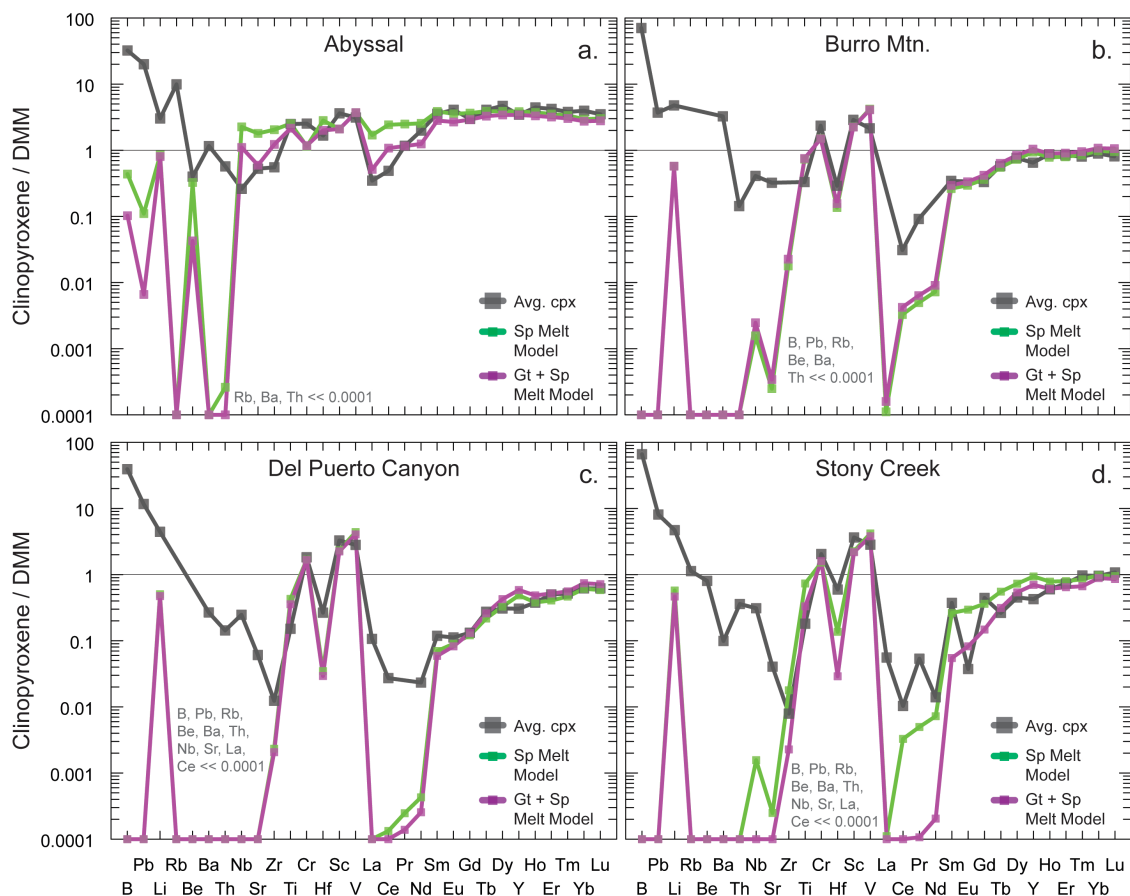


Figure A-3. Melt models of a DMM-source compared to an average of observed concentrations (grey squares). Spinel melt model (green squares) and Garnet + Spinel melt model (magenta squares). Elements plotted on lower axis are all less than $0.0001 \times$ DMM (effectively zero). Amounts of partial melting for each location: (a) abyssal: 2% spinel or 1% garnet+3% spinel facies; (b) Burro Mountain: 15% spinel or 1% garnet+14% spinel; (c) Del Puerto: 19% spinel or 5% garnet+17% spinel; (d) Stony Creek: 15% spinel or 8% garnet+15% spinel.

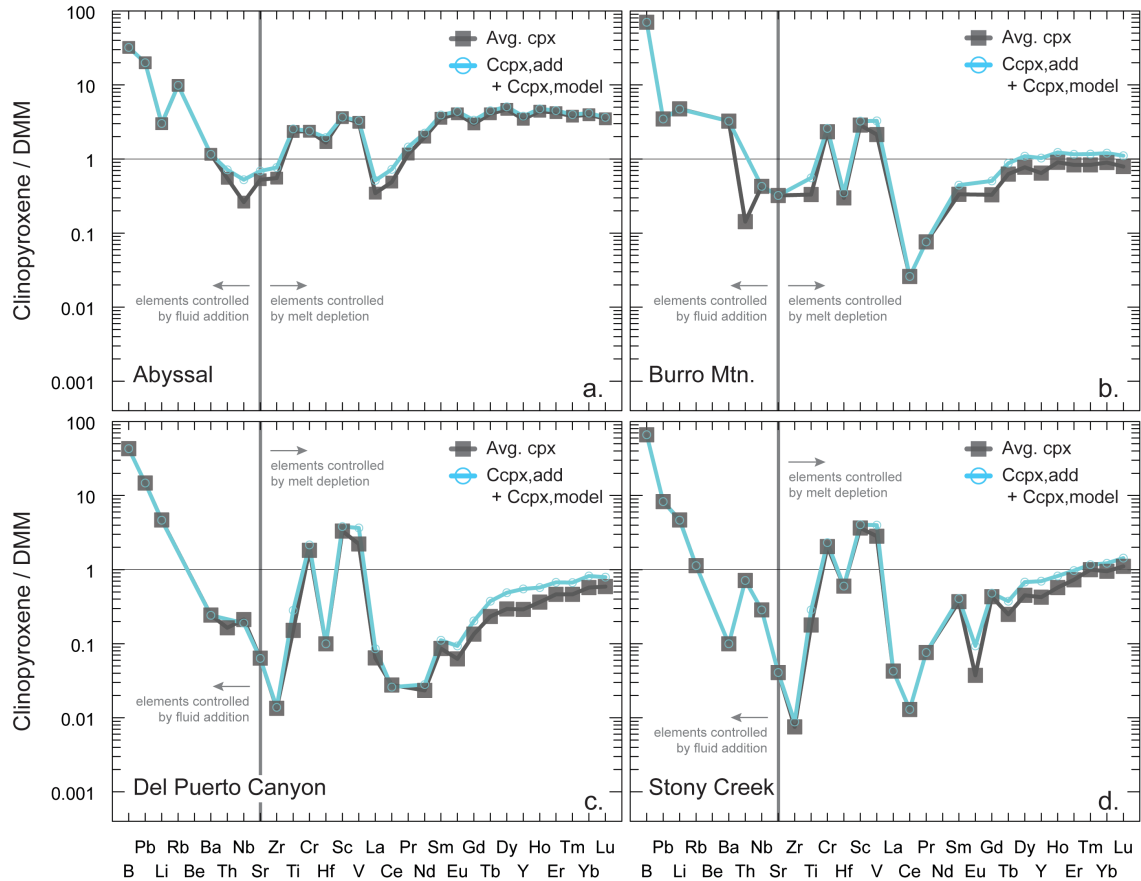


Figure A-4. DMM-normalized compositions of the fluid-added to the clinopyroxene (from equation 4) plus the clinopyroxene melt model (equation 1) compared to observed compositions (see equation 3). The observed fits show that our model for fluid-mobile element addition captures the concentrations of these elements added to the mantle wedge during melting, as reflected in the residual pyroxene compositions.

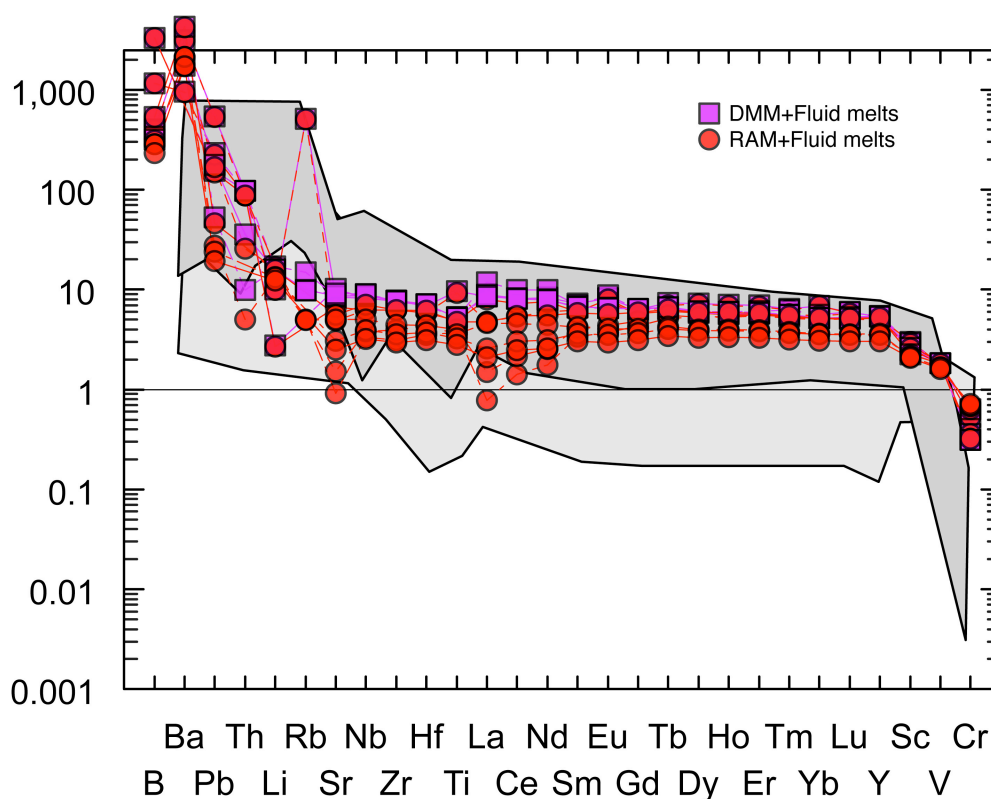


Figure A-5. Model volcanic arc melt compositions derived from FME-enriched sources as calculated in text ($C_{0,wr} + C_{wr,add}$) compared to primitive arc volcanics and boninites. Squares = 10% non-modal batch melt of DMM + Fluid for each locale; circles = 10% non-modal batch melt of refractory arc mantle (RAM) formed by early garnet phase melting. In all cases, fluid composition added is for 0.5% fractional melt. The correspondence of the model arc volcanic melts with primitive arc volcanics shows that our algorithm for calculating FME addition is consistent with our inferred process of continuous FME enrichment during melting. Note that melts derived from the DMM source have flat REE patterns, whereas melts derived from the RAM sources show light REE depletion, similar to boninites; however, all sources are FME enriched. Normalized to DMM (Salters and Stracke, 2004). Data sources: Kuroda et al., 1978; Shiraki et al., 1980; Jenner et al., 1987; Arculus et al., 1992; Gill et al., 1992; Pearce et al., 1992; Matsumoto et al., 1993; Taylor et al., 1994; Hochstaedter et al., 2000; Münker, 2000.

APPENDIX B
SNAKE RIVER PLAIN - WENDELL RASA FLOW GROUP
STATISTICAL ANALYSIS

Other drill cores in the Snake River Plain, e.g., WO2 and NPRES at INL (Shervais et al. 2006a), Test Area North (Geist et al. 2002a,b), and USGS-132 (Miller and Hughes 2009) display geochemical cycles. These cycles have been defined via MgO versus depth plots, where decreasing MgO up-section is viewed as a sign of fractionation and increasing MgO up-section is viewed as a sign of recharge. These cycles are inferred to represent fractionation and recharge of basaltic magma in a series of sill-like layered mafic intrusions located in the middle crust.

Wendell RASA major element geochemical trends (Chapter 4) shows that it is possible to group each of the Wendell RASA lavas into 11 flow groups. Flow Group 1 (3.1 – 13.6 m; 4 flows), Flow Group 2 (27.3 – 32.4 m; 5 flows), Flow Group 3 (36.2 – 54.6 m; 5 flows), Flow Group 4 (59.7 – 85.8 m; 4 flows), Flow Group 5 (74.8 – 116.1 m; 11 flows), Flow Group 6 (187.7 – 196.8 m; 2 flows), Flow Group 7 (211.9 – 227.9 m; 4 flows), Flow Group 8 (229.9 – 242.4 m; 4 flows), Flow Group 9 (252.9 – 262.9 m; 6 flows), Flow Group 10 (266.4 – 285.9 m; 10 flows), and Flow Group 11 (293.3 – 322.4 m; 7 flows).

The question remains “are the proposed geochemical divisions statistically significant?” To answer this question, linear regressions were performed on the geochemical data plotted as a function of depth. If the goodness of fit is perfect, then the coefficient of determination (r^2) should equal 1; lower r^2 values represent bad fits of data to the model. This appendix discusses the regression models performed on Snake River and Idaho Group flow groups and their implications.

Figure B-1 displays regression models for the Snake River Group section of the Wendell RASA drill core. Flow Group 1 consists of 4 lava flows and has an $r^2 = 0.0134$. However, flow 3 from this group has a different MgO-content than the flows above or below it (fig. B-1a). If this flow were removed from the regression, the r^2 value increases to 0.5386 (fig. B-1, inset). Since this unit is nearest to the surface, it might be possible to identify the vent from which this flow originated, in order to determine whether it is different from the rest of the group. Flow Group 2, overall, has an r^2 value of 0.3262 (fig. B-1b). Again, the first lava flow in this unit is separated from the rest of the group by almost 3 meters; if this flow were removed from the regression the

goodness of fit increases to 0.7421 (fig. B-1, inset). Flow Groups 3, 4, and 5 all have a high goodness of fit, e.g., r^2 of 0.9036, 0.9465, and 0.8601, respectively (fig. B-1c,d,e).

Idaho Group basalts offer similar relationships to the Snake River Group (fig. B-2). Flow Group 6 was not regressed because it only contains two samples, but it is a possible recharge group. This is also endorsed by its TiO_2 trend. Flow Groups 7 and 8 have a high goodness of fit: 0.935 and 0.8164, respectively (fig. B-2a,b). Flow Group 9 has a low goodness of fit ($r^2=0.0384$; fig. B-2c). Similarly, Flow Group 10 has a low goodness of fit overall ($r^2=0.335$; fig. B-2d). It is unclear whether Flow Group 9 can be broken into smaller sub-units, which would increase the goodness of fit; however, unlike Flow Group 9, Flow Group 10 can definitely be divided into 3 sub-units, therefore increasing the goodness of fit for each sub-unit. Unit 11 has an r^2 of 0.7592 (fig. B-2e).

Overall, the proposed flow group divisions based on geochemistry are strong. However, one point of contention remains: that is the interleaving of Flow Groups 4 and 5. This has never been documented before in SRP drill cores. An alternate interpretation of these two groups such as viewing flow 16b as a separate group, followed by a separate cycle of fractionation-recharge-fractionation recharge cycle, or alternatively lava flows 16a to 8 as a complex cycle would be plausible if these eruptions originated from a single volcano (cf. Chapter 4). This is clearly not the case in the central SRP, where lavas erupting from vents up 20 km's away, are flowing over the future drill site, so a complex geochemical pattern is expected. In addition, the 3 lava flows that overlie flow 16b, continues the fractionation trend observed for Flow Group 4. The 3 lava flows that lie above the sedimentary unit at ~ 70 mbs, continue the fractionation trend started with flow 16b. In the alternate scenario this would be considered a coincidence. We feel our interpretation best represents the data, but acknowledge that it is possible for each cycle to represent distinct events.

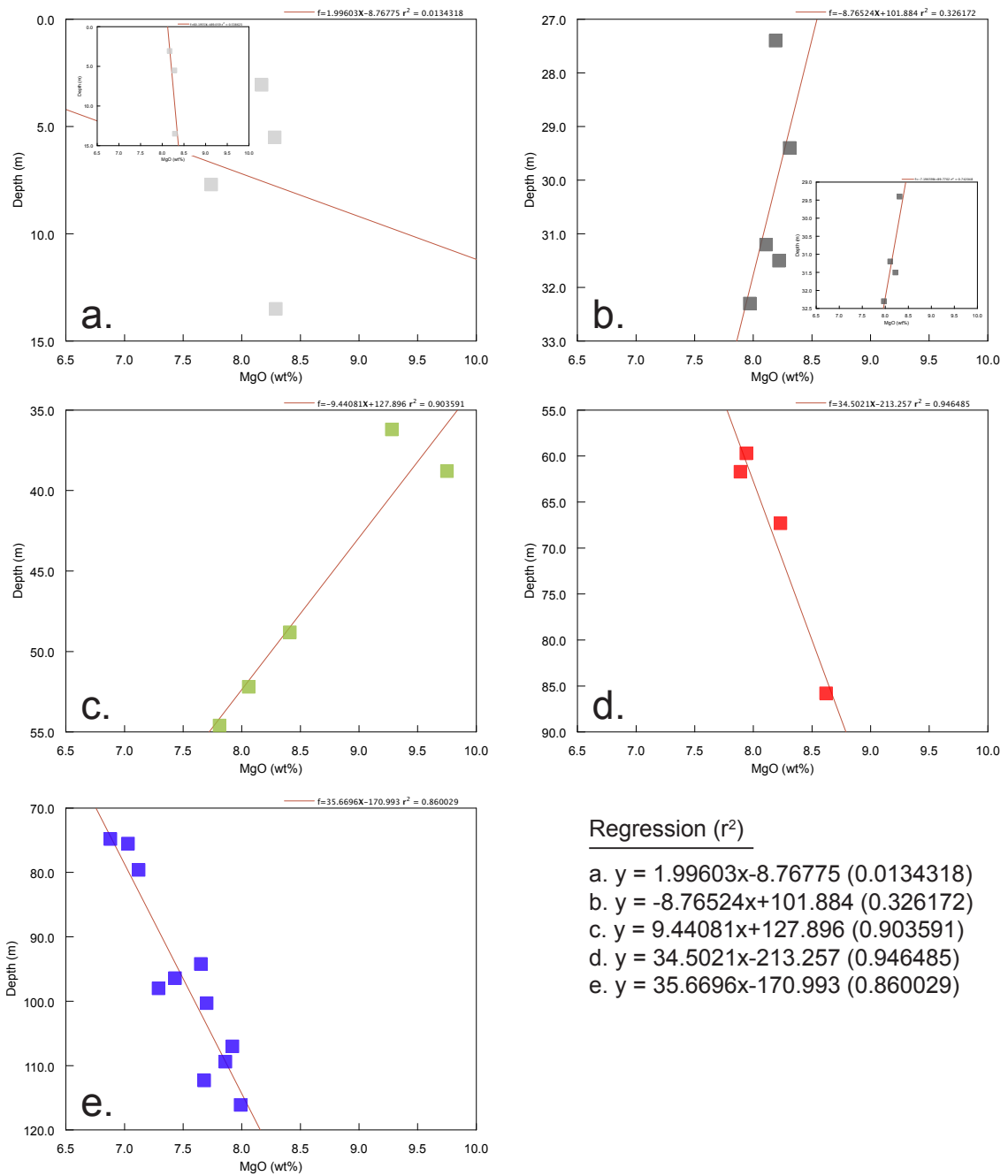


Figure B-1. Regression analysis of Snake River Group lava flows.

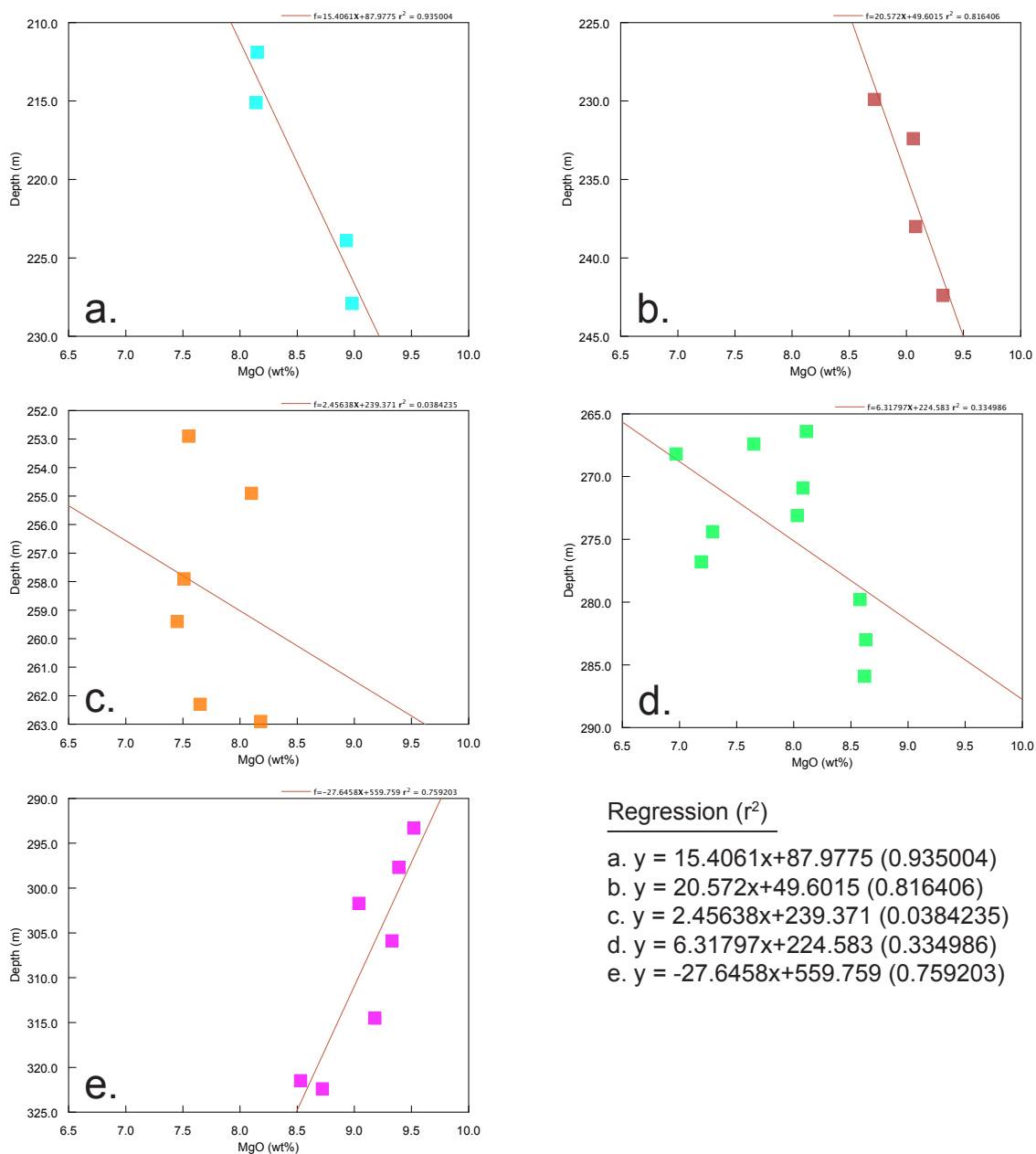


Figure B-2. Regression analysis of Idaho Group lava flows.

APPENDIX C

CO-AUTHOR AND JOURNAL REPRINT RELEASE LETTERS

MARLON JEANUtah State University
Department of Geology
Logan UT 84322-4505T (435) 512-7690
F (435) 797-1588

July 5, 2011
Sung Hi Choi
Associate Professor
Dept of Earth and Environmental Sciences
Chungnam National University
79 Daehangno, Yuseong-gu
Daejeon 305-764, S. Korea

Dear Dr. Choi,

I am in the process of preparing my dissertation in the Geology department at Utah State University. I hope to complete my dissertation in the summer of 2011.

I am requesting your permission to include the attached material as shown. I will include acknowledgments and/or appropriate citations to your work as shown and copyright and reprint rights information in a special appendix.

Please indicate your approval of this request by signing in the space provided, attaching any other form or instruction necessary to confirm permission. If you charge a reprint fee for use of your material, please indicate that as well. If you have any questions, please call at the number above.

I hope you will be able to reply immediately. If you are not the copyright holder, please forward my request to the appropriate person or institution.

Thank you for your cooperation,

Marlon Jean



I hereby give permission to Marlon Jean to reprint the following material in his dissertation:

Jean MM, Shervais JW, Choi SH, Mukasa SB (2010) Melt Extraction and Melt Refertilization in Mantle Peridotite of the Coast Range Ophiolite: An LA-ICP-MS Study. Contributions to Mineralogy and Petrology, vol. 159, no. 1, p. 113 – 136

MARLON JEANUtah State University
Department of Geology
Logan UT 84322-4505T (435) 512-7690
F (435) 797-1588

July 1, 2011
Samuel Mukasa
Professor of Geology
Dean of CEPS
University of New Hampshire
214 James Hall
56 College Road
Durham, NH 03824

Dear Dr. Mukasa,

I am in the process of preparing my dissertation in the Geology department at Utah State University. I hope to complete my dissertation in the summer of 2011.

I am requesting your permission to include the attached material as shown. I will include acknowledgments and/or appropriate citations to your work as shown and copyright and reprint rights information in a special appendix.

Please indicate your approval of this request by signing in the space provided, attaching any other form or instruction necessary to confirm permission. If you charge a reprint fee for use of your material, please indicate that as well. If you have any questions, please call at the number above.

I hope you will be able to reply immediately. If you are not the copyright holder, please forward my request to the appropriate person or institution.

Thank you for your cooperation,

Marlon Jean



Samuel B. Mukasa 7/1/2011

I hereby give permission to Marlon Jean to reprint the following material in his dissertation:

Jean MM, Shervais JW, Choi SH, Mukasa SB (2010) Melt Extraction and Melt Refertilization in Mantle Peridotite of the Coast Range Ophiolite: An LA-ICP-MS Study. Contributions to Mineralogy and Petrology, vol. 159, no. 1, p. 113 – 136

MARLON JEANUtah State University
Department of Geology
Logan UT 84322-4505

T (435) 512-7690

F (435) 797-1588

October 17, 2011
Duane E. Champion
US Geological Survey
345 Middlefield Rd.
Menlo Park CA 94025

Dear Dr. Champion,

I am in the process of preparing my dissertation in the Geology department at Utah State University. I am requesting your permission to include the attached material as shown. I will include acknowledgments and/or appropriate citations to your work as shown and copyright and reprint rights information in a special appendix.

Please indicate your approval of this request by signing in the space provided, attaching any other form or instruction necessary to confirm permission. If you charge a reprint fee for use of your material, please indicate that as well. If you have any questions, please call at the number above.

I hope you will be able to reply immediately. If you are not the copyright holder, please forward my request to the appropriate person or institution.

Thank you for your cooperation,

Marlon Jean

A handwritten signature in black ink that reads "Duane E. Champion". The signature is written in a cursive style and is positioned above a solid horizontal line.

I hereby give permission to Marlon Jean to reprint the following material in his dissertation:

Jean MM, Shervais JW, Champion DE (2011) Early Pliocene to Quaternary Basalts from the Wendell RASA test well: Assimilation-Fractionation-Recharge processes of the central Snake River Plain, Idaho. Submitted to Bulletin of Volcanology.

**SPRINGER LICENSE
TERMS AND CONDITIONS**

Jun 23, 2011

This is a License Agreement between Marlon M Jean ("You") and Springer ("Springer") provided by Copyright Clearance Center ("CCC"). The license consists of your order details, the terms and conditions provided by Springer, and the payment terms and conditions.

All payments must be made in full to CCC. For payment instructions, please see information listed at the bottom of this form.

License Number	2694940998001
License date	Jun 23, 2011
Licensed content publisher	Springer
Licensed content publication	Contributions to Mineralogy and Petrology
Licensed content title	Melt extraction and melt refertilization in mantle peridotite of the Coast Range ophiolite: an LA-ICP-MS study
Licensed content author	Marlon M. Jean
Licensed content date	Jan 1, 2009
Volume number	159
Issue number	1
Type of Use	Thesis/Dissertation
Portion	Full text
Number of copies	1
Author of this Springer article	Yes and you are the sole author of the new work
Order reference number	
Title of your thesis / dissertation	The Chemical Geodynamics of Oceanic and Continental Lithosphere
Expected completion date	Jul 2011
Estimated size(pages)	200
Total	0.00 USD

Terms and Conditions

Introduction

The publisher for this copyrighted material is Springer Science + Business Media. By clicking "accept" in connection with completing this licensing transaction, you agree that the following terms and conditions apply to this transaction (along with the Billing and

Payment terms and conditions established by Copyright Clearance Center, Inc. ("CCC"), at the time that you opened your Rightslink account and that are available at any time at <http://myaccount.copyright.com>).

Limited License

With reference to your request to reprint in your thesis material on which Springer Science and Business Media control the copyright, permission is granted, free of charge, for the use indicated in your enquiry. Licenses are for one-time use only with a maximum distribution equal to the number that you identified in the licensing process.

This License includes use in an electronic form, provided it is password protected or on the university's intranet, destined to microfilming by UMI and University repository. For any other electronic use, please contact Springer at (permissions.dordrecht@springer.com or permissions.heidelberg@springer.com)

The material can only be used for the purpose of defending your thesis, and with a maximum of 100 extra copies in paper.

Although Springer holds copyright to the material and is entitled to negotiate on rights, this license is only valid, provided permission is also obtained from the (co) author (address is given with the article/chapter) and provided it concerns original material which does not carry references to other sources (if material in question appears with credit to another source, authorization from that source is required as well). Permission free of charge on this occasion does not prejudice any rights we might have to charge for reproduction of our copyrighted material in the future.

Altering/Modifying Material: Not Permitted

However figures and illustrations may be altered minimally to serve your work. Any other abbreviations, additions, deletions and/or any other alterations shall be made only with prior written authorization of the author(s) and/or Springer Science + Business Media. (Please contact Springer at permissions.dordrecht@springer.com or permissions.heidelberg@springer.com)

Reservation of Rights

Springer Science + Business Media reserves all rights not specifically granted in the combination of (i) the license details provided by you and accepted in the course of this licensing transaction, (ii) these terms and conditions and (iii) CCC's Billing and Payment terms and conditions.

Copyright Notice:

Please include the following copyright citation referencing the publication in which the material was originally published. Where wording is within brackets, please include verbatim.

"With kind permission from Springer Science+Business Media: <book/journal title, chapter/article title, volume, year of publication, page, name(s) of author(s), figure number(s), and any original (first) copyright notice displayed with material>."

Warranties: Springer Science + Business Media makes no representations or warranties

with respect to the licensed material.

Indemnity

You hereby indemnify and agree to hold harmless Springer Science + Business Media and CCC, and their respective officers, directors, employees and agents, from and against any and all claims arising out of your use of the licensed material other than as specifically authorized pursuant to this license.

No Transfer of License

This license is personal to you and may not be sublicensed, assigned, or transferred by you to any other person without Springer Science + Business Media's written permission.

No Amendment Except in Writing

This license may not be amended except in a writing signed by both parties (or, in the case of Springer Science + Business Media, by CCC on Springer Science + Business Media's behalf).

Objection to Contrary Terms

Springer Science + Business Media hereby objects to any terms contained in any purchase order, acknowledgment, check endorsement or other writing prepared by you, which terms are inconsistent with these terms and conditions or CCC's Billing and Payment terms and conditions. These terms and conditions, together with CCC's Billing and Payment terms and conditions (which are incorporated herein), comprise the entire agreement between you and Springer Science + Business Media (and CCC) concerning this licensing transaction. In the event of any conflict between your obligations established by these terms and conditions and those established by CCC's Billing and Payment terms and conditions, these terms and conditions shall control.

Jurisdiction

All disputes that may arise in connection with this present License, or the breach thereof, shall be settled exclusively by the country's law in which the work was originally published.

CURRICULUM VITAE

EDUCATION

- 2012 Doctor of Philosophy: The Chemical Evolution of Continental and Oceanic Lithosphere: Case Studies in the US Cordillera
Utah State University
Dr. John Shervais, Principal Advisor
- 2007 Master of Science: The Central Sierra Nevada volcanic field of California: A Geochemical Study of a Transitional Arc
California State University, Fresno
Dr. Keith Putirka, Principal Advisor
- 2004 Bachelor of Science
University of Michigan, Ann Arbor
- 2000 Diploma – High Point High School, Beltsville, Maryland

PRINCIPAL INTERESTS

Aqueous Geochemistry	Volcanology
Igneous Petrology	X-Ray Fluorescence
Isotope Geochemistry	Electron Microprobe
Mineral Inclusions	ICP-MS: Solution and Laser
Mineral Petrography	Scientific Drilling

PROFESSIONAL ORGANIZATIONS

Geological Society of America
American Geophysical Union
Mineralogical Society of America

PUBLICATIONS - REFERRED

In print

no. of citations: 13

4. Putirka KD, **Jean MM**, Cousens B, Sharma R, Torrez G, Carlson C (2012) Cenozoic Volcanism in the Sierra Nevada and Walker Lane, California, and a New Model for Lithosphere Degradation. *Geosphere*, v. 8, no. 2, doi:10.1130/GES00728.1
3. Shervais JW, Evans JP, Christiansen EJ, Schmitt DR, Kessler JA, Potter KE, **Jean MM**, Sant CJ, Freeman TG (2011) Project Hotspot – The Snake River Scientific Drilling Project. *Geothermal Resources Council Transactions*, v. 35, p. 995–1003.

2. **Jean MM**, Shervais JW, Choi SH, Mukasa SB (2010) Melt Extraction and Melt Refertilization in Mantle Peridotite of the Coast Range Ophiolite: An LA-ICP-MS Study. *Contributions to Mineralogy and Petrology*, v. 159, no. 1, p. 113–136.

1. Kesler SE, Reich M, **Jean MM** (2007) Geochemistry of fluid inclusion brines from Earth's oldest Mississippi Valley-type (MVT) deposits, Transvaal Supergroup, South Africa. *Chemical Geology*, v. 237, p. 274–288.

Submitted

Jean MM, Shervais JW, Champion DE Early Pliocene to Quaternary Basalts from the Wendell RASA test well: Assimilation-Fractionation-Recharge processes of the central Snake River Plain, Idaho (*Bulletin of Volcanology*)

Jean MM, Hanan BB, Shervais JW Multi-component mixing for Yellowstone–Snake River Plain basalts: Implications for sub–continental lithospheric mantle sources and their interaction with the Yellowstone hotspot (*EPSL*)

Shervais JW, **Jean MM** Inside the Subduction Factory: Modeling fluid mobile trace element additions to the mantle wedge above a subduction zone (*Geochimica et Cosmochimica Acta*)

In Preparation

Jean MM, Shervais JW The Role of Orthopyroxene in the middle-Jurassic Cordilleran Mantle Wedge: A View from the Coast Range Ophiolite, California

GEOLOGIC MAPS PRODUCED

2008 Geologic Map of the Senter and Black Ridge Crater 7.5' quadrangles, Lincoln County, Idaho (1/24000)

PRESENTED WORKS

American Geophysical Union

2011 Plume-Lithosphere Interaction beneath the Snake River Plain, Idaho: Constraints from Pb, Sr, Nd, and Hf Isotopes

2010 Fluid-Mobile Element Enrichment in the Mantle Wedge of Subduction Zones: A View from the Coast Range Ophiolite, California

2010 Space-Time-Isotopic Trends of Snake River Plain Basalts

2008 Melt Extraction and Melt Refertilization in Mantle Peridotite of the Coast Range Ophiolite: An LA-ICP-MS Study

2008 In-situ LA-ICP-MS Analysis of Pyroxene in the Peridotite of the Coast Range Ophiolite, California

2006 The Central Sierra Nevada Volcanic Field: A Geochemical Study of a Transitional Arc

Geological Society of America

2010 Scientific Drilling in the Snake River Plain, Idaho: Chemical-Stratigraphic Relationships in Wendell RASA and Sugar City Drill core

2008 In-situ LA-ICP-MS Analysis of Pyroxene in the Peridotite of the Coast Range Ophiolite, California

CONFERENCE ABSTRACTS

10. **Jean MM**, Hanan BB, Shervais JW (2011) Plume-Lithosphere Interaction beneath the Snake River Plain, Idaho: Constraints from Pb, Sr, Nd, and Hf Isotopes, Abstract T51H-2474 presented at 2011 Fall Meeting, AGU, San Francisco, Calif., 5-9 Dec.
9. Lowry AR, Schutt D, Putirka KD, **Jean MM**, Perez-Gussinye M (2011) Hypothesis-testing proposed control of strain weakening by crustal quartz abundance, Abstract T54A-08 presented at 2011 Fall Meeting, AGU, San Francisco, Calif., 5-9 Dec.
8. Shervais JW, **Jean MM** (2010) Fluid-Mobile Element Enrichment in the Mantle Wedge of Subduction Zones: A View from the Coast Range Ophiolite, California, Abstract V11F-08 presented at 2010 Fall Meeting, AGU, San Francisco, Calif., 13-17 Dec.
7. **Jean MM**, Hanan BB, Shervais JW (2010) Space-Time-Isotopic Trends of Snake River Plain Basalts, Abstract V11B-2268 presented at 2010 Fall Meeting, AGU, San Francisco, Calif., 13-17 Dec.
6. **Jean MM**, Shervais JW (2010) Scientific Drilling in the Snake River Plain, Idaho: Chemical-Stratigraphic Relationships in Wendell RASA and Sugar City Drill core; GSA Abstracts with Programs, v. 42, no. 5
5. Shervais JW, Choi SH, **Jean MM**, Mukasa SB (2010) Initiation of Proto-Franciscan Subduction along a Transform Fault Zone: Evidence from Serpentinite Melange of the Coast Range Ophiolite Complex; GSA Abstracts with Programs, v. 42, no. 5
4. **Jean MM**, Choi SH, Shervais JW, Mukasa SB (2008) In-Situ LA-ICP-MS Analysis of Pyroxene in the Peridotite of the Coast Range Ophiolite, California; Eos Trans. AGU, 89 (53), Fall Meeting, T43C-2035
3. **Jean MM**, Choi SH, Shervais JW, Mukasa SB (2008) In-Situ LA-ICP-MS Analysis of Pyroxene in the Peridotite of the Coast Range Ophiolite, California; GSA Abstracts with Programs, v. 40, no. 1, p. 34
2. Shervais JW, **Jean MM**, Choi SH, Mukasa SB (2008) Geochemical Flux in the Mantle Wedge: Insights from Suprasubduction Zone Ophiolites; *Geochimica et Cosmochimica Acta*, Volume 72, Issue 12, Supplement 1, Pages A1-A1144, S1-S14
1. **Jean MM**, Putirka KD, Busby C, Hagan J (2006) The Central Sierra Nevada Volcanic Field: A geochemical study of a transitional arc; Eos Trans. AGU, 87 (52), Fall Meeting, V11A-0570

SHORT COURSES/TRAINING COURSES ATTENDED

- 2010 ICDP Training Course, Windischeschenbach, Germany - Lighting the Darkness: From Borehole Measurements to Earth Models
- 2008 Mineralogical Society of America, San Francisco, California - Minerals, Inclusions, and Volcanic Processes
- 2008 AGU Chapman Conference, Mount Shasta, California - Shallow Mantle Composition and Dynamics, Fifth International Orogenic Lherzolite Conference

PROFESSIONAL POSITIONS

- Fall 2009 Lecturer, Utah State University
- 2008 – 2010 Teaching assistant, Utah State University
- 2005 – 2007 Lab Instructor, California State University, Fresno

AWARDS

- 2010 Outstanding Graduate Researcher – Utah State University
- 2007 Outstanding Earth & Environmental Science Graduate – California State University, Fresno
- 2007 Outstanding Student Award – California State University, Fresno
- 2007 Special Recognition Award – California State University, Fresno
- 1996 Central American Young Scholar Award – The Center for the Advancement of Hispanics in Science and Engineering Education

GRANTS

- 2011 \$2000 USU - Dept. of Geology Graduate Benchmark fellowship
- 2010 \$1000 USU - Graduate Student Senate Research and Projects Grant
- 2009 \$1000 USU - J. Stewart Williams graduate fellowship
- 2006 \$2000 CSU Fresno - College of Science and Mathematics Research Award

GRADUATE ADVISORS

- | | |
|-------------------------------------|--------------------------------------|
| Lewis, S.D. (M.S) | California State University – Fresno |
| Putirka, K.D. (advisor M.S.; Ph.D.) | California State University – Fresno |
| Wakabayashi, J. (M.S) | California State University – Fresno |
| Dehler, C.M. (Ph.D.) | Utah State University |
| Evans, J.P (Ph.D.) | Utah State University |
| Hanan, B.B. (Ph.D.) | San Diego State University |
| Lowry, A. (Ph.D.) | Utah State University |
| Shervais, J.W. (advisor, Ph.D.) | Utah State University |